Study of interference between ϕ and $\Lambda(1520)$ near the photoproduction threshold

DISSERTATION
Submitted in Partial Fulfillment of
the Requirements for the Degree of
Doctor of Science

Department of Physics
Faculty of Science
Osaka University

February, *2015*

e-mail : syryu@rcnp.osaka-u.ac.jp

Abstract

The ϕ-meson production has the unique feature that the gluon dynamics dominates in the reaction process because the process is OZI suppressed due to the dominant $s\bar{s}$ structure of the ϕ-meson, which is predicted to proceed by the exchange of color singlet gluonic objects such as the Pomeron trajectory with $J^{PC} = 0^{++}$. Extrapolation of ϕ photoproduction cross sections from the high-energy region predicts a smooth energy dependence of the cross section down to the threshold energy for the reaction. However, the LEPS observation has shown a strong indication of a bump structure at around $E_\gamma = 2$ GeV. However, the bump structure from CLAS appears only at forward angles, so that resonance interpretation looks unlikely. Recent theoretical works relate this to a coupling between the ϕp and $K^+\Lambda(1520)$ channels, since the bump structure appears very close to the threshold of $\Lambda(1520)$ production.

We have measured ϕ photoproduction from protons at SPring-8. Compton backscattered photons were incident on a 150-mm thick liquid hydrogen target with linear polarization. A large-aperture dipole spectrometer (LEPS) reconstructed charged particles at forward angles. With a full data set of the LH_2 runs a new analysis on ϕ-$\Lambda(1520)$ photoproduction has been performed using kinematic fits and simultaneous fits on the K^+K^- and K^-p mass spectra with Monte-Carlo templates. Interference effects could appear as differences in ϕ photoproduction cross-sections obtained with and without the overlapped region between the ϕ and $\Lambda(1520)$ mass bands in the scatter plot of K^+K^- and K^-p masses. It should be emphasized that we have first measured ϕ-$\Lambda(1520)$ interference in $\gamma p \to K^+K^-p$ reaction near ϕ photoproduction threshold. We reconfirmed that forward differential cross sections for ϕ photoproduction show a clear bump structure at around $E_\gamma = 2$ GeV. We have observed a clear ϕ-$\Lambda(1520)$ interference in the energy ranges from 1.673 to 2.173 GeV. From the fit with the interference amplitude term, the relative phase measurement results suggest a strong constructive interference when K^+K^- pairs are observed at forward angles, while destructive interferences when protons emit at forward angles. There is a change in phase signs for the events with K^-p detected at forward angles.

PACS numbers : 25.20.Lj, 13.60.Le, 13.60.Rj, 14.20.Jn, 14.40.Be
Keywords : ϕ meson, photoproduction, interference, $\Lambda(1520)$, LEPS.

Acknowledgement

The writing of this dissertation would obviously have been impossible without the personal and practical support of numerous people. First and foremost I must thank my esteemed supervisor Takashi Nakano for his acedemic guidance and unflagging support throughour my graduate studies at Osaka. I also deeply acknowledge him for his lucid lectures on hadron physics, which actually motivated this study.

I would like to reserve this place to thank other than the members of my dissertation committee. I would like to address my deeply acknowledgements to Prof. Hideto En'yo of Nishina Center, RIKEN for supporting my graduate study under the IPS program. I also do appreciate his valuable advice, which proved to be indispensable. I would also like to thank my previous supervisor, Prof. Jung Keun Ahn of Korea University for initiating me into the field of hadron physics.

Apart from Prof. Takashi Nakano and Prof. Hideto En'yo, the other members of my dissertation committee were Prof. Masaru Yosoi, Prof. Nori Aoi, Prof. Atsushi Hosaka, Prof. Tadafumi Kishimoto. I am grateful to them for accepting the heavy task of going through my dissertation. I also appreciate their fruitful remarks that helped me to correct mistakes and finally to improve the quality of the dissertation very much.

I owe special thanks to Prof. Atsushi Hosaka of Osaka University and Prof. Seung-il Nam of Pukyung National University for theoretical predictions and comments. I also appreciate their patience in responding to some of my trivial questions.

I would like to take this time to acknowledge all of my colleagues in the LEPS collaboration. I am particularly grateful to Dr. Wen-Chen Chang of Academia Sinica, Taiwan and Dr. Jia-Ye Chen for their fruitful advice and comments on a Monte Carlo simulation. I would also like to thank Dr. Tomoaki Hotta and Dr. Hideki Kohri of RCNP, Dr. Norihito Muramatsu of ELPH, Prof. Mizuki Sumihama of Gifu University, Dr. Yuji Kato of Nagoya University, Dr. Yuji Ohashi and Dr. Schin Daté of JASRI and Mr. Yukiyoshi Kon whom I have worked most closely for their dedicate advice.

I would like to extend my thanks to whom I shared most of my stay in Japan, Ms. Mayumi Matsuda and Ms. Naohiko Otsuka of the RCNP office, for their patience in responding to my frequent questions on Japanese language and custom, which still remain in my reminiscence.

Finally, and definitely not least, I wish to acknowledge all of my family. It is impossible to express my gratitute to my parents for their encouragement and long patience throughout the long and long process.

Contents

Chapter 1

Introduction

1.1 Experimental Motivation of This Work

While many experimental efforts have been extensively performed to date for photoproduction of the ϕ vector mesons near threshold, the 2.1-GeV bump structure of forward differential cross sections still awaits a good explanation on its nature, which has first been reported by the LEPS collaboration [1]. Although Pomeron exchange is understood as a dominant mechanism of the ϕ photoproduction, there is a sizable violation of helicity conservation in both s- and t-channels, which suggests contributions from other mechanisms such as nucleon resonances, rescattering processes, and interference between ϕ and $\Lambda(1520)$ resonances [2, 3, 4]. The first interpretation with nucleon resonance has been almost ruled out by recent high-statistics data from CLAS [5]. The rescattering process could also account for the bump structure. However, recent theoretical calculation suggests a large suppression of Pomeron exchange near the threshold and the rescattering process as a dominant production mechanism. The ϕ-$\Lambda(1520)$ interference could be also a possible explanation and has never been measured to date in K^+K^-p photoproduction.

To clarify the situation the SPring-8/LEPS LH_2 data taken from the year 2002 to 2007 are analyzed. The importance of this analysis includes that event selection for $\gamma p \rightarrow K^+K^-p$ was based on the 4C-3 kinematic fit, and that the yields for ϕ and $\Lambda(1520)$ were obtained from a simultaneous fit in the $m_{K^+K^-}$ and m_{K^-p} invariant masses with templates from Monte-Carlo simulation. This self-consistent analysis makes it possible to investigate a possible interference between the ϕ and $\Lambda(1520)$.

A primary aim of this work is to first confirm the ϕ-$\Lambda(1520)$ interference and to measure the relative phase angles by building an amplitude interference function from the Breit-Wigner lineshape for the ϕ and the Monte-Carlo template distributions for the $\Lambda(1520)$ in the kinematic region which the two resonances appear. Experimental details are discussed in Chapter 2 before a full description of data analysis is described in Chapter 3. The results and conclusions come in Chapter 4, and later but not the least, the work of this dissertation is summarized in Chapter 5.

1.2 Photoproduction of ϕ Vector Meson

The ϕ is a neutral isoscalar meson at a mass of 1019.461 MeV with spin, parity and charge conjugation identical to the photon, namely, $J^{PC} = 1^{--}$ [6]. The mass difference between two kaons and the ϕ meson yields only $m_\phi - 2m_{K^\pm} \approx 32$ MeV, which implies that the decay kaons carry small average momenta of ≈ 127 MeV in the rest frame of the ϕ meson. Little phase space is available for two kaons from the ϕ decay, so the natural width of the ϕ is very small, namely 4.3 MeV.

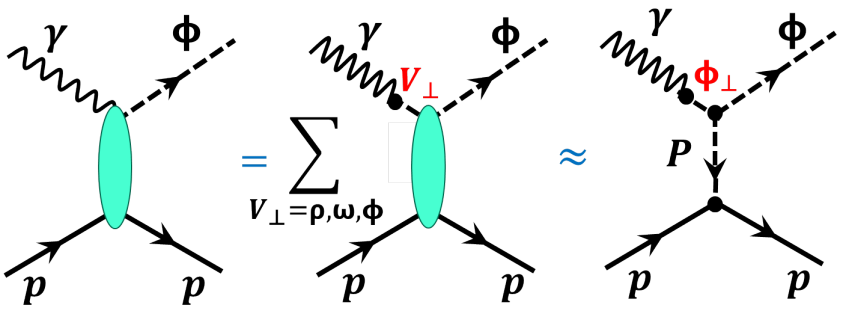

Figure 1.1: Diagrams for ϕ photoproduction in the vector dominance model

Due to the similarity of the ϕ and γ quantum numbers, the vector-meson dominance model (VDM) [7] describes an equivalence between the amplitude f_γ of the photoproduction reaction $\gamma p \to \phi p$, and that caused by a transversely polarized vector meson ($V_\perp p \to \phi p$):

$$f_\gamma(\gamma p \to \phi p) = \sum_{V'} \sqrt{\frac{\alpha}{4}\frac{4\pi}{\gamma_V^2}} \cdot f_V(V' p \to \phi p) \approx \sqrt{\frac{\alpha}{4}\frac{4\pi}{\gamma_\phi^2}} \cdot f_{\phi p \to \phi p}(q_\phi, \theta),$$

where α is the fine structure constant, $\gamma_V^2/4\pi$ is the $\gamma - V$ coupling constant, and V' represents the transverse part of the vector mesons ρ, ω, ϕ and p the target proton. We are now in a position to take only the diagonal term when contributions from mixed terms ($\rho p \to \phi p$) are assumed to be negligible.

The imaginary part of the amplitude $\mathrm{Im} f^*_{\phi p \to \phi p}(q_\phi, \theta)$ in the center of mass for forward elastic $\phi p \to \phi p$ scattering is related to the ϕp total cross section, $\sigma_{\phi p}$, by an optical theorem as $\mathrm{Im} f^*_{\phi p \to \phi p}(q_\phi, \theta = 0) = q_\phi/4\pi \cdot \sigma_{\phi p}$, where q_ϕ and θ is the ϕ-meson momentum and scattering angle in the ϕp center of mass system, respectively [8].

The $\gamma p \to \phi p$ differential cross section at $t = t_{\min}$ can be written as

$$\left.\frac{d\sigma}{dt}\right|^{\gamma p \to \phi p} = \frac{1}{64\pi s q_\gamma^2} |T^{\gamma p \to \phi p}|^2, \qquad \left.\frac{d\sigma}{dt}\right|^{\gamma p \to \phi p}_{t=0} = \frac{\alpha}{16\gamma_\phi^2} \frac{q_\phi^2}{q_\gamma^2} (1 + \alpha_\phi^2) \sigma_{\phi p}^2,$$

where $\alpha_\phi = \mathrm{Re}\ T_{\gamma p \to \phi p} / \mathrm{Im}\ T_{\gamma p \to \phi p}$ [9, 10]. The invariant reaction amplitude for the $\gamma p \to \phi p$ reaction $T^{\gamma p \to \phi p} \approx \frac{\sqrt{\pi\alpha}}{\gamma_\phi} T^{\phi p \to \phi p}$, where α is the fine structure constant, γ_ϕ is the photon coupling to the ϕ meson. The imaginary part of the Lorentz invariant scattering amplitude $T^{\phi p \to \phi p}$ is given by $\mathrm{Im} T_{\phi p \to \phi p}(\theta = 0) = -8\pi\sqrt{s}\ \mathrm{Im} f^*_{\phi p \to \phi p} = -2\sqrt{s} q_\phi \sigma_{\phi p}$.

The quark model in SU(3) flavor symmetry assigns an almost pure $\overline{s}s$ configuration to the ϕ, assuming an ideal singlet octet-mixing. If the strangeness component of the proton is small, the Okubo-Zweig-Iizuka (OZI) rule suppresses direct exchanges of quarks between the ϕ and the proton. Moreover, there are no strong s- and u-channel resonances which could couple to the ϕ, so only the t-channel exchanges with $J^{PC} = 0^{++}$ and $I = 0$ can contribute. Therefore, ϕ photoproduction is predicted to proceed by the exchange of color singlet gluonic objects such as the Pomeron trajectory which has the same quantum numbers as the vacuum.

Figure 1.2 represents the cross sections for photoproduction of vector mesons such as ρ, ω, and ϕ [11]. There exist similar increases in the cross sections for the three vector mesons at high energies. However, the near-threshold behavior of the cross sections look different. While enhanced cross sections for ρ and ω photoproduction are observed near threshold, the cross section for ϕ photoproduction indicates no such significant enhancements in the near-threshold region, which could be understood as due to the OZI suppression of pseudoscalar meson-exchange processes.

In Regge phenomenology the non-perturbative soft hadron-hadron interaction is viewed as due to exchanges of collective states called Regge poles [12, 13].

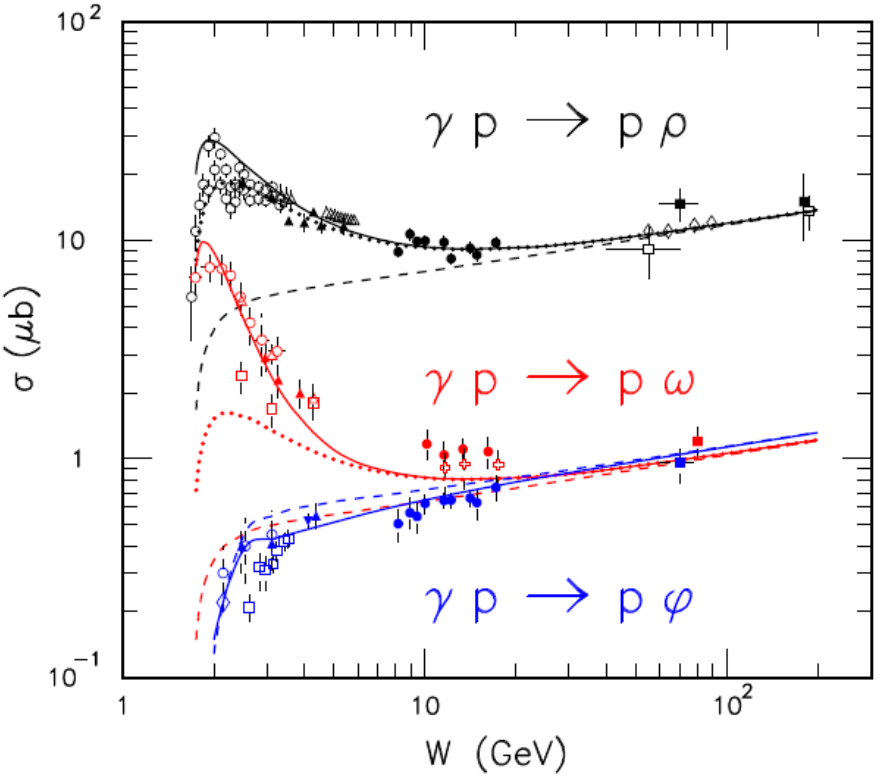

Figure 1.2: Cross sections for photoproduction of ρ, ω, and ϕ vector mesons. Dashed curves indicate Pomeron exchange contribution, while dotted curves for Pomeron and f_2 exchange contributions [11].

The Regge poles with quantum numbers of mesons form linear trajectories in the (m^2, J) plane, where m is the mass of the meson and J its spin, as shown in Fig. 1.3. The continuation of a trajectory to negative values of m^2 leads to a parametrization in terms of t:

$$\alpha(t) = \alpha_0 + \alpha' t,$$

where α_0 is the intercept and α' is the slope of the trajectory.

A special family of the poles with the quantum numbers of the vacuum is called the pomeron (P) trajectory with the parameters $\alpha_P = 1.08 + 0.25t$. There have been no known hadrons to date lying on this trajectory, and glueballs would be expected to form this trajectory. The Pomeron trajectory also provides the leading contribution to the high-energy behavior of the total cross section:

$$\sigma_{\text{tot}} = \frac{1}{s}\text{Im } A(s, t = 0) \propto s^{\alpha_P(0)-1}.$$

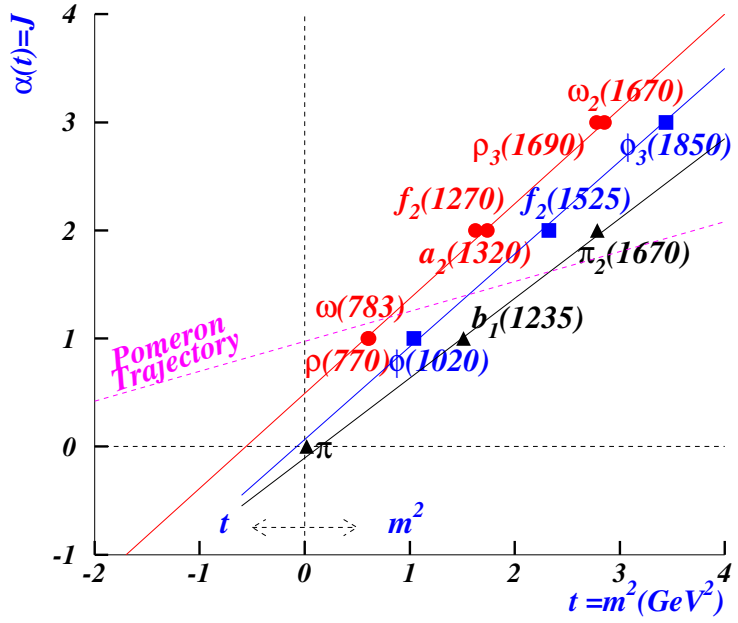

Figure 1.3: The ρ (circles), ϕ (squares), and π (triangles) trajectories are shown as well as the Pomeron trajectory displayed as a pink dashed line.

Photoproduction is a particularly interesting process for the study of diffractive reactions since the photon has both an isoscalar and an isovector component and has spin $J = 1$. On top of that, photoproduction of ϕ mesons brings a unique probe for diffractive production with pure $\bar{s}s$ contents in the initial state. The cross section for ϕ photoproduction as a function of photon energy and is about 0.5 μb and slowly rising a little as the energy increases, as shown in Fig. 1.4 [14]. For diffractive scattering with Pomeron exchange, the total cross section stays almost constant with energy and the width of the forward peak decreases only logarithmically with energy. The additional features which we expect from a diffractive process are such that it includes mainly imaginary scattering amplitude, and that the spin structure of the scattering process is dominantly s-channel helicity conserving (SCHC).

The decay angular distributions of ϕ mesons with linearly polarized photons can be viewed in the rest frame of the ϕ meson, as shown in Fig. 1.5. The production plane of $\gamma p \to \phi p$ reaction contains the x-z axes, and the decay polar and azimuthal angles of the K^+, with respect to the quantization axis, are θ and ϕ [15]. The production plane is defined perpendicular to the $\vec{p}_\gamma \times \vec{p}_\phi$, where in turn de-

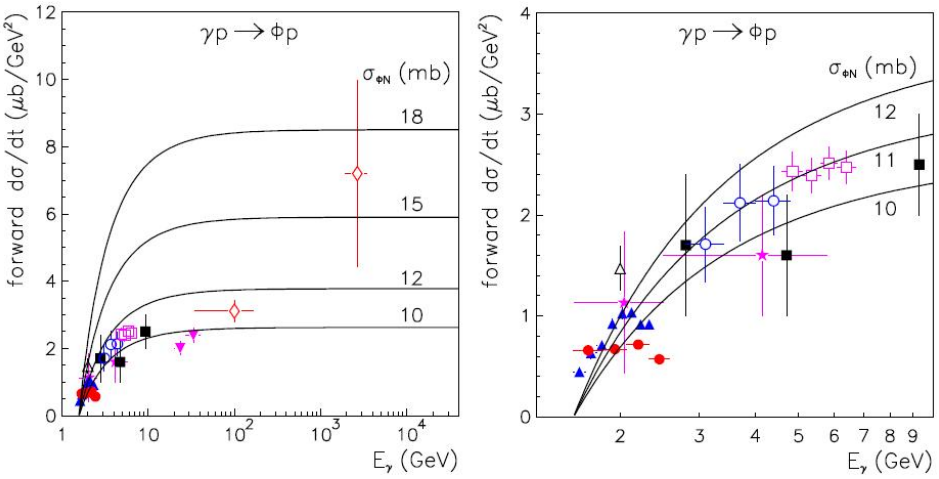

Figure 1.4: Forward differential cross sections for ϕ photoproduction near threshold.

fines the y-axis. Linear polarization P_γ is taken as $\vec{P}_\gamma = \vec{P}_\gamma(-\cos 2\Psi, -\sin 2\Psi, 0)$, where Ψ is the angle between polarization vector $\hat{\varepsilon} = (\cos\Psi, \sin\Psi, 0)$ and the production plane.

The decay angular distributions are represented in terms of nine parameters for linearly polarized photons:

$$W(\cos\theta, \phi, \Phi) = W^0(\cos\theta, \phi) - P_\gamma \cos 2\Phi W^1(\cos\theta, \phi) - P_\gamma \sin 2\Phi W^2(\cos\theta, \phi),$$

where W^0, W^1, and W^2 are defined as

$$\begin{aligned}
W^0(\cos\theta, \phi) &= \frac{3}{4\pi}\left[\frac{1}{2}(1-\rho^0_{00}) + \frac{1}{2}(3\rho^0_{00}-1)\cos^2\theta \right. \\
&- \left. \sqrt{2}\mathrm{Re}\rho^0_{10}\sin 2\theta\cos\phi - \rho^0_{1-1}\sin^2\theta\cos 2\phi\right] \\
W^1(\cos\theta, \phi) &= \frac{3}{4\pi}\left[\rho^1_{11}\sin^2\phi + \rho^1_{00}\cos^2\theta \right. \\
&- \left. \sqrt{2}\rho^1_{10}\sin 2\theta\cos\phi - \rho^1_{1-1}\sin^2\theta\cos 2\phi\right] \\
W^2(\cos\theta, \phi) &= \frac{3}{4\pi}\left[\sqrt{2}\mathrm{Im}\rho^2_{10}\sin 2\theta\cos\phi + \mathrm{Im}\rho^2_{1-1}\sin^2\theta\cos 2\phi\right],
\end{aligned}$$

where the spin-density matrix elements $\rho^i_{\lambda,\lambda'}$ $(i = 0, 1, 2)$ are related to the helicity amplitudes. ρ^0_{00} accounts for a single spin-flip transition $\lambda_\gamma \to \lambda_V = 0$, and ρ^0_{1-1} accounts for double spin-flip transitions $\lambda_\gamma \to \lambda_V = -\lambda_\gamma$. For unnatural-parity ($\pi^0$) exchange, the spin operator does not flip the helicity of the photon, i.e. the transition from $\lambda_\gamma = \pm 1$ to $\lambda_V = 0$ vanish. For natural-parity (P) exchange in the diffractive process, all but two of the density matrix elements

vanish. For 0^+ (helicity frame) and 0^- (Gottfried-Jackson frame) exchanges all but the ρ^1_{1-1} and Imρ^2_{1-1} density matrix elements are zero. Therefore, ρ^0_{00}, ρ^0_{10}, and ρ^0_{1-1} should be zero.

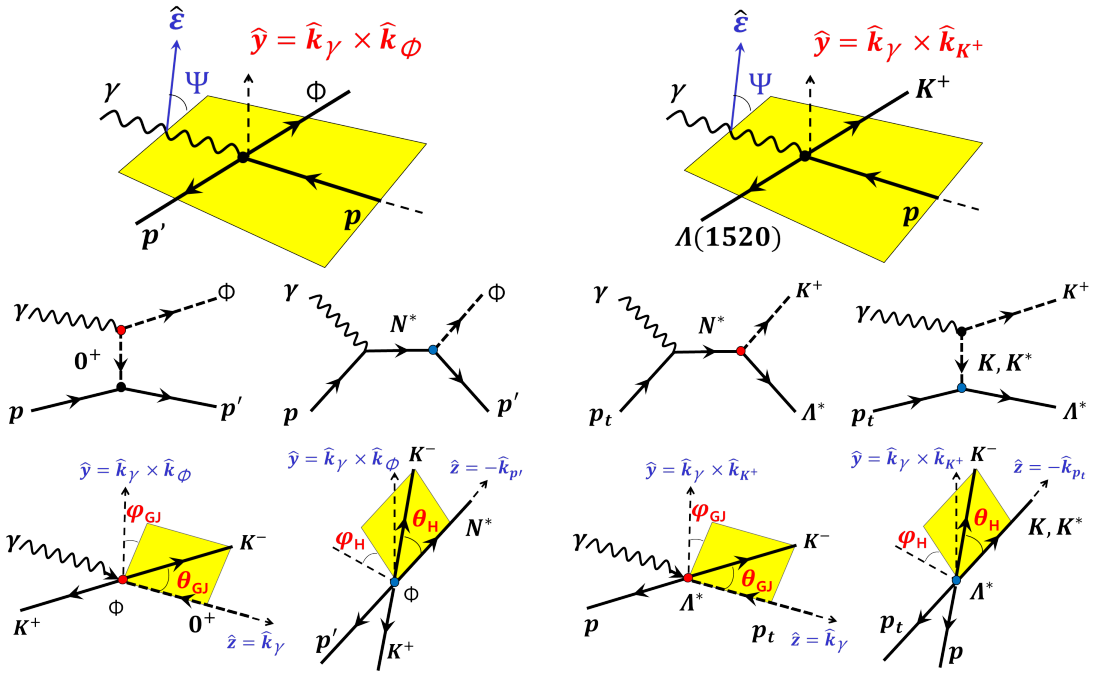

Figure 1.5: Reaction planes for ϕ and $\Lambda(1520)$ photoproduction processes in the total c.m. systems, respectively, are represented in the top two figures. Quantization axes for the decay angles in both the Gottfried-Jackson and Helicity frames are also displayed in the bottom.

Helicity conservation ensues when $\lambda_\gamma = \lambda'_V$. In the Vector Dominance Model, helicity conservation implies that only two spin-density matrix elements have non-zero values, i.e. ρ^1_{1-1} and Imρ^2_{1-1} Other 7 spin-density matrix elements are nonconserving and zero. For pure natural- and unnatural-parity exchange $|\rho^1_{1-1}| = |-\text{Im}\rho^2_{1-1}| = 0.5$. The difference between the helicity frame and the Gottfried-Jackson frame is the choice of the z- or quantization axis. In the Vector Dominance Model spin-density matrix elements should be zero but ρ^1_{1-1} and Imρ^2_{1-1}. For Pomeron exchange $(\rho^1_{1-1}, \text{Im}\rho^2_{1-1}) = (1/2, 1/2)$, while for meson exchange $(\rho^1_{1-1}, \text{Im}\rho^2_{1-1}) = (-1/2, 1/2)$ [16].

The decay angular distribution of the ϕ meson from the linearly polarized laser beam experiment, shows the familiar $\sin^2\theta\cos^2\psi$ correlation implying natural parity exchange dominance and s-channel helicity conservation in the production process. The polarization asymmetry parameter, Σ, and the parity ex-

change asymmetry P_σ [15]:

$$\Sigma = \frac{\sigma_\parallel - \sigma_\perp}{\sigma_\parallel + \sigma_\perp} = \frac{\rho^1_{11} + \rho^1_{1-1}}{\rho^0_{11} + \rho^0_{1-1}}, \qquad P_\sigma = \frac{\sigma_+ - \sigma_-}{\sigma_+ + \sigma_-} = 2\rho^1_{1-1} - \rho^1_{00},$$

where $\sigma_+(\sigma_-)$ is the cross section for $\gamma p \to \phi p$ due to natural (unnatural parity exchange. The asymmetry parameter of the ϕ photoproduction, $\Sigma \approx 1$ implies natural parity exchange and no spin-flip in the ϕ production.

1.3 Previous Measurements for ϕ Photoproduction

Early ϕ photoproduction measurements from SLAC confirmed the dominance of natural-parity (Pomeron) exchange over unnatural-parity (π) exchange [17]. Later, results from DESY [18], Cornell [19, 20], SLAC [21], Fermilab [22, 23], Daresbury [24, 25], and HERA [26, 27] have been reported mostly at high energies, as shown in Fig. 1.6

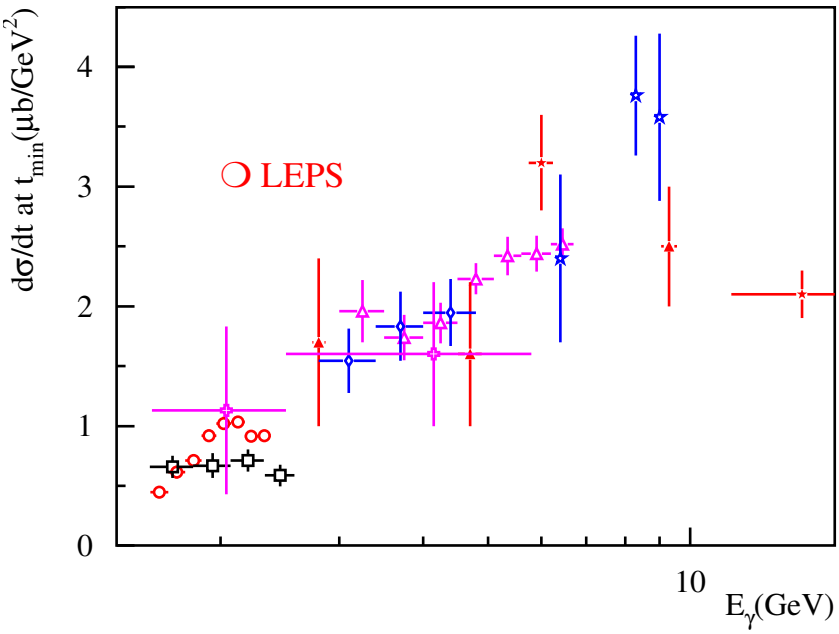

Figure 1.6: Forward differential cross sections for ϕ photoproduction near threshold.

While the early ABBHHM results [28] provided some data at low energy, the near-threshold ϕ photoproduction was first measured at Bonn [29], with more recent results from SAPHIR [30] and LEPS [1]. Although both the Bonn and SAPHIR results covered the $E_\gamma = 2.0$ GeV (or $\sqrt{s} \approx 2.15$ GeV) energy

region, the LEPS collaboration [1] first took note of a localized 'bump' around $E_\gamma \approx 2.0$ GeV, where a simple Pomeron exchange model predicts a smooth rise from threshold.

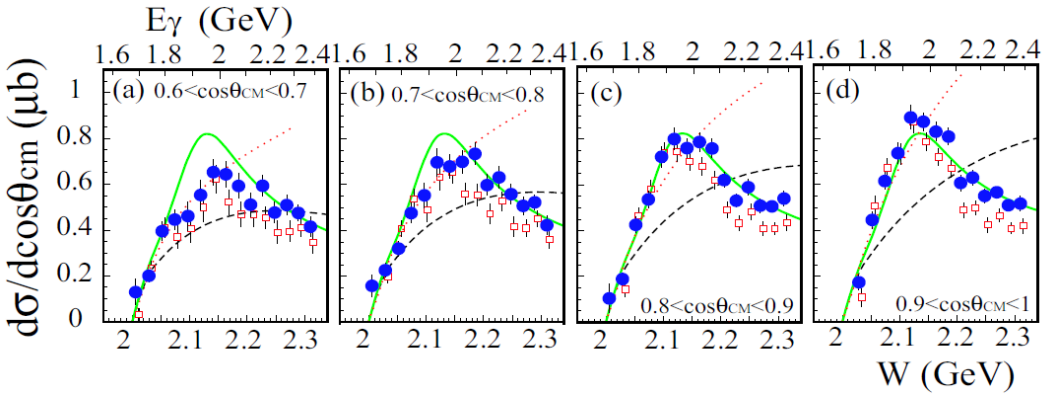

Figure 1.7: Differential cross sections for the $\vec{\gamma}p \to K^+\Lambda(1520)$ reaction at (a) $0.6 < \cos\theta^K_{\rm CM} < 0.7$, (b) $0.7 < \cos\theta^K_{\rm CM} < 0.8$, (c) $0.8 < \cos\theta^K_{\rm CM} < 0.9$, and (d) $0.9 < \cos\theta^K_{\rm CM} < 1$. The circles are the LEPS data [31]. The open squares are the results obtained by using the sideband subtraction method and are shifted by $+5$ MeV for display purposes. The solid and dashed curves are the results of calculations which fit to the present data by Nam [31]. with and without a nucleon resonance, respectively. The dotted curves are the results of calculations by Titov [32].

Recently, the LEPS collaboration [33] has published near-threshold measurements for the ρ^1 and ρ^2 spin-density matrix elements. From their ρ^1_{1-1} measurements in the Gottfried-Jackson frame, they have estimated a nonzero contribution from unnatural-parity (π, η) exchanges in the t channel, at these low energies. If ϕ photoproduction does proceed diffractively, the angular distribution of ϕ mesons produced with (polarized) photons should tell us about the spin-dependence of diffractive scattering. If the photon helicity is conserved, then one expects $\lambda_\phi = \pm 1$ in this helicity-conserving frame, resulting in a $\sin^2\theta$ distribution, while $\lambda_\phi = 0$ gives a $\cos^2\theta$ distribution. Another feature is that for natural-parity exchange the kaons emerge preferentially in the plae of the photon polarization ($\Psi \approx 0^o$), while for unnatural-parity exchange they emerge perpendicular to it ($\Psi \approx 90^o$).

The CLAS collaboration [34] also reported an interesting feature, a slight rise in the cross section at the backward angles. Very recently, high-statistics measurements of differential cross sections and spin-density matrix elements for the $\gamma p \to \phi p$ reaction have been reported from CLAS [5]. On top of that, the new

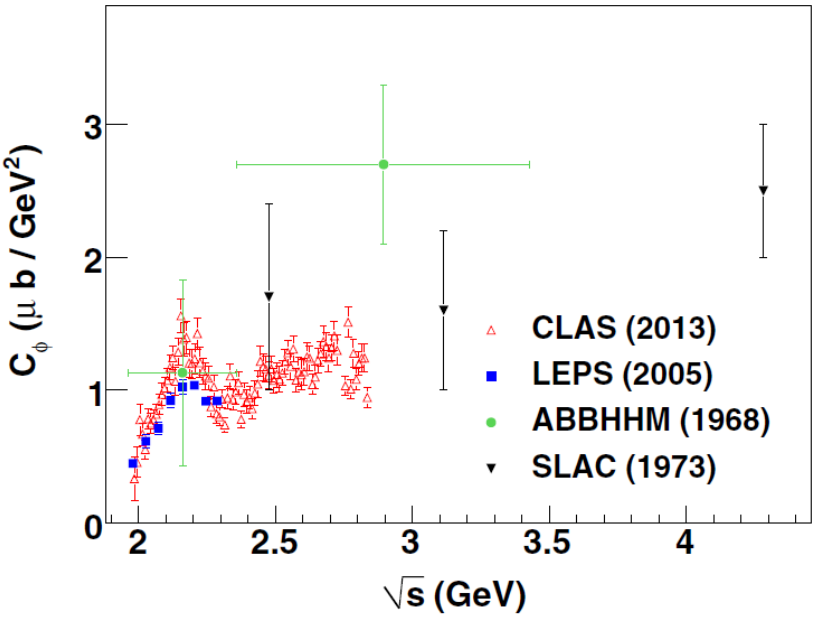

Figure 1.8: Forward differential cross sections ($\mathrm{d}\sigma/\mathrm{d}t$ at $t = t_{\mathrm{min}}$) from recent CLAS results are represented as red open triangles [5].

data from CLAS with the wide-angle coverage almost rules out a resonance interpretation for the 2.1-GeV bump structure.

For the spin-density matrix elements, it has long been observed that diffractive vector meson photoproduction roughly follows s-channel helicity conservation, while t-channel helicity conservation is broken. However, the recent CLAS measurement confirmed that both s-channel and t-channel helicity conservations are broken. Helicity nonconservation in any frame refers to the deviation of the ρ^0_{00} SDME from zero in that frame. The coupling for the Pomeron in the t-channel is the same as the exchange of a spin-0 (scalar) particle. As a result, one can expect the t-channel helicity conservation (no helicity flip in the t channel) [16].

1.4 Theoretical Predictions

Photoproduction of ϕ mesons are consistent with diffractive production via Pomeron-exchange as a dominant mechanism. Enhanced ϕ photoproduction near threshold above the level predicted by the Pomeron exchange suggests a contribution from other production mechanisms such as scalar and tensor me-

son exchange, glueball exchange, or s-channel processes.

The cross section of ϕ-photoproduction increases with increasing energy which can be explained by a Pomeron and meson exchange model. Interestingly, the LEPS recent observation has shown a strong indication of a bump structure at around $E_\gamma = 2$ GeV. The bump structure appears very close to the threshold of $\Lambda(1520)$ production. To explain this nonmonotonic behavior, theoretical groups suggest some different explanations.

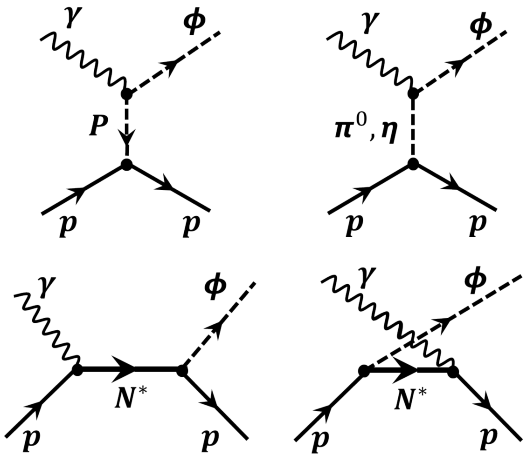

Figure 1.9: Feynman diagram for ϕ photoproduction

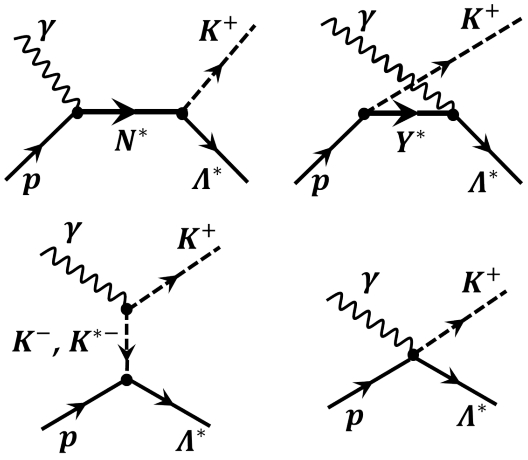

Figure 1.10: Feynman diagram for $\Lambda(1520)$ photoproduction

First, the works by Ozaki *et al.* [2] and Ryu *et al.* [4] relate this to a coupling between the ϕp and $K^+\Lambda(1520)$ channels. Ozaki *et al.* proposed a coupled-channel effect based on the K-matrix formalism. They included the $\gamma N \to K\Lambda(1520)$ and $K\Lambda(1520) \to \phi N$ kernels in the coupled-channel formalism in addition to the $\gamma N \to \phi N$ and $\phi N \to \phi N$ ones. On top of that, a nucleon resonance ($J^p = 1/2^-$) with large $\bar{s}s$ content was also taken into account. Interestingly, the coupled-channel contributions proved to be not enough to explain the bump-like structure at $E_\gamma \approx 2.0$ GeV, while the possible N^* resonance could account for the 2.0-GeV structure as a destructive interference [35].

In the kinematic regime 2 GeV ($\sqrt{s} \approx 2.2$ GeV), the $\phi p \to K^+K^-p$ charged mode and the $K^+\Lambda(1520) \to K^+pK^-$ decay mode have the same final states. Therefore, rescattering effects can occur between the two channels. Recently, Ryu *et al.* [4] argue that hadronic coupled-channel interactions may be responsible for the observed local enhancement of the forward cross section, in particular, with the $K\Lambda(1520)$ rescattering effects. Instead, they formulated that the

Pomeron exchange process was suppressed in the near-threshold region.

The main reason for this is the proximity of the energy threshold of two processes, $\gamma p \to K^+\Lambda(1520)$ and $\gamma p \to \phi p$. Therefore, the first intermediate process may affect the observed cross section of the second one due to the final state (or coupled-channel) interaction. Recent LEPS results [31] confirm that enhancement at $W = 2.15$ GeV is not due to the resonance with $J \leq 3/2$. It could be due to either of high-spin (J$\geq 5/2$) resonance or interference effect.

Ryu *et al.* [4] employed the effective Lagrangian approach in addition to Pomeron exchange at higher energies. The invariant amplitude for the Feynman diagrams in Fig. 1.11 can be written as

$$\begin{aligned}\mathcal{M}_{\gamma N\to\phi N}(p,p';s) &= \mathcal{M}^{\rm Born}_{\gamma N\to\phi N}(p,p';s) + \sum_i \int {\rm d}^3q \frac{E_{M_i}+E_{B_i}}{(2\pi)^3 2E_{M_i}E_{B_i}} \\ &\quad \mathcal{M}_{\gamma N\to M_iB_i}(p,q;s)\frac{1}{s^2-(E_{M_i}+E_{B_i})^2+i\varepsilon}\mathcal{M}_{M_iB_i\to\phi N}(q,p';s),\end{aligned}$$

where the first Born term $\mathcal{M}^{\rm Born}_{\gamma N\to\phi N}$ includes all the tree-level diagrams. On the other hand, the off-shell terms $\mathcal{M}_{\gamma N\to M_iB_i}$ and $\mathcal{M}_{M_iB_i\to\phi N}$ account for the $\gamma p \to M_iB_i$ and $M_iB_i \to \phi p$, respectively.

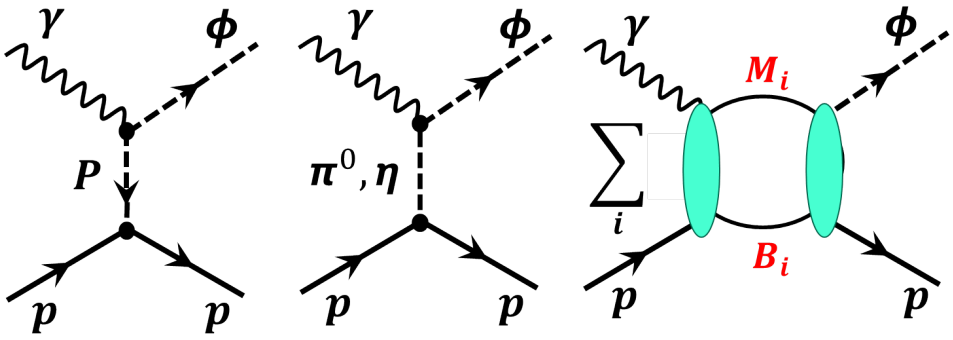

Figure 1.11: Photoproduction of K^-K^+p via ϕ and $\Lambda(1520)$ resonances produced by Pomeron and K/K^* exchanges, respectively.

They have chosen the suppression factor for the Pomeron-exchange amplitude, $R(E) = 1 - \exp[-(E - E_{\rm th})^3)]$, where $E_{\rm th}$ denotes the threshold energy of ϕ photoproduction. It should be noted that they have taken only the imaginary part of the transition amplitudes involved in the rescattering diagrams into account. As a result, the $K\Lambda(1520)$ rescattering effect turned out to be dominant beyond the contributions from other processes such as the π and η meson exchanges. Further theoretical efforts for the full coupled-channel formalism for

the rescattering diagrams are needed, and also their arbitrary choice of the cut-off energy for Pomeron-exchange process should be validated. Yet, it should be emphasized that the rescattering diagrams deserve much attracted.

An alternative explanation of the non-monotonic energy dependence of the forward cross section is proposed in Ref. [3], where the authors interpret the existence of the bump in the differential cross sections at forward angles and near the reaction threshold as being due to an excitation of missing nucleon resonances $N(2080)$ with a nonnegligible strangeness content. The bump structure appears only at forward angles. CLAS data [5] (for both K^+K^- and $K^0_L K^0_S$ channels) show that resonance interpretation looks unlikely.

Due to the proximity of the energy threshold of two processes, $\gamma p \rightarrow K^+\Lambda(1520)$ and $\gamma p \rightarrow \phi p$, the interference between the two transition amplitudes could account for the non-monotonic energy dependence of forward differential cross sections, keeping a general understanding of $\gamma p \rightarrow \phi p$ photoproduction, where meson-exchanges are suppressed, and diffractive Pomeron exchange dominates even at low energies.

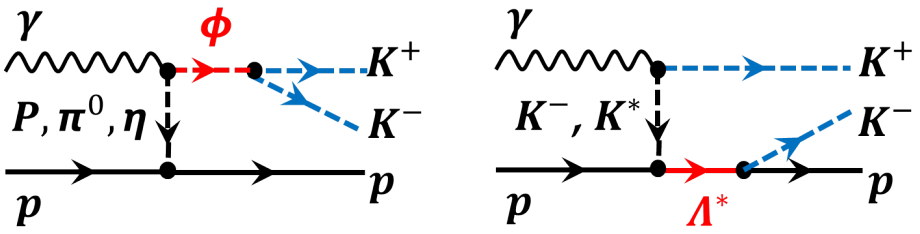

Figure 1.12: Photoproduction of K^-K^+p via ϕ and $\Lambda(1520)$ resonances produced by Pomeron and K/K^* exchanges, respectively.

The double differential cross section for $\gamma p \rightarrow K^+K^-p$ reaction can be written as:

$$\frac{\mathrm{d}^2\sigma}{\mathrm{d}m_{K^+K^-}\mathrm{d}m_{K^-p}} = \int \frac{m_{K^+K^-}m_{K^-p}\mathrm{d}\cos\theta_{K^+}\mathrm{d}\phi_p}{128\,\pi^4\,k\sqrt[3]{s}}\,|\overline{\mathcal{M}}|^2,$$

where $|\overline{\mathcal{M}}|^2$ represents the spin-polarization averaged amplitude:

$$|\overline{\mathcal{M}}|^2 = \frac{1}{4}\sum_{\text{spin}}\sum_{\text{pol}}|\mathcal{M}|^2$$

and the invariant masses $m_{K^+K^-}$ and m_{K^-p} satisfy the kinematic bounds:

$$(m_{K^-}+M_{K^+})^2 \leq m^2_{K^+K^-} \leq (\sqrt{s}-M_p)^2, \quad (m_{K^-}+M_p)^2 \leq m^2_{K^-p} \leq (\sqrt{s}-M_{K^+})^2.$$

The differential cross sections can then be decomposed into

$$\begin{aligned}\frac{d^2\sigma}{dm_{K^+K^-}dm_{K^-p}} &\propto |\mathcal{M}_\phi + \mathcal{M}_{\Lambda(1520)}|^2 \\ &= |\mathcal{M}_\phi|^2 + |\mathcal{M}_{\Lambda(1520)}|^2 + \mathcal{M}_\phi^*\mathcal{M}_{\Lambda(1520)} + \mathcal{M}_\phi\mathcal{M}_{\Lambda(1520)}^*,\end{aligned}$$

where $\mathcal{M}_\phi$ and $\mathcal{M}_{\Lambda(1520)}$ are the complex amplitudes for ϕ and $\Lambda(1520)$ production processes, respectively. p_f and p_i are momenta of final and initial at

Let the complex amplitudes $\mathcal{M}_\phi$ and $\mathcal{M}_{\Lambda(1520)}$ be replaced by $\mathcal{M}_\phi = A\exp i\psi_a$ and $\mathcal{M}_{\Lambda(1520)} = B\exp i\psi_b$, where $A(m)$ and $B(m)$ are the magnitudes of the amplitudes and ψ_a and ψ_b are the phases. Now that we look at the interference effect in terms of the K^+K^- mass (m), the amplitude A can be given in the form of the relativistic Breit-Wigner distribution:

$$A = \frac{a}{m_\phi^2 - m^2 - im_\phi\Gamma_\phi},$$

where

$$\Gamma_\phi(m) = \Gamma_0\frac{m_\phi}{m}\left[\frac{q(m)}{q(m_\phi)}\right]^3,$$

where $q(m) = \sqrt{m^2/4 - m_K^2}$ [37].

Consequently, the double differential cross section is then represented in terms of the K^+K^- mass (m):

$$\frac{\mathrm{d}^2\sigma}{\mathrm{d}m_{K^+K^-}\mathrm{d}m_{K^-p}} \propto |\mathcal{M}_\phi + \mathcal{M}_{\Lambda(1520)}|^2 = \left|\frac{a}{m_\phi^2 - m^2 - im_\phi\Gamma_\phi} + B(m)e^{i\psi}\right|^2,$$

where ψ is the relative phase between a and B. Rationalizing the Breit-Wigner amplitude, the amplitude sum can be rearranged as:

$$\begin{aligned}&\left|\frac{a}{m_\phi^2 - m^2 - im_\phi\Gamma_\phi} + B(m)e^{i\psi}\right|^2 = \left|\frac{a(m_\phi^2 - m^2 + im_\phi\Gamma_\phi)}{(m_\phi^2 - m^2)^2 + m_\phi^2\Gamma_\phi^2} + B(m)e^{i\psi}\right|^2 \\ = \;& \frac{|a|^2}{(m_\phi^2 - m^2)^2 + m_\phi^2\Gamma_\phi^2} + |B(m)|^2 + \\ & \frac{|aB|\{[(m_\phi^2 - m^2) + im_\phi\Gamma_\phi]e^{-i\psi} + [(m_\phi^2 - m^2) - im_\phi\Gamma_\phi]e^{i\psi}\}}{(m_\phi^2 - m^2)^2 + m_\phi^2\Gamma_\phi^2}.\end{aligned}$$

The third interference term can be further rearranged as

$$I(m) = 2|aB|\frac{(m_\phi^2 - m^2)\cos\psi + \Gamma_\phi m_\phi\sin\psi}{(m_\phi^2 - m^2)^2 + m_\phi^2\Gamma_\phi^2},$$

where we have used the trigonometric relations: $2\cos\psi = e^{i\psi} + e^{-i\psi}$ and $2\sin\psi = -i(e^{i\psi} - e^{-i\psi})$.

The maximum and minimum values of the interference term can be obtained by differentiating the nominator with respect to ψ:

$$\tan\psi_m = \frac{\Gamma_\phi m_\phi}{(m_\phi^2 - m^2)},$$

which yields the phase values for the maximum and minimum interference effects at $\psi_{\max} = \pi/2$ and $-\pi/2$, respectively.

Figure 1.13 shows the lineshapes the K^+K^- invariant mass due to the interference term in terms of the phase ψ. The lineshapes for the maximum and minimum interference are of the symmetric Breit-Wigner forms with opposite signs. Others are asymmetric due to the term $(m_\phi^2 - m^2)$ in front of $\cos\psi$.

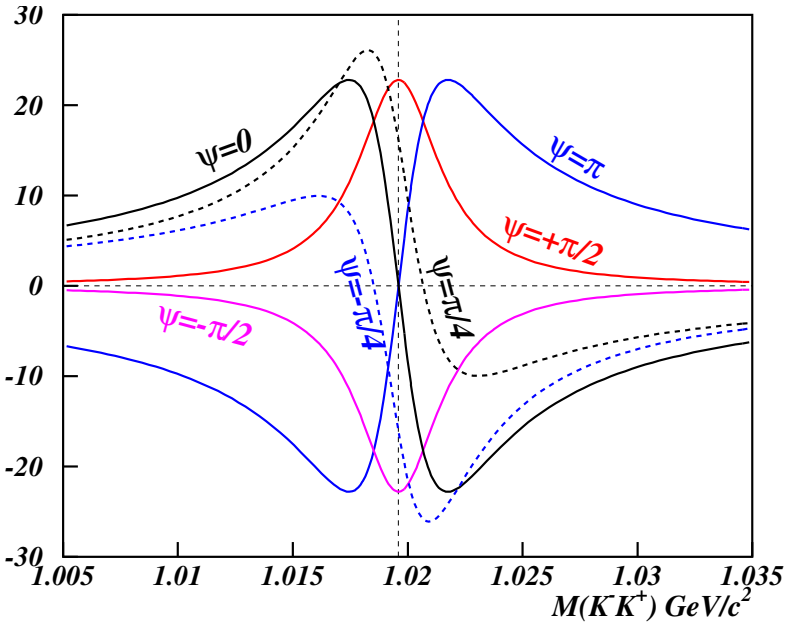

Figure 1.13: Lineshapes of the interference term from $\psi = -\pi/2$ to $+\pi/2$.

The integral of the interference term over dm is sensitive only to the second

term with $\sin\psi$ since the integral of the first term vanishes.

$$\begin{aligned} I &= \int \frac{2(m_\phi^2 - m^2)|aB|\cos\psi + 2\Gamma_\phi m_\phi |aB|\sin\psi}{(m_\phi^2 - m^2)^2 + m_\phi^2\Gamma_\phi^2}\mathrm{d}m \\ &= \int \frac{\Gamma_\phi m_\phi |aB|\sin\psi}{(m_\phi^2 - m^2)^2 + m_\phi^2\Gamma_\phi^2}\mathrm{d}m = \Gamma_\phi m_\phi |aB|\sin\psi \cdot \frac{1}{\Gamma_\phi m_\phi}\tan^{-1}\frac{(m_\phi^2 - m^2)}{\Gamma_\phi m_\phi}, \end{aligned}$$

where we have used the integral formula:

$$\int \frac{1}{a^2 + x^2}dx = \frac{1}{a}\tan^{-1}\frac{x}{a},$$

where $a = m_\phi^2\Gamma_\phi$ and $x = m_\phi^2 - m^2$. The definite integral $I(m_1, m_2)$ over the symmetric mass interval between m_1 and m_2 is then given by

$$I(m_1, m_2) = |aB|\sin\psi\tan^{-1}\frac{(m_\phi^2 - m^2)}{\Gamma_\phi m_\phi}\Bigg|_{m_1}^{m_2} = |aB|\sin\psi(\pi + \theta_0 - \theta_0) = \pi|aB|\sin\psi,$$

where $m_1 = m_\phi - \Delta m/2$ and $m_2 = m_\phi + \Delta m/2$, and $\tan^{-1}\theta_0 = (m_\phi^2 - m_{1,2}^2)/(\Gamma_\phi m_\phi)$. The integral is then zero when $\sin\psi = 0$, which can be also seen in Fig. 1.13.

Very recently, Nam [38] reports that ϕ-$\Lambda(1520)$ interference based on the effective Lagrangian approach with ϕ photoproduction via a Pomeron exchange and $\Lambda(1520)$ photoproduction via a pseudoscalar K-meson exchange. The effective Lagrangians for the interaction vertices in his calculation are

$$\begin{aligned} \mathcal{L}_{\gamma KK} &= ie_K\left[(\partial^\mu K^\dagger)K - (\partial^\mu K)K^\dagger\right]A_\mu + \mathrm{h.c.}, \\ \mathcal{L}_{\gamma BB} &= -\bar{B}\left[e_B \not{A} - \frac{e_Q\kappa_B}{4m_B}\sigma\cdot F\right]B, \\ \mathcal{L}_{\gamma B^*B^*} &= \frac{e_Q\kappa_{B^*}}{4m_{B^*}}\bar{B}^{*\mu}(\sigma\cdot F)B_\mu^* + \mathrm{h.c.}, \\ \mathcal{L}_{KNB} &= -ig_{KNB}\bar{B}\Gamma_5 KN, \\ \mathcal{L}_{KNB^*} &= \frac{g_{KNB^*}}{m_{B^*}}\bar{B}^{*\mu}\partial_\mu K\Gamma_5\gamma_5 N + \mathrm{h.c.}, \\ \mathcal{L}_{\gamma KNB^*} &= -i\frac{e_N g_{KNB^*}}{m_{B^*}}\bar{B}^{*\mu}A_\mu K\Gamma_5\gamma_5 N + \mathrm{h.c.}, \\ \mathcal{L}_{\phi KK} &= ig_{KK\phi}\phi^\mu\left[(\partial_\mu K^\dagger)K - (\partial_\mu K)K^\dagger\right] + \mathrm{h.c.}, \\ \mathcal{L}_{\gamma\phi NN} &= \frac{\mathcal{F}(s,t)}{m_\phi m_N^2}\bar{N}\partial_\mu\phi_\nu F^{\mu\nu}N + \mathrm{h.c.}, \end{aligned}$$

where K, A, B, B^*, and ϕ stand for the pseudoscalar kaon, photon, spin-1/2 baryon, spin-3/2 baryon, and ϕ-meson fields, respectively. e and κ denote the

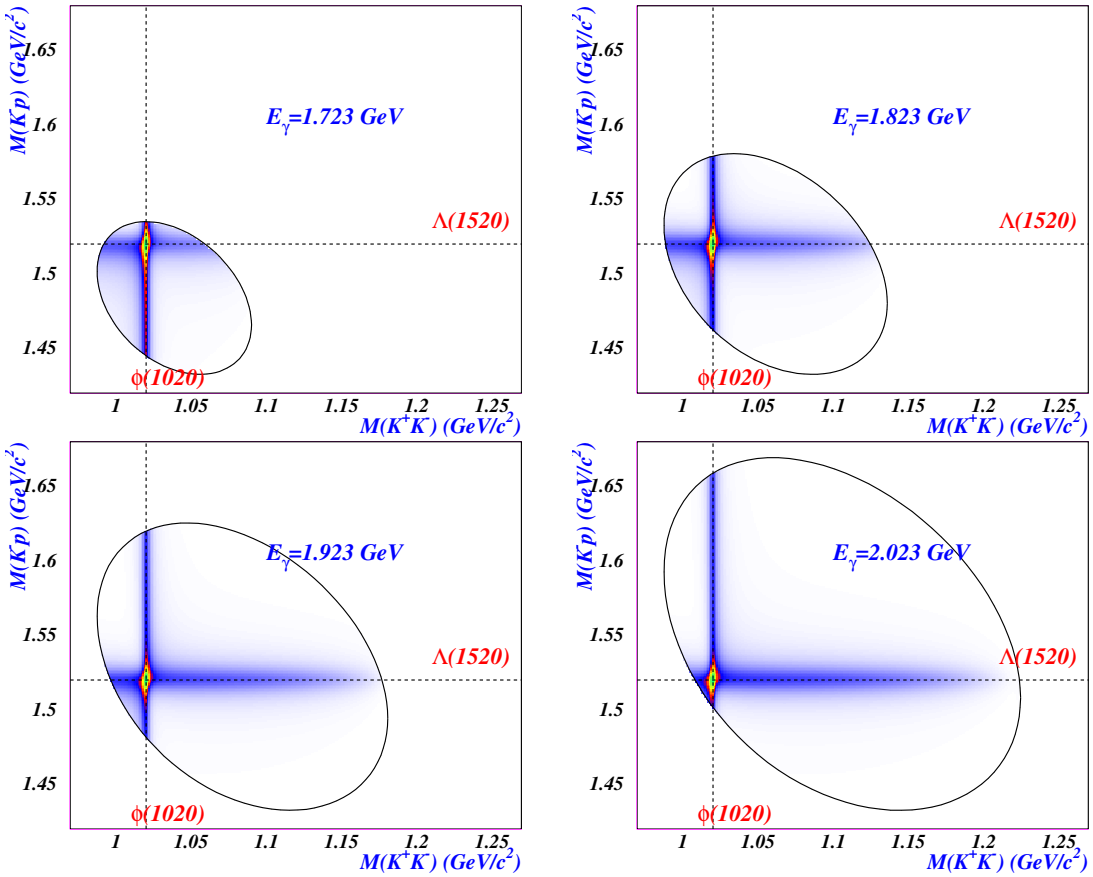

Figure 1.14: Two-dimensional K^+K^- and K^-p mass distributions from Nam's calculation for the energy range in which the overlap of the ϕ and $\Lambda(1520)$ mass bands are kinematically allowed. The solid contours represent the kinematical boundaries. The bright spots in the cross region indicate some interference effects.

electric charge and anomalous magnetic moment for the particles. $\Gamma_5 = \gamma_5$ for positive-parity, while $\Gamma_5 = \mathbf{1}_{4\times4}$ for negative-parity particles.

For the $\gamma\phi NN$ interaction, the effective lagrangian can be defined as

$$\mathcal{L}_{\gamma\phi NN} = \bar{N}\mathcal{F}'(s,t)\Gamma_{\mu\nu}\phi^\mu A^\nu N,$$

based on the Donnachie-Landshoff model with the Pomeron ($\mathcal{P}$) exchange. The function $\mathcal{F}'(s,t)$ corresponds to the Regge parameterization, which is defined as:

$$\mathcal{F}'(s,t) = \frac{C_P F_1(t) F_2(t)}{s}\left[\frac{s}{s_P}\right]^{\alpha_P(t)} \exp\left[-\frac{i\pi}{2}\alpha_P(t)\right],$$

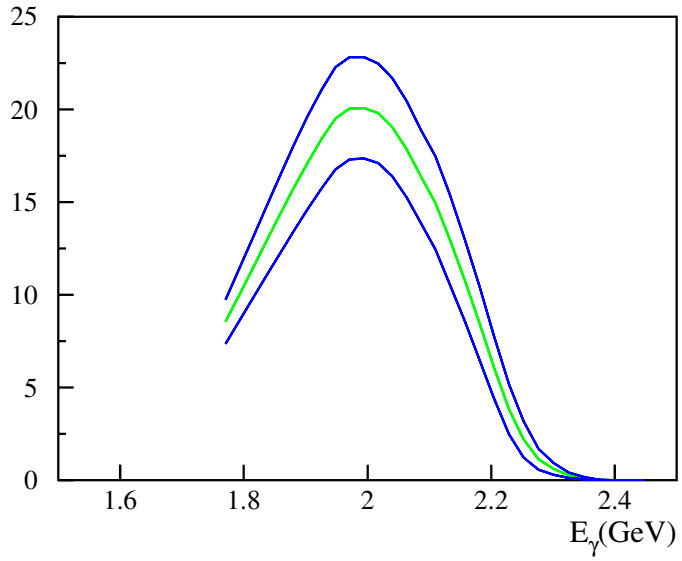

Figure 1.15: Differential cross sections for $\gamma p \to K^+K^-p$ reaction in the cross region of $1.0 < m_{K^+K^-} < 1.04$ GeV/c^2 and $1.5 < m_{K^-p} < 1.54$ GeV/c^2 when K^+K^- are produced at forward angles. The middle line indicates the predicted cross sections, while the two blue lines are the maximum and minimum bounds predicted by Nam's calculation.

where the form factors $F_{1,2}(t)$ relates to the $\gamma\phi\mathcal{P}$ interaction vertex:

$$F_1(t) = \frac{4m_N^2 - a_N^2 t}{(4m_N^2 - t)(1 - t/t_0)^2}, \qquad F_2(t) = \frac{2\mu_0^2}{(1 - t/m_\phi^2)(2\mu_0^2 + m_\phi^2 - t)},$$

where $C_P \approx 11e_Q$, $s_P = 4\,\mathrm{GeV}^2$, $a_N = 2$, $\mu_0^2 = 1.1\,\mathrm{GeV}^2$, $t_0^2 = 0.7\,\mathrm{GeV}^2$ and $\alpha_P(t) = 1.08 + 0.25t$.

Figure 1.14 shows the two-dimensional K^+K^- and K^-p mass distributions from Nam's calculation for the energy range in which the overlap of the ϕ and $\Lambda(1520)$ mass bands are kinematically allowed. The bright spots in the cross region indicate some interference effects. Figure 1.15 shows the differential cross sections for $\gamma p \to K^+K^-p$ reaction in the cross region of $1.0 < m_{K^+K^-} < 1.04$ GeV/c^2 and $1.5 < m_{K^-p} < 1.54$ GeV/c^2 when K^+K^- are produced at forward angles. The middle line indicates the predicted cross sections, while the two blue lines are the maximum and minimum bounds predicted by Nam's calculation.

Chapter 2

Experimental Setup

The experiment has been carried out at the Laser Electron Photon beam line (LEPS) at the Super Photon ring 8-GeV facility (SPring-8). The Compton backscattered photon beam facility and the LEPS spectrometer system are described in more detail.

2.1 SPring-8 Facility

The SPring-8 is a third-generation synchrotron-radiation facility which has been operated since 1997. It consists of an injector linac, a booster synchrotron, and a low-emittance and high-brightness storage ring. Figure 2.1 shows the schematic view of the accelerator complex. Electrons are generated at an electron gun and are accelerated to 1 GeV in the injector linac with a length of 140 m.

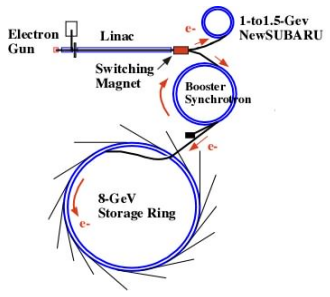

Figure 2.1: The SPring-8 accelerator complex.

The 1-GeV electron beam is then transported to the booster synchrotron with a 396 m circumference, and is accelerated up to 8 GeV. The 8-GeV electron beam is injected into the storage ring in every minutes. The storage ring has a 1436 m circumference The 8-GeV electrons circulate along the storage ring of a 1436-m circumference with a RF frequency of 500.88 MHz.

The time interval of the successive electron bunches is then 1.966 ns. Electrons are however filled with various filling patterns. For example, the A-mode filling pattern contains 203 electron bunches in equal time intervals (23.6 ns), while the B-mode filling pattern has 84 trains of 4 successive electron bunches, so each of 4-bunch trains comes in 51.1 ns. The other modes fill electron bunches in every 1.966 ns for 1/12 or other fractions of the total circumference and additional single bunches in longer time interval. The electron beam current is 100 mA for top-up operation.

2.2 Backward Compton-scattered Photon Beam

When a laser photon with an energy k_1 impinges on a relativistic electron with a high-energy E_e with the angle $\theta_1 = \hat{k}_1 \cdot \hat{k}_e \simeq \pi$, it is scattered with the angle of $\theta_2 = \hat{k}_1 \cdot \hat{k}_\gamma$. The energy of Compton backscattered photon is given by

$$E_\gamma = k_1 \frac{1-\beta\cos\theta_1}{1-\beta\cos\theta_2+\dfrac{k_1(1-\cos(\theta_2-\theta_1))}{E_e}} \longrightarrow \frac{4E_e^2 k_1}{m_e^2+4E_e^2k_1+\theta_2^2\gamma^2m_e^2},$$

where β is the velocity of an incident electron relative to the speed of light.

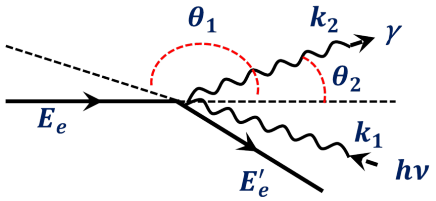

Figure 2.2: The principle of backward Compton-scattered photon generation.

For head-on collisions with highly relativistic electrons ($\gamma = E_e/m_e \gg 1$, $\beta \sim 1$, $\theta_1 \sim \pi$ and $\theta_2 \ll 1$), the energy E_γ can be rewritten as above. The maximum energy of the Compton backscattered photon (at Compton edge) is obtained as

$$E_\gamma^{\max} = \frac{4E_e^2k_1}{m_e^2+4E_ek_1}.$$

Differential cross section for backward Compton scattering is given by [39]

$$\frac{d\sigma}{dE_\gamma} = \frac{2\pi r_e^2 a}{E_\gamma^{\max}}\left[\frac{\rho^2(1-a)^2}{1-\rho(1-a)}+1+\left\{\frac{1-\rho(1+a)}{1-\rho(1-a)}\right\}^2\right],$$

where

$$a = \frac{m_e^2}{m_e^2+4E_ek_1}, \qquad \rho = \frac{E_\gamma}{E_\gamma^{\max}},$$

where $r_e = 2.818$ fm the classical electron radius.

The linear polarization is given by

$$P_\gamma = P_{\rm laser} \frac{\left[1 - \dfrac{1-\rho(1+a)}{1-\rho(1-a)}\right]^2}{2\left[\dfrac{\rho^2(1-a)^2}{1-\rho(1-a)} + 1 + \left\{\dfrac{1-\rho(1+a)}{1-\rho(1-a)}\right\}^2\right]},$$

which reaches the maximum polarization at the Compton edge. The maximum linear polarization is given by $P_\gamma^{\rm max} = P_{\rm laser} \cdot 2a/(1+a^2)$. It corresponds to 94% for the LEPS case with 8-GeV electrons colliding with 351-nm laser photons.

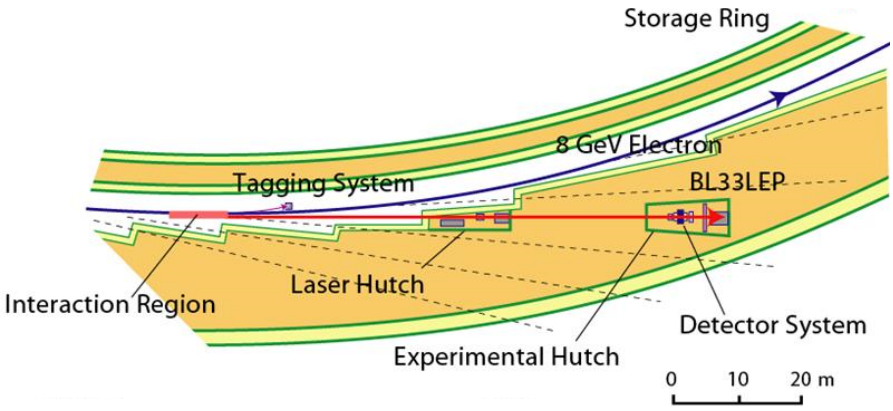

Figure 2.3: The BL33LEP beam line.

At the BL33LEP beam line of SPring-8, a linearly polarized photon beam was generated by backward Compton scattering of laser light from 8-GeV electrons in the storage ring, as shown in Figure 2.3. The laser light was injected to a 7.8-m straight section of the storage ring. The direction and the polarization of the laser light were tuned using mirrors, half-wavelength plates, and a light expander at the laser hutch.

2.2.1 Laser System

In the 2002/2003 runs we used a 5-W multi-line Ar-ion laser (Innova Sabre, Coherent). The wavelength ranges from 333 nm to 364 nm. In the 2006/2007 runs we utilized two 8-W solid-state lasers (Paladin, Coherent) with a single line of

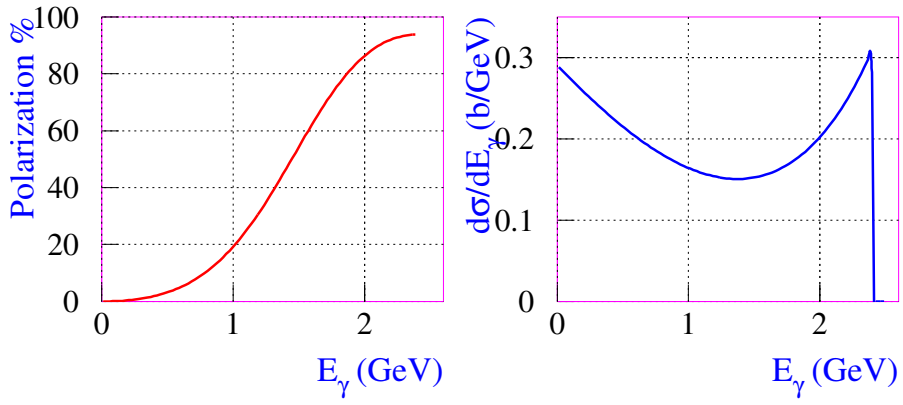

Figure 2.4: Linear polarization and differential cross sections for Compton scattering with a laser of 355-nm wavelength.

355 nm.

A vertically polarized laser beam passed through the $\lambda/2$-plate and changed its polarization direction according to the orientation of the $\lambda/2$-plate. In the 2002/2003 runs the $\lambda/2$-plate was exposed directly to the laser light, while in the later runs the beam expander was placed between the laser and the $\lambda/2$-plate, in order to extend lifetime of the $\lambda/2$-plate with lower light intensity per unit area [40].

The first and second mirrors are made of Al coated silicon with good heat conductivity and 100 mm in diameter. Both are placed in the vacuum chamber. The first mirror is 6 mm thick, while the second mirror is 19 mm thick. Compton back-scattered photon beam passes through the first mirror with water cooling. The third and fourth mirrors are made of quartz with 80 mm in diameter and 12 mm in thickness, and are rotated for optical tuning. The laser polarization is measured with a Glan-Laser polarizer.

2.2.2 Tagging System

The incident photon energy (E_γ) is determined by subtracting the measured recoil-electron energy ($E_{e'}$) from the electron energy in the storage ring. In the 2002/2003 runs the tagger was composed of a silicon strip detector (SSD) placed upstream of a layer of plastic scintillators (TAG-PL). The TAG-PL consists of 2 layers of 5 plastic scintillation counters with 10×7.4 mm^2 and 3 mm in thickness. The counter placed closest to the 8-GeV electron trajectory is 5.5 mm wide. The plastic scintillators are stacked alternatively to have 2.7 mm overlapped

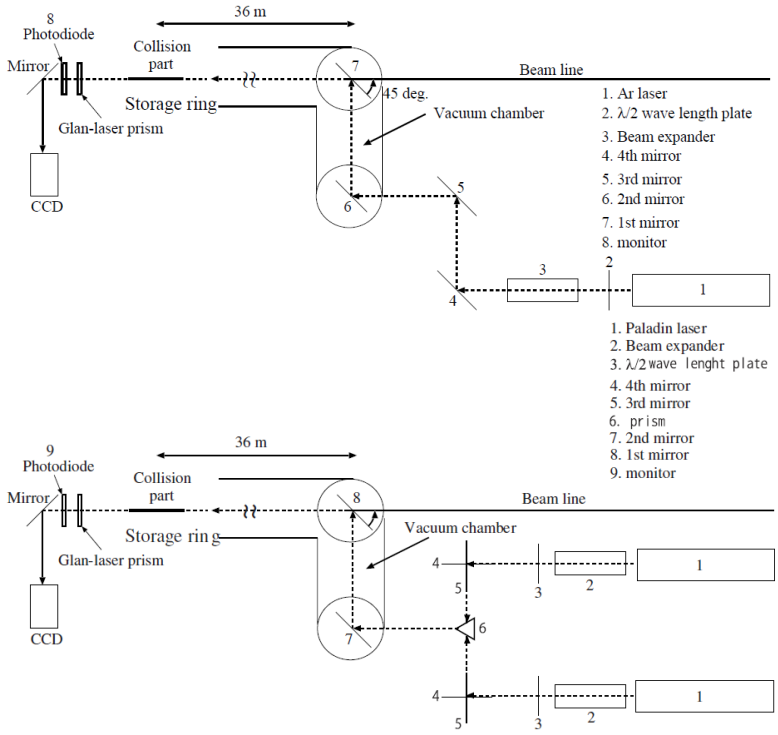

Figure 2.5: The laser systems with an Ar-ion laser (top) and two solid-state lasers (bottom).

with adjacent counters, and are read by photomultiplier tubes (HAMAMATSAU H3164-10).

However, the timing resolution of the SSD was not enough to tag recoil electrons above 1 MHz. Therefore, the new tagger was implemented in later runs. It consists of two super-layers (TAG-SFF and TAG-SFB) of plastic scintillating fibers substituted for silicon strip detectors. Each super-layer consists of 6 layers of 55 round scintillating fibers with the cross section of 1×1 mm^2, as shown in Fig. 2.7. The fiber signals are read by photomultiplier tubes (HAMAMATSU R5900-00-M4, H6568-10) in a coincidence with the TAG-PL.

2.3 LEPS Spectrometer

2.3.1 Charged Veto Counter UpVeto

The incident photons are converted in part to e^+e^- pairs in residual gas or aluminum window of the beam pipe, and in air downstream from the end-face

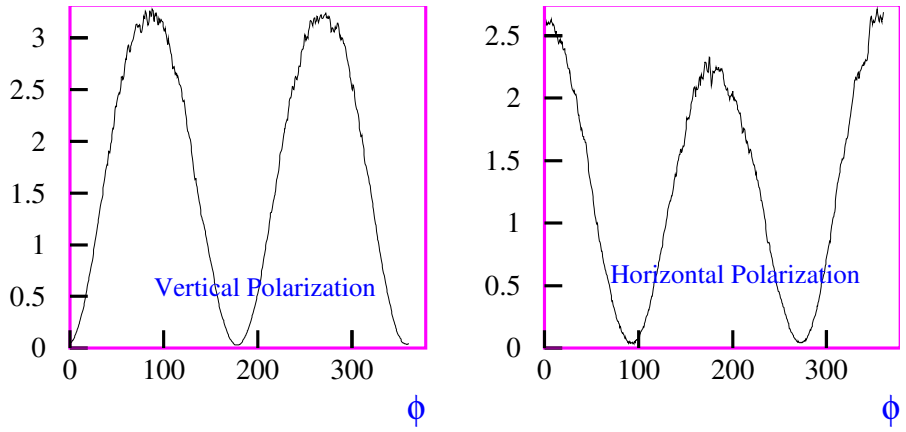

Figure 2.6: Intensity distributions for vertical (left) and horizontal (right) polarizations in terms of the polarization angle about the vertical axis.

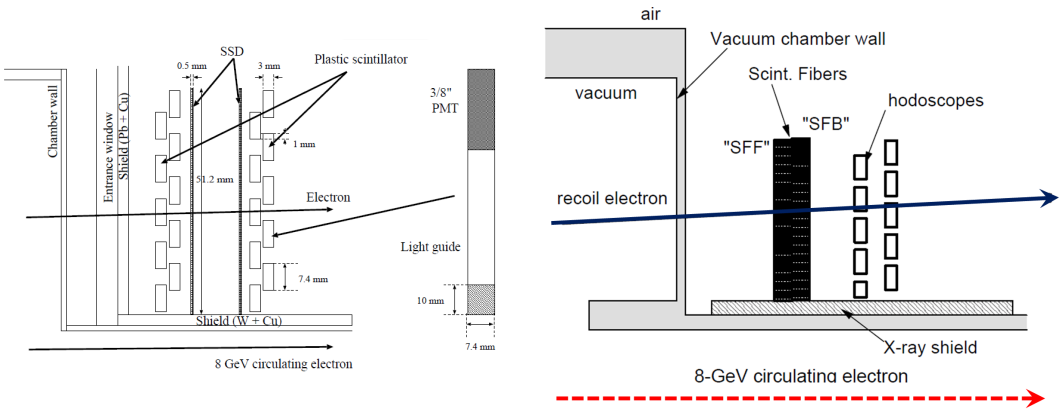

Figure 2.7: Tagging systems with silicon strip detectors (left) and scintillating fibers (right).

of the beam pipe. The upstream-veto scintillator was used to reject the signals associated with such charged particles produced before the target. The plastic scintillator (BC-408) of $190 \times 200(h) \times 5(t)$ mm^3 was located at 4 m upstream from the target, coupled to a 2-in photomultiplier (H7195) through a fish-tail light guide.

2.3.2 Aerogel Cherenkov Counter

Pair production is the dominant process by which gamma rays interact with matter in the energy regime above the threshold energy for creating e^+e^- pairs. The total e^+e^- pair-production cross section is approximately given by $\sigma = 7/9(A/X_0N_A)$, where X_0 denotes radiation length and N_A is Avogadro's

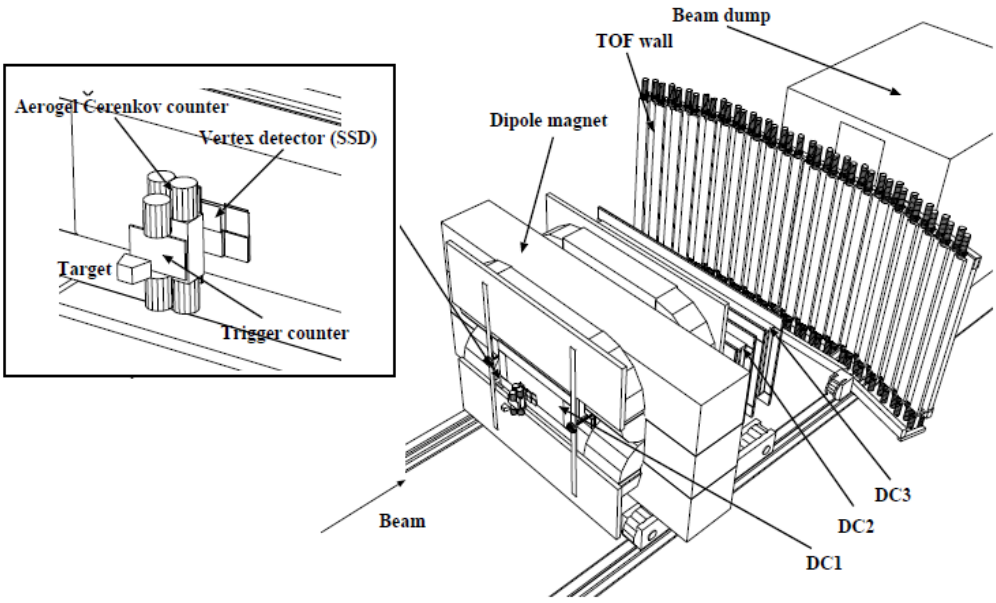

Figure 2.8: The LEPS spectrometer

number, thereby yielding about 21 mb for a hydrogen target, which is two orders of magnitude higher than that for hadronic photoproduction (≈ 150 μb). In a plastic trigger scintillator the cross section of the e^+e^- pair production is 380 mb while that of hadronic reactions is about 2.0 mb.

A silica-aerogel Cerenkov counter (AC) was used to reject the e^+e^- pairs at the online trigger level. The refractive index of the silica aerogel radiator is 1.03, so that Cherenkov light is emitted when the charged particles exceed threshold momenta of 0.002 GeV/c, 0.57 GeV/c and 2.0 GeV/c for e^+e^-, pions and kaons, respectively. The AC is installed just behind the trigger counter to veto e^+e^- pairs which emerge within a very small angle ($< 0.12^o$). The light box is made of black papers with 150 mm high, 120 mm wide, and 60 mm thick. A tile of silica aerogel radiator is 110×110 mm^2 in a cross-sectional area and 25 mm in thickness. Two tiles of radiators are used to make an effective thickness of 50 mm. The light box is covered with a diffuse reflection material, Gortex$^{\mathrm{TM}}$ (white sheet) with a reflectivity of 95%. The Cherenkov lights are read by four 2-inch fine-mesh photomultiplier tubes (HAMAMATSU H6614-01) from the upper and bottom ends of the box. The detection efficiency was found to be about 99.9 %. The analog signal is fed into a CAMAC FERA ADC module through a CR high-pass filter with $C = 4.7$ nF and $R = 100$ kΩ [40].

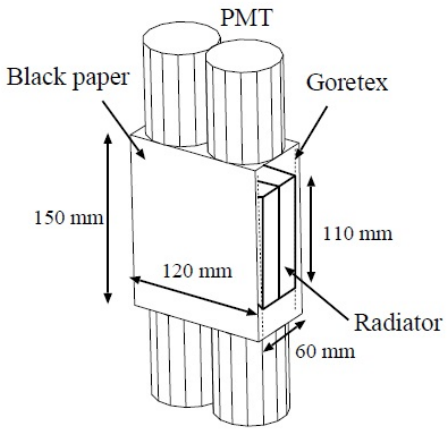

Figure 2.9: A silica-aerogel Cherenkov detector

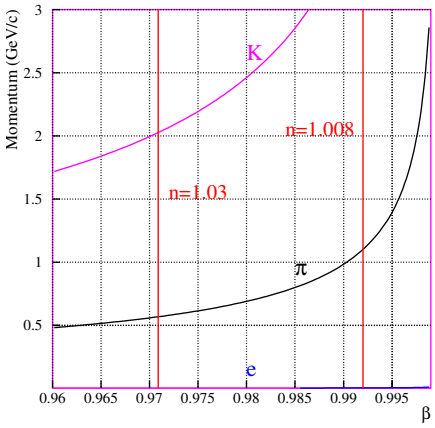

Figure 2.10: Threshold momenta and velocities of charged particles for Cherenkov radiation with silica aerogel of $n = 1.03$ and $n = 1.008$

2.3.3 Silicon Vertex Detector (SVTX)

A silicon vertex detector (SVTX) is placed just after the AC. The SVTX consists of two layers of silicon strip detectors (SSD). One layer measures horizontal coordinates of charged particle tracks, while the other does their vertical coordinates. The strip pitch is 120 μm and the thickness is 300 μm. The SVTX has a rhombic beam-through hole of 10×10 mm^2 at the center. The SSDs are read out by VA (VLSI) chips on a hybrid printed circuit board. The signals are then fed into a repeater card which contains level converters for logic signals, buffer amplifier for analog output signals, and adjustable bias supplied for the VA chip. The VA ship is controlled by a VME board. Analog signals from the VA chip are sent to a flash ADC module through the repeater card.

2.3.4 Trigger Counter

A plastic trigger counter is placed 150 mm downstream from the center of the target cell. The plastic scintillator is 150×94 mm^2 wide and 5 mm thick. Two fine-mesh photomultiplier tubes (H6614-01) read the signal at both top and bottom ends through round light guides with 15 mm in thickness.

2.3.5 Liquid Hydrogen Target

The liquid hydrogen (LH_2) target system is shown in Fig 2.13. The trapezoidal target cell is 150 mm long and its volume is 660 cm^3. The target cell is made of

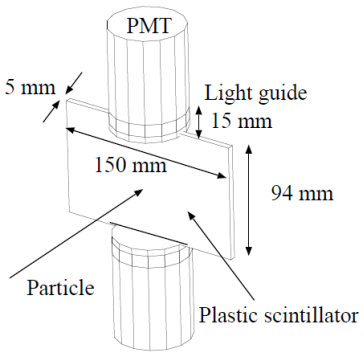

Figure 2.11: Trigger counter

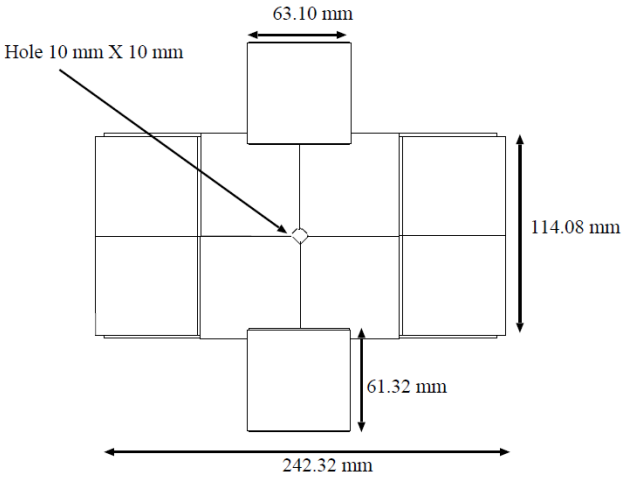

Figure 2.12: Silicon vertex detector

8-mm thick copper plates. The entrance and exit windows are covered with 125-μm thick Kapton films. The target was placed 995 mm upstream from the center of the dipole magnet. The target pressure was kept at 1.05 atm and 20.5 K. Due to the target pressure the effective target thickness becomes 160 mm. The refrigerator uses He gas in the cooling process of adiabatic expansion. Hydrogen gas is supplied through a SUS pipe from the reservoir to the target cell.

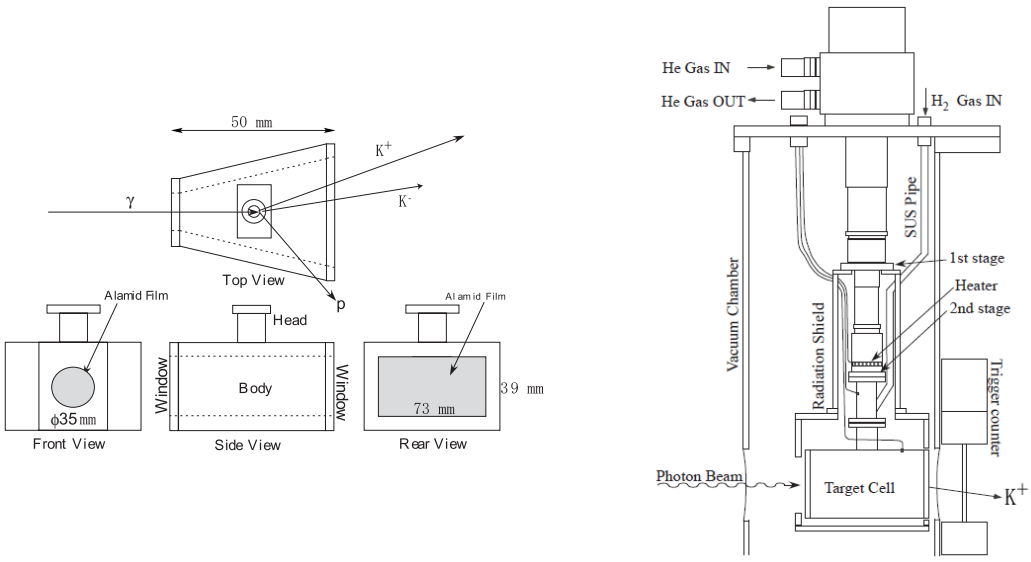

Figure 2.13: The liquid hydrogen target system

2.3.6 Drift Chambers

Charged particle trajectories are reconstructed by using hit information from the SVTX and three multi-wire drift chambers (DC). DC1 is located upstream of the dipole magnet, which has 6 planes, x1, x2, u1, u2, v and x3 with the active area of 600×300 mm^2. The last wire plane (x3) measures charged particle trajectories which begin to bend in the magnetic field. Sense wires of x1-x2 and u1-u2 are positioned with a 6 mm spacing and wires of x3 and v are positioned with a 12 mm spacing. The field wires are arranged in a hexagonal shape. The shield wires are positioned along the windows to shape the electric field. The inclination angle of the u and v wires is 45^o with respect to the horizontal plane.

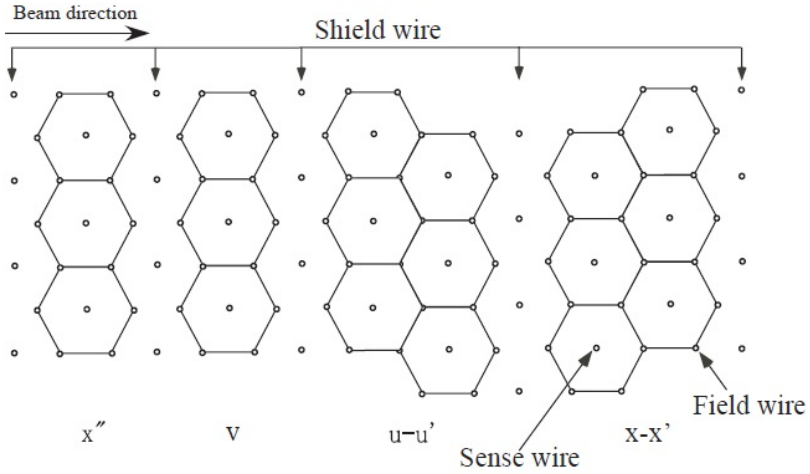

Figure 2.14: Wire configuration of drift chambers

DC2 and DC3 are installed downstream of the dipole magnet and have the active area of 2000×800 mm^2. Both DC2 and DC3 have 5 planes, x1, x2, u1, u2 and v. The drift cell structure of DC2 and DC3 is the same as DC1, but there is no x3 plane in DC2 and DC3. Sense wires of the x1-x2 and u1-u2 planes are positioned with a 10 mm spacing, and the wires of the v plane are positioned with a 20 mm spacing The u and v direction are inclined by 30^o with respect to the vertical plane. The material of the sense wires is gold-plated tungsten (Au-W) and the wire diameter is 25 μm and 30 μm for DC1 and DC2, DC3, respectively. The field and shield wires are made of Au-BeCu with a diameter of 100 μm. The windows are covered with $1250 -$ μm thick mylar sheets. The gas mixture used to operate the DC's is 70 % argon and 30 % isobutane. The efficiency is more than 98% and is typically 99%.

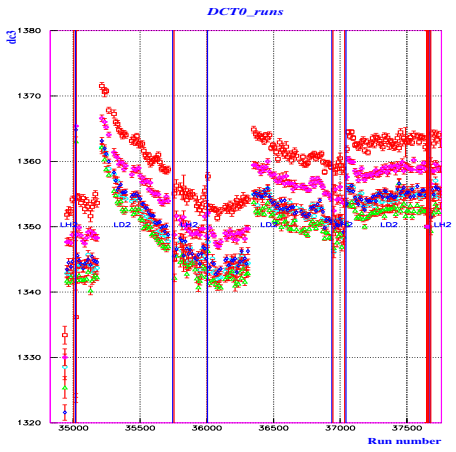

Figure 2.15: Time evolution of t0 parameters for DC3 wires.

Possible systematic changes in t_0 parameters of drift chambers were studied for the whole runs in the 2006/2007 LD2 data set. Such a global shift in t0 parameters and wire-dependent shifts should be calibrated. The TDC spectrum was fitted with the function,

$$y = \texttt{FREQ}\Big(\frac{(x-b)}{c}\Big),$$

where FREQ is a normal frequency function given by $\texttt{FREQ}(x) = (1/\sqrt{2\pi})\int \exp(-t^2/2)dt$. Figure 2.15 shows a time-evolution of t0 parameters for the DC3.

2.3.7 Dipole Magnet

A large-aperture dipole magnet is used to measure momenta of charged particles. The magnet has an aperture with 55 cm high and 135 cm wide. The length of the pole along the beam direction is 60 cm. The magnetic field strength was measured with a hall probe. The measured distribution was then compared with the calculated one using a commercial software TOSCA (Opera3D), which proved to be in a good agreement. The magnetic field points upward, and the magnetic field strength is 0.7 T (1.1 T) at the center when the current is set at 800 A (1510 A). The current was set at 800 A for the present experiment.

2.3.8 e^+e^- Blocker

e^+e^- pairs from the target and trigger counter spread out mostly in the median plane in the magnet due to their small production angle ($\approx 1/\gamma$). Low energy electron or positron of the pair could come out beyond the acceptance of the beam dump located behind the spectrometer, hitting directly thin walls of the experimental hutch, which may cause radiation safety problems.

The e^+e^- blocker with two lead blocks is placed 20 cm downstream of the center of the magnet. Each Pb block is 4 cm high, 44 cm wide, and 10 cm thick. The gap between the two Pb blocks is 15.5 cm, which allow only e^+e^- pairs above 1 GeV/c to pass through the gap. The e^+e^- pair emerges mostly asymmetrically in energy. In most cases, one of pairs is blocked by the blocker, while the other survives and escapes through the 15.5 cm gap and is stopped by the

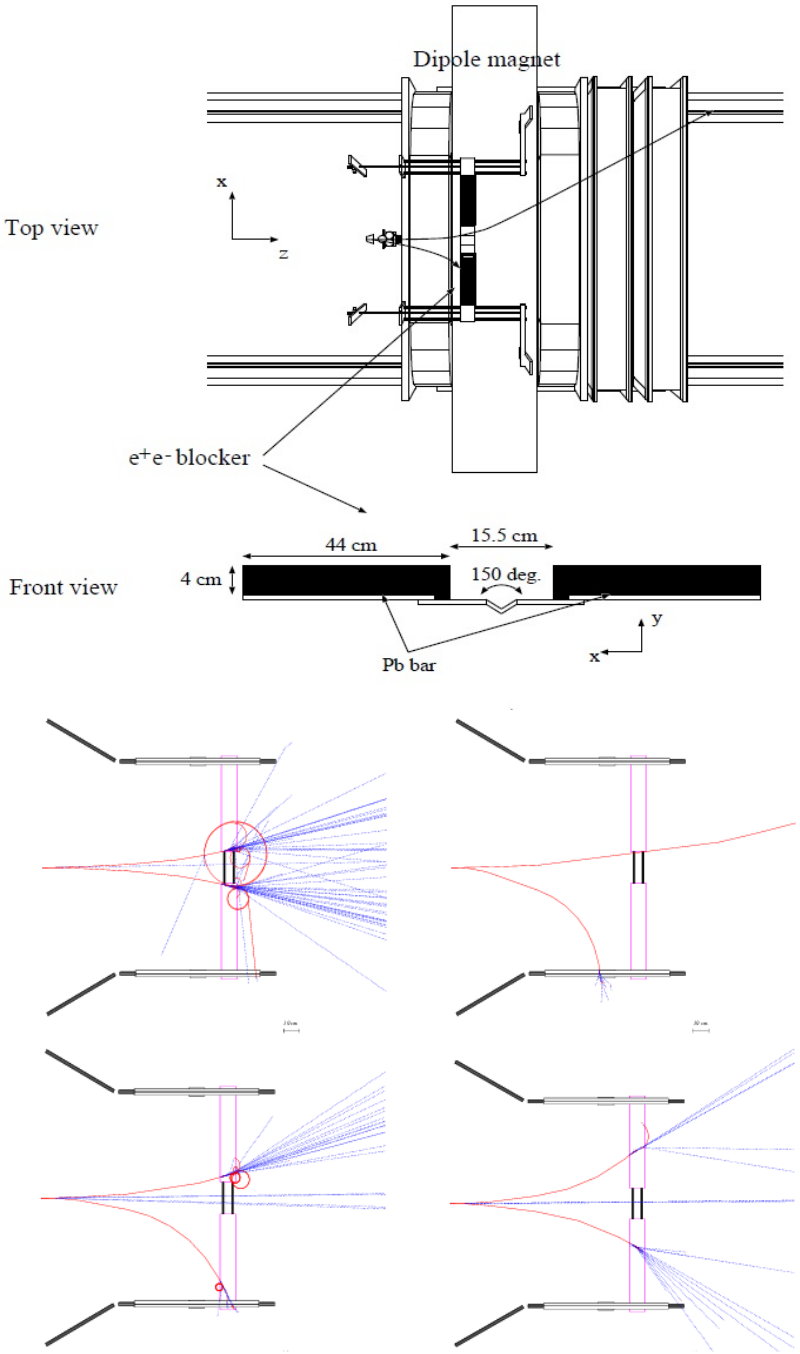

Figure 2.16: The e^+e^- blocker (top) and simulated trajectories of e^+e^- pairs from the target (bottom).

beam dump. The Pb blocks are supported by two thin channels with a 0.2 cm in thickness. A V-shaped thin bar (SUS) with a thickness of 0.5 cm connects a thin channel with one another in the center. The V-shape structure opens at 150^o and has 1.5 cm in depth to allow photon beam pass through. The blocker has been sagged by its weight, and the center in the y-direction is -7 mm.

2.3.9 Time-of-Flight Detector

The time-of-flight (TOF) wall was placed downstream of the DC3. The TOF wall consists of 40 slats of plastic scintillator (BC-408), each being 200 cm high, 12 cm wide and 4 cm thick. Two 2-in photomultiplier tubes (H7195) read TOF signals at both ends. A 3-cm thick cylindrical light guide was placed between the PMT and the scintillator. The adjacent TOF slats were overlapped by 1 cm. Out of 40 TOF slats, each of 10 slats is placed in the left or right-side wing. The side wings are tilted by 15 degrees towards the magnet. There are 4 cm gap between two central slats for beam-through. The TOF wall is movable on the rail [40].

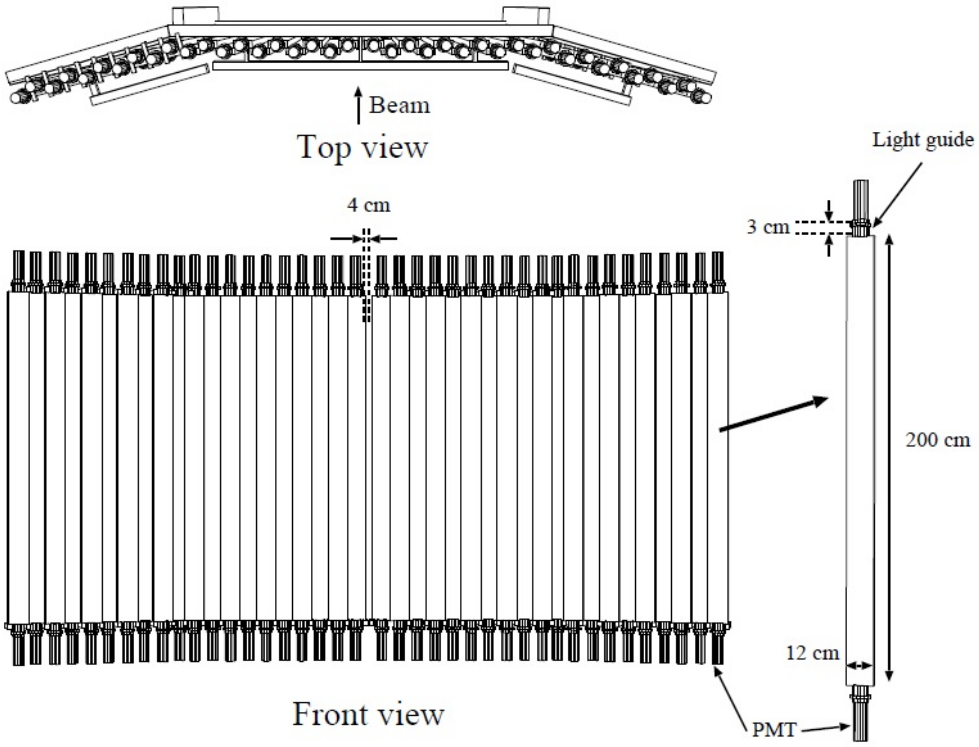

Figure 2.17: Time-of-flight detector

The RF signal is used to determine a start timing for the time-of-flight mea-

surement. The RF signals are pre-scaled with a factor of $1/87$ using prescaler modules (17K32 508-MHz 30 bit counters, Digital Laboratory). Out of three logic output signals two outputs are fed into the FASTBUS TDC (1875S) for the time-of-flight measurement. One of the two is delayed by 86 ns relative to the other signals. The RF logic signal and the delayed signal are prepared to prevent the event loss due to the dead time of the trigger timing.

The third pre-scaled output is again fed to a prescaler with a factor of $1/28$. Two of three output signals are delayed by 1.8 μs and 3.6 μs relative to the other signal. These three signals are then read by the FASTBUS TDC 1877A module for the accidental rate study in the tagging system.

2.4 Trigger and Data Aquisition System

2.4.1 Hadron Trigger

LeCroy 4300B FERA (Fast Encoding & Readout ADC) systems are used to read analog signals from plastic hodoscopes in the tagging system, the upstream-veto counter, the trigger counter, the AC, and the TOF counters. The gate width of FERA modules was set to 150 ns. VME flash ADC modules read analog signals from the silicon strip detectors (SVTX). LeCroy FASTBUS 1877S TDC modules read out the discriminated signals from the TAG-SFF and TAG-PL, and the drift timing signals from the DC1, DC2 and DC3, which have time resolution of 0.5 ns/channel and 1-μs dynamic range. LeCroy FASTBUS 1875A TDC modules read out the discriminated signals from the TAG-PL, upstream-veto counter, the trigger counter, the AC and the TOF counters, and RF signals, which have timing resolution of 0.025 ns/channel with 100-ns dynamic range.

Figure 2.19 shows a readout diagram for the TAG, the upstream-veto counter, the trigger counter, the AC and TOF counters, and logic circuits for the trigger. The signals from the DC's and SSD's, and RF signals are not used in the trigger logic.

In the tagging system, the AND gate signal of two OR signals from the TAG-PL and TAG-SF is used in the trigger logic. A logic signal from the upstream-veto counter is used as a veto signal. A coincidence signal from both photomultiplier tubes of the trigger counter is used in the trigger logic. The coincidence signal provides the common start for the FASTBUS 1875A TDC module and the common stop for the FASTBUS 1877S TDC module. The width of the coincidence signal was set to 25 ns. An OR gate signal of four photomultiplier tubes of the AC provides a veto signal for a trigger logic. In the TOF system, a mean

time of the logic signals from two PMT's of the TOF slab is made using a mean timer module (CAMAC C561), which is then fed into the majority logic unit module 4532 (CAMAC). The signal of the multiplicity ≥ 1 was accepted for the trigger logic.

The hadron trigger was defined as

$$\mathrm{Hadron} = \mathrm{TAG} \otimes \overline{\mathrm{UPveto}} \otimes \ \mathrm{TRG} \otimes \overline{\mathrm{AC}} \otimes \ \mathrm{TOF},$$

while the e^+e^- trigger was defined as

$$e^+e^- = \mathrm{TAG} \otimes \overline{\mathrm{UPveto}} \otimes \ \mathrm{TRG} \otimes \ \mathrm{TOF}$$

The e^+e^- trigger signals are pre-scaled to be about 20% of the rate of the hadron trigger.

2.4.2 Data Acquisition System

The LEPS data acquisition system consisted of digitizers, buffer sequencers, CPUs for local DAQ systems, and a data collection server. The buffer sequencer module stored several events in buffer memory. The buffer data were then transfered to a CPU. We used three local DAQ systems. The first system handled pulse-height signals from TAG-PL, UPveto, TRG, AC and TOF counters.

Digitized data from FERAs were collected with the universal I/O VME module (UIO) through a FERA divider. The buffer data in the 8-MB UIO memory were fed into the data server through the VME CPU-board The second local system worked for SSDs of the TAG and the SVTX. A Viking chip read signals from 128 strips of the SSD. The 128 analog signals were sent to a flash ADC module (FADC). Pedestal-subtracted data from several FADC modules were then collected by the UIO module. A VME CPU board computer again read the buffer data and sent them to a data server.

The Next-Generation FASTBUS (NGF) worked as both buffer sequencer module and FASTBUS-VME interface. The NGF read out and store the data from the FASTBUS TDC modules (1877S and 1875A). The CPU read buffer data from the NGF memory and sent them to the data server when the buffer-change request came to the interrupt register of the NGF.

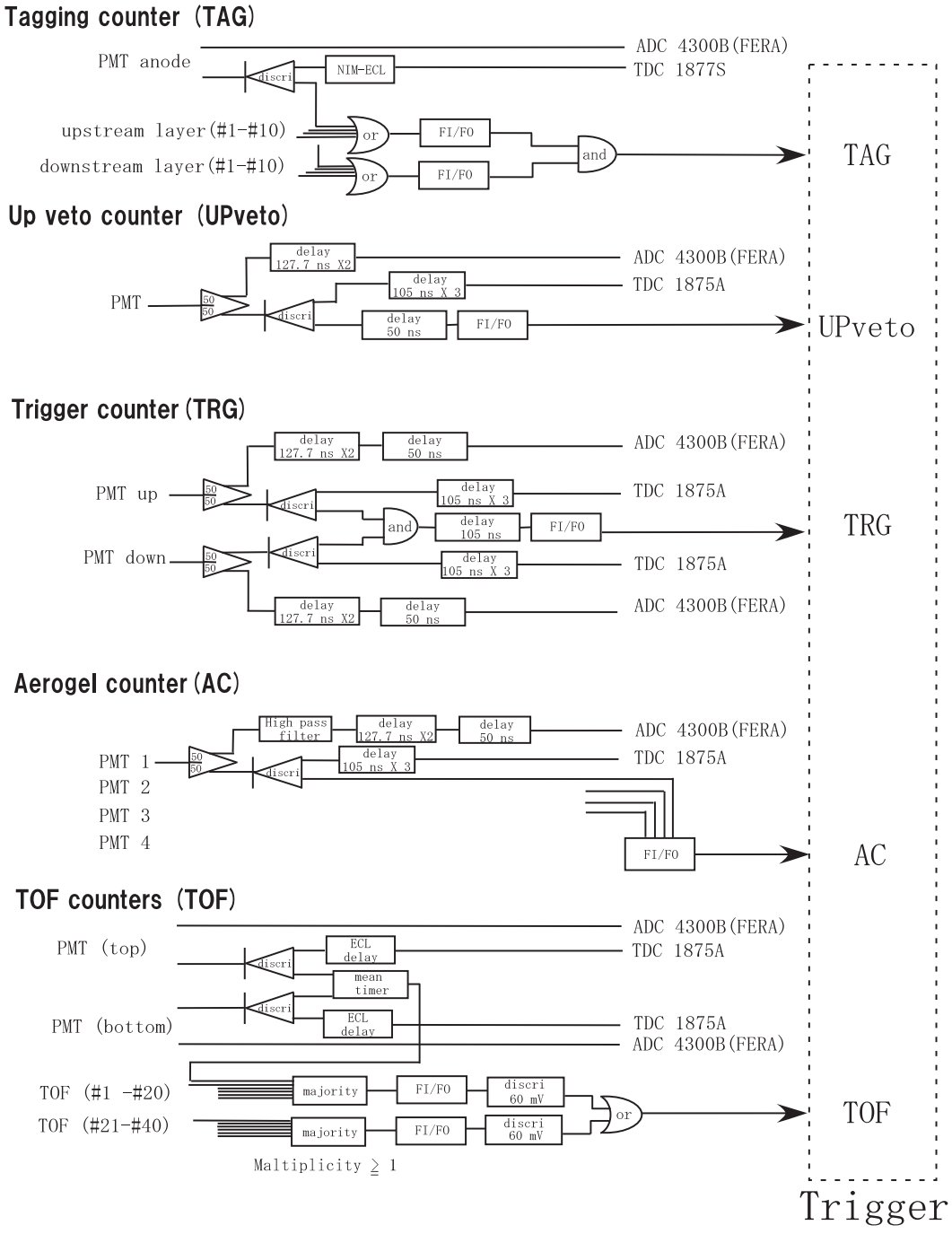

Figure 2.18: Trigger diagram

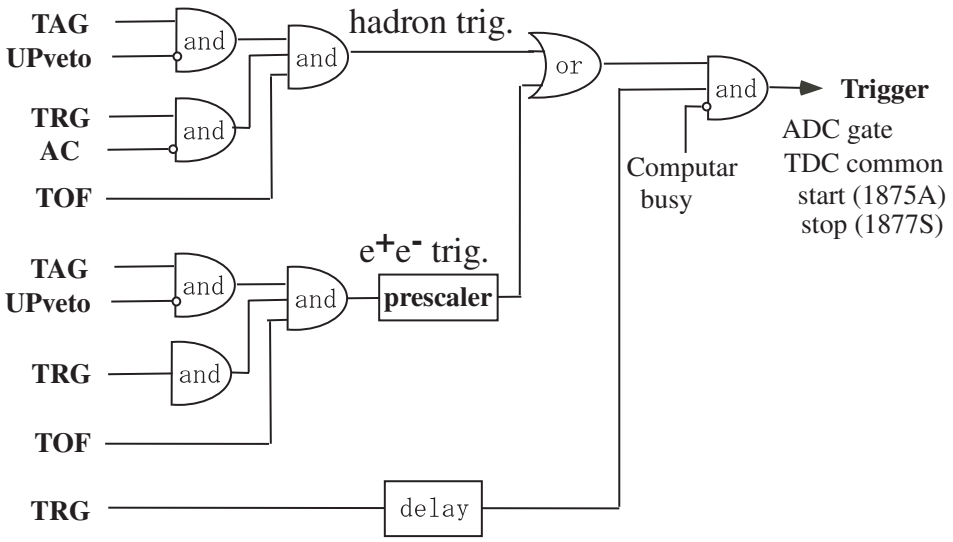

Figure 2.19: Hadron trigger

Chapter 3

Data Analysis

3.1 Photon Tagging and Flux Determination

Good tagger hits were selected by requiring that the number of tagger hits is equal to unity or larger than 1 when the TAG-SSD hit (in the 2002/2003 runs) or the fiber hit (in the 2006/2007 runs) in either of the two layers is correlated to the hit in the plastic scintillator (TAG-PL) hodoscopes. A further constraint was imposed on the number of hits in the plastic scintillator hodoscope, which should be one in either of the two layers, since some of high-energy recoil electrons could leave background hits from electromagnetic shower by hitting a shielding plate placed close to the storage ring.

In the 2002/2003 runs there were a few dead strips in the SSD layers, so the photon energy bins ($1.91 < E_\gamma < 1.93$ and $2.27 < E_\gamma < 2.30$) corresponding to the dead strip of the SSD were accepted only with the number of tagger hits (ntag) equals unity. For the 2006/2007 runs two superlayers of the scintillating fiber tagger recorded recoil electrons in front of the TAG-PL. Fiber hits are clusterized in each superlayer. If either of the TAG-SFF cluster or the TAG-SFB cluster is associated with the TAG-PL hit, they are identified as a tagged event.

The integrated photon beam flux was calculated from the number of tagged photons, tagger efficiencies, a beam transmission factor between the tagging point to a LH_2 target in the experimental hutch (0.526). The total number of photon beams was $N_\gamma = 4.8 \times 10^{12}$ in $E_\gamma = 1.573 - 2.473$ GeV from the 2002/2003 and the 2006/2007 data sets.

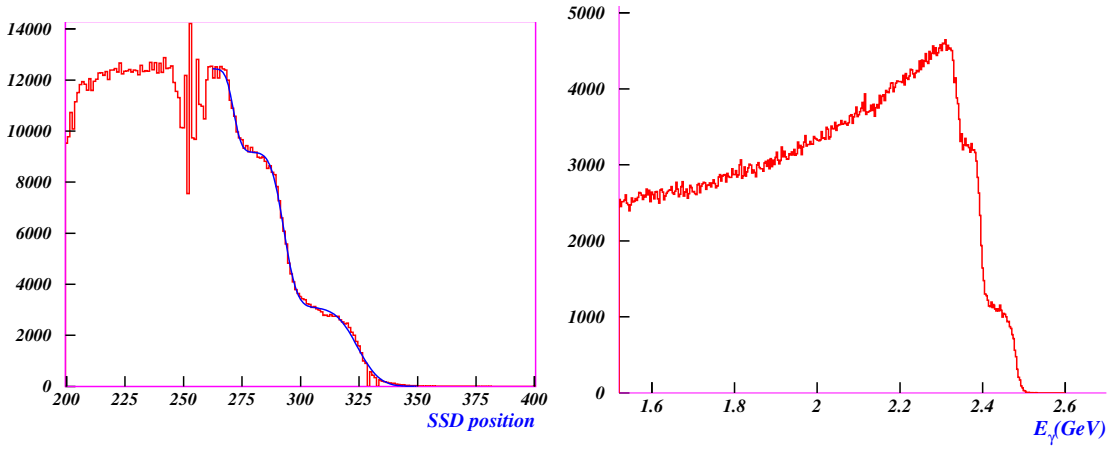

Figure 3.1: Tagger SSD hit distribution was fitted with functions of Compton-edge parameters (left). Simulated spectrum of Compton-backscattered photons with best-fit parameters (right).

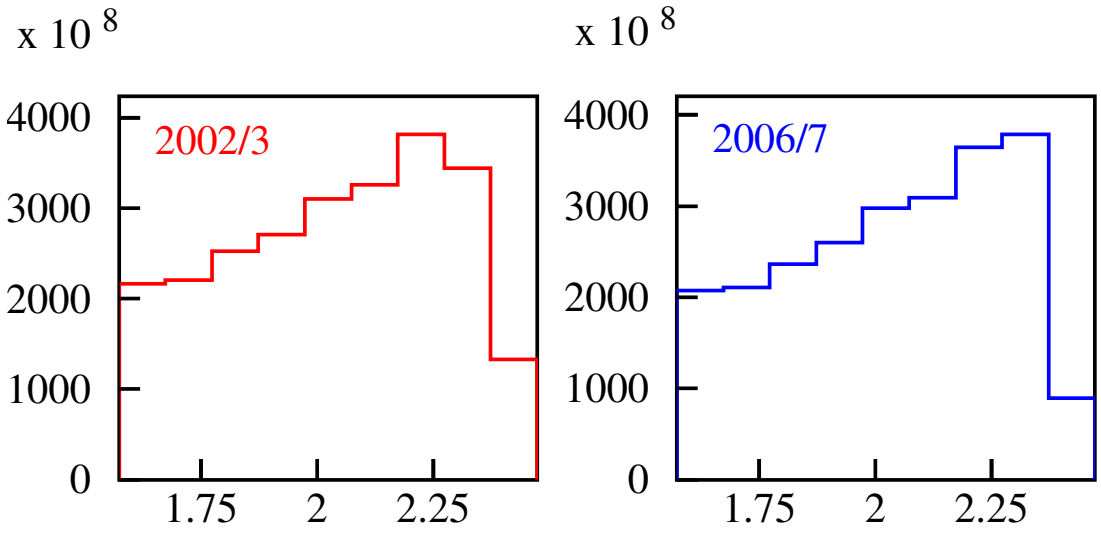

Figure 3.2: Photon beam energy distributions for the 2002/2003 runs and the 2006/2007 runs, respectively, are shown with 100-MeV bins from the threshold energy of 1.573 GeV.

3.2 Event Selection

In this analysis both the 2002/2003 and the 2006/2007 LH_2 data sets were used with 'good' runs in the run numbers of $23690 - 24058$, $25452 - 25968$, and $34827 - 37759$. Both runs were taken with a liquid hydrogen target of 150 mm

in length and a $n = 1.03$ aerogel Cherenkov detector. For the 2002/2003 runs, a multi-line laser (Coherent Innova SABRE 25/5) was used with 1 W each for 351.1 and 363.8 nm wavelengths and 5 W in total for wavelengths spanning from 333.6 to 363.8 nm, thereby producing multi-step Compton-edges near 2.4 GeV. For the 2006/2007 runs, Compton backscattered photons were produced from 1.5 GeV to 2.4 GeV at a single Compton edge due to a single-line laser of 355.5-nm wavelength.

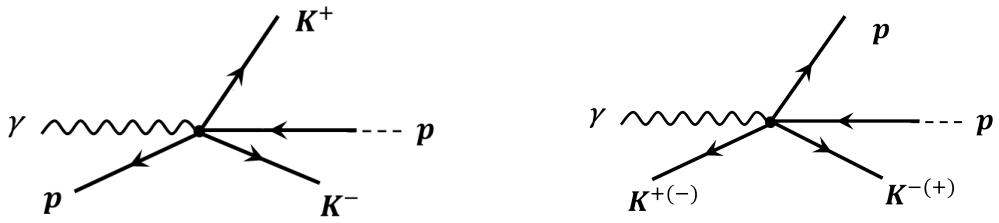

Figure 3.3: Event topologies for K^+K^- events (left) and for both K^-p and K^+p events (right) at the total c.m. system.

For the K^-K^+p final-state analysis, the data sets were first skimmed by requiring that at least two charged tracks were detected ("two-track" events). Among them, the two-track events were used with either of K^-K^+, K^-p, or pK^+ detected. Event topologies for K^+K^-, K^-p and K^+p events at the total c.m. system are displayed in Figure 3.3.

Close to the ϕ photoproduction threshold energy kaons from the ϕ decay carry about 0.5 GeV/c only, as shown in Fig. 3.4, so that only one-third of kaons can reach the ToF array located 4.3 m away from the target. Probability for detecting K^+K^- will then be less than one-tenth. Survival rate of the 0.5 GeV/c kaons traveling 4.3 m distance between the target and the ToF is given by $P \propto \exp(-L/c\tau\beta\gamma)$, where $L = 4.3$ m, $c\tau_K = 3.7$ m, and $\beta\gamma = p/m_K \sim 1$. Therefore, $P_{Kp} \sim 30\%$ for the Kp detection mode, while $P_{K^+K^-} \sim 9\%$ for the K^+K^- detection mode. The K^+p detection mode has the same kinematical acceptance as the K^-p detection mode, but it contains large background from K^+ photoproduction associated with hyperons.

Mode	t Region	Feature
K^+K^-	Small t	Dominant in-flight decay near threshold
K^-p	Wide t	Clean sample near threshold
K^+p	Wide t	Large background from (γ, K^+)
K^+K^-p	Small t	Complete kinematics but small yield

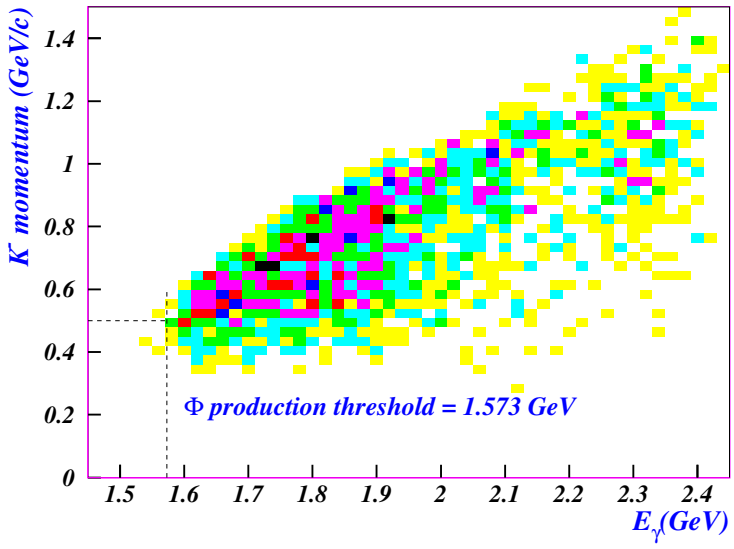

Figure 3.4: Scatter plot for kaon momentum versus photon energy in the K^-p detection mode.

Momenta of charged particles were determined using tracking information from the vertex detector (SVTX) and the three drift chambers. The equation of motion for the trajectory of a charged particle under inhomogeneous magnetic field was solved using the Runge-Kutta integration method [40].

The vertical position at the ToF slat was calculated from the time difference of the TDC signals between the two photomultiplier signals at both ends. The spatial resolution was σ =18 mm in the vertical direction. The vertical hit information was used to reject in-flight decays of charged particles between the DC3 and the ToF.

The start signal of the time-of-flight measurement was provided by the RF signal from the 8-GeV electron storage ring where a bunch of electrons was circulated in the 2-ns time-bucket [1] with a 12-ps (rms) width.

The masses of reconstructed charged particles were calculated from the relation $m^2 = p^2(1-\beta^2)/\beta^2$, where β is the speed of a charged particle passing the flight length L in time of flight (ToF), $\beta = L/(c \cdot ToF)$. c is the speed of light. Figure 3.5 shows reconstructed mass distributions for charged particles. The typical mass resolution was 30 MeV/c^2 for 1 GeV/c kaons.

[1] RF frequency for a storage ring is 508.58 MHz, so the time interval is 1.9663 ns.

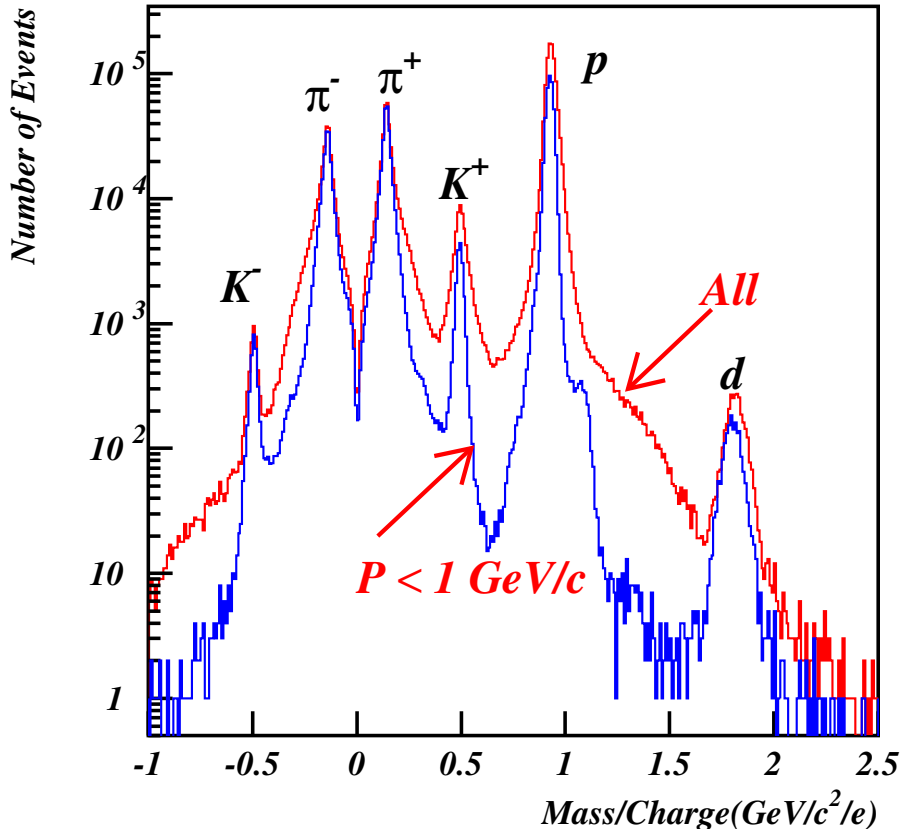

Figure 3.5: Reconstructed mass distributions for charged particles. Red spectrum indicates the whole momentum range, while blue one for the charged particles below 1 GeV/c.

Taking partial derivatives of

$$m^2 = p^2\Big(\frac{1}{\beta^2} - 1\Big) = p^2\Big(\frac{t^2}{L^2} - 1\Big),$$

in terms of p, t (time-of-flight), and L (flight length), the mass resolution $\sigma(m^2)$ can be give as:

$$\mathrm{d}(m^2) = 2p\mathrm{d}p\Big(\frac{t^2}{L^2} - 1\Big) + 2t\mathrm{d}t\frac{p^2}{L^2} - 2\frac{\mathrm{d}L}{L^3}p^2t^2,$$

where $t^2/L^2 - 1 = m^2/p^2$. Since $\beta^2 = p^2/E^2 = L^2/t^2$,

$$\frac{p^2t^2}{L^2} = E^2 = m^2 + p^2$$

. Therefore,

$$\mathrm{d}(m^2) = 2m^2\frac{\mathrm{d}p}{p} + 2E^2\frac{\mathrm{d}t}{t} - 2E^2\frac{\mathrm{d}L}{L}.$$

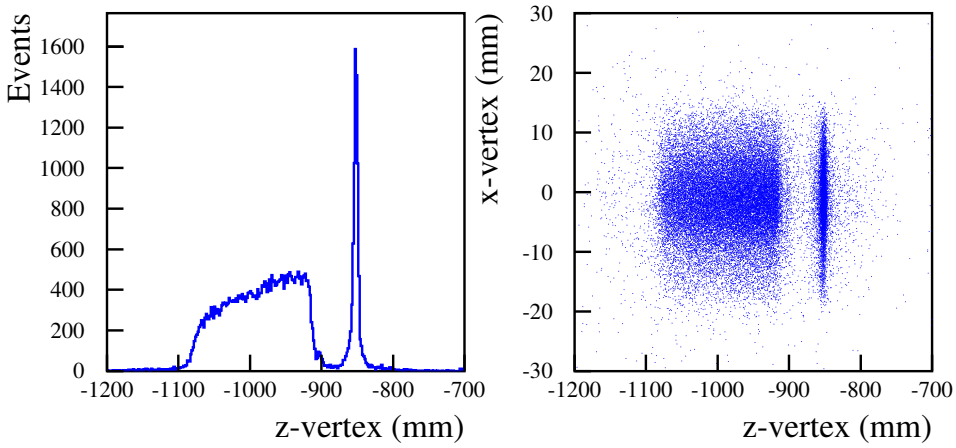

Figure 3.6: Vertex distributions near the target position.

The mass resolution is then given by

$$\sigma(m^2) = 2\Big[m^4\Big(\frac{\sigma_p}{p}\Big)^2 + (p^2+m^2)^2\Big(\frac{\sigma_t}{t}\Big)^2 + (p^2+m^2)^2\Big(\frac{\sigma_L}{L}\Big)^2\Big]^{1/2}.$$

Since σ_L/L is negligibly small and multiple Coulomb scattering can be parametrized as $\sigma_p^{MS}/p = a_1/\beta$, the mass resolution can be then rewritten as

$$\begin{aligned}\sigma(m^2) &= 2\Big[m^4\Big\{\Big(\frac{\sigma_p}{p}\Big)^2 + \Big(\frac{\sigma_p^{MS}}{p}\Big)^2\Big\} + (p^2+m^2)^2\Big(\frac{\sigma_t}{t}\Big)^2\Big]^{1/2} \\ &= 2\Big[m^4\Big\{\Big(\frac{\sigma_p}{p}\Big)^2 + \frac{a_1^2}{\beta^2}\Big\} + (p^2+m^2)^2\Big(\frac{\sigma_t}{t}\Big)^2\Big]^{1/2}\end{aligned}$$

Using $t = L/(c\beta)$ and $\beta^2 = p^2/(p^2+m^2)$, and taking parameterizations of $\sigma_p/p = a_2 p$ (from $\sigma_p/p \propto p$) and $a_3 \equiv \sigma_t$,

$$\sigma(m^2) = 2\Big[m^4 a_2^2 p^2 + m^4\frac{(m^2+p^2)}{p^2}a_1^2 + (p^2+m^2)a_3^2 p^2\frac{c^2}{L^2}\Big]^{1/2}$$

or

$$\sigma^2(m^2) = 4m^4\Big(1+\frac{m^2}{p^2}\Big)a_1^2 + 4m^4p^2a_2^2 + 4p^2(p^2+m^2)\frac{c^2}{L^2}a_3^2,$$

where the fit parameters are given as $a_1 = 0.00458$, $a_2 = 0.00323$ and $a_3 = 0.123, 0.175$, respectively. m is the particle mass, c the speed of light, and L represents the typical path length of charged particles in the LEPS spectrometer. Further particle identification was based on the above momentum-dependent mass resolution relation with three times σ_m^2 boundaries and the cut-off ($\Delta m^2 = 0.1764$) on the mass difference between π and K.

Next, the standard cuts for event selection were imposed:

1. `decaycut.f`> 0, the ToF hit consistency is required. It contains the constraints on the valid ToF hit (`ithtofhit(itrk)`>0), the consistency between the hit positions determined by the ToF time difference and by tracking ($|$`ytof(itrk)`$-$`tofdiff(itrk)`$| < 80$), the active ToF bar number matching ($|$`itof(itrk)`$-$`tofid(itrk)`$| < 2$), the χ^2 probability of the 'estimated' track positions compared with chamber hits is larger than 2%, the outlier hit rejection (`noutl(itrk)`≤ 6), and the e^+e^--associated ToF hit rejection ($|$`ytof(itrk)`$| > 30$).

2. `itagc.f`> 0, the number of tagged photons is at least 1.

3. `vertex.f`, the z position of the two-track vertex should lie between -1100 mm and -906 mm and its x position be within 25 mm.

Using the `vtxmomlh2.f` function the momentum vectors at the two-track vertex were recalculated. Photon energy E_γ (given by the `photonenergy.f` function) was calculated from the energy-momentum balance in $\gamma p \to K^-K^+p$ reaction. The corrected kinematic values are used as initial parameters for the kinematic fit described in later sections.

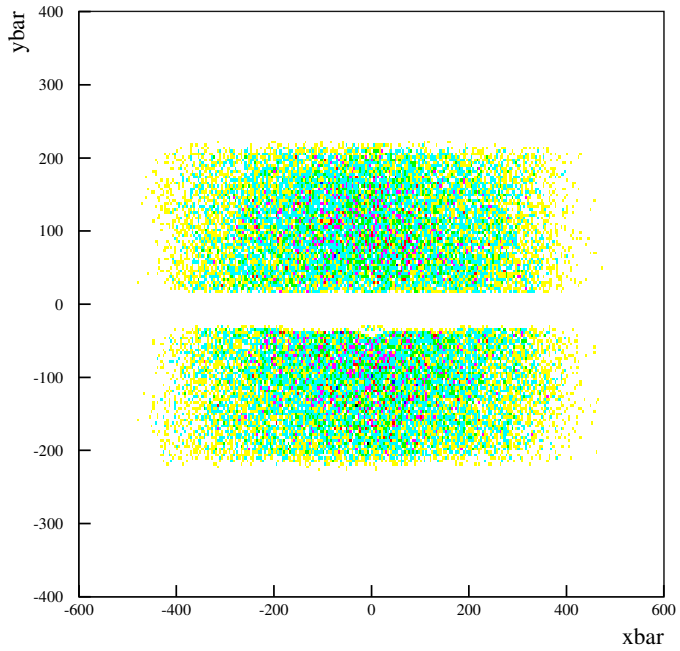

Figure 3.7: Track positions in the virtual plane at the e^+e^- blocker.

To select K^+K^-p production events with equal footing on the kinematic constraints in terms of the combination of two detected tracks (the detection mode),

we have performed a kinematic fit with 4C−3 constraints on the $\gamma p \to K^+K^-p$ reaction. Before the kinematic fit, we imposed only the three event selection criteria as described earlier: (1) `decaycut.f`, (2) `itagc.f`, and `vertex.f`.

Runs	2002/2003					
Modes	K^+K^-		K^-p		pK^+	
Cuts	Survived	Ratio	Survived	Ratio	Survived	Ratio
mode	14870	–	12669	–	82547	–
tagger	10200	68.6%	8469	66.8%	51300	62.1%
vertex	7387	72.4%	6109	72.1%	35729	69.6%
decay	6526	88.3%	5305	86.8%	31643	88.6%
e^+e^-	6298	96.5%	5141	96.9%	30669	96.9%
$P(\chi^2)$	5587	88.7%	3106	60.4%	7200	23.5%

Runs	2006/2007					
Modes	K^+K^-		K^-p		pK^+	
Cuts	Survived	Ratio	Survived	Ratio	Survived	Ratio
mode	12962	–	11414	–	76871	–
tagger	11480	88.6%	10038	87.9%	65379	85.1%
vertex	8400	73.2%	7331	73.0%	45748	70.0%
decay	7847	93.4%	6682	91.1%	42616	93.2%
e^+e^-	7623	97.1%	6492	97.2%	41583	97.6%
$P(\chi^2)$	6742	88.4%	4091	63.0%	9121	21.9%

Table 3.1: The numbers of events survived with cutoffs for the 2002/2003 and 2006/2007 runs. Consequently this analysis is based on a total of 35847 K^+K^-p events, consisting of 12329 events with K^+K^- detected, 7197 events with K^-p detected, and 16321 events with pK^+ detected.

Table 3.1 represents the event statistics with selection criteria for both the 2002/2003 and 2006/2007 runs. The numbers of survived events to with cutoffs and the survival ratios are quoted in the table. Consequently this analysis is based on a total of 35847 K^+K^-p events, consisting of 12329 events with K^+K^- detected, 7197 events with K^-p detected, and 16321 events with pK^+ detected. The 2006/2007 runs showed higher survival ratios for tagger selection criteria than those for the 2002/2007 runs, which could be understood as being due to a high tagging efficiency with the scintillating fiber tagger. In both 2002/2003 and 2006/2007 runs, the pK^+ events survived much less than the other-mode events with the $P(\chi^2)$ cut, since hyperon-production background events were rejected with the cutoff.

Figure 3.8 shows scatter plots of the K^+K^- and K^-p mass distributions for the 2002/2003 (top 6 plots) and the 2006/2007 runs (bottom 6 plots) by requiring that K^+K^- tracks are detected (top left), for the events further imposed with `itagc.f` (top middle), with `vertex.f` (top right) further with `decaycut.f` (bottom left) and with an additional cutoff on the y position at the e^+e^- bar (bottom middle), and finally with a χ^2 probability for the kinematic fit which will be discussed in the next section (bottom right). Figures 3.9 and 3.10 show the distributions by requiring that K^-p tracks and pK^+ tracks, respectively. Again the top 6 plots correspond to the 2002/2003 runs, while the bottom 6 plots the 2006/2007 runs.

3.3 Kinematic Fit for $\gamma p \to K^+K^-p$

Kinematic fit minimizes the deviation of measured quantities from constraints like energy and momentum conservation, performed on an event-by-event basis. The kinematic fit was used to calculate the photon energy and the four-momenta of the missing particle in the K^-K^+p final state.

- y_n : N measured parameters
- η_n : N fitted parameters
- ξ_j : J unmeasured parameters
- K constraints expressed as

$$f_k(\eta_1, \cdots, \eta_N; \xi_1, \cdots, \xi_J) = 0, \quad k = 1 \cdots K$$

The total χ^2_T that should be minimized is given by

$$\chi^2_T = (\vec{y} - \vec{\eta})^T V^{-1} (\vec{y} - \vec{\eta}) + 2\vec{\lambda}^T \cdot \vec{f}(\vec{\eta}, \vec{\xi})$$

where K additional unknowns λ_k are the Lagrange multipliers that forms a vector $\vec{\lambda}$.

$$\begin{aligned}
\partial_\eta \chi^2_T &= -2V^{-1} \cdot (\vec{y} - \vec{\eta}) + 2\vec{F}^T_\eta \cdot \vec{\lambda} = \vec{0}, \quad \text{(N equations)} \\
\partial_\xi \chi^2_T &= \vec{F}^T_\xi \cdot \vec{\lambda} = \vec{0}, \quad \text{(J equations)} \\
\partial_\lambda \chi^2_T &= 2\vec{f}(\vec{\eta}, \vec{\xi}) = \vec{0}, \quad \text{(K equations)}
\end{aligned}$$

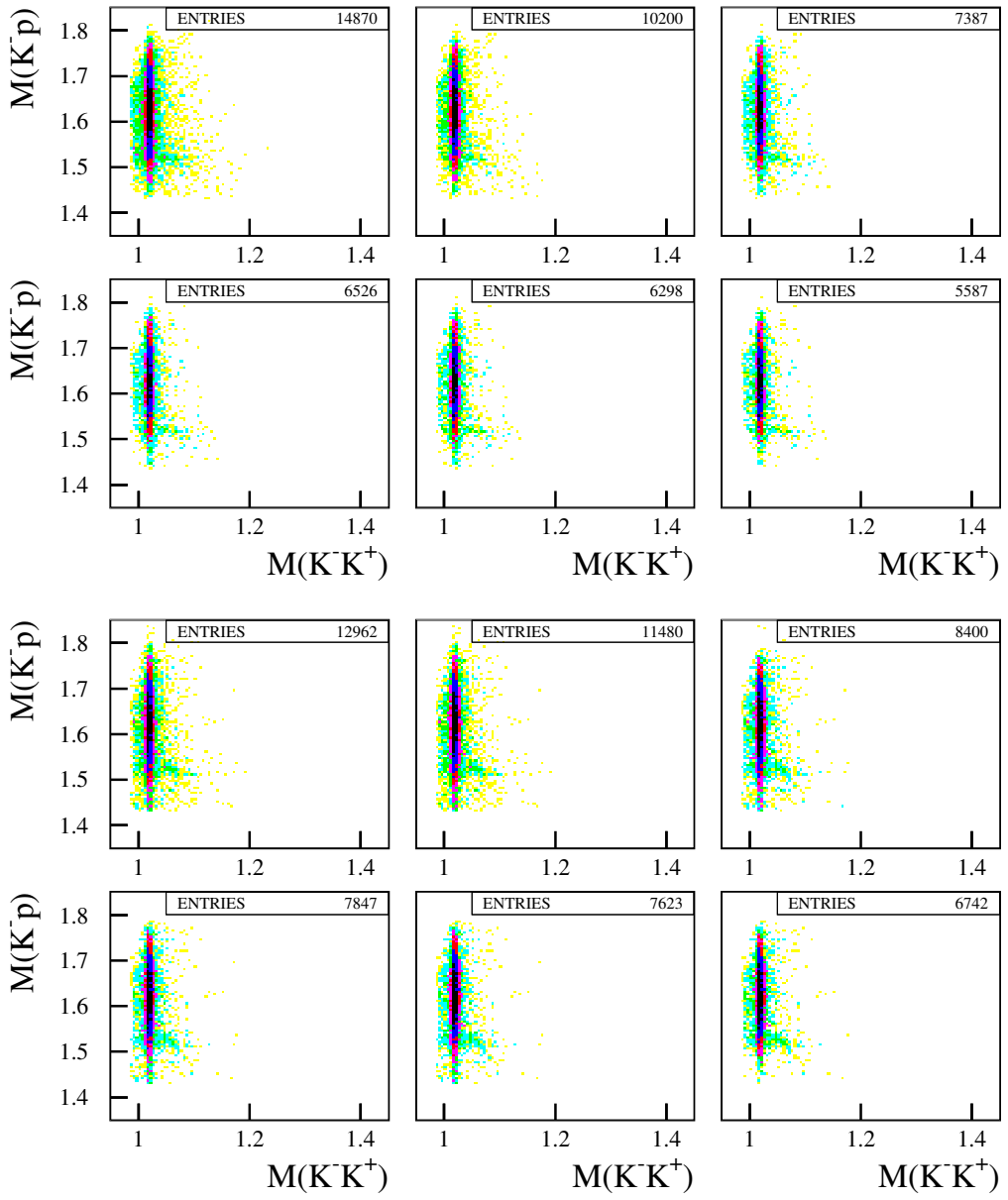

Figure 3.8: Scatter plots of the K^+K^- and K^-p mass distributions for the 2002/2003 data set (top 6 plots) and the 2006/2007 data set (bottom 6 plots) by requiring that K^+K^- tracks are detected (top left), for the events further imposed with `itagc.f` (top right), with `vertex.f` (middle left) further with `decaycut.f` (middle right) and with an additional cutoff on the y position at the e^+e^- bar (bottom left), and finally with a χ^2 probability for the kinematic fit which will be discussed in the next section (bottom right).

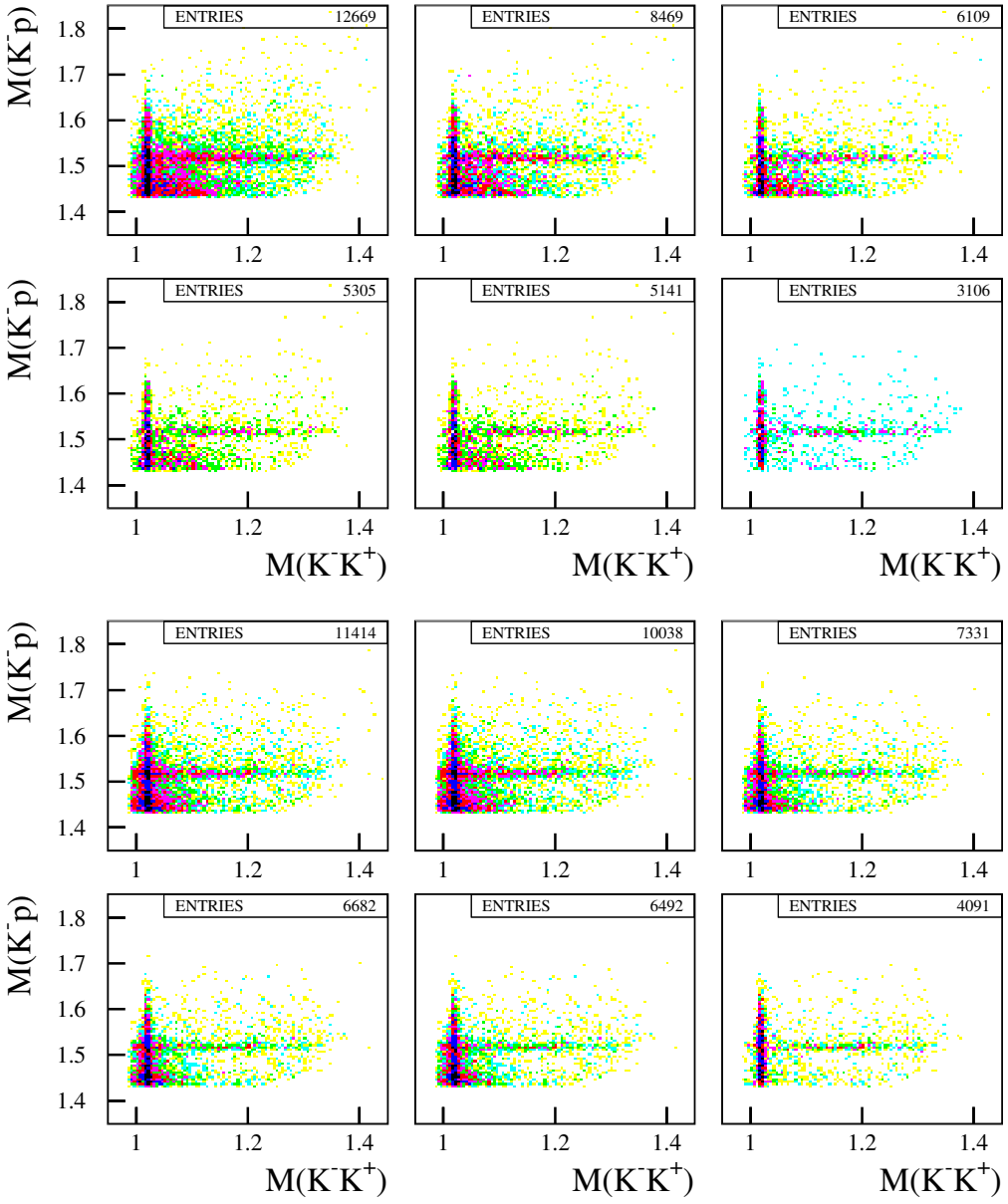

Figure 3.9: Scatter plots of the K^+K^- and K^-p mass distributions for the 2002/2003 data set (top 6 plots) and the 2006/2007 data set (bottom 6 plots) by requiring that K^-p tracks are detected (top left), for the events further imposed with `itagc.f` (top right), with `vertex.f` (middle left) further with `decaycut.f` (middle right) and with an additional cutoff on the y position at the e^+e^- bar (bottom left), and finally with a χ^2 probability for the kinematic fit which will be discussed in the next section (bottom right).

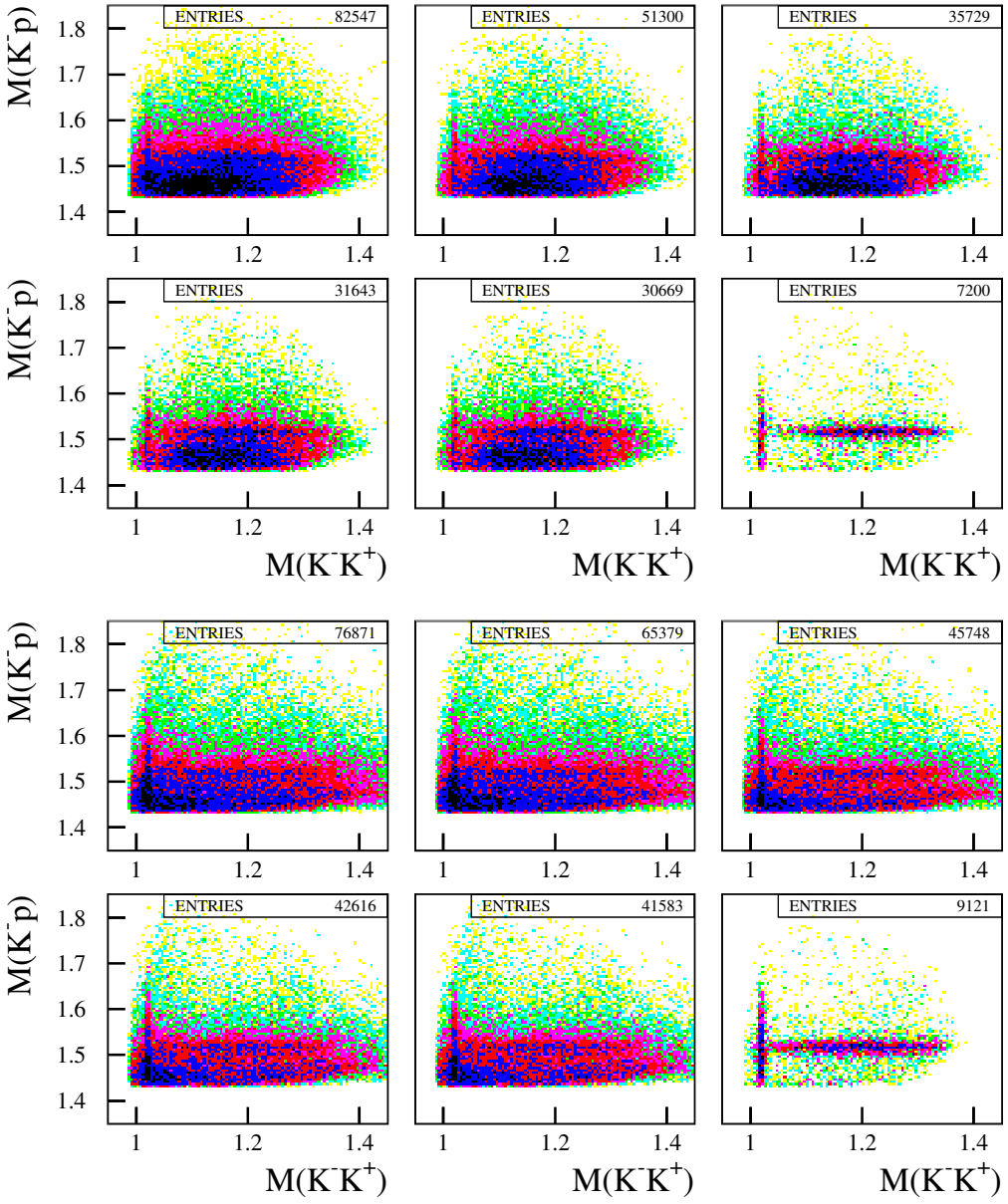

Figure 3.10: Scatter plots of the K^+K^- and K^-p mass distributions for the 2002/2003 data set (top 6 plots) and the 2006/2007 data set (bottom 6 plots) by requiring that K^+p tracks are detected (top left), for the events further imposed with `itagc.f` (top right), with `vertex.f` (middle left) further with `decaycut.f` (middle right) and with an additional cutoff on the y position at the e^+e^- bar (bottom left), and finally with a χ^2 probability for the kinematic fit which will be discussed in the next section (bottom right).

where F_η and $F_x i$ are matrices of dimension $K \times N$ and $K \times J$, respectively, defined as

$$(F_\eta)_{kn} = \frac{\partial f_k}{\partial \eta_n},$$
$$(F_\xi)_{kj} = \frac{\partial f_k}{\partial \xi_j},$$

After dropping the factors of 2:

$$\begin{aligned} \vec{0} &= V^{-1} \cdot (\vec{\eta} - \vec{y}) + \vec{F}_\eta^T \cdot \vec{\lambda} \\ \vec{0} &= \vec{F}_\xi^T \cdot \vec{\lambda} \\ \vec{0} &= \vec{f}(\vec{\eta}, \vec{\xi}) \end{aligned}$$

Since the constraints $\vec{f}(\vec{\eta}, \vec{\xi})$ and their derivatives F_η and $F_x i$ are in general non-linear functions, this system of equations has to be solved iteratively.

Let $\vec{\eta}^\nu$ and $\vec{\xi}^\nu$ denote the values at iteration ν. Then we can make a Taylor expansion around this point, and write (neglecting terms of the second and higher order)

$$\vec{f}(\vec{\eta}^{\nu+1}, \vec{\xi}^{\nu+1}) = f(\vec{\eta}^\nu, \vec{\xi}^\nu) + F_\eta^\nu \cdot (\vec{\eta}^{\nu+1} - \vec{\eta}^\nu) + F_\xi^\nu \cdot (\vec{\xi}^{\nu+1} - \vec{\xi}^\nu)$$

Now the equations read

$$\begin{aligned} \vec{0} &= V^{-1} \cdot (\vec{\eta}^{\nu+1} - \vec{y}) + (\vec{F}_\eta^\nu)^T \cdot \vec{\lambda}^{\nu+1}, \\ \vec{0} &= (\vec{F}_\xi^\nu)^T \cdot \vec{\lambda}^{\nu+1}, \\ \vec{0} &= f(\vec{\eta}^\nu, \vec{\xi}^\nu) + F_\eta^\nu \cdot (\vec{\eta}^{\nu+1} - \vec{\eta}^\nu) + F_\xi^\nu \cdot (\vec{\xi}^{\nu+1} - \vec{\xi}^\nu) \end{aligned}$$

One can solve

$$\vec{0} = V^{-1} \cdot (\vec{\eta}^{\nu+1} - \vec{y}) + (\vec{F}_\eta^\nu)^T \cdot \vec{\lambda}^{\nu+1}$$

for $\vec{\eta}^{\nu+1}$:

$$\vec{\eta}^{\nu+1} = \vec{y} - V \cdot (F_\eta^\nu)^T \cdot \vec{\lambda}^{\nu+1}$$

and insert that into

$$\vec{0} = f(\vec{\eta}^\nu, \vec{\xi}^\nu) + F_\eta^\nu \cdot (\vec{\eta}^{\nu+1} - \vec{\eta}^\nu) + F_\xi^\nu \cdot (\vec{\xi}^{\nu+1} - \vec{\xi}^\nu)$$

to get

$$\vec{0} = f(\vec{\eta}^\nu, \vec{\xi}^\nu) + F_\eta^\nu \cdot (\vec{y} - V \cdot (F_\eta^\nu)^T \cdot \vec{\lambda}^{\nu+1} - \vec{\eta}^\nu) + F_\xi^\nu \cdot (\vec{\xi}^{\nu+1} - \vec{\xi}^\nu)$$

$$\vec{r} + F_\xi^\nu \cdot (\vec{\xi}^{\nu+1} - \vec{\xi}^{\nu}) = S \cdot \vec{\lambda}^{\nu+1}$$

where we have introduced

$$\begin{aligned} \vec{r} &= \vec{f}^{\nu} + F_\eta^\nu \cdot (\vec{y} - \vec{\eta}^{\nu}) \\ S &= F_\eta^\nu \cdot V \cdot (F_\eta^\nu)^T \end{aligned}$$

S is a symmetric $K \times K$ matrix that can be inverted, provided that each constraint depends on at least one measured parameter. Since V is symmetric and positive definite, also S is symmetric and positive definite.

- The definition of S in $\vec{S} = F_\eta^\nu \cdot V \cdot (F_\eta^\nu)^T$ leads to a singular matrix if some constraints do not depend on any measured parameter.
- This is the case because for such a constraint k we have $(F_\eta)_{kn} = 0$ for all $n = 1, \cdots N$, and hence $S_{kk'} = \sum_{n,n'} (F_\eta)_{kn} V_{n,n'} (F_\eta)_{k'n'} = 0$ for this particular value of k.
- The reason for this problem is that the two equations alone are not sufficient to determine $\vec{\lambda}^{\nu+1}$.
- We have to use $\vec{0} = \vec{F}_\xi^T \cdot \vec{\lambda}$ as well.

Multiply $\vec{0} = \vec{F}_\xi^T \cdot \vec{\lambda}$ by F_ξ^ν (which is a $K \times J$ matrix) to arrive at this set of K equations :

$$\vec{0} = F_\xi^\nu \cdot (F_\xi^\nu)^T \cdot \vec{\lambda}^{\nu+1}$$

We subtract this from the constraint equation to get ($\vec{0} = \vec{0} - \vec{0}$)

$$\begin{aligned} \vec{0} = \vec{f}^{\nu} &+ F_\eta^\nu \cdot (\vec{y} - V \cdot (F_\eta^\nu)^T \cdot \vec{\lambda}^{\nu+1} - \vec{\eta}^{\nu}) \\ &+ F_\xi^\nu \cdot (\vec{\xi}^{\nu+1} - \vec{\xi}^{\nu}) - F_\xi^\nu \cdot (F_\xi^\nu)^T \cdot \vec{\lambda}^{\nu+1} \end{aligned}$$

A new S is then rewritten as

$$S = F_\eta^\nu \cdot V \cdot (F_\eta^\nu)^T + F_\xi^\nu \cdot (F_\xi^\nu)^T$$

The new term $F_\xi^\nu \cdot (F_\xi^\nu)^T$ is evidently symmetric. Multiply

$$\vec{r} + F_\xi^\nu \cdot (\vec{\xi}^{\nu+1} - \vec{\xi}^{\nu}) = S \cdot \vec{\lambda}^{\nu+1}$$

with S^{-1} to get

$$S^{-1} \cdot \left(\vec{r} + F_\xi^\nu \cdot (\vec{\xi}^{\nu+1} - \vec{\xi}^{\nu}) \right) = \vec{\lambda}^{\nu+1}$$

which inserted in $\vec{0} = (\vec{F}_\xi^\nu)^T \cdot \vec{\lambda}^{\nu+1}$ yields

$$\vec{0} = (\vec{F}_\xi^\nu)^T \cdot S^{-1} \cdot \left(\vec{r} + F_\xi^\nu \cdot (\vec{\xi}^{\nu+1} - \vec{\xi}^\nu)\right)$$

We can solve for $\vec{\xi}^{\nu+1} - \vec{\xi}^\nu$ and insert the result back into

$$\vec{r} + F_\xi^\nu \cdot (\vec{\xi}^{\nu+1} - \vec{\xi}^\nu) = S \cdot \vec{\lambda}^{\nu+1}$$

Finally,

$$\begin{aligned}
\xi^{\nu+1} &= \xi^\nu - \left((F_\xi^\nu)^T \cdot s^{-1} \cdot F_\xi^\nu\right) \cdot s^{-1} \cdot \vec{r} \\
\vec{\lambda}^{\nu+1} &= s^{-1} \cdot \left(\vec{r} + F_\xi^\nu \cdot (\xi^{\nu+1} - \xi^\nu)\right) \\
\eta^{\nu+1} &= \vec{y} - V \cdot (F_\eta^\nu)^T \cdot \vec{\lambda}^{\nu+1},
\end{aligned}$$

where

$$\begin{aligned}
\vec{r} &= \vec{f}^\nu + F_\eta^\nu \cdot (\vec{y} - \vec{\eta}^\nu) \\
S &= F_\eta^\nu \cdot V \cdot (F_\eta^\nu)^T
\end{aligned}$$

3.3.1 χ^2 Probability

If $\vec{y}(\vec{\eta})$ are the vectors corresponding to initial (final) values of the measured parameters, the χ^2 value of the fit is defined as

$$\chi^2_T = (\vec{y} - \vec{\eta})^T V^{-1} (\vec{y} - \vec{\eta}),$$

where V^{-1} is the inverse of the covariance matrix.

The distribution of χ^2 values of all events is $f(\chi^2)$, which is given by:

$$f(\chi^2) = \frac{1}{\Gamma(\lambda) \cdot 2^\lambda} (\chi^2)^{\lambda-1} e^{-\frac{1}{2}\chi^2},$$

where $\lambda = k/2$. The quantity k is the number of degrees of freedom.

If all measurement errors were properly estimated and no systematic errors are present, the above distribution should follow the χ^2 that is obtained by adding quadratically a number of Gaussians of $\mu = 0$, $\sigma = 1$. The number of Gaussians in the sum is equal to the number of degrees of freedom (ndf) in the problem. Such a standard χ^2 distribution is called a $f_{st}(\chi^2)$. Events that do not fulfill the requirements imposed by the constraints will have a distribution which peaks at higher or lower χ^2 values than this standard χ^2 distribution.

The χ^2 probability is related to the χ^2 via:

$$P(\chi^2) = 1 - \left(\int_0^{\chi^2} f_{st}(\chi^2)d\chi^2\right)$$

The χ^2 probability runs from 0 to 1, where a high χ^2 value corresponds to a χ^2 probability close to 0, and a low χ^2 value corresponds to a χ^2 probability close to 1. If the measured values are distributed according to a Gaussian distribution around the values calculated by the fit, and the measurement errors have been estimated correctly, we have $f(\chi^2) = f_{st}(\chi^2)$ and the χ^2 probability distribution will be flat.

3.3.2 Pull Distributions

The kinematic fit can provide a handle on systematic errors in the measured values. If no such errors exist, the difference between the measured and the fitted values should form a distribution centered at zero, as the fit will be just as likely to increase a specific value as to decrease it. A systematic error will cause a shift in the distribution to either positive or negative values. If that distribution is normalized to the error into the calculation, the result should be a Gaussian distribution with a sigma of 1. A broader distribution indicates the measurement errors were estimated incorrectly.

$$P_i = \frac{y_i - \eta_i}{\sqrt{\sigma_{y_i}^2 - \sigma_{\eta_i}^2}}$$

If the σ of the pull distribution is equal to 1, the measurement errors were correctly estimated. If the σ of the pull distribution deviates from 1, the measurement errors were either too large or too small. If no systematic errors were present in the measurement, the pull distribution should be centered at 0. A deviation of the mean from 0 points to systematic errors in the measurement. A non-Gaussian form of the pull distribution indicates the measurement errors were not Gaussian-distributed.

3.3.3 Kinematic Fit Results with 4C-3 Unknowns

We selected events with either K^+K^-, K^-p, or K^+p final state detected. We used the kinematic fit to reconstruct a missing particle (unmeasured for the K^-K^+p final state). We have $N = 7$ measured parameters (y_n) and 7 fit parameters (η_n):

$$E_\gamma,\ p_p,\ \left.\frac{dx}{dz}\right|_p,\ \left.\frac{dy}{dz}\right|_p,\ p_{K^-},\ \left.\frac{dx}{dz}\right|_{K^-},\ \left.\frac{dy}{dz}\right|_{K^-}$$

The number of unmeasured parameters (ξ_j) is $J = 3$:

$$p_{K^+},\ \left.\frac{dx}{dz}\right|_{K^+},\ \left.\frac{dy}{dz}\right|_{K^+}$$

From the energy and momentum conservation, we have $K = 4$ constraints ($f_k = f_k(\eta_1, \cdots, \eta_N; \xi_1, \cdots, \xi_J)$) which are given by

$$\begin{aligned} E_\gamma + m_p &= E_{K^-} + E_{K^+} + E_p \\ \vec{p}_\gamma &= \vec{p}_{K^-} + \vec{p}_{K^+} + \vec{p}_p. \end{aligned}$$

As a result, we have an overdetermined system with 4 constraints and 3 unknowns, called the 4C-3 fit. Figure 3.11 shows the kinematic fit results for K^+K^- events. The χ^2 probability distribution is flat over the whole region. The average standard deviation of pull distributions is 1.02, which is close to unity. Figures 3.12 and 3.13 show the kinematic fit results for K^-p and K^+p events, respectively. For all the three event sets, the χ^2 probability distributions are flat except the region close to $P(\chi^2) = 0$, which proves the kinematic fit results with reasonably estimated measurement errors.

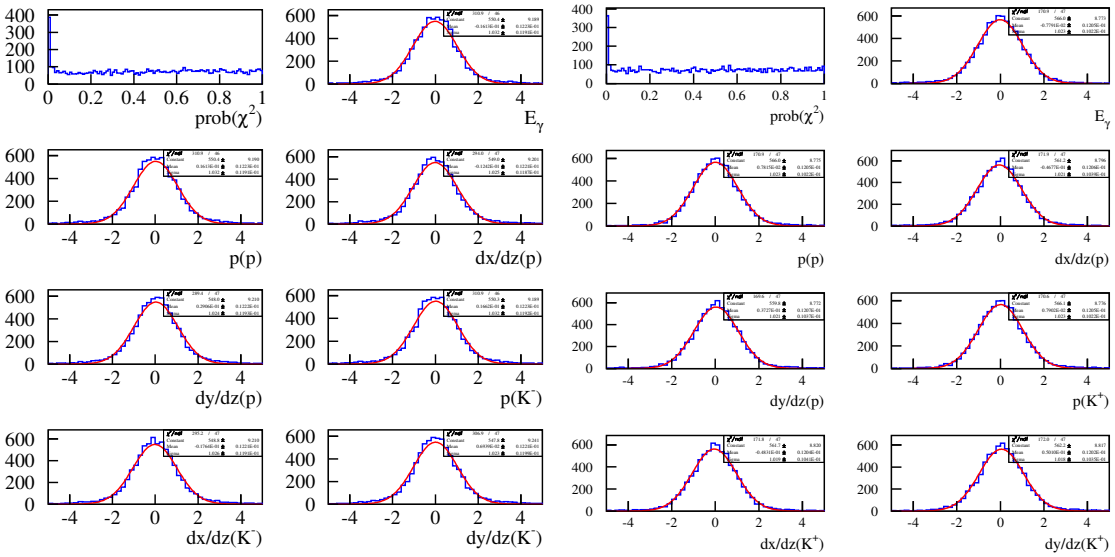

Figure 3.11: χ^2 probability and pull distributions for E_γ, and p, dx/dz, dy/dz for p and K^+. Left 6 plots are the kinematic fit results for the K^+K^- events from the 2002/2003 data set and the right ones for the 2006/2007 data set.

Figures 3.14 and 3.15 show the photon beam energy distributions for 2002/2003 and 2006/2007 data set respectively. The Blue line histograms indicate the photon beam energy distribution after the kinematic fit, red ones are before the kinematic fit.

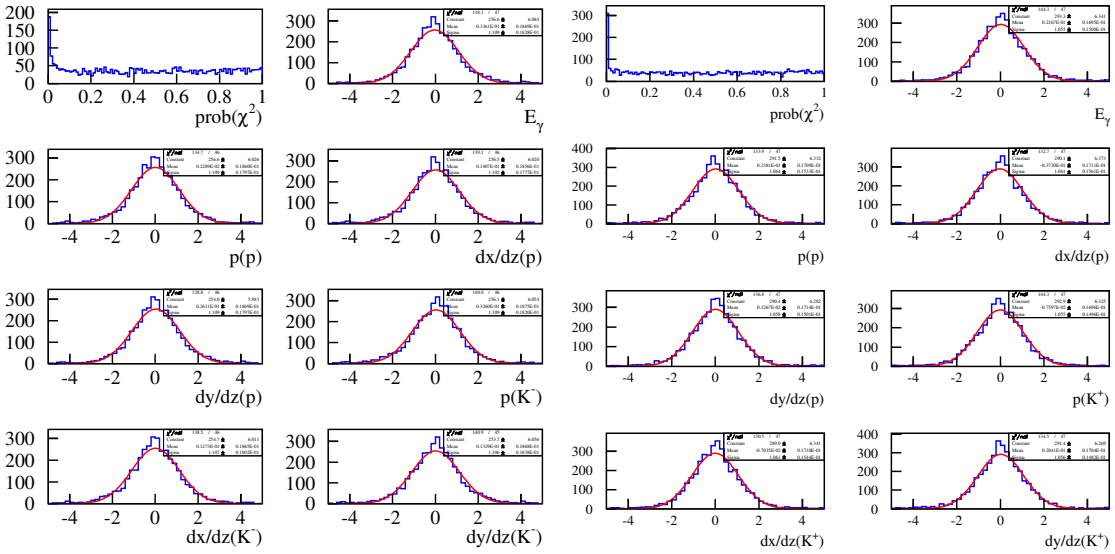

Figure 3.12: χ^2 probability and pull distributions for E_γ, and p, dx/dz, dy/dz for p and K^+. Left 6 plots are the kinematic fit results for the K^-p events from the 2002/2003 data set and the right ones for the 2006/2007 data set.

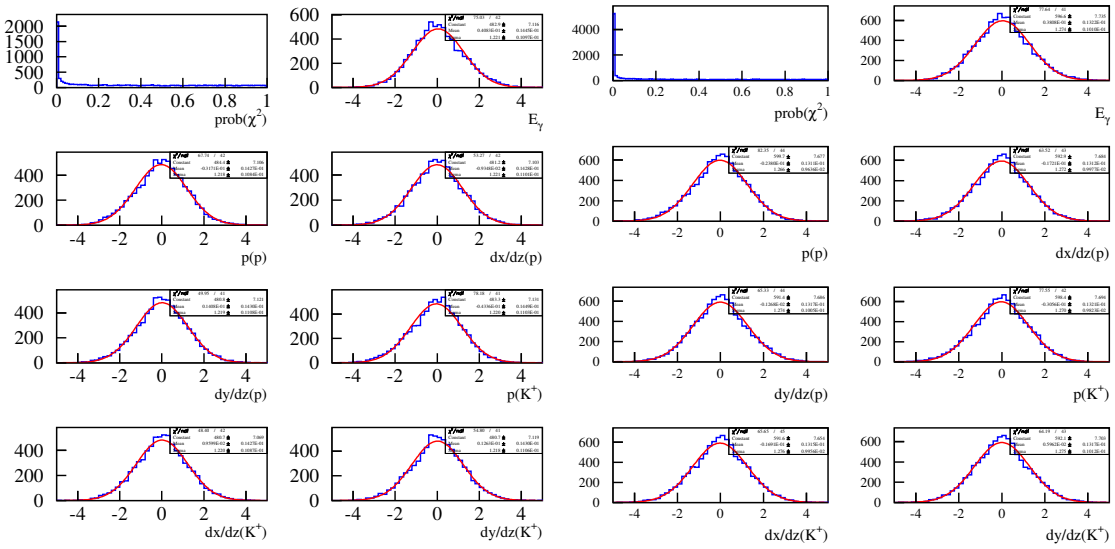

Figure 3.13: χ^2 probability and pull distributions for E_γ, and p, dx/dz, dy/dz for p and K^+. Left 6 plots are the kinematic fit results for the K^+p events from the 2002/2003 data set and the right ones for the 2006/2007 data set.

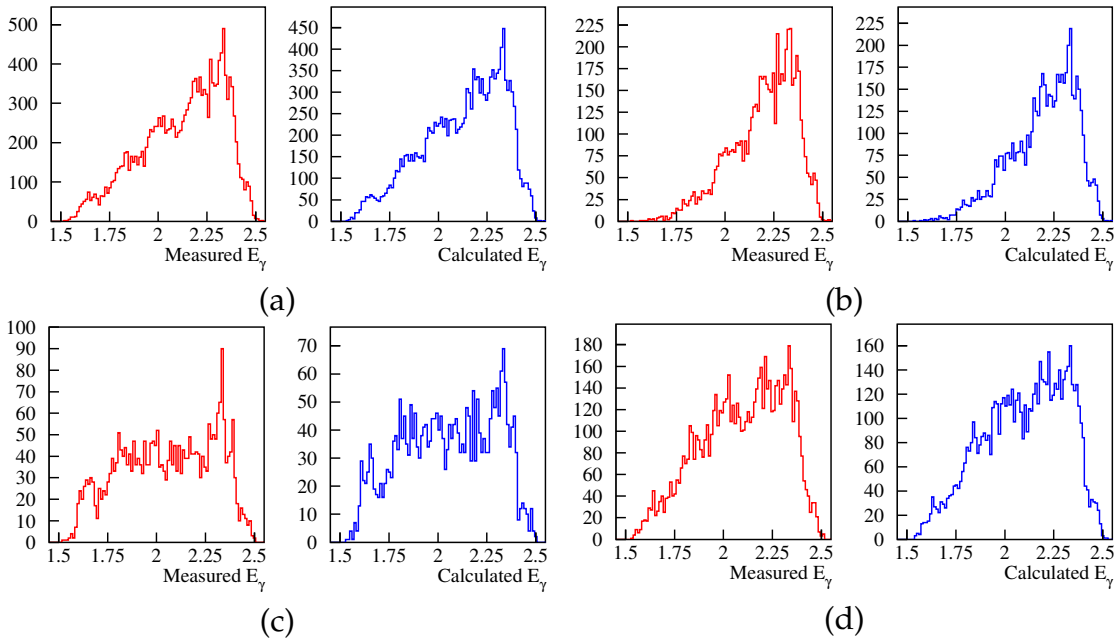

Figure 3.14: Photon beam energy distributions for the 2002/2003 data set (red) before and (blue) after the kinematic fit ; (a) the total events, (b) the events with K^-K^+ detected, (c) with K^-p detected, and (d) with K^+p detected.

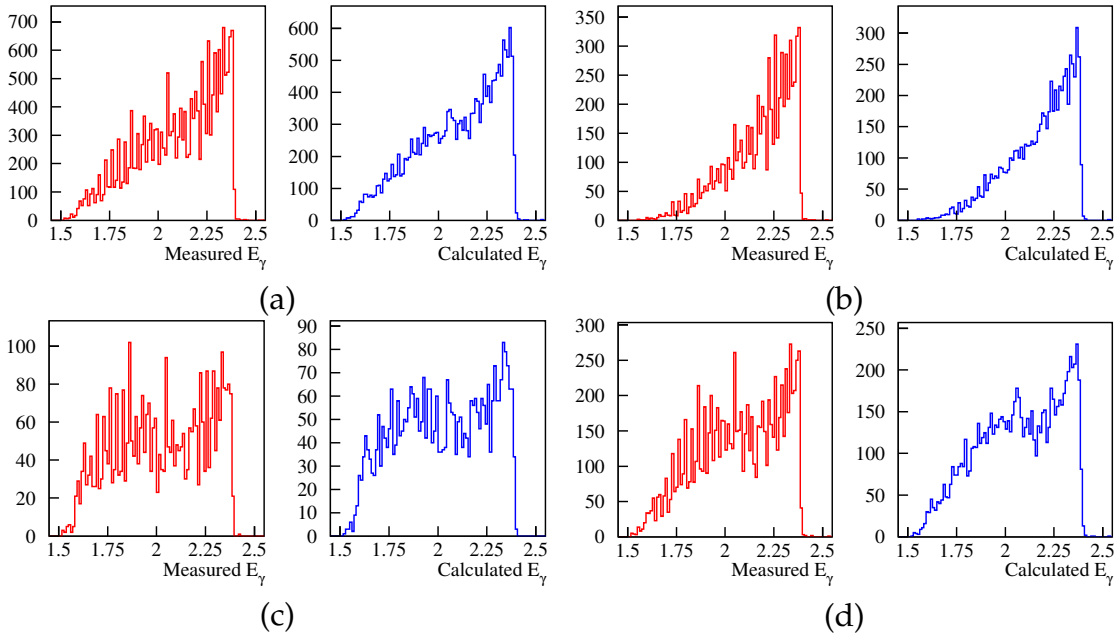

Figure 3.15: Photon beam energy distributions for the 2006/2007 data set (red) before and (blue) after the kinematic fit ; (a) the total events, (b) the events with K^-K^+ detected, (c) with K^-p detected, and (d) with K^+p detected.

3.4 Event Selection for $\gamma p \to K^- K^+ p$ Reactions

Using kinematic fit results, we selected the events for $\gamma p \to K^+ K^- p$ reaction by requiring that the confidence level of the kinematic fit is larger than 0.02. Figure 3.16 shows a scatter plot of the reconstructed masses for $K^- K^+$ and $K^- p$ systems for all energy ranges and all combinations of the two measured particles. A strong vertical band indicates the ϕ meson production, while a horizontal band corresponds to the $\Lambda(1520)$ photoproduction. The ϕ band is defined as the $K^+ K^-$ mass region satisfied with $|m_{K^+K^-} - m_\phi| \leq 4\Gamma_\phi$, where $m_\phi = 1019.455$ MeV and $\Gamma_\phi = 4.26$ MeV. On the other hand, the $\Lambda(1520)$ band is required to satisfy that $|m_{K^-p} - m_{\Lambda(1520)}| \leq 2\Gamma_{\Lambda(1520)}$, where $m_{\Lambda(1520} = 1519.5$ MeV and $\Gamma_{\Lambda(1520)} = 15.6$ MeV.

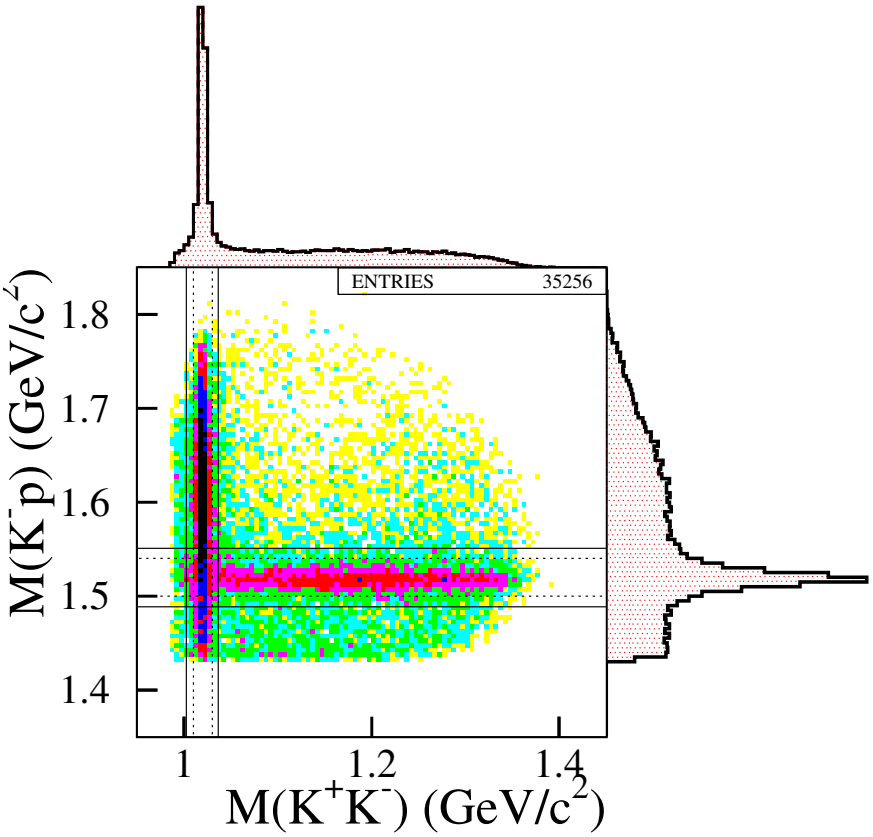

Figure 3.16: A scatter plot of the reconstructed masses for $K^- K^+$ and $K^- p$ systems. Overlaid histograms are the projected $K^+ K^+$ mass (top) and the $K^- p$ mass (right) distributions, respectively.

The overlaid dashed lines indicate the second selection region with narrow mass bands. The mass widths span from 1.01 to 1.03 GeV for the ϕ, while from

1.50 to 1.54 GeV for the $\Lambda(1520)$. We study the ϕ-$\Lambda(1520)$ interference in the two regions to confirm a consistency between results with the two different regions. For each energy bin, the same scatter plots of the K^+K^- mass versus the K^-p mass are displayed in Fig. 3.17, 3.18, 3.19, 3.20, 3.21, and 3.22. Top plots of the Figures 3.18, 3.19, 3.20, 3.21, and 3.22 are the distributions for K^+K^- events, the middle ones for K^-p events, and the bottom ones for K^+p events. The boundaries of the two-dimensional mass distributions (seen as the contours) correspond to the phase space available for $\gamma p \to K^+K^-p$ reaction at a given energy. In each mass spectrum, the events beneath the peak are due to the kinematic reflection of the other resonance and non-resonant processes which share the phase space for the K^+K^-p production.

We first selected the events within the two bands and excluded the events in the box region crossed by two bands for ϕ and $\Lambda(1520)$ resonances, respectively, where a possible interference between the ϕ and $\Lambda(1520)$ production amplitudes appears. We then applied the same requirement to the simulated data on ϕ, $\Lambda(1520)$ and other background processes. Figure 3.32 shows the invariant mass distributions in the selected region from the real data and the simulated spectra for S-wave K^+K^- production, ϕ and $\Lambda(1520)$ production processes.

In the total c.m. system for $\gamma p \to K^+K^-p$ reaction the angular distributions for p and K^+ particles are shown in Figs. 3.23, 3.24, and 3.25. The $\cos\theta^*_p$ distributions in the ϕ mass region defined as $|m_{K^+K^-} - m_\phi| \leq 4\Gamma_\phi$ are displayed in left columns, and the $\cos\theta^*_{K^+}$ distributions in the $\Lambda(1520)$ mass region with $|m_{K^-p} - m_\Lambda| \leq 2\Gamma_\Lambda$ in the middle column. The third column represents the $\cos\theta^*_p$ distributions for the interference box region crossed by the two mass bands. The angular distributions are displayed according to the three different data sets with K^+K^-, K^-p, and K^+p events in the energy regions in which the ϕ and $\Lambda(1520)$ can interfere. Protons emit in opposite directions to the ϕ mesons, and K^+ particles do against the $\Lambda(1520)$ resonances. From the angular distributions we can learn that the ϕ production angles move from the backward to the forward directions in the interference energy intervals. Backward $\Lambda(1520)$ production is dominant in the K^+K^- and K^+p data sets, while the forward $\Lambda(1520)$ production is selected by tagging K^-p in the forward LEPS spectrometer. It should be noted that the LEPS covers the whole angular range of the ϕ-$\Lambda(1520)$ interference.

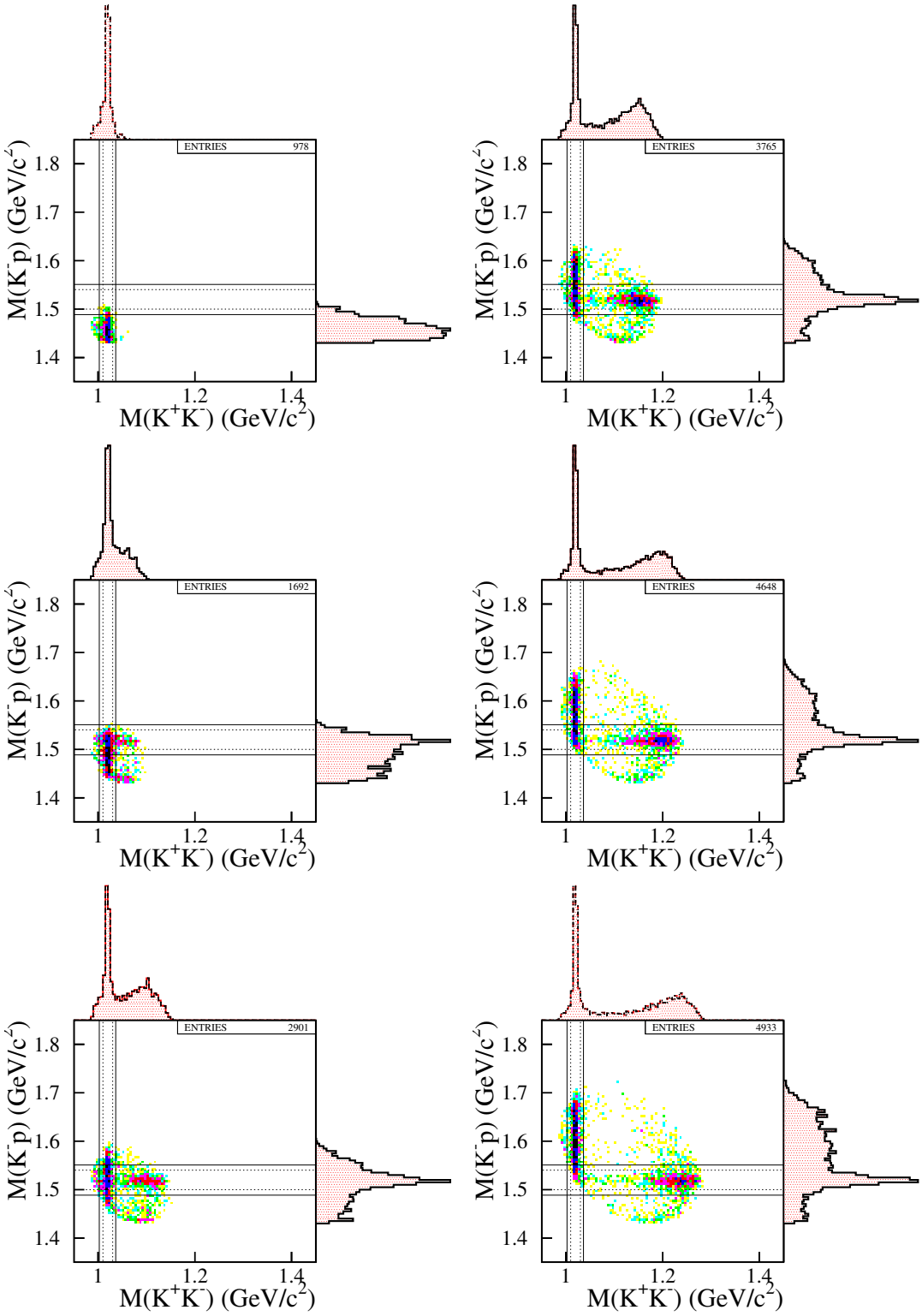

Figure 3.17: Scatter plots for the $K^- K^+$ mass versus the $K^- p$ mass for $K^+ K^- p$ data sets (two of the three detected) in the energy range from threshold to 1.873 GeV (in the left column), and from 1.873 to 2.173 GeV (right).

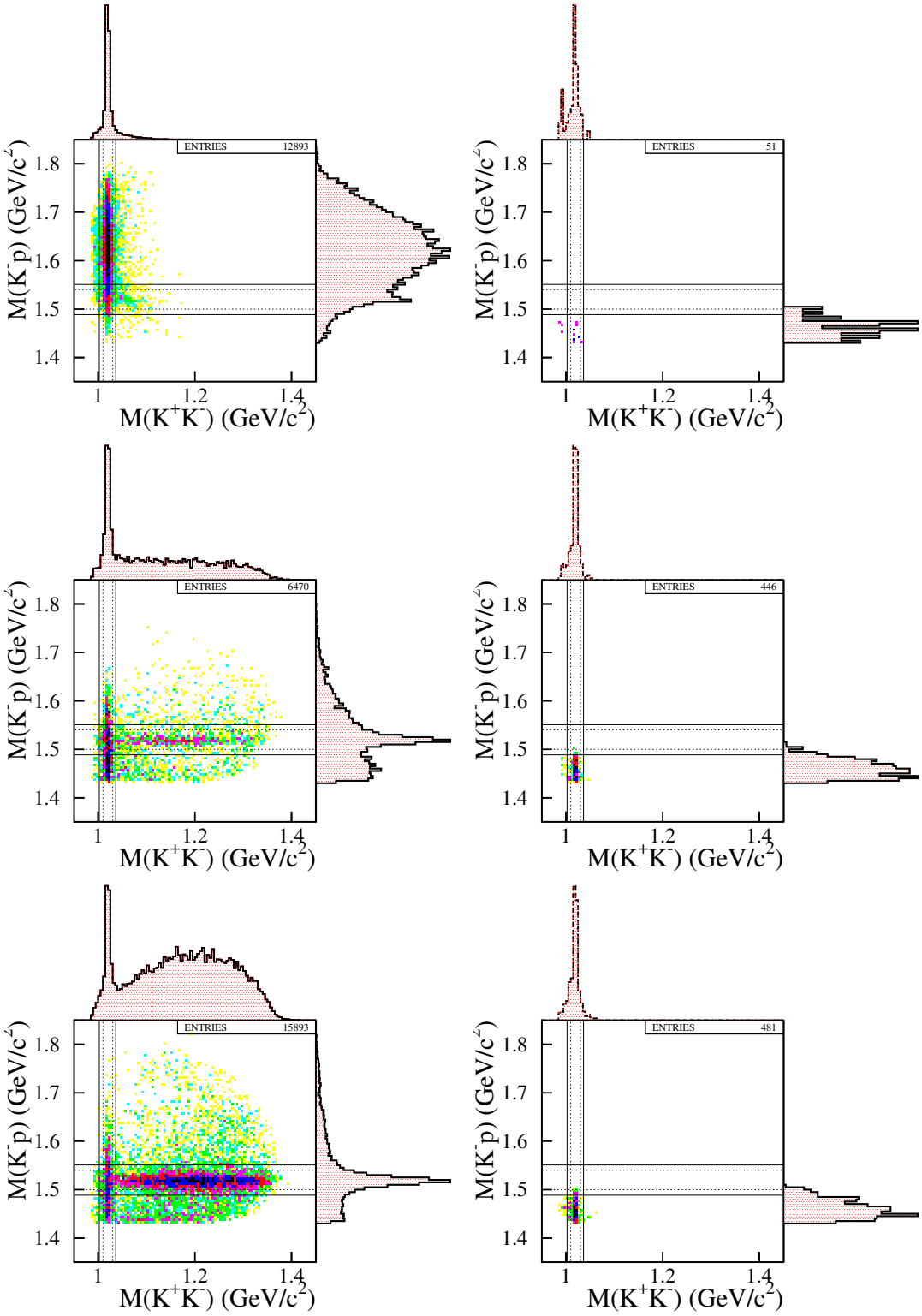

Figure 3.18: Scatter plots for the K^-K^+ mass versus the K^-p mass spectra in the whole energy region (left column) and in the range of 1.573-1.673 GeV (right). The K^+K^- (top), K^-p (middle), and K^+p (bottom) data sets are displayed.

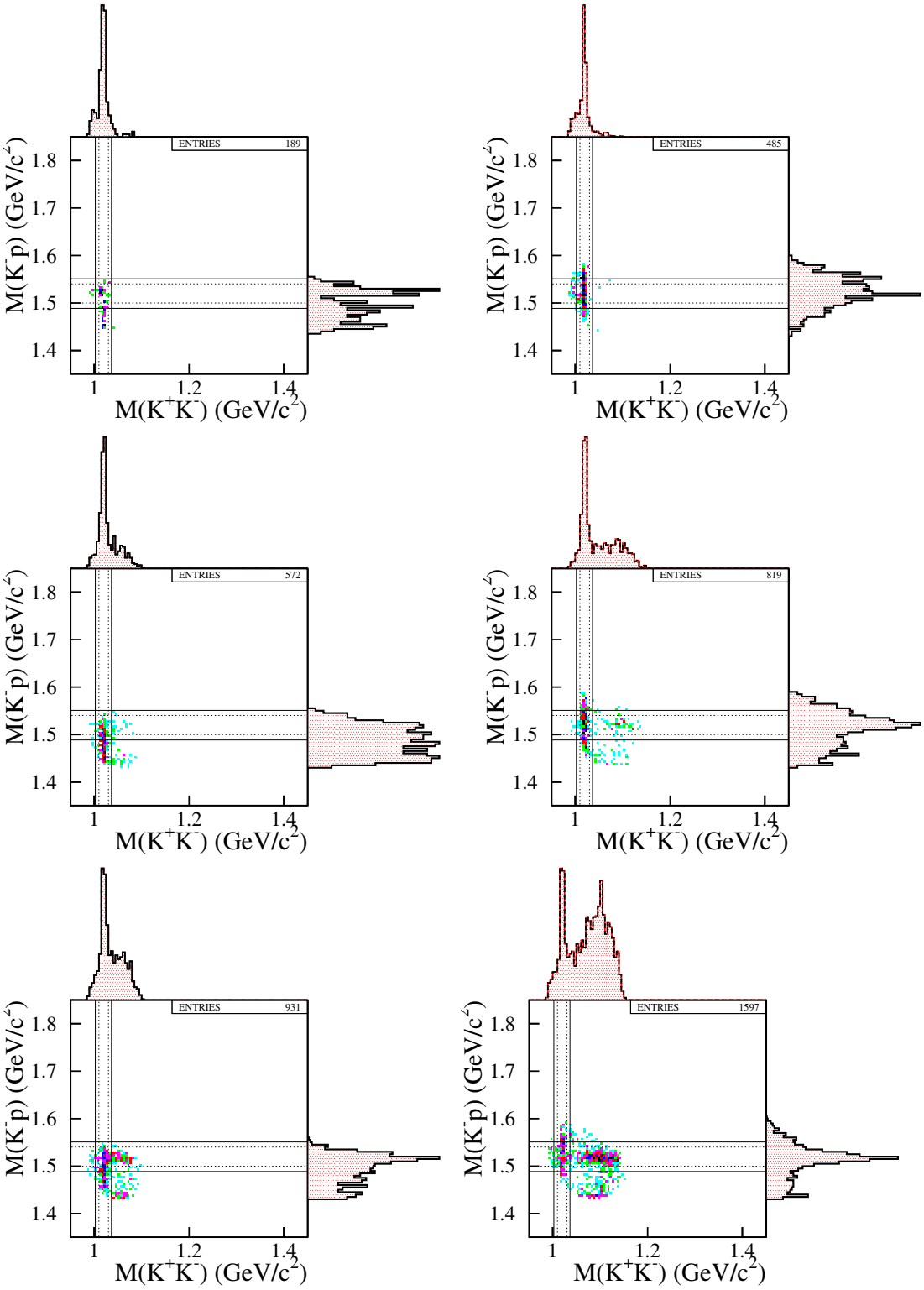

Figure 3.19: Scatter plots for the $K^- K^+$ mass versus the $K^- p$ mass in the energy region of 1.673-1.773 GeV (left column) and in the range of 1.773-1.873 GeV (right). The $K^+ K^-$ (top), $K^- p$ (middle), and $K^+ p$ (bottom) data sets are displayed.

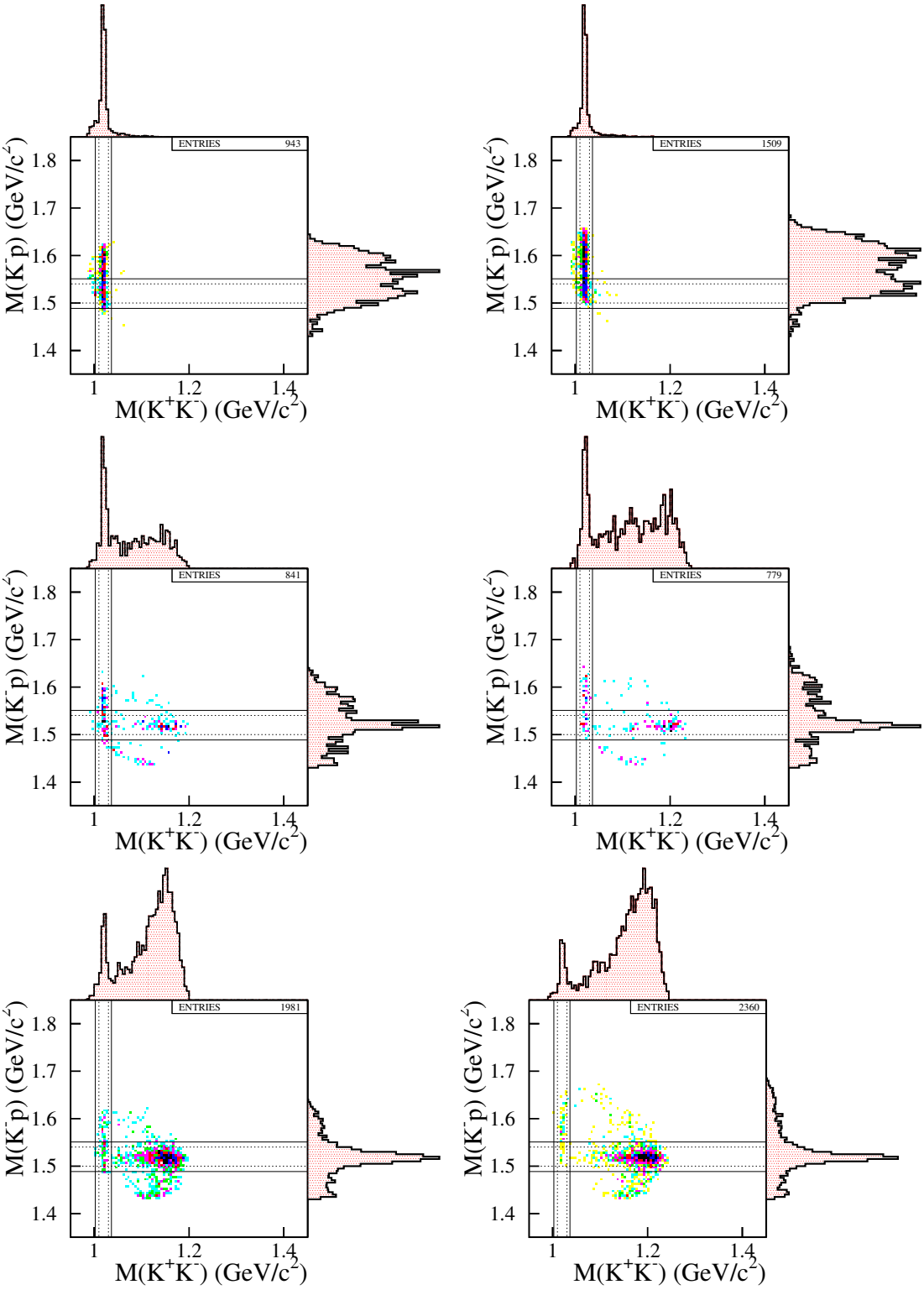

Figure 3.20: Scatter plots for the K^-K^+ mass versus the K^-p mass in the energy region of 1.873-1.973 GeV (left column) and in the range of 1.973-2.073 GeV (right). The K^+K^- (top), K^-p (middle), and K^+p (bottom) data sets are displayed.

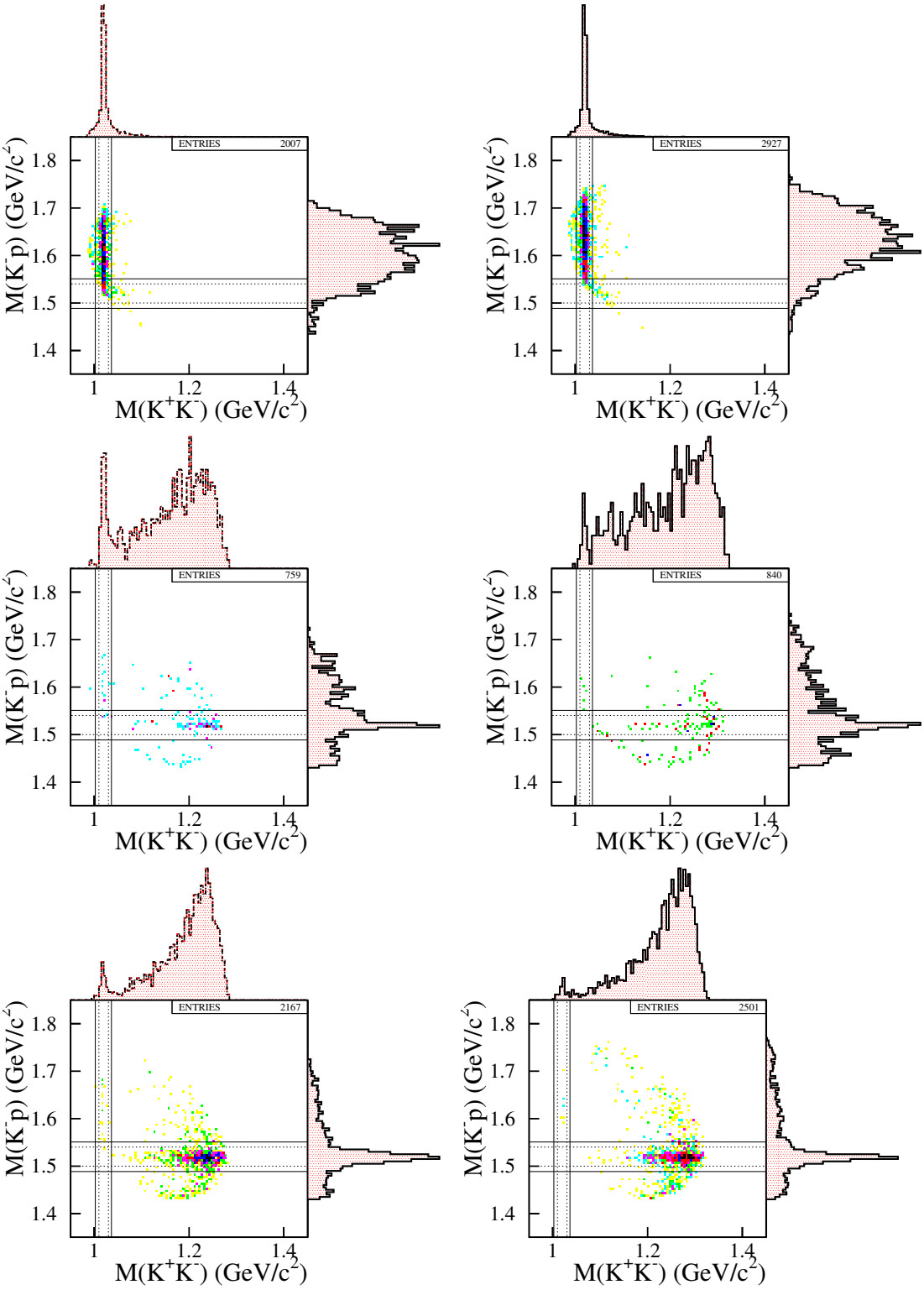

Figure 3.21: Scatter plots for the $K^- K^+$ mass versus the $K^- p$ mass in the energy region of 2.073-2.173 GeV (left column) and in the range of 2.173-2.273 GeV (right). The $K^+ K^-$ (top), $K^- p$ (middle), and $K^+ p$ (bottom) data sets are displayed.

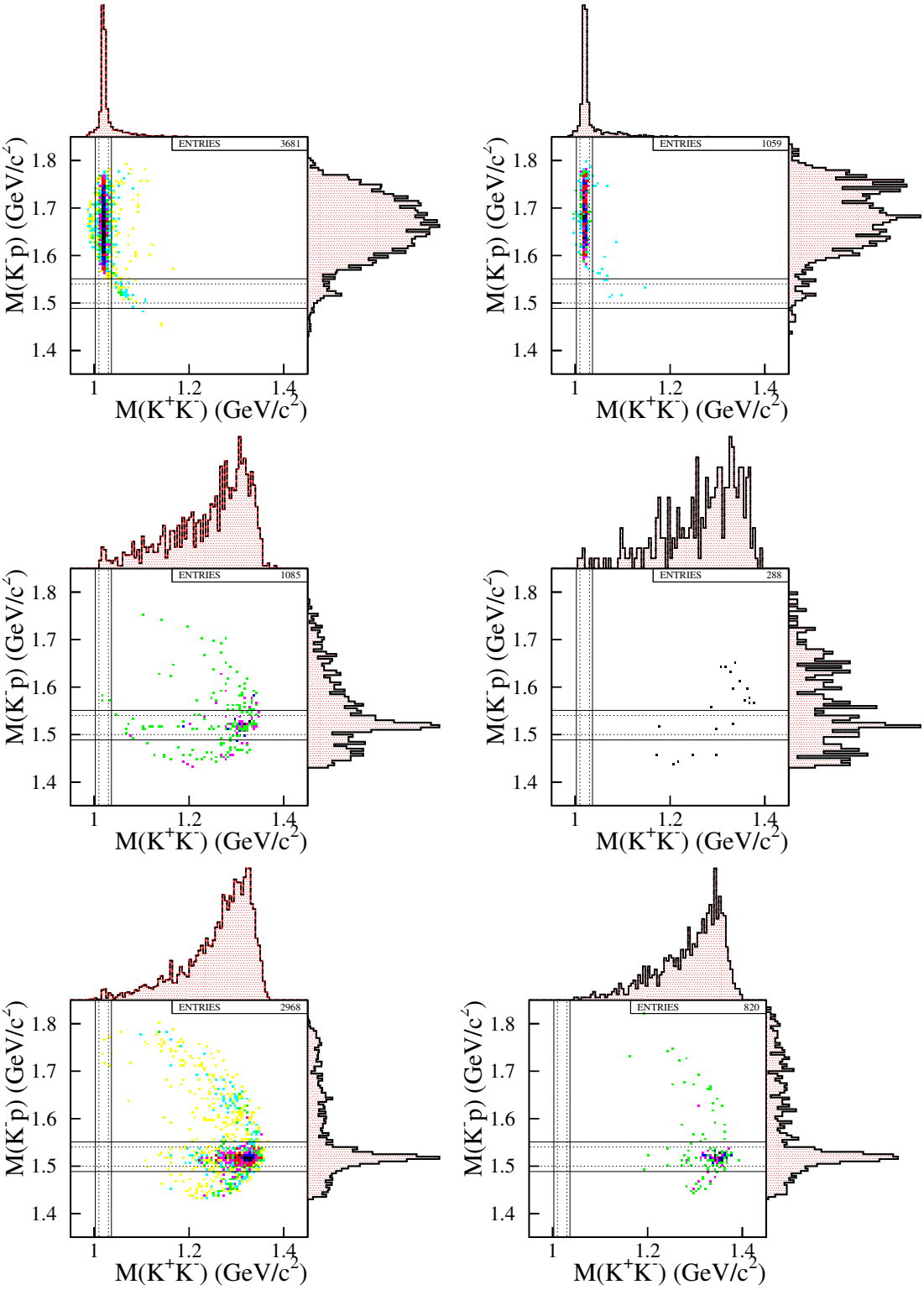

Figure 3.22: Scatter plots for the K^-K^+ mass versus the K^-p mass in the energy region of 2.273-2.373 GeV (left column) and in the range of 2.373-2.473 GeV (right). The K^+K^- (top), K^-p (middle), and K^+p (bottom) data sets are displayed.

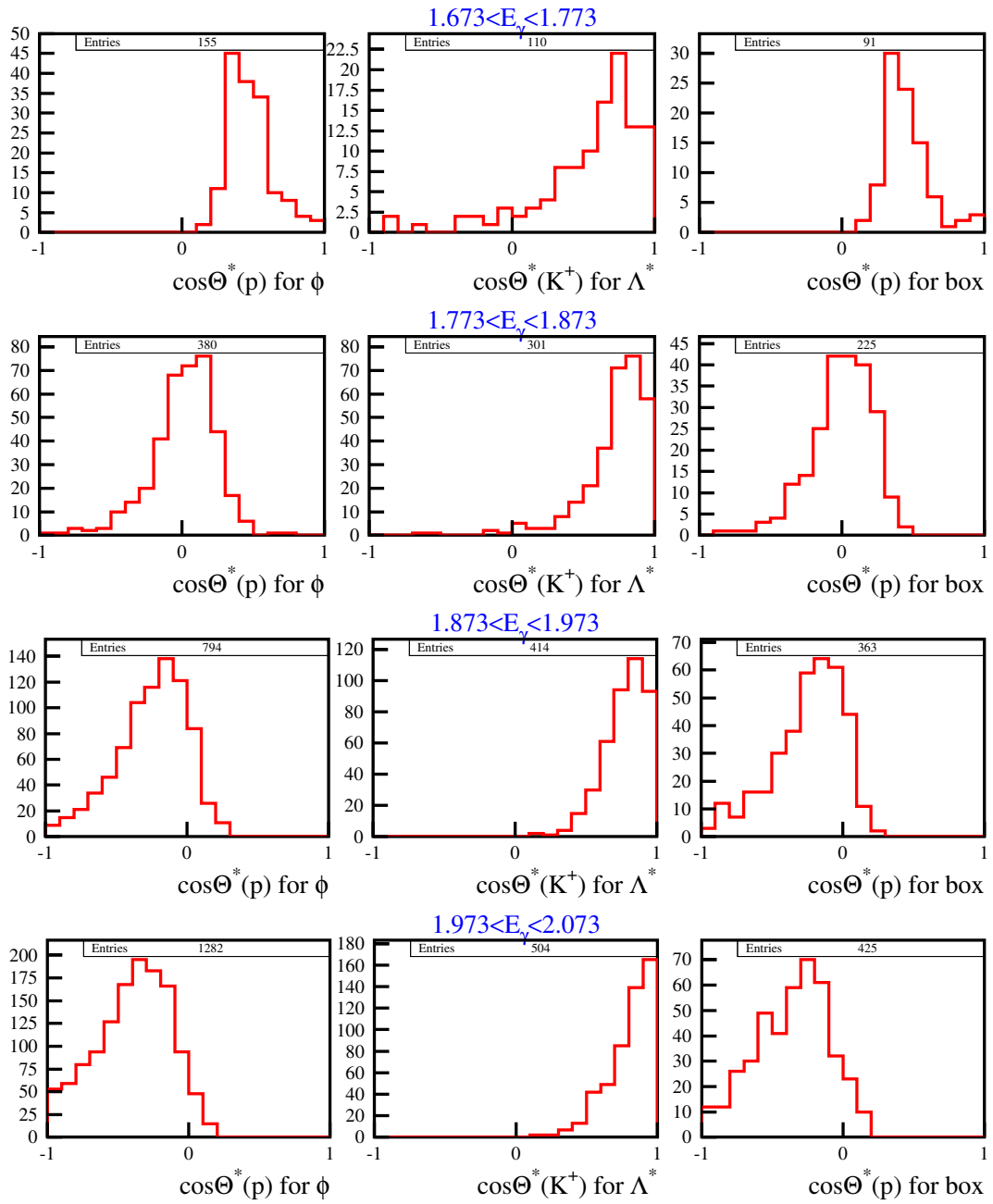

Figure 3.23: The $\cos\theta^*_p$ distributions at the total c.m. system for $\gamma p \to K^+ K^- p$ reaction are shown in the ϕ mass region defined as $|m_{K^+K^-} - m_\phi| \leq 4\Gamma_\phi$ (left column), the $\cos\theta^*_{K^+}$ distributions in the $\Lambda(1520)$ mass region with $|m_{K^-p} - m_\Lambda| \leq 2\Gamma_\Lambda$ (middle column), and the $\cos\theta^*_p$ distributions (right column) in the interference box region crossed by the two mass bands for K^+K^- detection mode.

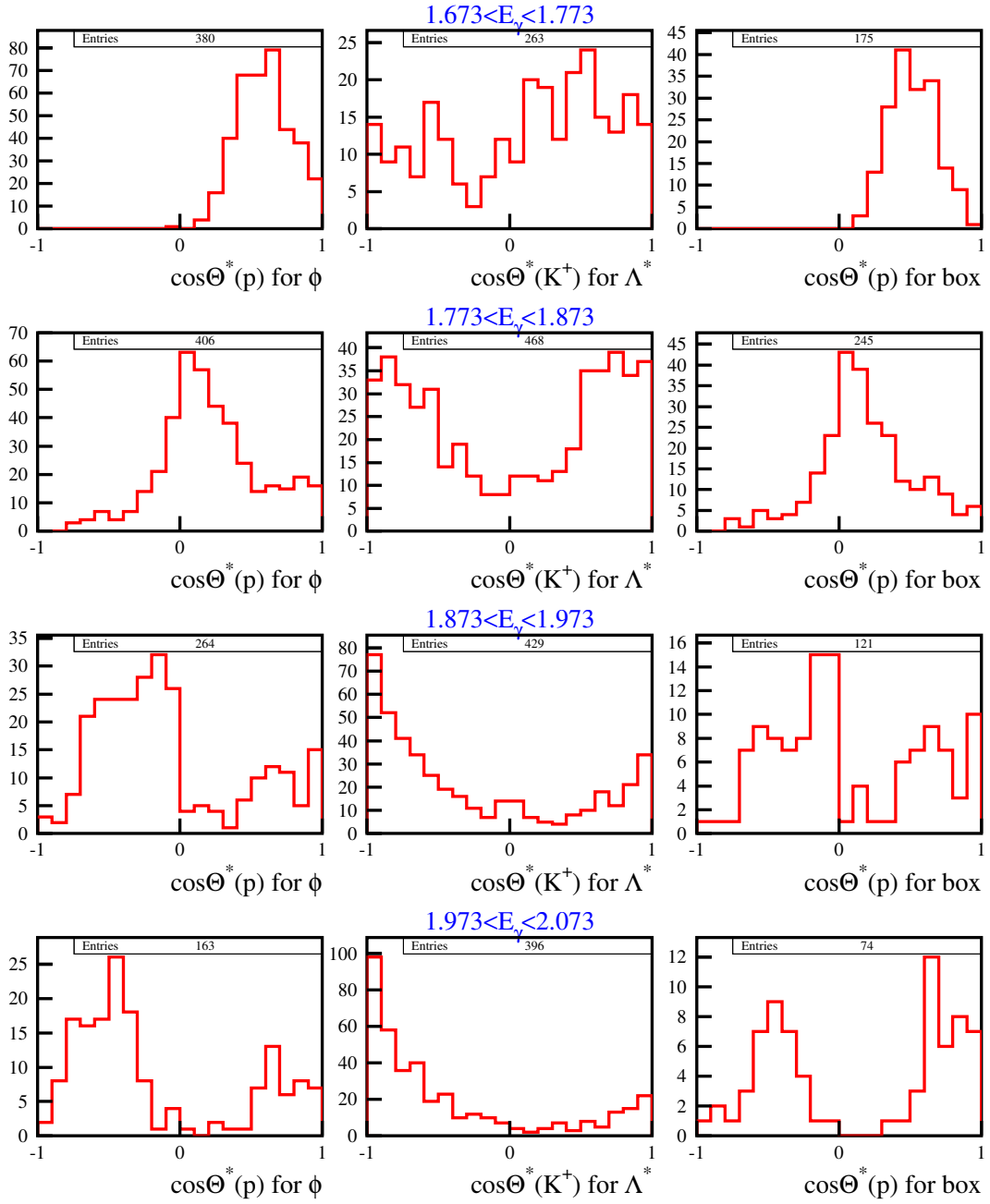

Figure 3.24: The $\cos\theta^*_p$ distributions at the total c.m. system for $\gamma p \to K^+K^-p$ reaction are shown in the ϕ mass region defined as $|m_{K^+K^-} - m_\phi| \leq 4\Gamma_\phi$ (left column), the $\cos\theta^*_{K^+}$ distributions in the $\Lambda(1520)$ mass region with $|m_{K^-p} - m_\Lambda| \leq 2\Gamma_\Lambda$ (middle column), and the $\cos\theta^*_p$ distributions (right column) in the interference box region crossed by the two mass bands for K^-p detection mode.

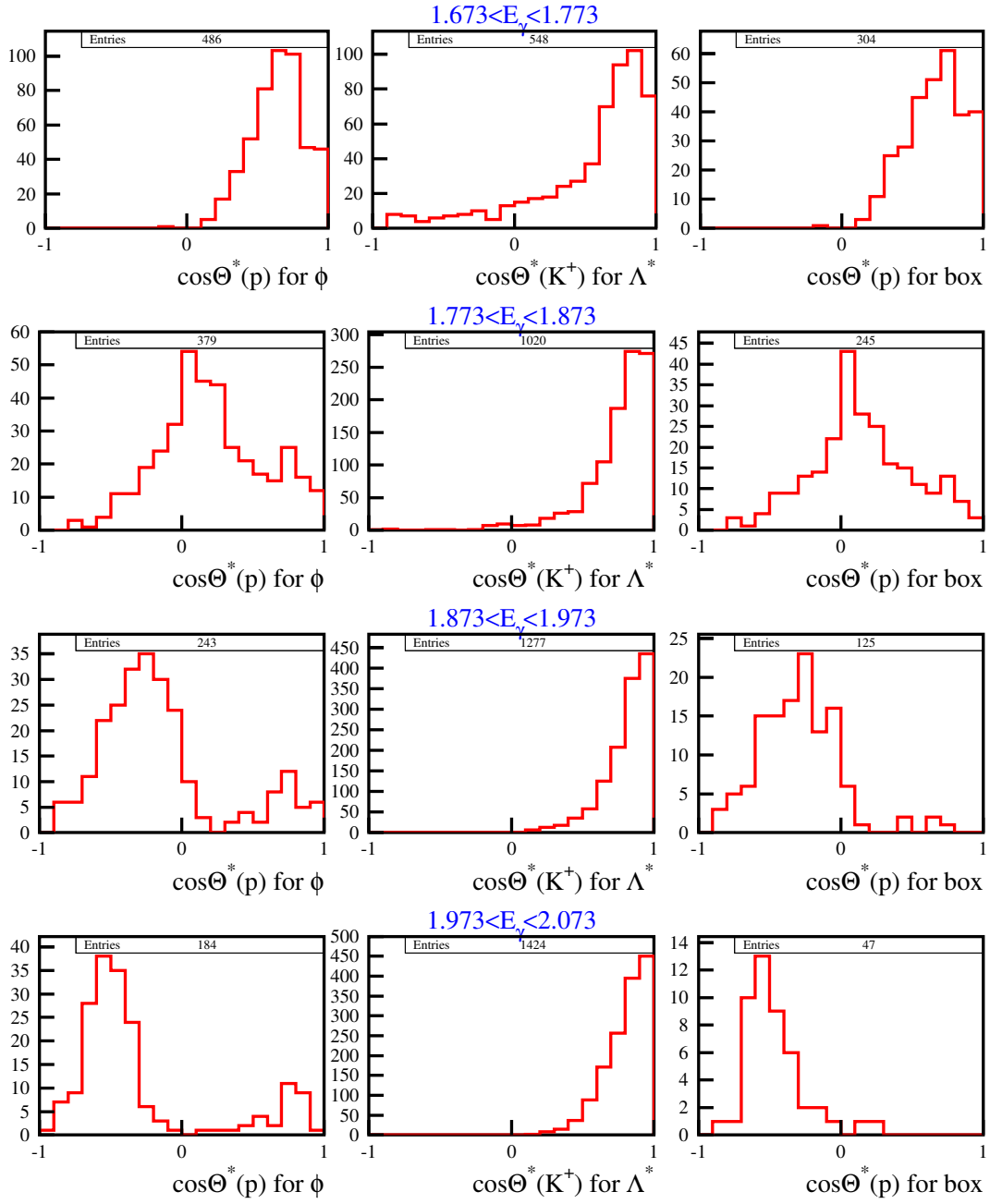

Figure 3.25: The $\cos\theta^*_p$ distributions at the total c.m. system for $\gamma p \to K^+ K^- p$ reaction are shown in the ϕ mass region defined as $|m_{K^+K^-} - m_\phi| \leq 4\Gamma_\phi$ (left column), the $\cos\theta^*_{K^+}$ distributions in the $\Lambda(1520)$ mass region with $|m_{K^- p} - m_\Lambda| \leq 2\Gamma_\Lambda$ (middle column), and the $\cos\theta^*_p$ distributions (right column) in the interference box region crossed by the two mass bands for $K^+ p$ detection mode.

3.5 Monte-Carlo Simulation on $\gamma p \to K^+K^-p$ Reactions

We generated simulation data sets of $\gamma p \to K^+K^-p$ reaction events in terms of the beam polarization, the 2002/2003 and 2006/2007 runs, and the helicity and Gottfreid-Jackson frames for ϕ and $\Lambda(1520)$ production. Compton-backscattered photon energy spectra were generated according to the measured results. Figure 3.1 shows the simulated multi-line photon spectrum with best-fit parameters. Photon energy resolutions are 13 MeV and 11 MeV for the 2002/2003 and the 2006/2007 runs, respectively. For a detector response, the same set of calibration parameters was implemented in a Monte-Carlo simulation as that for offline data analysis, which include efficiencies and resolutions of drift chambers and time-of-flight slats, as well as those for veto counters such as a silica aerogel counter and a UPveto counter. For efficient simulations, we allowed track propagation above the low-energy thresholds of 5 MeV for charged particles and 50 MeV for other particles, respectively. For hadronic interactions in detector materials, we chose GEISHA with secondary particles.

$$
\begin{aligned}
\gamma + p \quad &\to p + \phi \to K^+ + K^- + p \\
\gamma + p \quad &\to K^+ + \Lambda(1520) \to K^+ + K^- + p \\
\gamma + p \quad &\to K^+ + \Lambda(1520) \to K^+ + \Sigma^+ + \pi^- \to K^+ + p + \pi^0 + \pi^- \\
\gamma + p \quad &\to K(896)^0 + \Sigma^+ \to K^+ + \pi^- + p + \pi^0 \\
\gamma + p \quad &\to K^+ + K^- + p
\end{aligned}
$$

For ϕ photoproduction, we generated Monte-Carlo simulation events for $\gamma p \to \phi p$ reaction based on E_γ-dependent spin-density matrix elements from the previous LEPS results [33]:

$$W(\cos\theta, \phi, \Phi) = W^0(\cos\theta, \phi) - P_\gamma \cos 2\Phi W^1(\cos\theta, \phi) - P_\gamma \sin 2\Phi W^2(\cos\theta, \phi).$$

The decay angular distributions W^0, W^1, and W^2 are defined as

$$
\begin{aligned}
W^0(\cos\theta, \phi) &= \frac{3}{4\pi}\Big[\frac{1}{2}(1-\rho^0_{00}) + \frac{1}{2}(3\rho^0_{00}-1)\cos^2\theta \\
&- \sqrt{2}\mathrm{Re}\rho^0_{10}\sin 2\theta\cos\phi - \rho^0_{1-1}\sin^2\theta\cos 2\phi\Big] \\
W^1(\cos\theta, \phi) &= \frac{3}{4\pi}\Big[\rho^1_{11}\sin^2\phi + \rho^1_{00}\cos^2\theta \\
&- \sqrt{2}\rho^1_{10}\sin 2\theta\cos\phi - \rho^1_{1-1}\sin^2\theta\cos 2\phi\Big] \\
W^2(\cos\theta, \phi) &= \frac{3}{4\pi}\Big[\sqrt{2}\mathrm{Im}\rho^2_{10}\sin 2\theta\cos\phi + \mathrm{Im}\rho^2_{1-1}\sin^2\theta\cos 2\phi\Big],
\end{aligned}
$$

where θ and ϕ are the polar and azimuthal angles of the normal to decay plane of the vector meson with respect to the quantization axis, and P_γ is the degree of linear polarization. We first generated the ϕ events in both the helicity and Gottfried-Jackson frames and used the combined simulation data sets with equal footing. Moreover, we generated both the vertical and horizontal polarization photon cases. As a result, the acceptance is not changed even with the E_γ-dependent spin-density matrix elements.

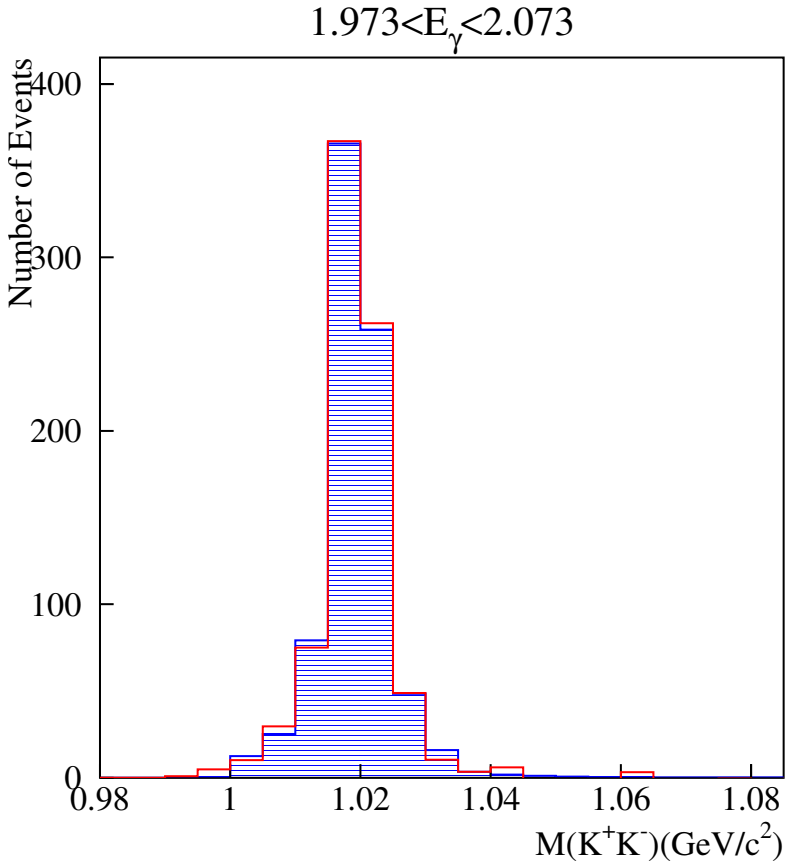

Figure 3.26: Simulated ϕ lineshape is compared with the measured ϕ spectrum. The data was taken from the events such that K^+K^- are detected at forward angles (MODE=1) in the energy region of our interest in the interference, 1.973-2.073 GeV.

The K^+K^- mass distribution for the ϕ meson was generated using a relativistic Breit-Wigner form with nominal values for the mass ($m_0 = 1.019413$ GeV) and decay width ($\Gamma_0 = 4.43$ MeV) quoted in Particle Data Book [6]. The K^+K^- mass spans from the mass threshold to the maximum limit allowed by

the K^+K^-p 3-body phase space for a given E_γ. Figure 3.26 shows the simulated ϕ lineshape compared with the measured ϕ spectrum. The data was taken from the events such that K^+K^- are detected at forward angles (MODE=1) in the energy region of our interest in the interference, 1.973-2.073 GeV. The known background lineshapes were subtracted. It turns out that the simulated lineshape reproduces the measured ϕ mass distribution very well, which provides a firm basis for the further interference study.

E_γ(GeV)	$E_\gamma < 1.93$	$1.93 \leq E_\gamma < 2.13$	$E_\gamma \geq 2.13$
ρ^0_{00}	0.09	0.09	0.04
Re ρ^0_{10}	0.07	0.08	0.07
ρ^0_{1-1}	0.02	0.00	0.05
ρ^1_{11}	0.03	-0.01	1.00
ρ^1_{00}	0.00	-0.03	-0.01
ρ^1_{10}	-0.01	-0.05	0.04
ρ^1_{1-1}	0.15	0.11	0.21
Im ρ^2_{10}	0.02	0.01	0.04
Im ρ^2_{1-1}	-0.19	-0.08	-0.16

Table 3.2: Energy-dependent spin-density matrix elements implemented in the Monte Carlo simulation.

For $\gamma p \rightarrow \Lambda(1520)K^+ \rightarrow K^-pK^+$ reaction the production threshold energy is 1.6906 GeV with the nominal value of the $\Lambda(1520)$ mass, 1.5195 GeV. A Monte Carlo simulation was based on the LEPS results on the $\Lambda(1520)$ [41]. The $J^p = 3/2^-$ $\Lambda(1520)$ photoproduction proceeds via K^- or K^{*-} exchange. The decay angular distribution was measured in the t-channel helicity frame, which is defined by taking a quantization axis for the opposite direction of the target proton. The decay angular distribution of K^- at the rest frame of the $\Lambda(1520)$ can be represented as

$$\begin{aligned} I(\cos\theta_{K^-}) &= \frac{3}{4\pi}\Big[\rho_{33}\sin^2\theta_{K^-} + \rho_{11}\Big(\frac{1}{3} + \cos^2\theta_{K^-}\Big)\Big] \\ &\propto (1-\alpha)\Big(\frac{1}{3} + \cos^2\theta_{K^-}\Big) + \alpha\sin^2\theta_{K^-}, \end{aligned}$$

where $\rho_{2M2M'}$ represents the spin density matrix elements with spin projection quantum numbers, M and M'. We parametrized $\alpha = 0.6$ for K^+ in the backward angles (or $\Lambda(1520)$ produced in the forward c.m. angles), while $\alpha = 0.9$ for the other angles.

For the $\Lambda(1520) \rightarrow \Sigma^+\pi^-$, the subsequent decay of the $\Sigma^+ \rightarrow p\pi^+$ can contribute to the events with K^+p detected. This reaction process was im-

plemented with the constraint from the branching fractions for $\Gamma(\Lambda(1520) \to K^-p)/\Gamma(\Lambda(1520) \to \Sigma^+\pi^-)$.

Near threshold the underlying background could largely be due to S-wave non-resonant K^+K^- pair production. Its different decay angular distribution could yield a different acceptance for the K^-p detection mode. In this analysis we called the `nonreso.f` function to generate K^+K^-p final states uniformly in Lorentz-invariant phase-space. The `phsp.f` function is internally called. The generated S-wave K^+K^- mass distribution is shown in Fig. 3.29. The K^+K^- invariant-mass distribution is generated at a given photon energy. Decay angular distributions of the K^+K^- system at the K^+K^- rest frame is displayed as a function of the K^+K^- mass.

For $K(896)^0\Sigma^+$ photoproduction the decay angular distribution of the $K(896)^0$ was generated in the Monte Carlo simulation, based on the LEPS results on spin-density matrix elements [42]. The subsequent $\Sigma^+ \to p\pi^+$ decay can contribute to the event sets with K^+p particles detected. The $K^+\pi^-$ mass distribution for the $K(896)^0$ meson was generated using a non-relativistic Breit-Wigner form with nominal values for the mass ($m_0 = 0.89581$ GeV) and decay width ($\Gamma_0 = 47.4$ MeV) quoted in Particle Data Book [6]. The $K^+\pi^-$ mass spans from the mass threshold to the maximum limit allowed by the $K^+\pi^-\Sigma^+$ 3-body phase space for a given E_γ. The production cross section was parametrized as $\mathrm{d}\sigma/\mathrm{d}t \propto \exp(-4.206t)$ which taken from the LEPS measurement result [42].

SDME	Helicity	GJ
ρ^0_{00}	0.086	0.153
Re ρ^0_{10}	-0.026	0.114
ρ^0_{1-1}	0.039	0.075
ρ^1_{11}	-0.008	0.043
ρ^1_{00}	-0.042	-0.124
ρ^1_{10}	0.004	-0.097
ρ^1_{1-1}	0.355	0.291
Im ρ^2_{10}	-0.038	0.123
Im ρ^2_{1-1}	-0.395	-0.321

Table 3.3: Spin-density matrix elements for $K(896)\Sigma^+$ photoproduction implemented in the Monte Carlo simulation.

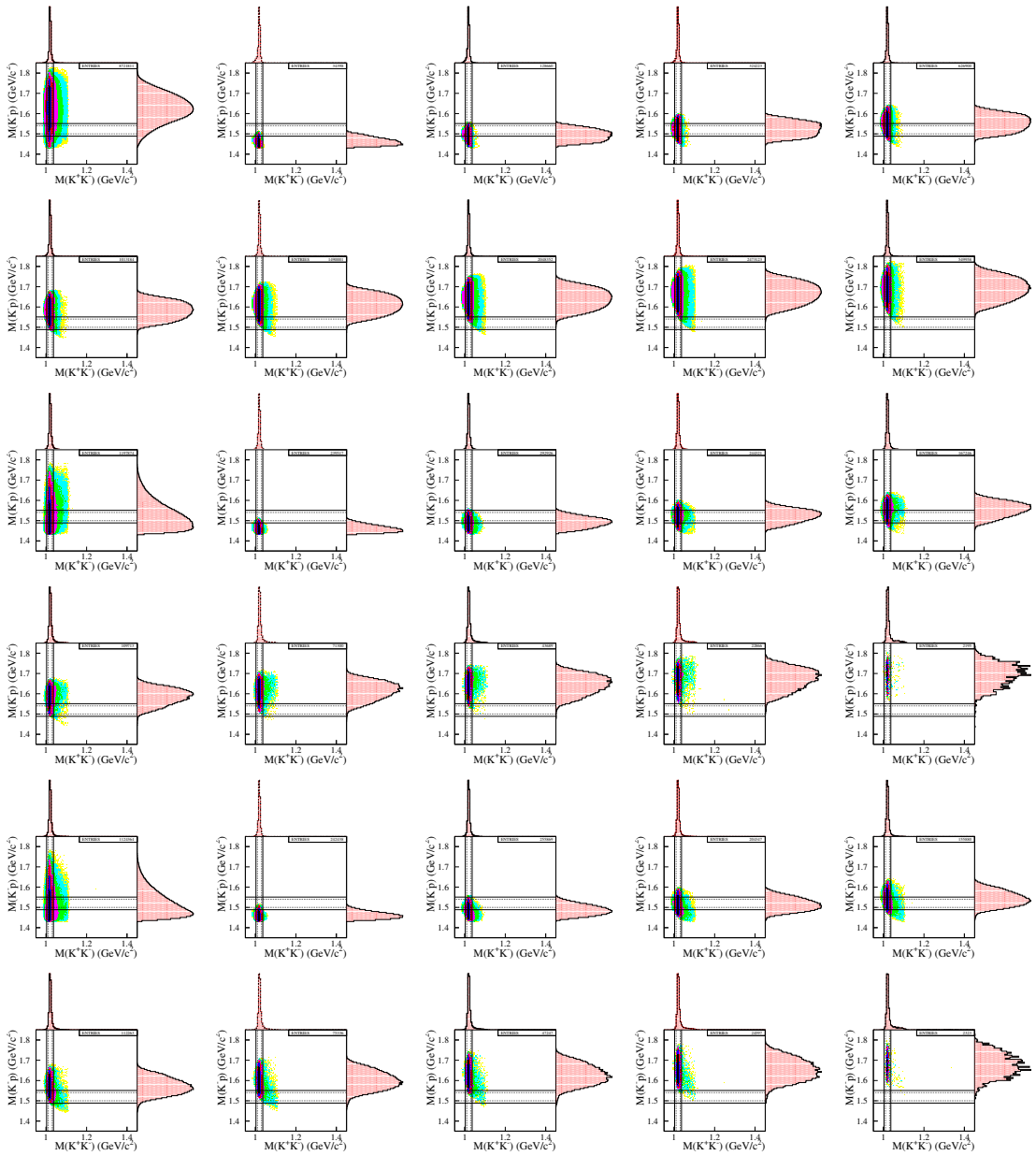

Figure 3.27: Simulated distributions for ϕ photoproduction are displayed in terms of the 0.1-GeV E_γ bin from 1.573 to 2.373 GeV. First 10 plots are the simulated events with K^-K^+ detected, the next 10 plots are the ones with K^-p detected, the last 10 plots are the ones with K^+p detected. In each set, the first plot is for a whole energy region.

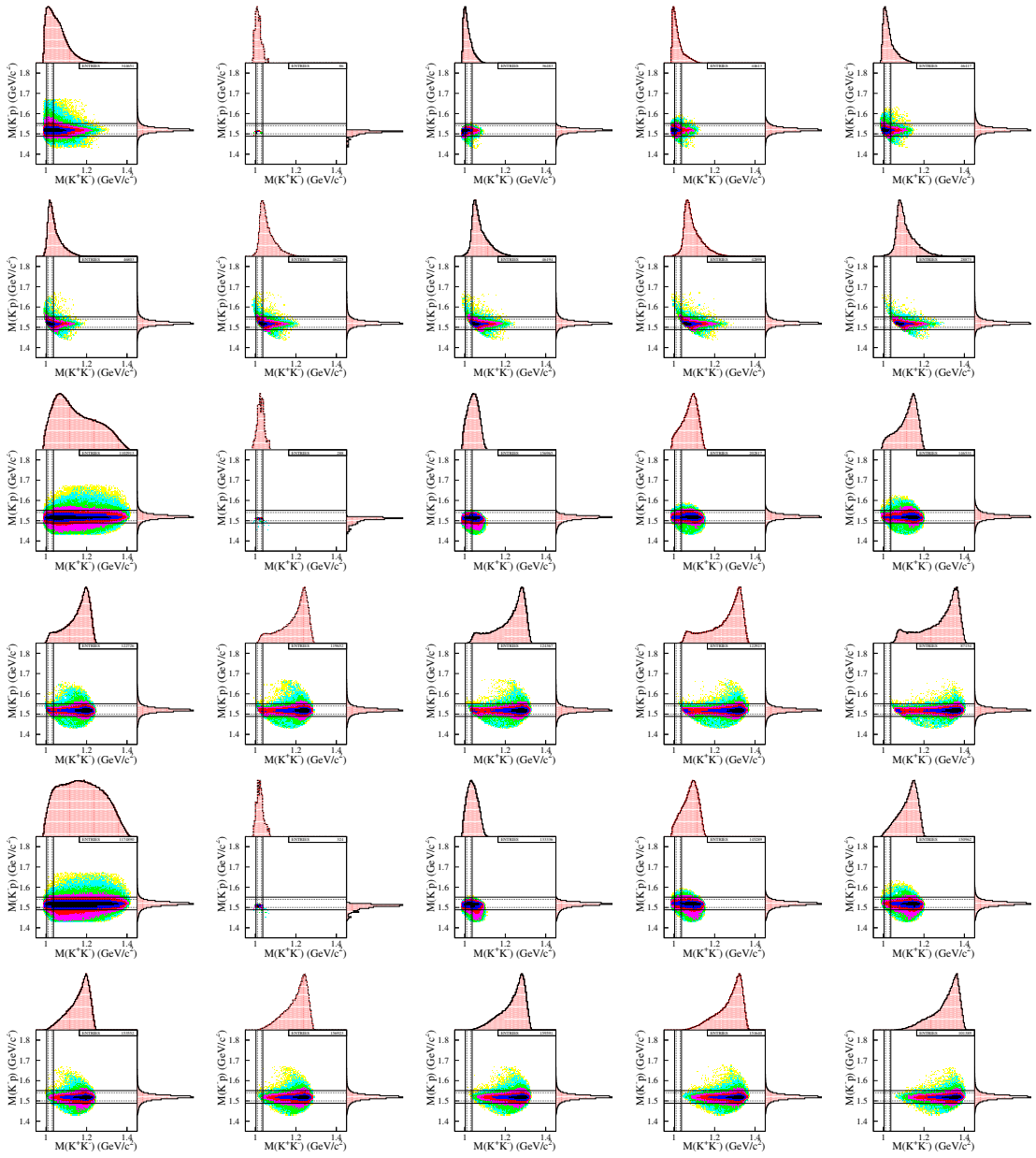

Figure 3.28: Simulated distributions for $\Lambda(1520)$ photoproduction are displayed in terms of the 0.1-GeV E_γ bin from 1.573 to 2.373 GeV. First 10 plots are the simulated events with K^-K^+ detected, the next 10 plots are the ones with K^-p detected, the last 10 plots are the ones with K^+p detected. In each set, the first plot is for a whole energy region.

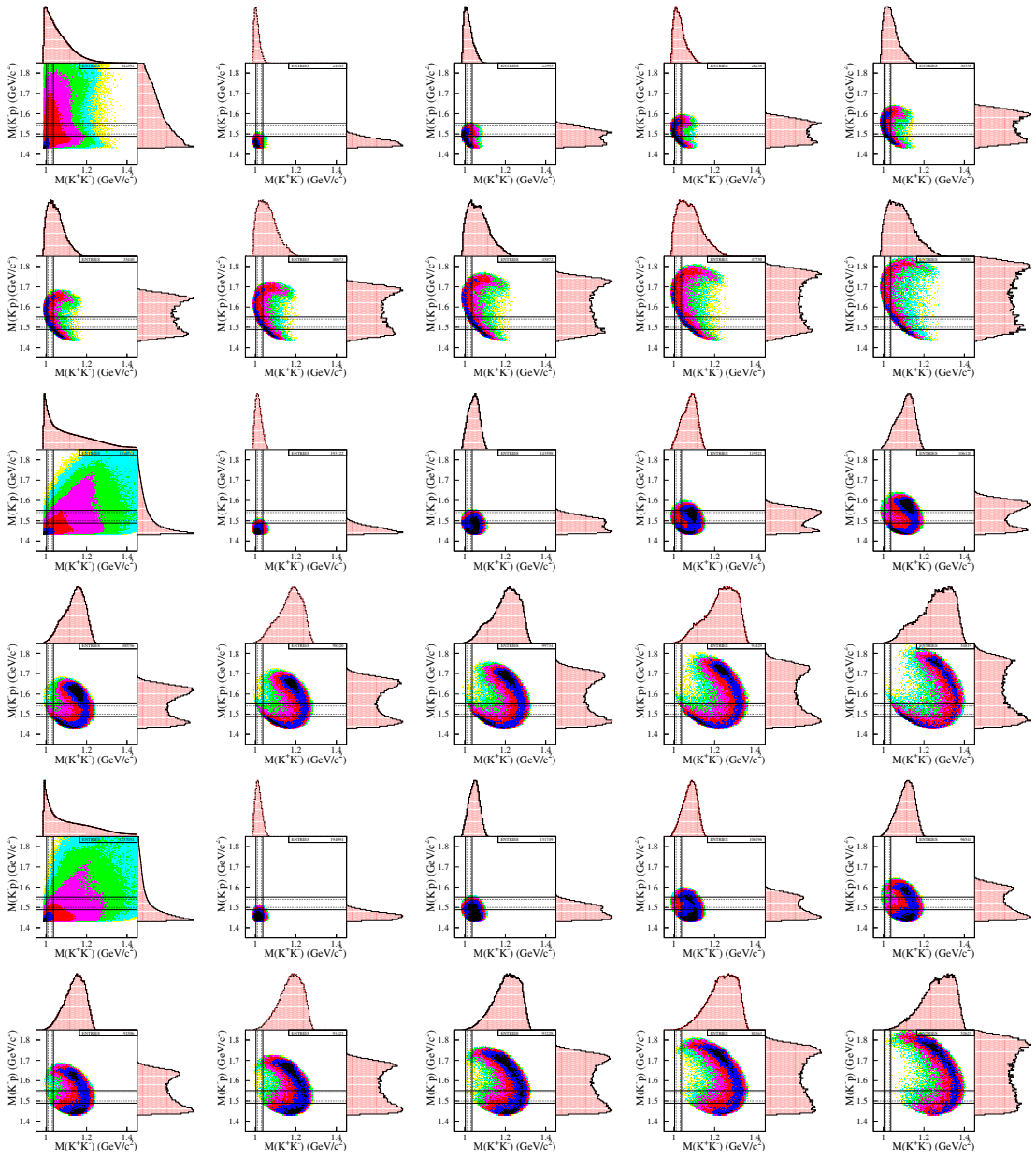

Figure 3.29: Simulated distributions for non-resonant K^-K^+ photoproduction are displayed in terms of the 0.1-GeV E_γ bin from 1.573 to 2.373 GeV. First 10 plots are the simulated events with K^-K^+ detected, the next 10 plots are the ones with K^-p detected, the last 10 plots are the ones with K^+p detected. In each set, the first plot is for a whole energy region.

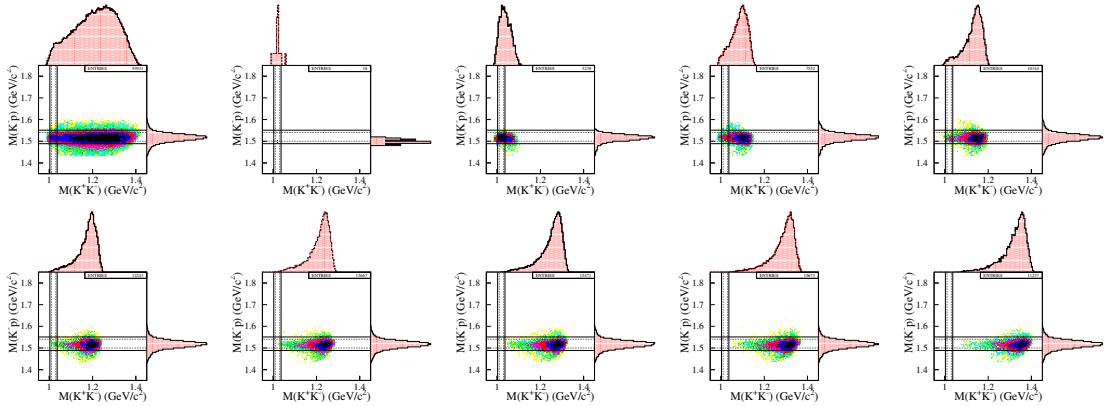

Figure 3.30: Simulated distributions for $\Lambda(1520) \to \Sigma^+\pi^-$, followed by $\Sigma^+ \to p\pi^0$, are displayed in terms of the 0.1-GeV E_γ bin from 1.573 to 2.373 GeV. The first plot is for a whole energy region.

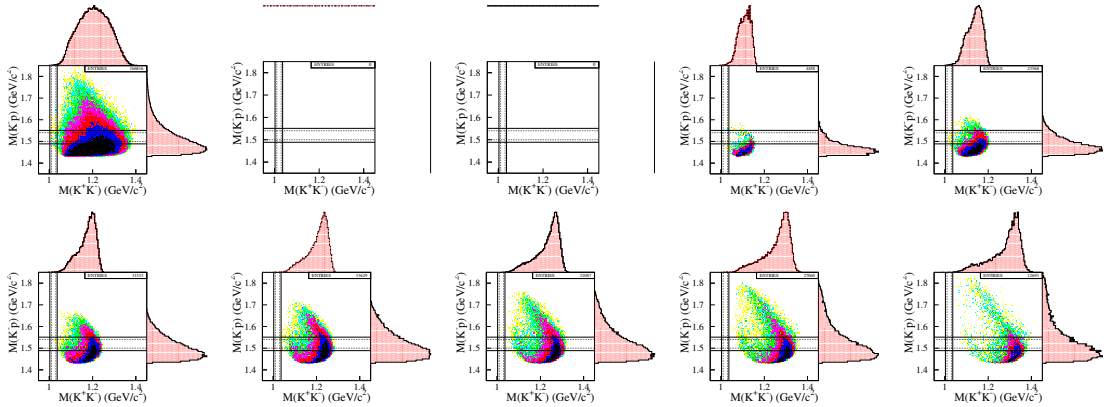

Figure 3.31: Simulated distributions for $K^*(892)$ photoproduction are displayed in terms of the 0.1-GeV E_γ bin from 1.573 to 2.373 GeV. The first plot is for a whole energy region.

3.6 A Simultaneous Fit with Monte Carlo Templates

Event selection was based on the mass bands with wide and narrow mass windows. It deserves noting that we fit both K^+K^- and K^-p mass spectra simultaneously with Monte-Carlo templates for the lineshapes. We did not bring any arbitrary functions to describe the so-called unknown background contributions. This simultaneous fit with Monte Carlo templates is a self-consistent way to reproduce the measured K^+K^- and K^-p mass spectra, which should pertain to the further study of the interference phase measurement. For the interference study, the relative amplitude should be determined beforehand in independent ways. The Monte Carlo template fits should provide us with the independent measurement of the relative amplitudes between the ϕ and the $\Lambda(1520)$.

K^+K^-p events were first selected in the mass region of $|m_{K^+K^-} - m_\phi| \leq 4\Gamma_\phi$ (ϕ-band) and $|m_{K^-p} - m_{\Lambda(1520)}| \leq 2\Gamma_{\Lambda(1520)}$ ($\Lambda(1520)$-band), which is called the 'wide' band. The second set of the K^+K^-p events was selected in the 'narrow' mass band of $1.01 < m_{K^+K^-} < 1.03$ GeV and $1.50 < m_{K^-p} < 1.54$ GeV. Furthermore, events were then excluded in the box region crossed by the ϕ and the $\Lambda(1520)$ bands, where the ϕ-$\Lambda(1520)$ interference may occur. The event selection with the wide and narrow bands was also imposed for all the simulated events as well as the event exclusion in the interference box.

The measured K^+K^- and K^-p mass spectra for the selected K^+K^-p events were fitted with the lineshapes of the simulated processes, ϕp, $\Lambda(1520)K^+$, and S-wave K^+K^-p. For the events with K^+p detected are fitted with the three processes plus $K(896)^0\Sigma^+$ and $K^+(\Lambda(1520) \to \Sigma^+\pi^-)$. A least-square fit to the mass distributions with Monte-Carlo templates by minimizing the χ^2:

$$\begin{aligned}\chi^2 &= \sum_{i=1}^{N} \frac{(Y_i(M_{KK}) - \sum_{j=1}^{3(5)} a_{ij} y_{ij}(m_{KK}))^2}{\sigma_i^2} \\ &+ \sum_{k=1}^{N} \frac{(Y_k(M_{K^-p}) - \sum_{l=1}^{3(5)} b_{kl} y_{kl}(m_{K^-p})^2}{\sigma_i^2},\end{aligned}$$

where each event yield in the K^-K^+ mass is equal to the other in the K^-p mass.

$$\sum_{i=1}^{N} Y_i(M_{KK}) = \sum_{k=1}^{N} Y_k(M_{K^-p}), \quad \sum_{i=1}^{N} a_i y_i(M_{KK}) = \sum_{k=1}^{N} b_i y_k(M_{K^-p})$$

The best-fit lineshapes for the ϕ are overlaid with light blue lines in the K^+K^- and the K^-p mass spectra, while those for the $\Lambda(1520)$ are represented

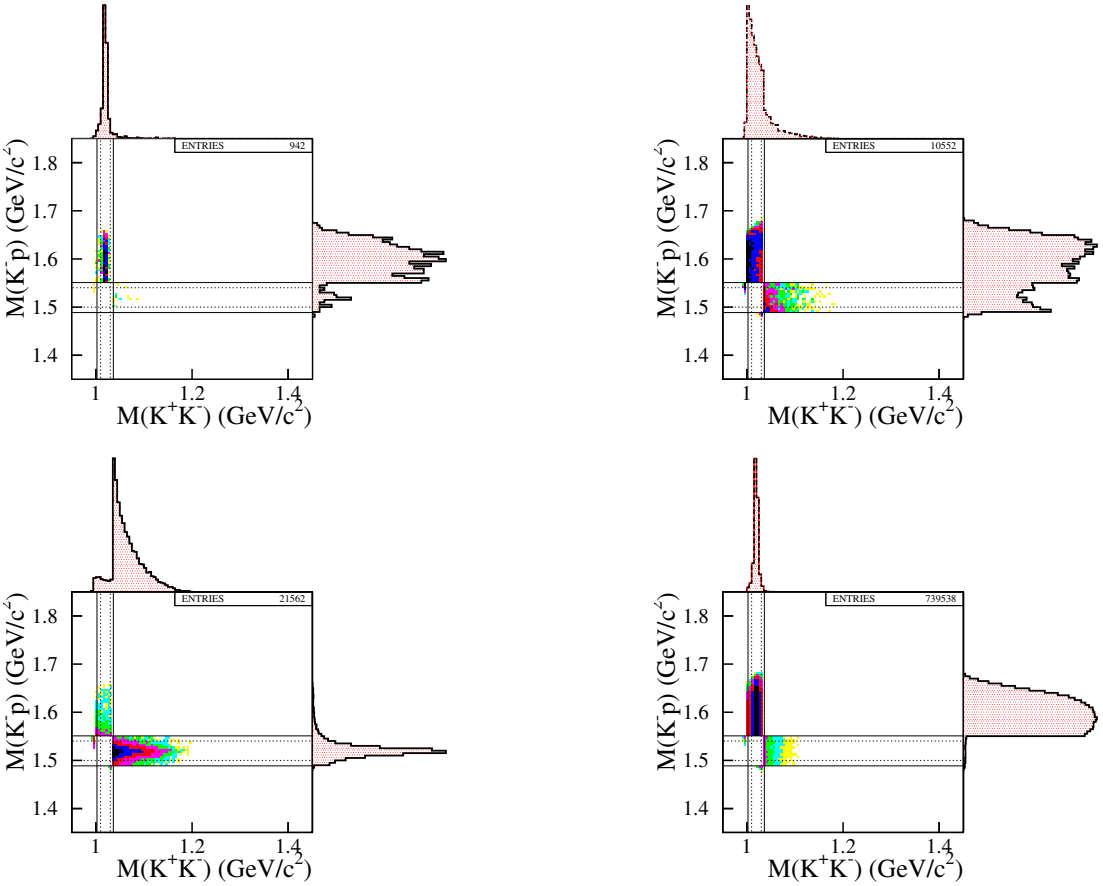

Figure 3.32: Invariant mass distributions in the selected region from the real data (top left) and the simulated spectra for S-wave K^+K^- production (top right), ϕ (bottom left) and $\Lambda(1520)$ (bottom right) production processes, respectively.

as pink lines. Non-resonant K^+K^-p production contributions are shown with blue lines. The green lines denote the contribution from $K^0(896)\Sigma+$ production.

The fit quality is represented as the log-likelihood ratio:

$$-2\ln\Delta = \sum_i N_i^{\rm sim} - N_i^{\rm dat} + N_i^{\rm dat}\ln\frac{N_i^{\rm dat}}{N_i^{\rm sim}},$$

which behaves like χ^2 at the limit of large N. The χ^2 probability $(P(\chi^2) = P(-2\ln\Delta)$ is quoted in each of the fitted K^+K^- and K^-p mass spectra.

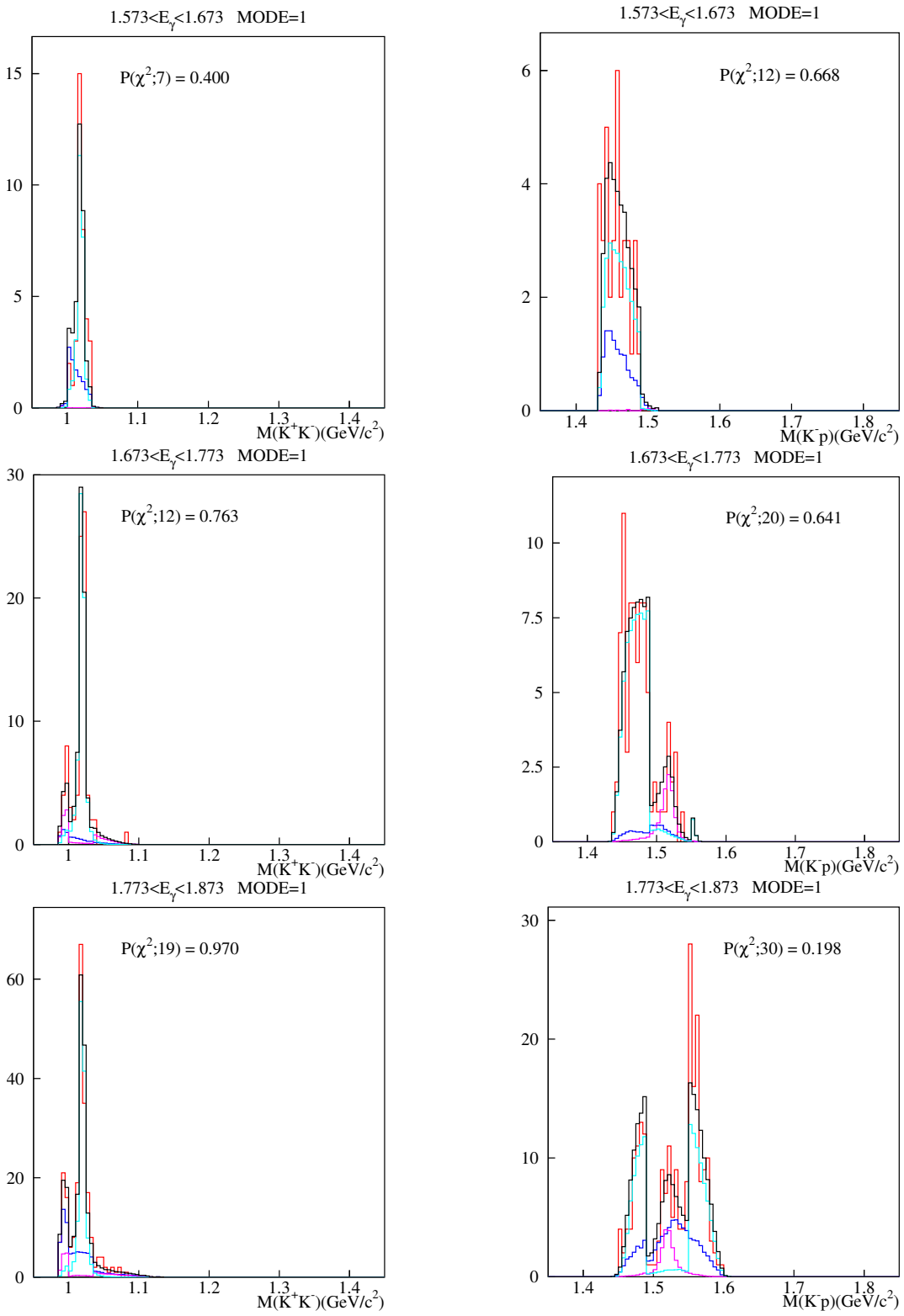

Figure 3.33: Fit with MC Templates for $\gamma p \to K^- K^+ (p)$

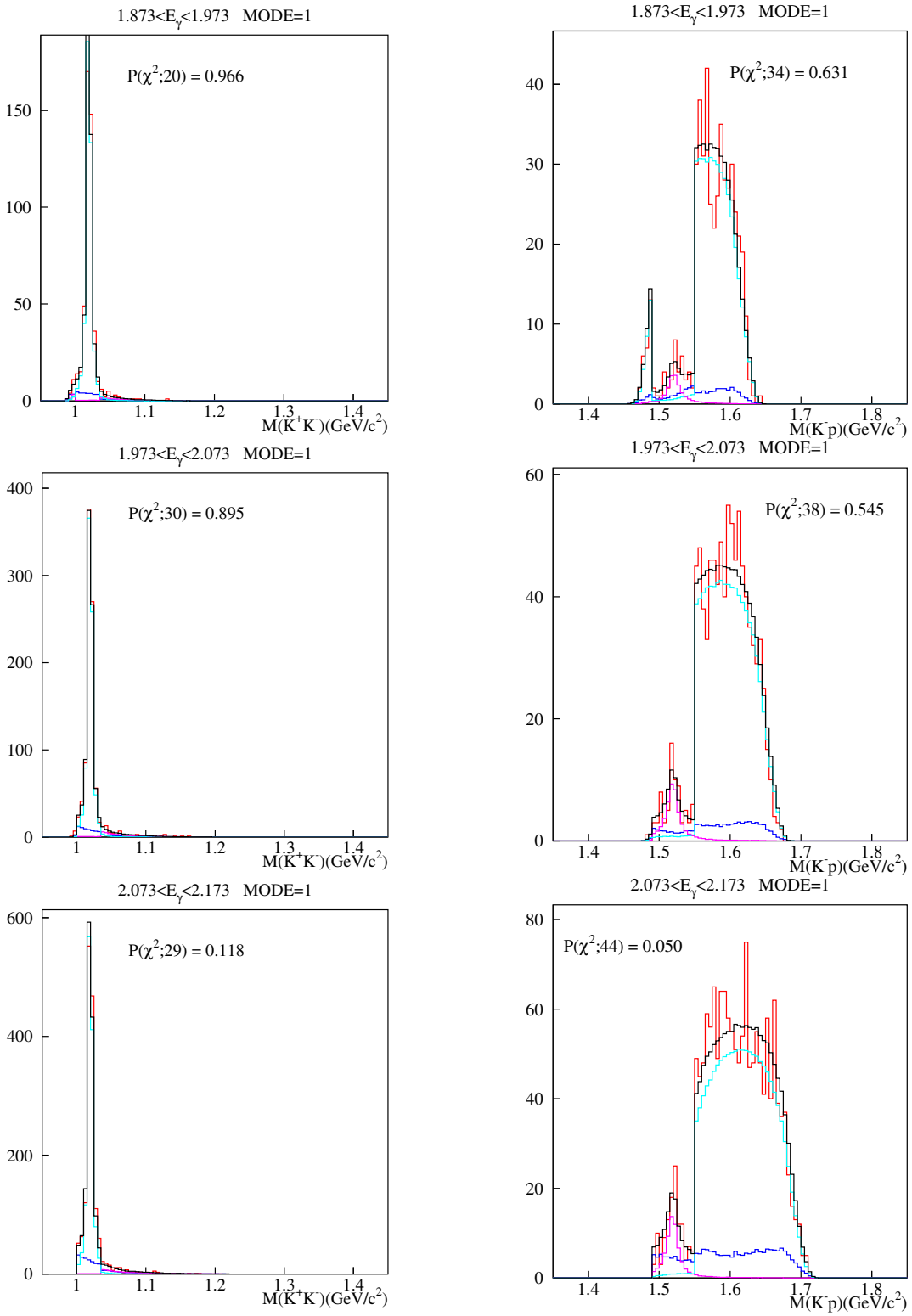

Figure 3.34: Fit with MC Templates for $\gamma p \to K^- K^+ (p)$

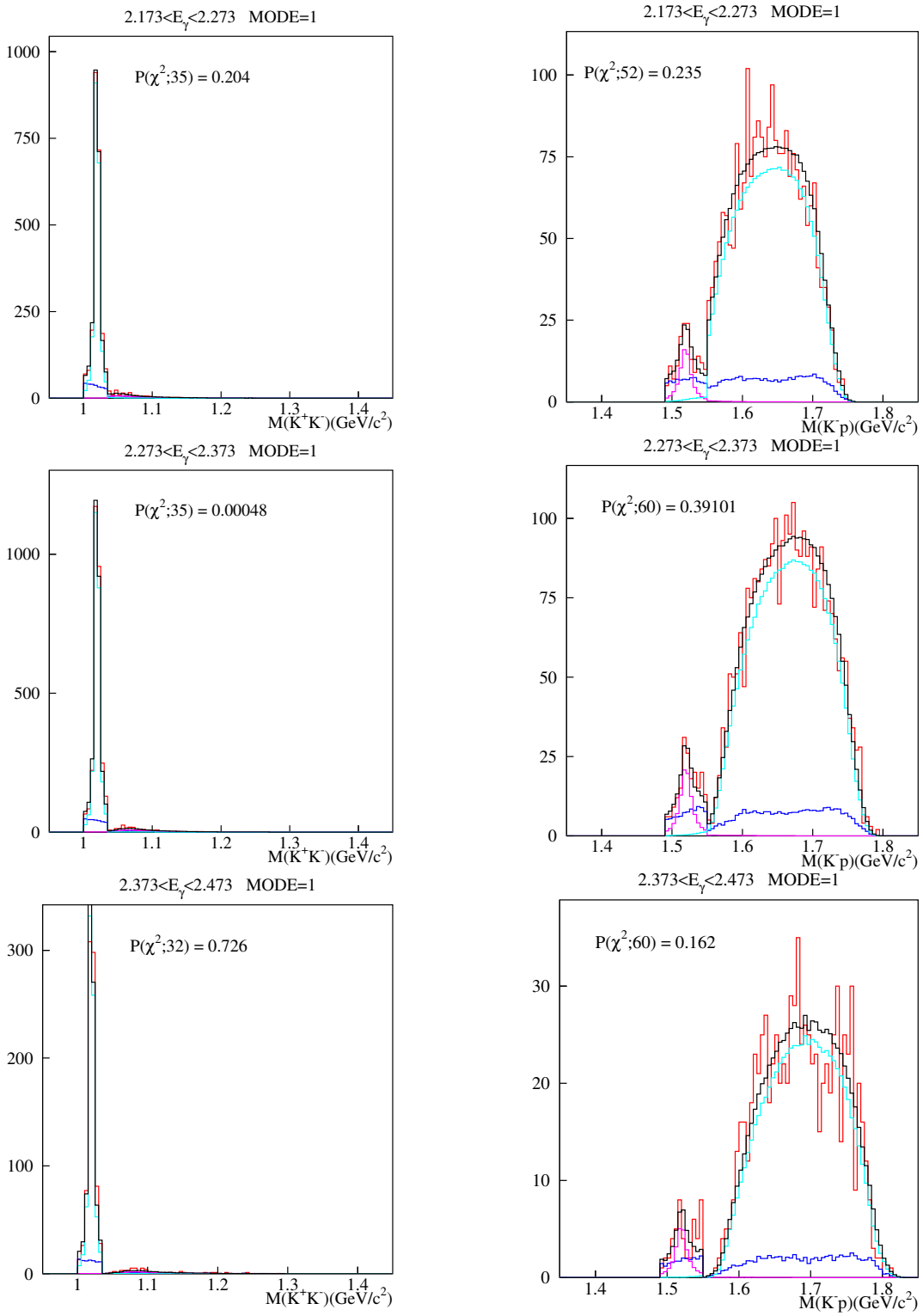

Figure 3.35: Fit with MC Templates for $\gamma p \to K^- K^+(p)$

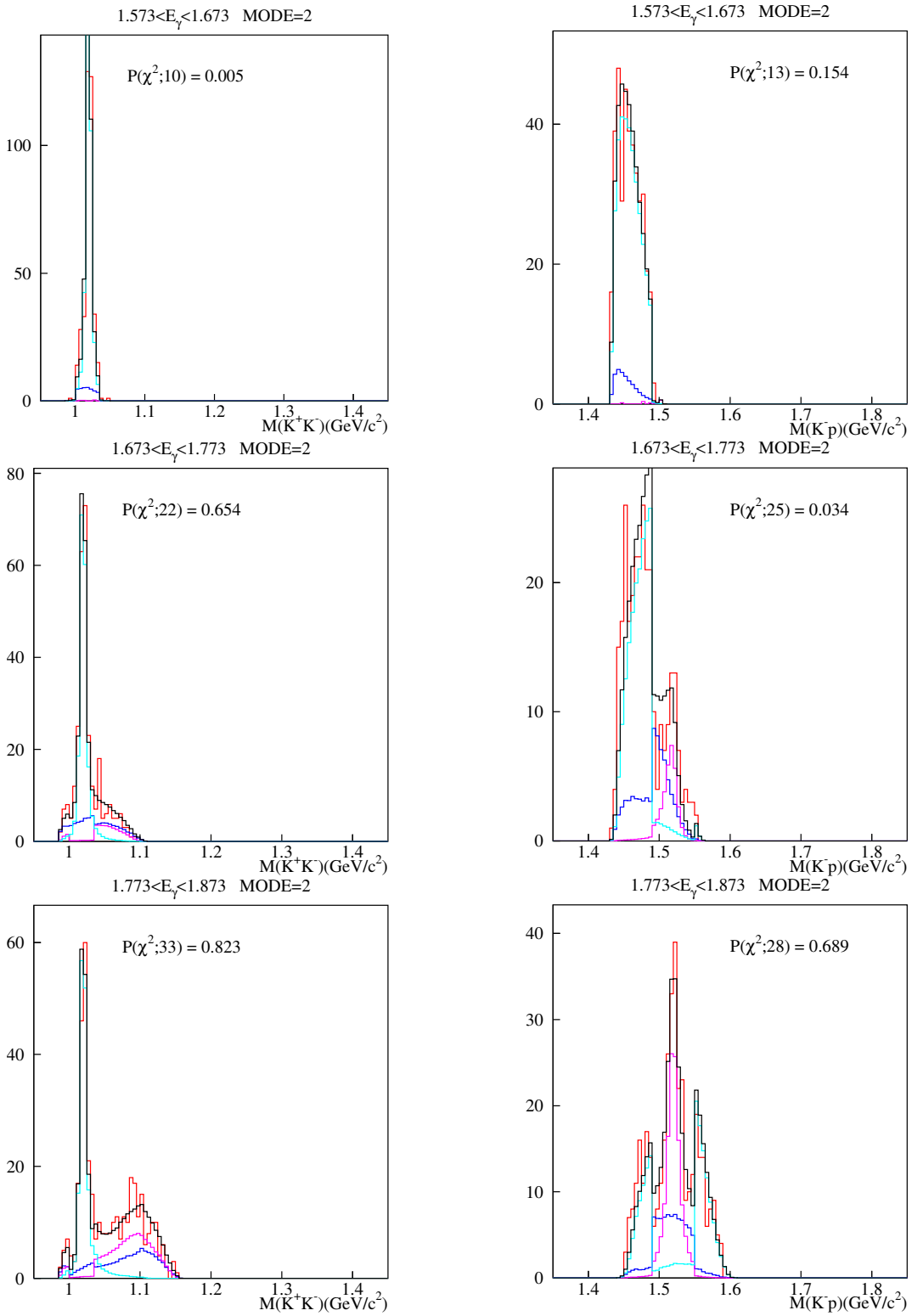

Figure 3.36: Fit with MC Templates for $\gamma p \to K^-(K^+)p$

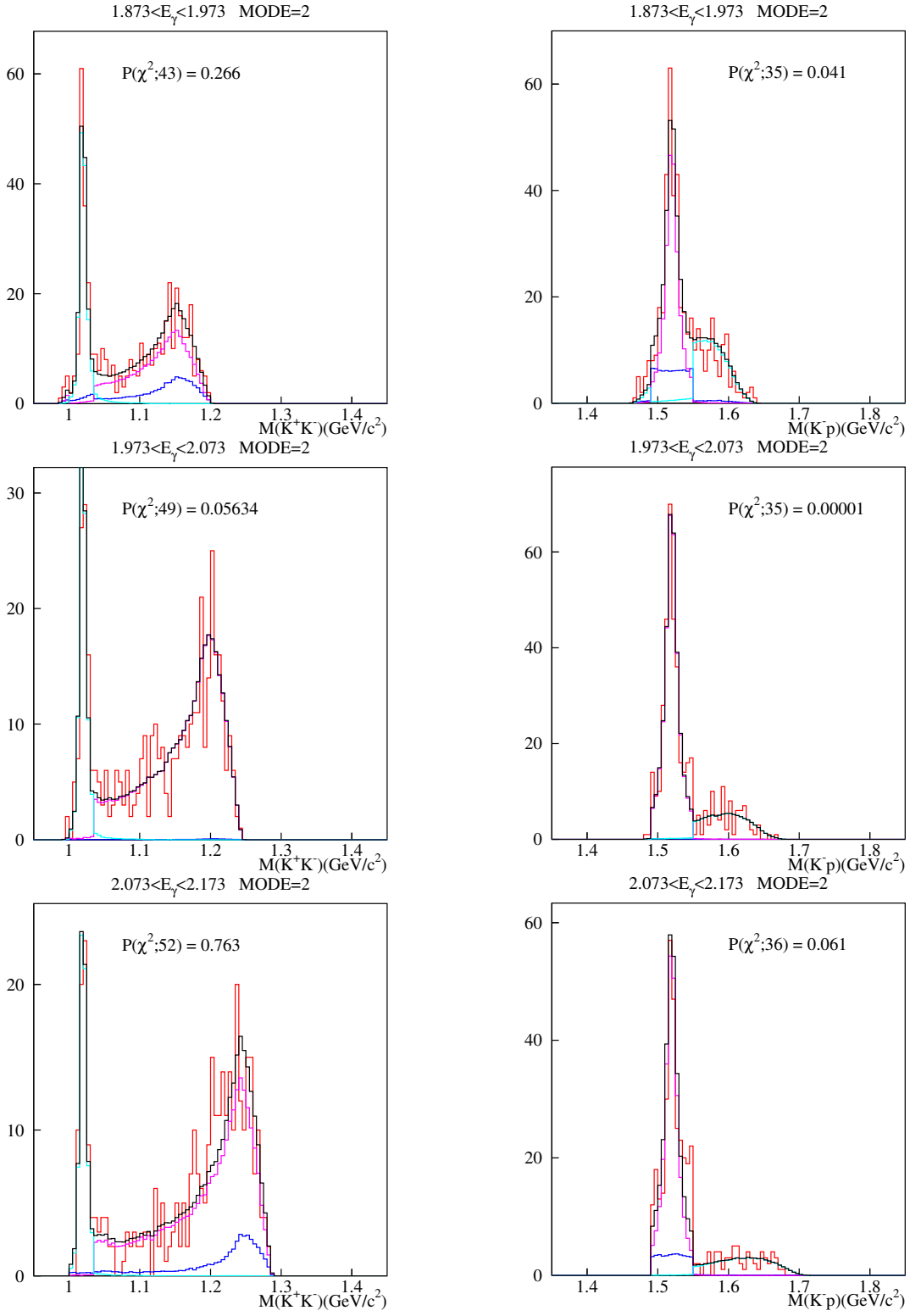

Figure 3.37: Fit with MC Templates for $\gamma p \to K^-(K^+)p$

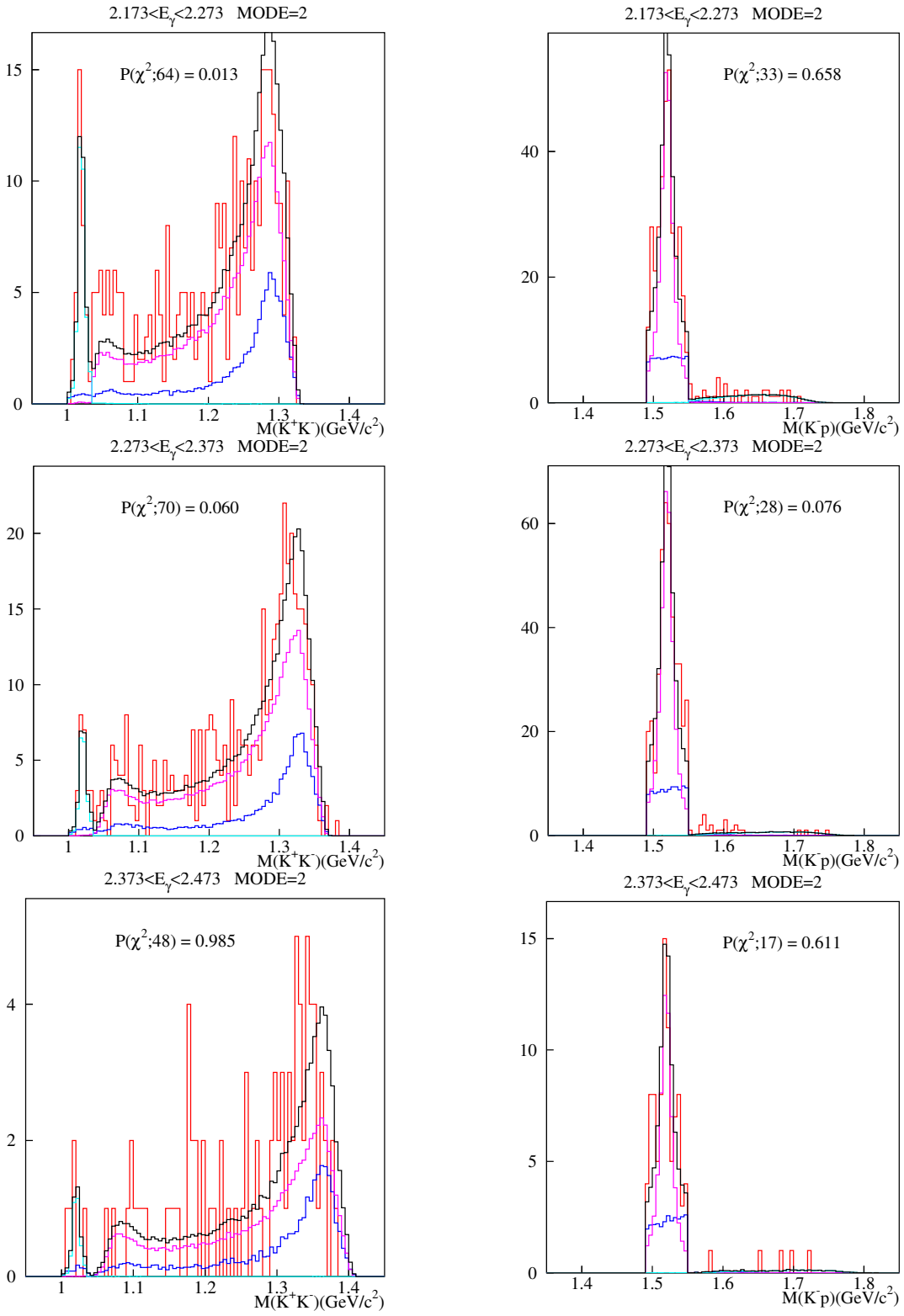

Figure 3.38: Fit with MC Templates for $\gamma p \to K^- p(K^+)$

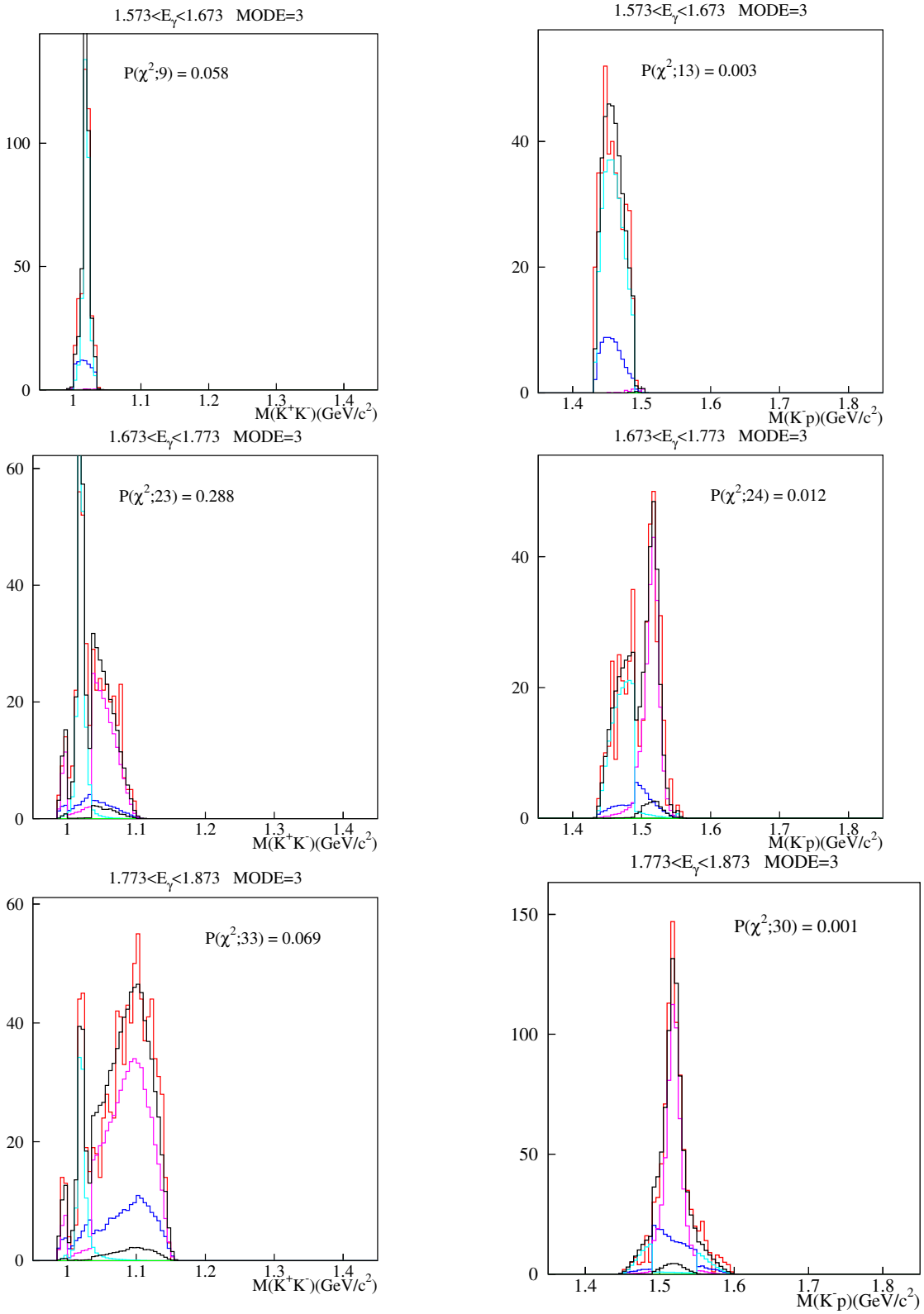

Figure 3.39: Fit with MC Templates for $\gamma p \to K^+ p(K^-)$

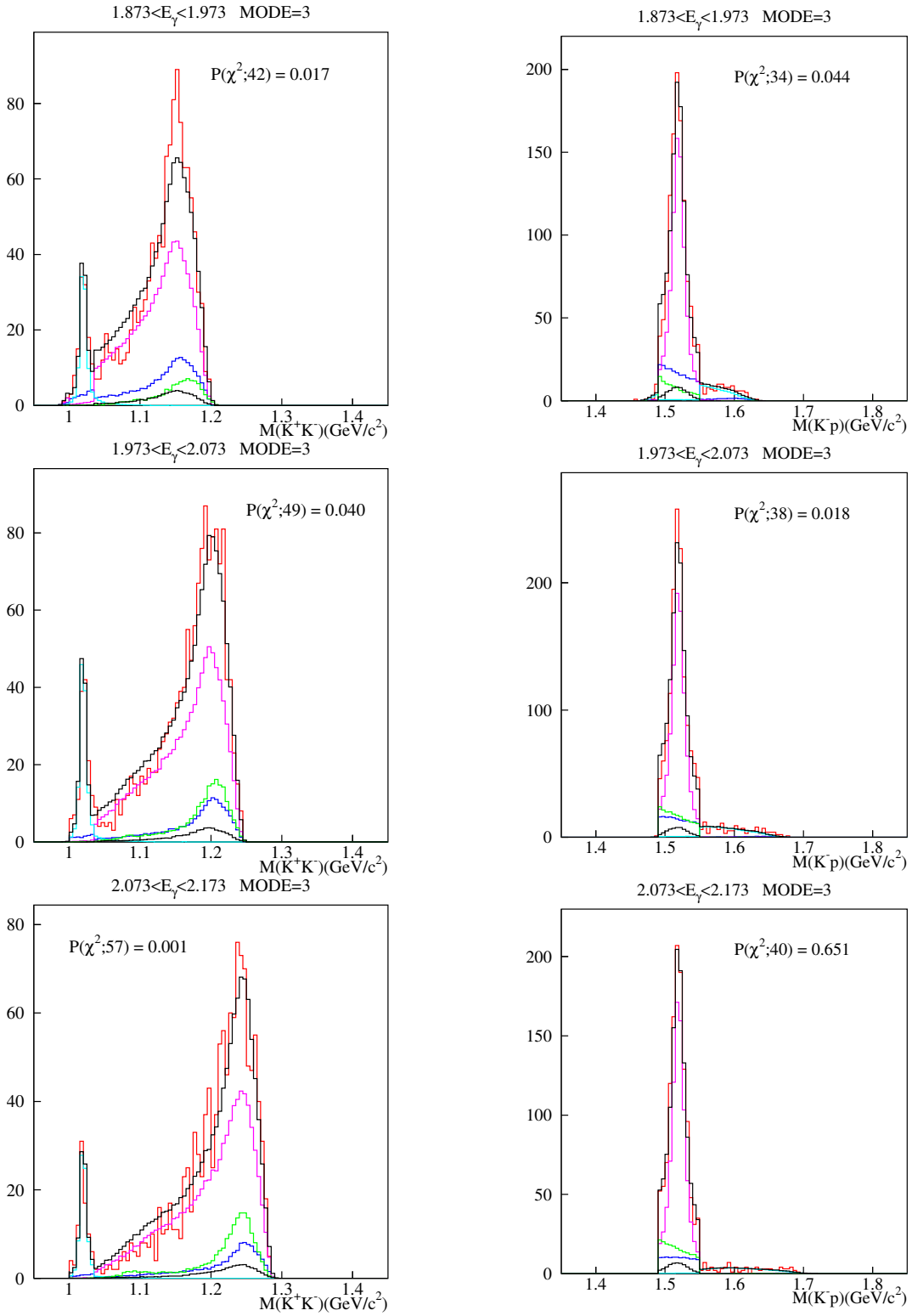

Figure 3.40: Fit with MC Templates for $\gamma p \to K^+ p(K^-)$

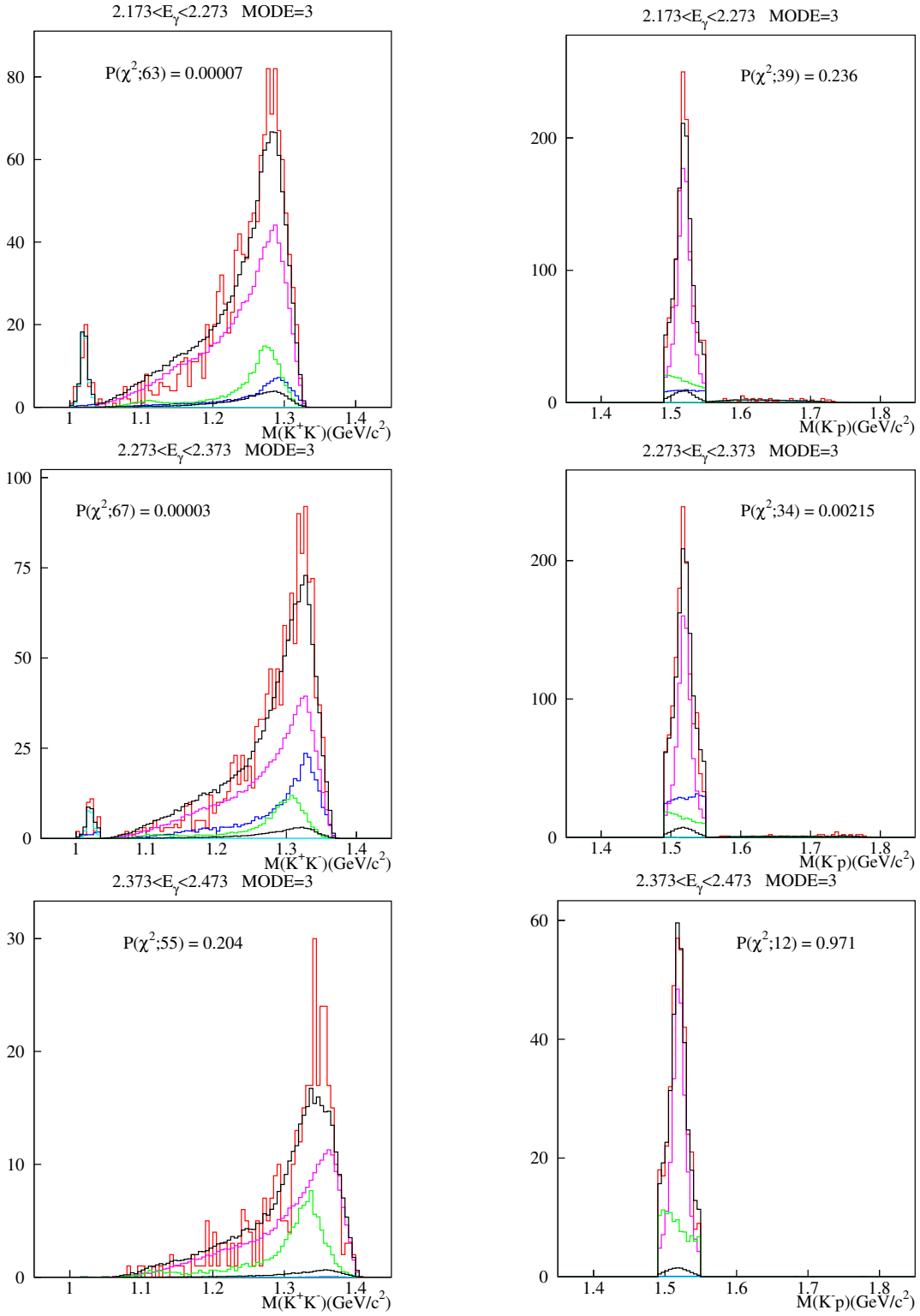

Figure 3.41: Fit with MC Templates for $\gamma p \to K^+ p(K^-)$

3.7 Mass Spectra in the Interference Box

The lineshape fits with Monte Carlo templates were based on the events out of the interference box. The fit results with Monte Carlo templates were then interpolated into the box region, keeping the strengths of the templates determined from the fit. Figures 3.42 3.43, 3.44 and figures 3.45, 3.46, 3.47 show the mass distributions for the box regions crossed by the wide band and the narrow band, respectively. Overlaid is the interpolated lineshape from the fit. Shaded area represents uncertainties in the fit.

In the mid-energy bins there are slightly some excess in the yield, compared to the interpolated lineshapes, which indicate possible constructive interference. In the low-energy bins there are some data points, yielding clearly less than the predicted level. The differences are obviously seen in the event sets with K^-p detected, as shown Figs. 3.43 and 3.46. Here, it should be stressed that the events with K^-p detected represent $\Lambda(1520)$ photoproduction at forward angles, while ϕ mesons are produced at large angles. The ϕ photoproduction proceeds at forward angles dominantly via a diffractive Pomeron exchange, while at large angles other contributions from non-diffractive processes could be emphasized.

As a result, the ϕ-$\Lambda(1520)$ interference is likely to appear in the angular region, where $\Lambda(1520)$ is produced at forward angles. The interference seems to be slightly destructive near the threshold and is changed constructively in the energy region with the maximum kinematic overlap between the ϕ and $\Lambda(1520)$ production bands.

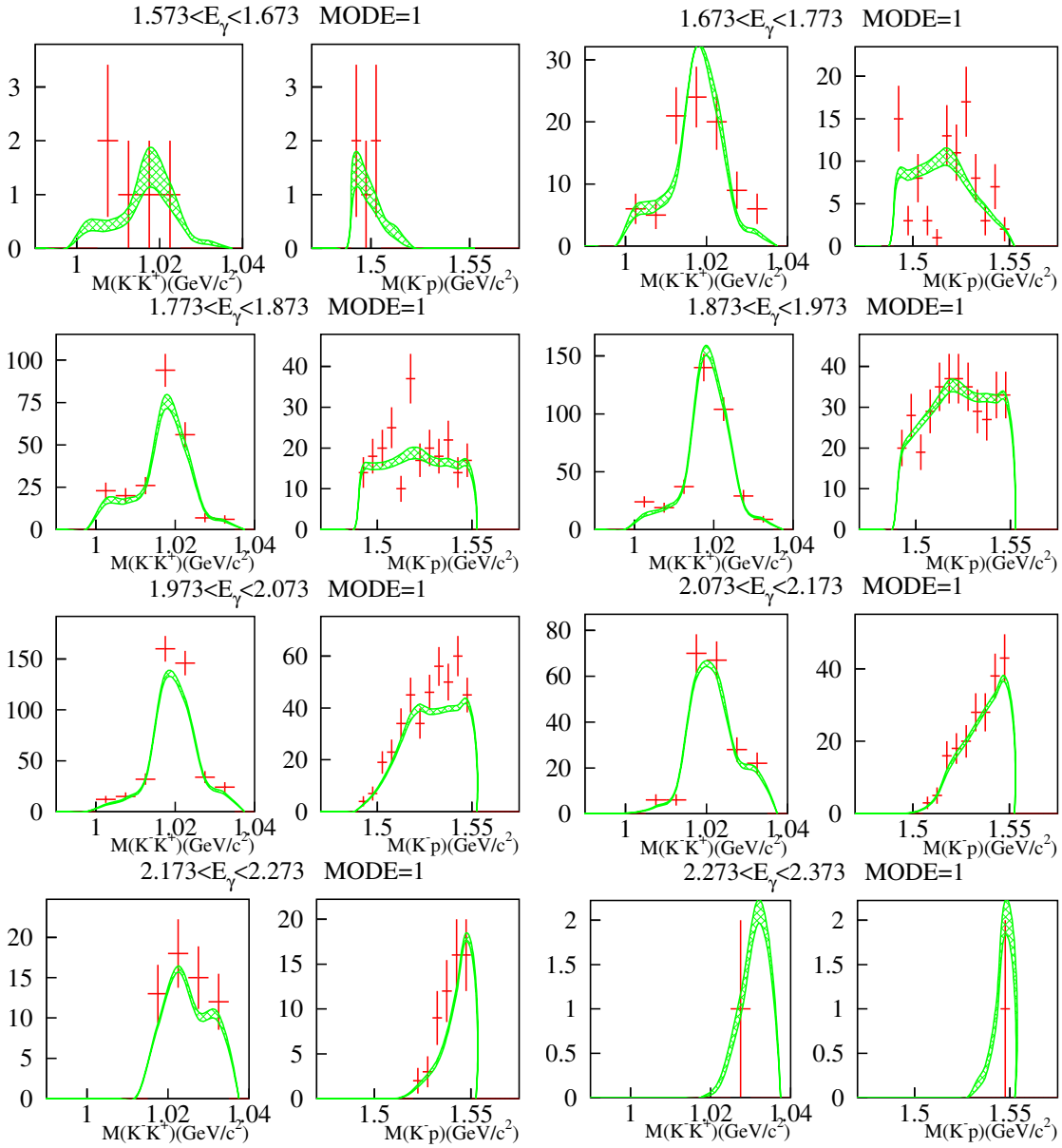

Figure 3.42: Data from the K^+K^- event set in the 'wide' ϕ-$\Lambda(1520)$ interference box region are compared with the estimated level from the results of the Monte Carlo template fit.

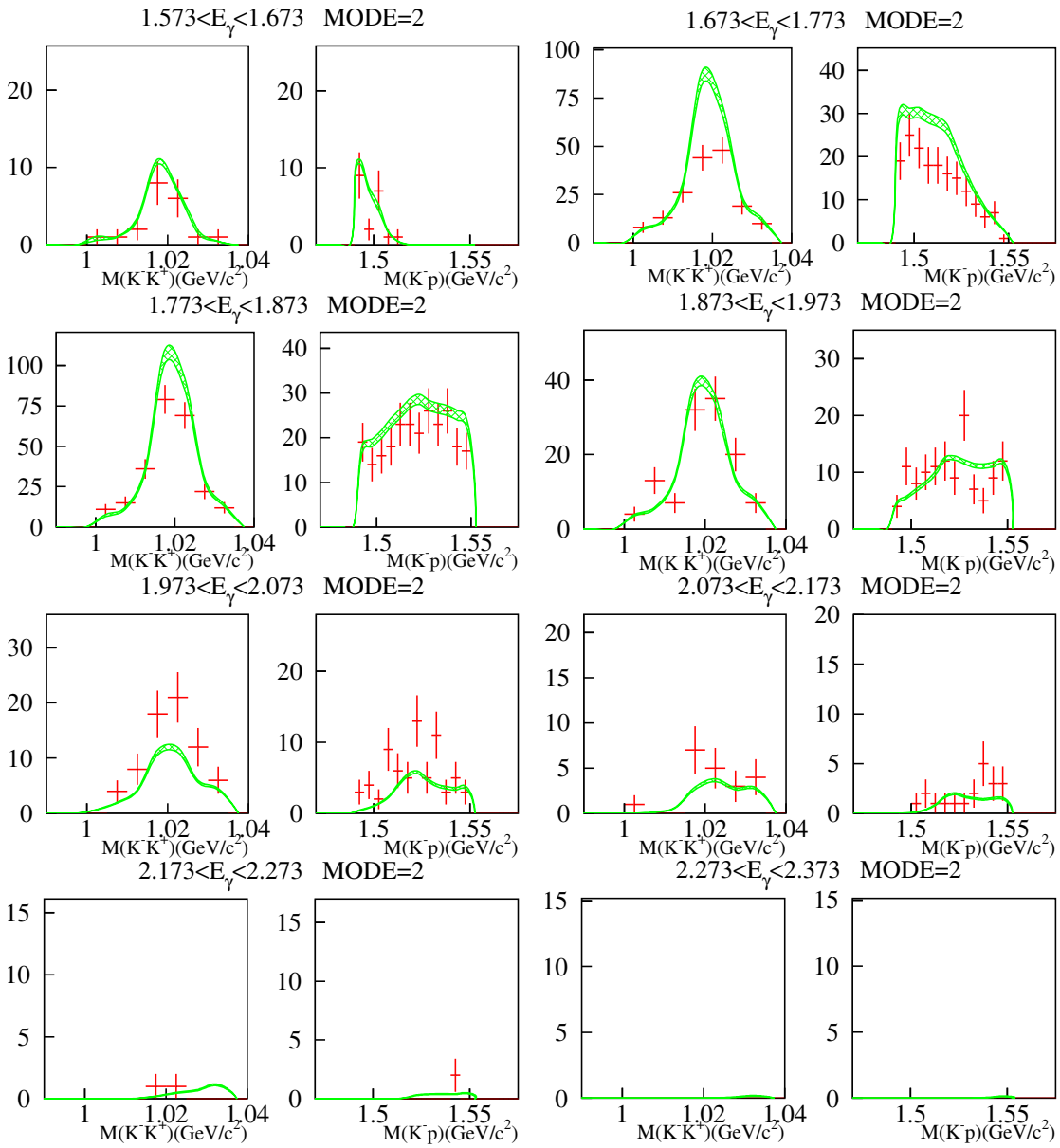

Figure 3.43: Data from the K^-p event set in the 'wide' ϕ-$\Lambda(1520)$ interference box region are compared with the estimated level from the results of the Monte Carlo template fit.

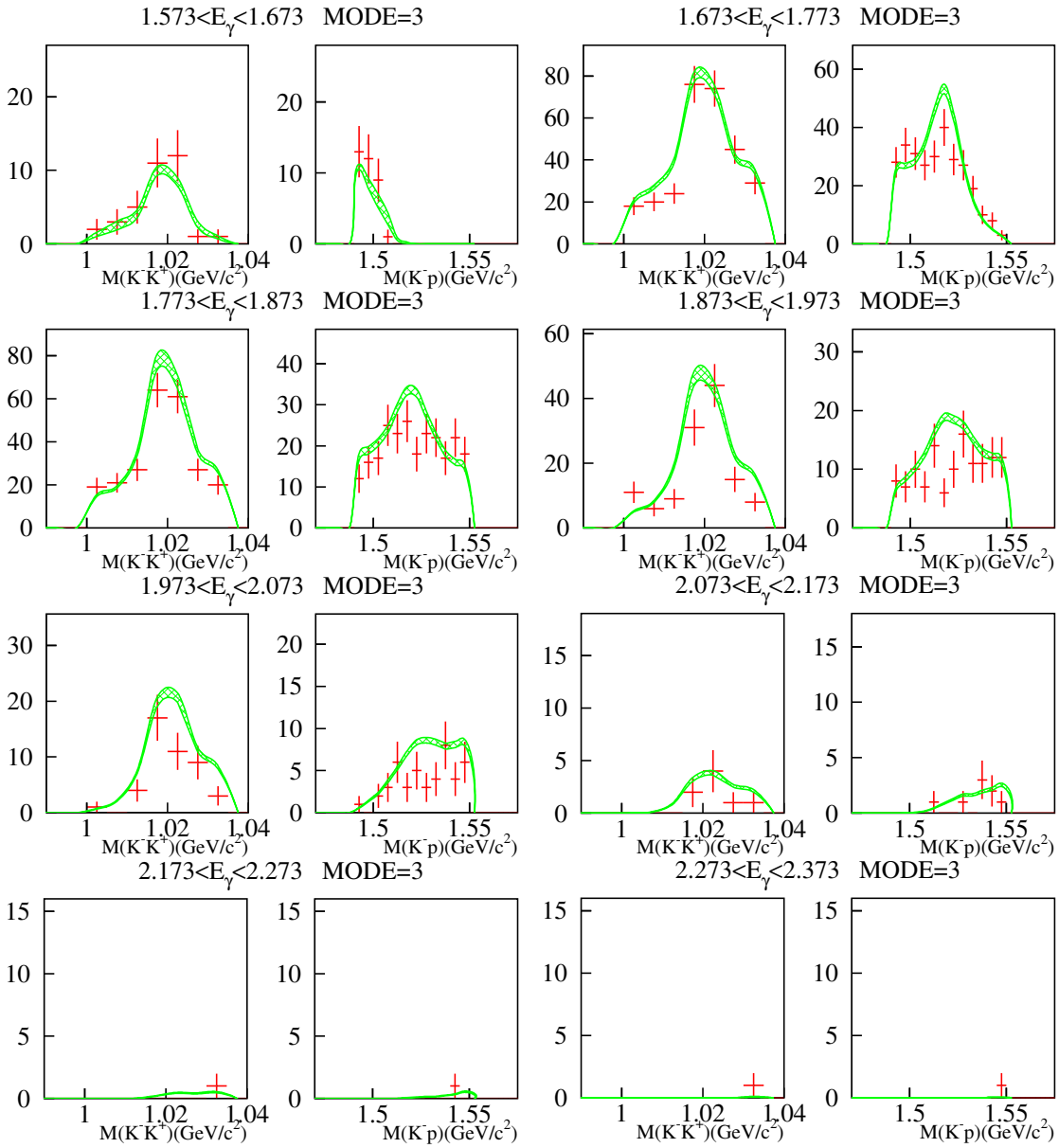

Figure 3.44: Data from the K^+p event set in the 'wide' ϕ-$\Lambda(1520)$ interference box region are compared with the estimated level from the results of Monte Carlo template fit.

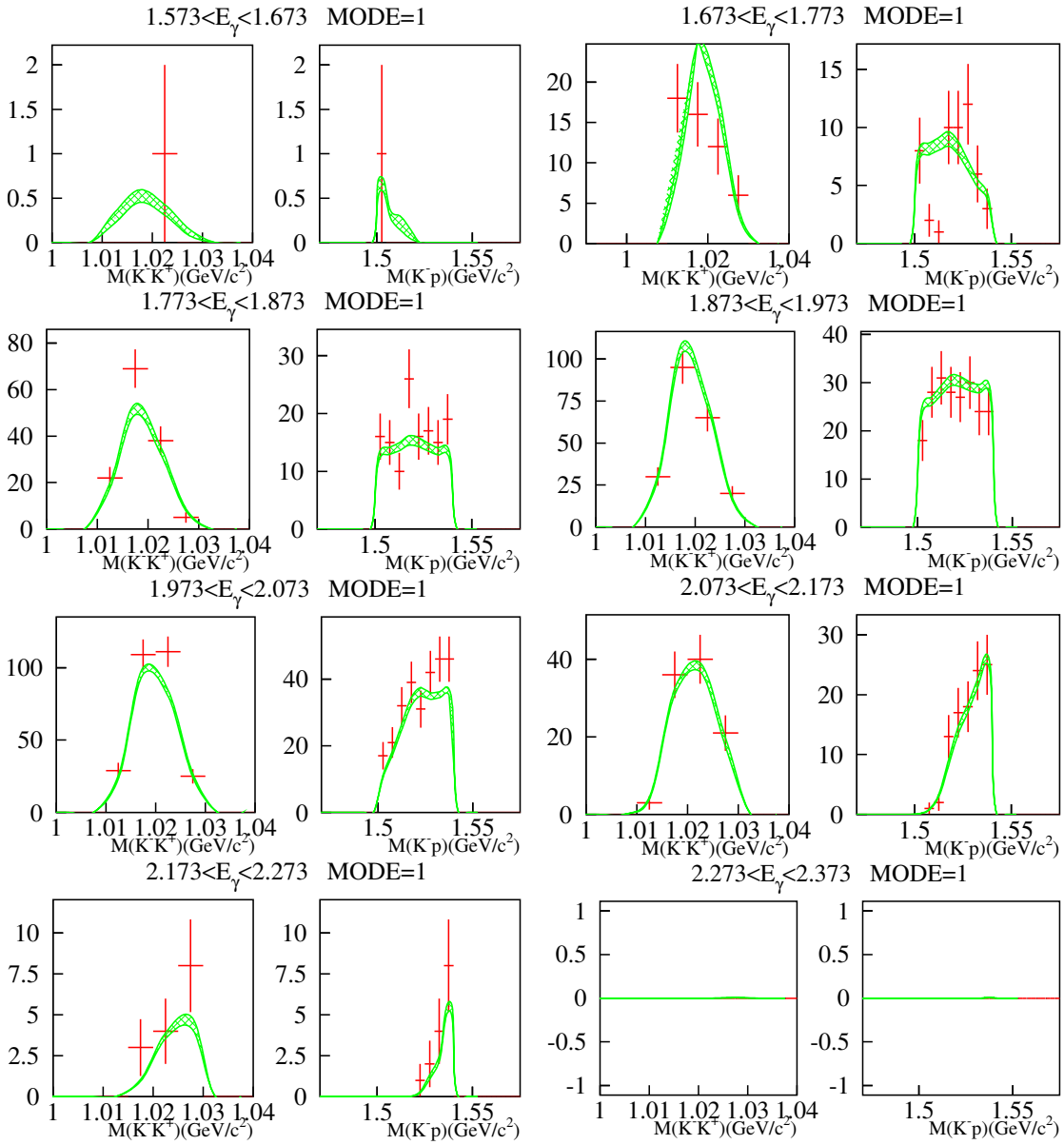

Figure 3.45: Data from the K^-K^+ event set in the 'narrow' ϕ-$\Lambda(1520)$ interference box region are compared with the estimated level from the results of the Monte Carlo template fit.

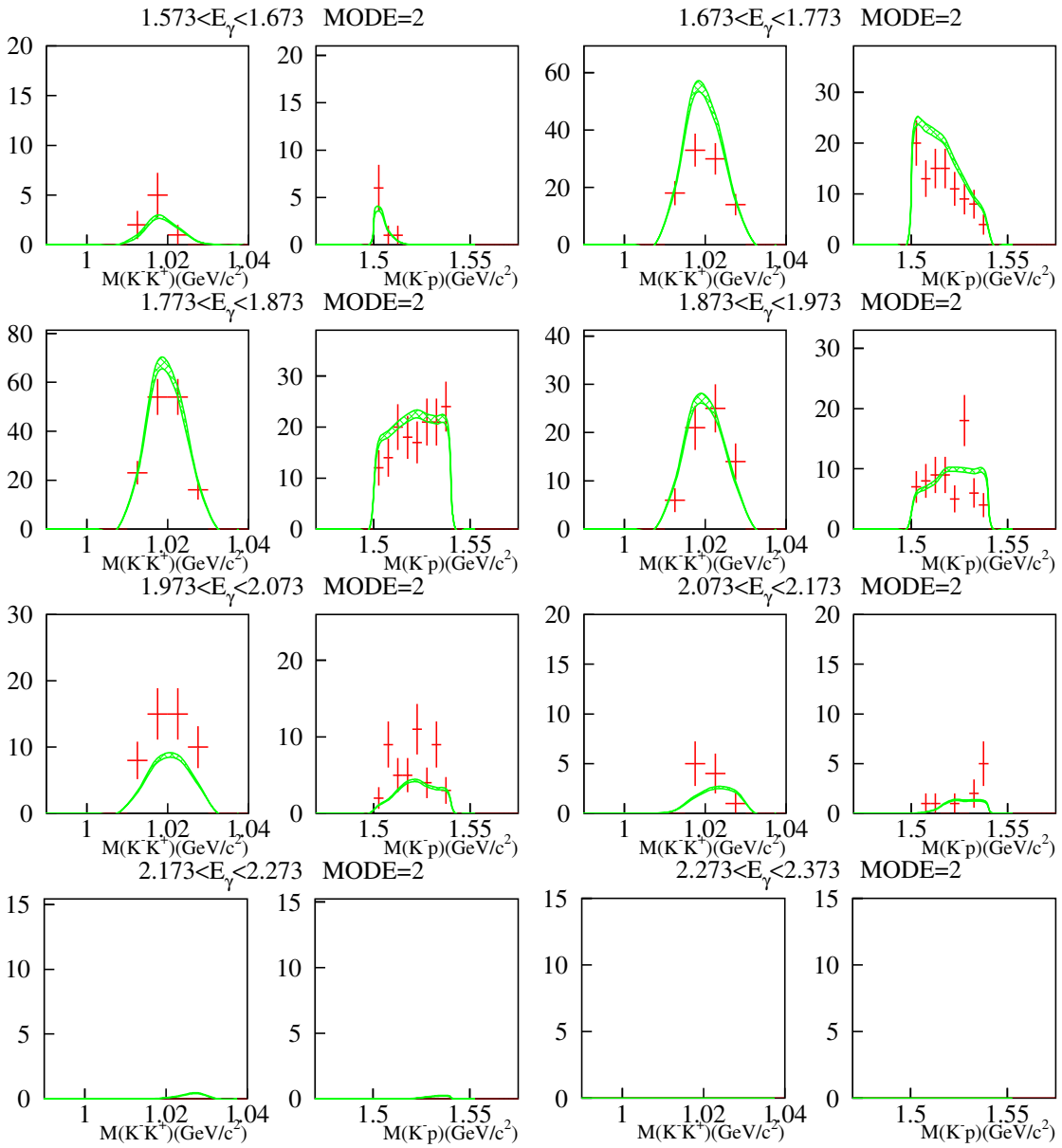

Figure 3.46: Data from the K^-p event set in the 'narrow' ϕ-$\Lambda(1520)$ interference box region are compared with the estimated level from the results of the Monte Carlo template fit.

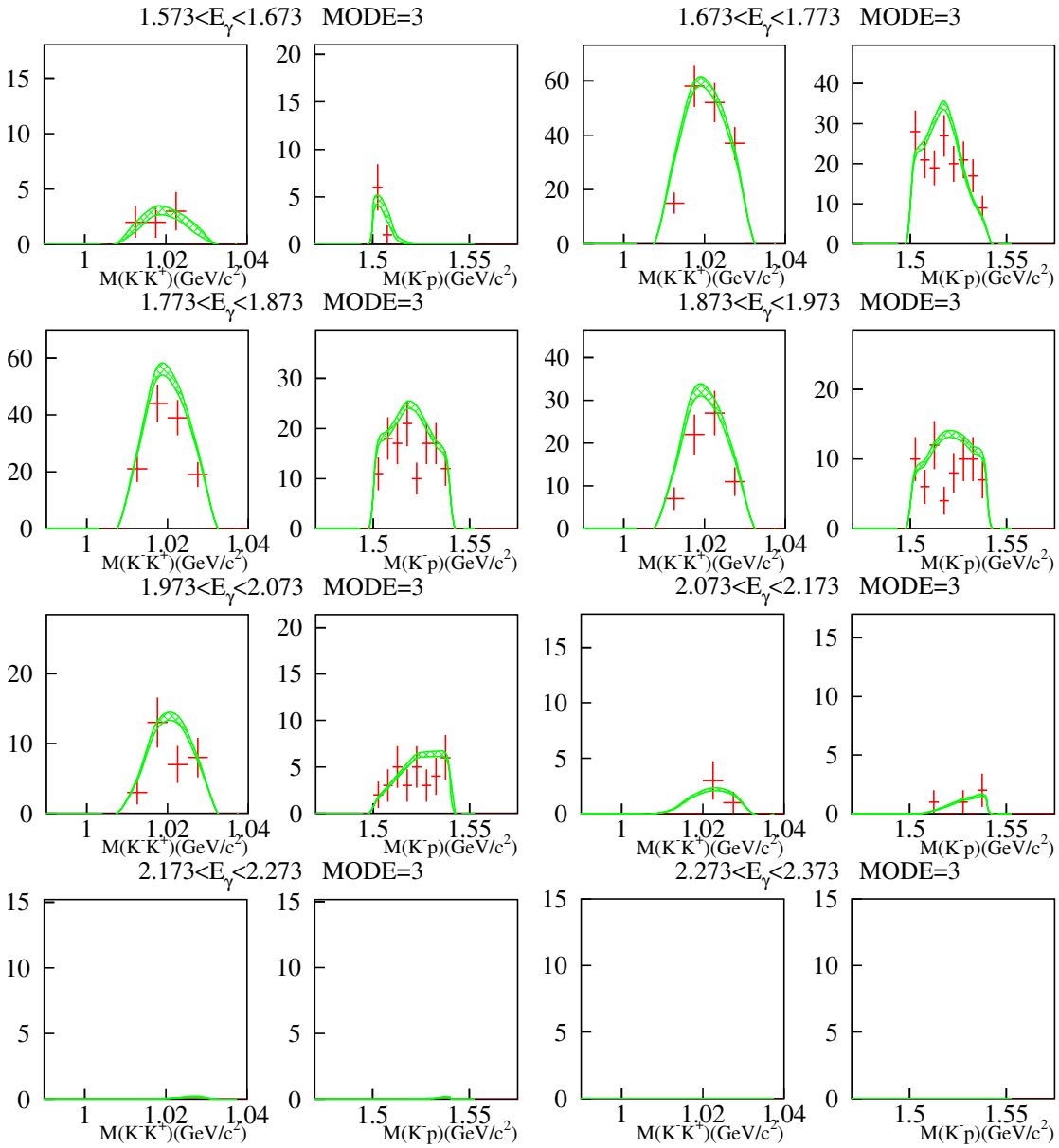

Figure 3.47: Data from the K^+p event set in the 'narrow' ϕ-$\Lambda(1520)$ interference box region are compared with the estimated level from the results of the Monte Carlo template fit.

3.8 Forward Cross Sections for ϕ Photoproduction

The differential cross sections $d\sigma/dt'$ for nine energy ranges are fitted with an exponential function:

$$\frac{d\sigma}{dt'} = \frac{d\sigma}{dt}\Big|_{t=t_{\min}} \exp(-b|t - t_{\min}|),$$

where $t' = |t - t_{\min}|$. t is the 4-momentum transfer between the photon and the ϕ, and $t_{\min}$ is the minimum momentum transfer for each K^+K^- mass:

$$t = (p_\gamma - p_\phi)^2 = (p_p - p'_p)^2 = -2E_\gamma E_\phi + 2\vec{p}_\gamma \cdot \vec{p}_\phi + m_\phi^2,$$

where 4-momenum $p_\gamma = (E_\gamma, \vec{p}_\gamma)$. In the center-of-mass frame

$$t = (E^*_\gamma - E^*_\phi)^2 - (p^*_\gamma - p^*_\phi)^2 - 4p^*_\gamma p^*_\phi \sin^2\frac{\theta^*_{\gamma\phi}}{2}$$

The limiting values are $t_{\min} = t(\theta^*_{\gamma\phi} = 0)$ and $t_{\max} = t(\theta^*_{\gamma\phi} = \pi)$, respectively ($t_{\min} > t_{\max}$).

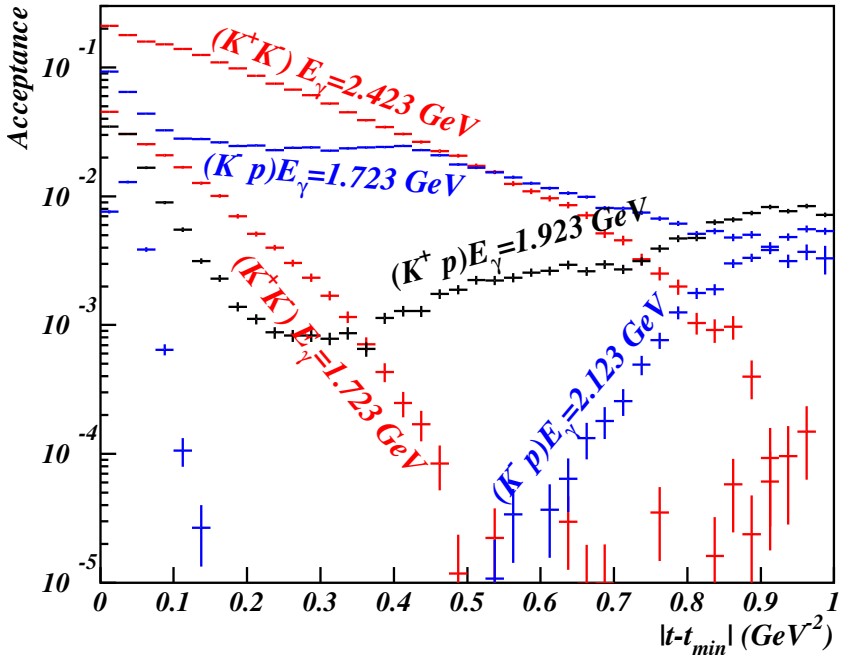

Figure 3.48: Calculated acceptance distributions in terms of the momentum transfer $|t - t_{\min}|$ for the K^+K^-, K^-p and K^+p events at some given energies.

From the $|t - t_{\min}|$ distributions for the ϕ-band events, the simulated distributions for $\Lambda(1520)$ and non-resonant K^+K^- productions (as well as K^* for

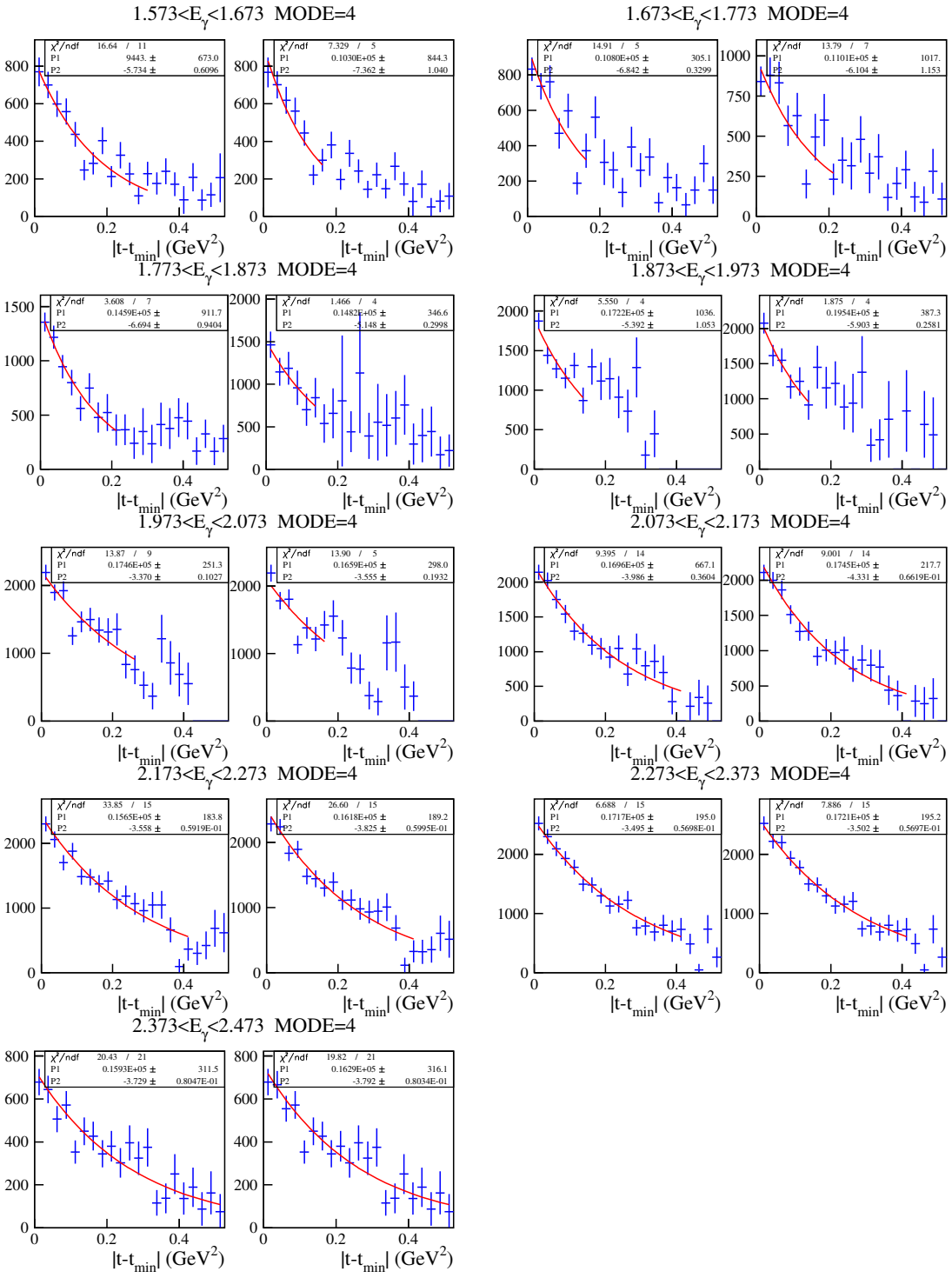

Figure 3.49: Acceptance-corrected $|t - t_{\min}|$ distributions for the whole event sets are shown with exponential fit results with varying slope parameters. In each energy range, the left plot shows the t-distribution with the interference box region, while the right one without the box region.

the K^+p analysis) were subtracted, based on the strengths of the simulated processes from the lineshape fit described earlier. The lineshape fit with Monte Carlo templates was done in two ways with and without the interference box.

Acceptances for the $|t - t_{\min}|$ distributions of the ϕ photoproduction are calculated using a Monte Carlo simulation, based on the same parameterizations such as the decay angular distributions and the detector configurations, but with flat cross sections in terms of $|t - t_{\min}|$, in order to obtain high-statistics Monte-Carlo events. The calculated acceptance distributions are shown in Fig.3.48. The acceptances are calculated in terms of the inclusion of the interference box. It shows good acceptance over the region from the minimum value to 1 GeV^2. For the K^+K^- detection the acceptance is enough only at small t regions, while for other K^-p and K^+p detection it is moderate at large t regions up to about 1 GeV^2.

The acceptance-corrected $|t - t_{\min}|$ distributions are then fitted with the following function:

$$\frac{dN}{dt} = C \cdot \exp(-b|t - t_{\min}|),$$

where C is the intercept and b represents the slope parameter. The exponential fits were performed with two free parameters C and b or a single free parameter C with a fixed slope. The fixed slope values were determined from the fit with the linear or constant function. The exponential fit were also done in terms of the detection mode, K^+K^-, K^-p and K^+p, and also in terms of the inclusion of the interference box to the mass lineshape fit. Figure 3.49 depict the exponential fit results for the combined data sets (MODE=4) from the three detection modes.

Using the integrated photon flux and the number of target protons per unit area, the intercept values from the exponential fit were converted to an optical point in the unit of μb/GeV^2:

$$\frac{d\sigma}{dt'} = \frac{d\sigma}{dt}\Big|_{t=t_{\min}} \exp(-b|t - t_{\min}|),$$

where $t' = |t - t_{\min}|$. The differential cross sections are obtained as:

$$\frac{d\sigma}{dt'} = \frac{\Delta N_\phi}{N_\gamma \cdot N_t \cdot \varepsilon_{\rm acc} \cdot {\rm Br}(\phi \to K^+K^-) \cdot \Delta t'},$$

where ΔN_ϕ is the number of ϕ events in a given $\Delta t'$ bin, $\varepsilon_{\rm acc}$ represents the detection acceptance, and ${\rm Br}(\phi \to K^+K^-) = 48.9\%$. The number of photon beams incident on the LH_2 target (N_γ) is given by a product of the number of

tagged photons, tagging efficiency and the transmission factor (52.6%). The number of target protons per unit area (N_t) is given by

$$N_t = \rho \frac{N_A}{W} L = 6.768 \times 10^{23}/\mathrm{cm}^2,$$

where $\rho = 0.708$ g/cm^3, Avogadro's number $N_A = 6.022 \times 10^{23}$/mole, atomic weight $W = 1.00794$ g/mole, and the effective target length $L = 16$ cm.

The forward differential cross sections for ϕ photoproduction were measured with three separate K^+K^-, K^-p and K^+p data sets in the two data runs taken in the 2002/2003 and 2006/2007 periods. For the K^+K^- data sets the first energy bin was excluded, while for the K^-p and K^+p data sets the energy bins above 2.073 GeV were excluded due to the lack of acceptance. Figure 3.50 shows the exponential fit results for three separate data sets with and without the events in the interference box. The first column plots show the results with two free parameters, the slope and the intercept. The slope parameters vary slowly with photon energy. The middle-column plots depict the results with the fixed slope parameter. We take a mean value of the slope parameters from the previous fit with varying slope parameters. In the right column the fit results with linearly decreasing slope parameters are shown. It turns out that the differential cross sections at $t = t_{\mathrm{min}}$ are little changed with respect to the choice of the slope parameterization. It is very interesting that the differential cross sections obtained with the events in both the ϕ and $\Lambda(1520)$ mass bands are consistent within the K^+K^-, K^-p, and K^+p data sets.

The $|t - t_{\mathrm{min}}|$ distributions for the three separate data sets were then added up and fitted with the same exponential functions. The results are shown in Figs. 3.51, 3.52, and 3.53. Blue open squares represent the forward differential cross sections obtained without the interference box, while red closed circles the results with the interference box. Figure 3.54 shows the results with the 'narrow' mass band, which is energy dependence of $d\sigma/dt|_{t=t_{\mathrm{min}}}$ with slopes $b(E_\gamma)$ with/without the interference box.

It turns out that there is little change in the differential cross sections $d\sigma/dt|_{t=t_{\mathrm{min}}}$ obtained with and without the interference box region. Since event statistics in the interference box is much smaller than the total statistics for the ϕ mass band, a possible change (excess or deficit) in the interference box is hardly seen in the differential cross sections.

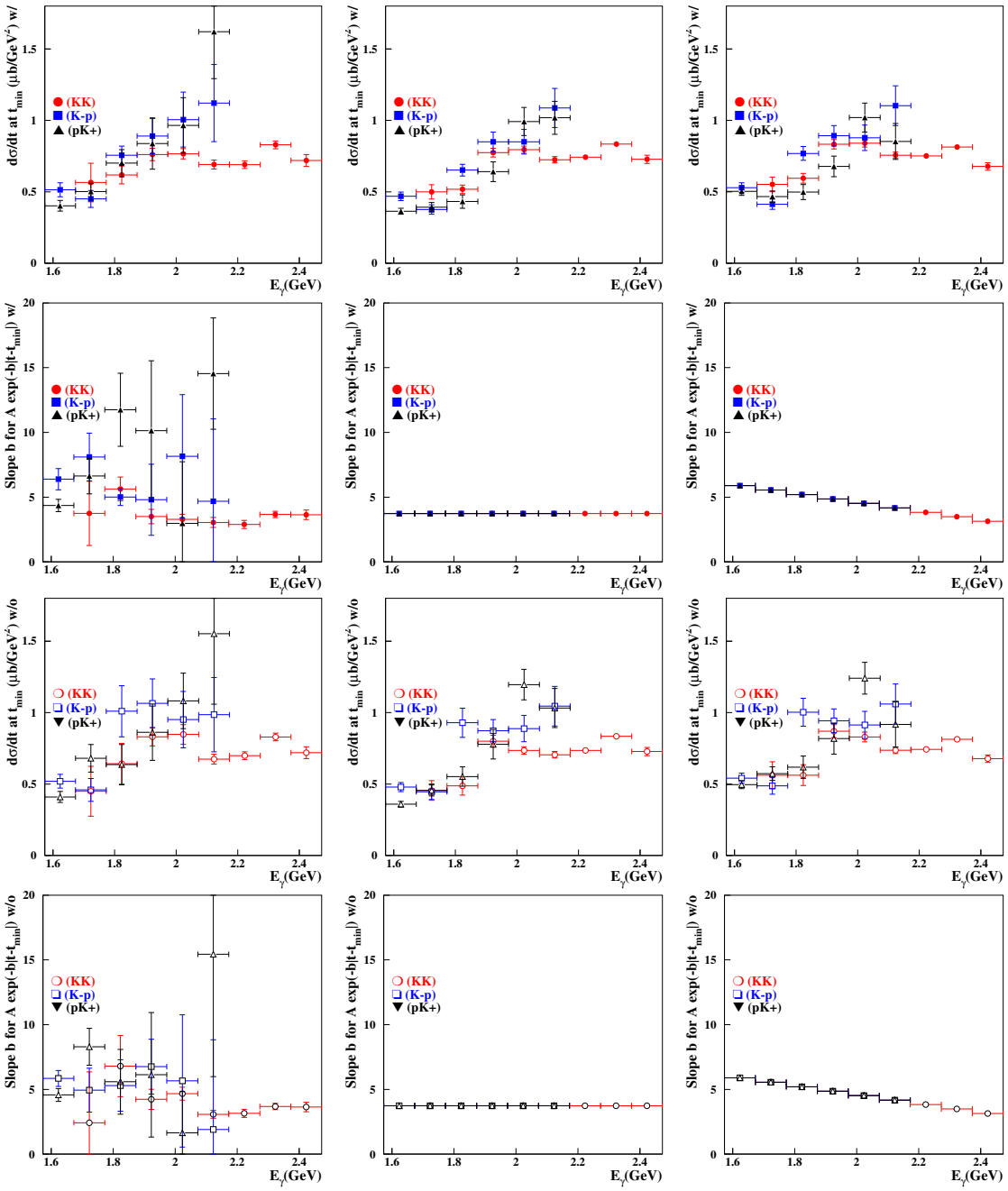

Figure 3.50: Intercepts with linear slope parameters for K^+K^-, K^-p, and K^+p modes with (closed symbols) and without (open symbols) interference box.

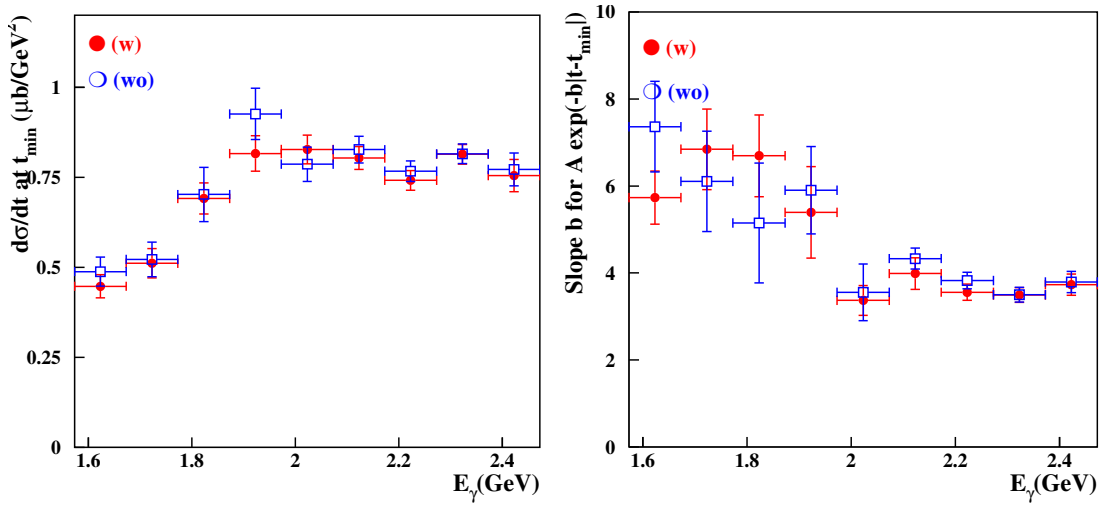

Figure 3.51: Energy dependence of $d\sigma/dt|_{t=t_{\min}}$ with varying slope parameter with/without the interference box.

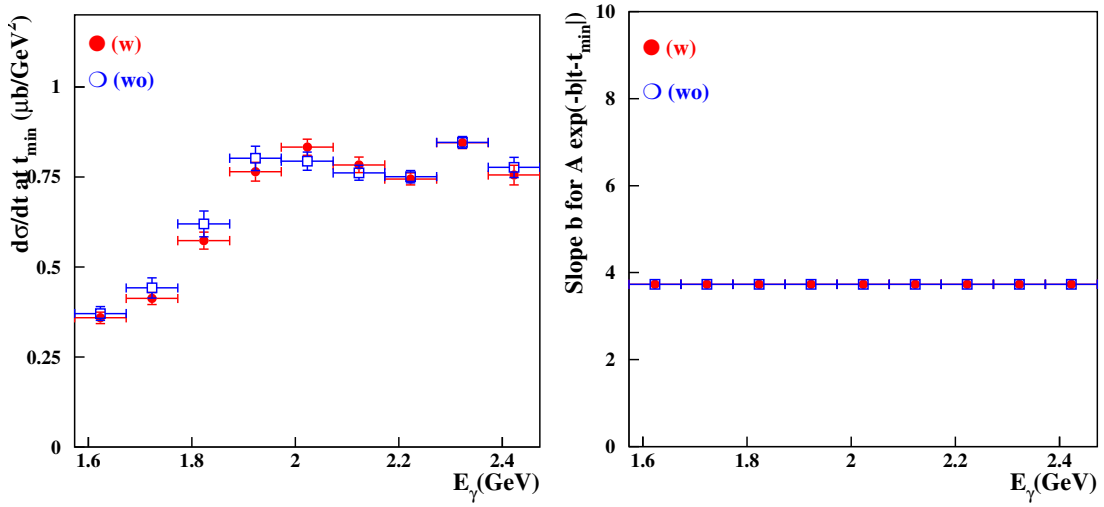

Figure 3.52: Energy dependence of $d\sigma/dt|_{t=t_{\min}}$ with a fixed slope $b = -3.67$ with/without the interference box.

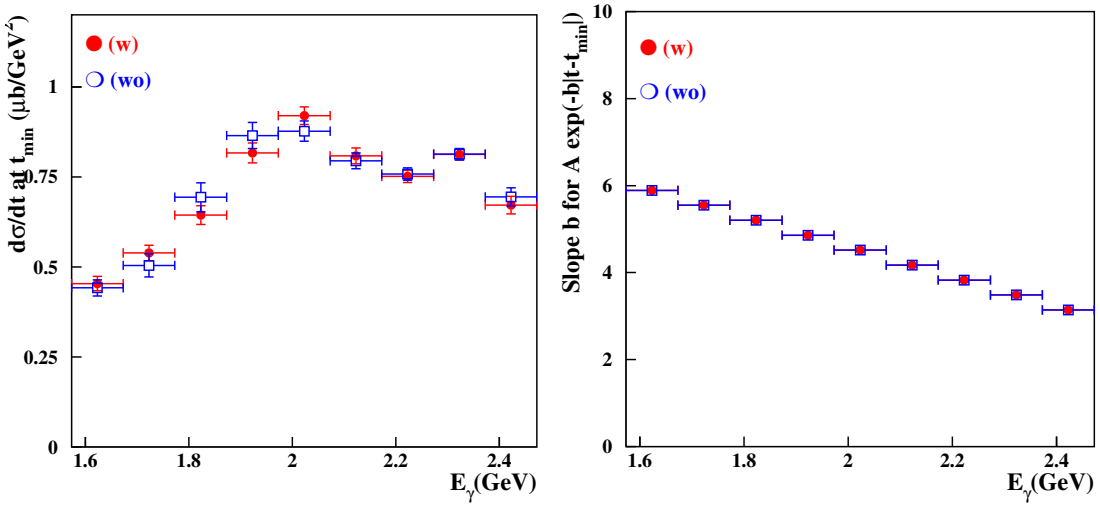

Figure 3.53: Energy dependence of $d\sigma/dt|_{t=t_{\min}}$ with slopes $b(E_\gamma)$ with/without the interference box.

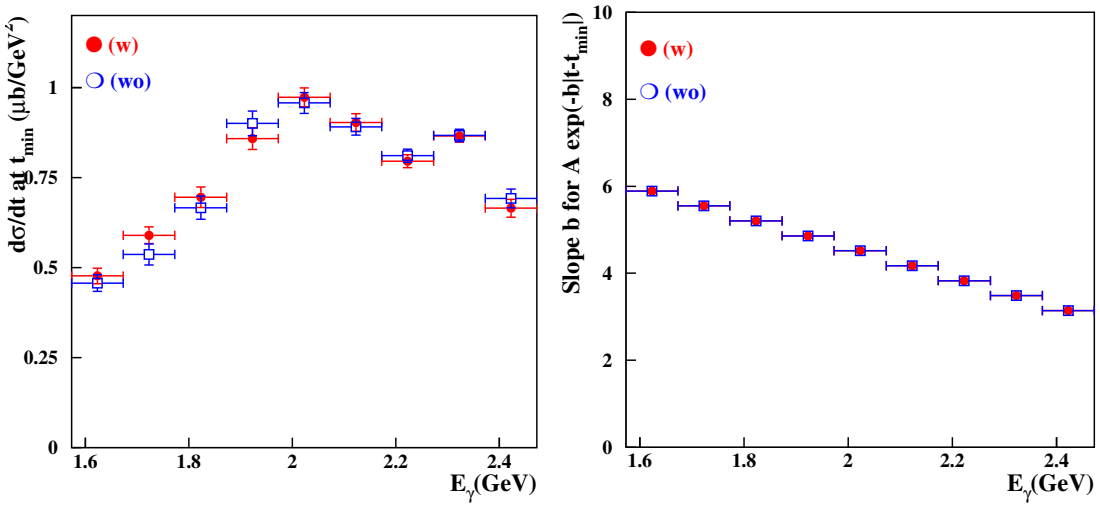

Figure 3.54: Energy dependence of $d\sigma/dt|_{t=t_{\min}}$ with slopes $b(E_\gamma)$ with/without the interference box. This results were obtained with the 'narrow' mass bands.

3.9 Angular Distributions for $\Lambda(1520)$ Photoproduction

Angular distributions for the $\Lambda(1520)$ production at the total c.m. system are displayed in Fig 3.55. The c.m. angle is defined as $\cos^{-1}\theta^{CM} = k_\gamma \cdot k_{\Lambda^*}$, so the forward K^+ production corresponds to $\cos\theta^{CM} = -1$. The backward $\Lambda(1520)$ production is dominant by requiring that a K^+ be detected at forward angles, which corresponds to both the K^+K^- and the K^+p event sets. Background contributions are subtracted from the data based on the fit results with MC templates.

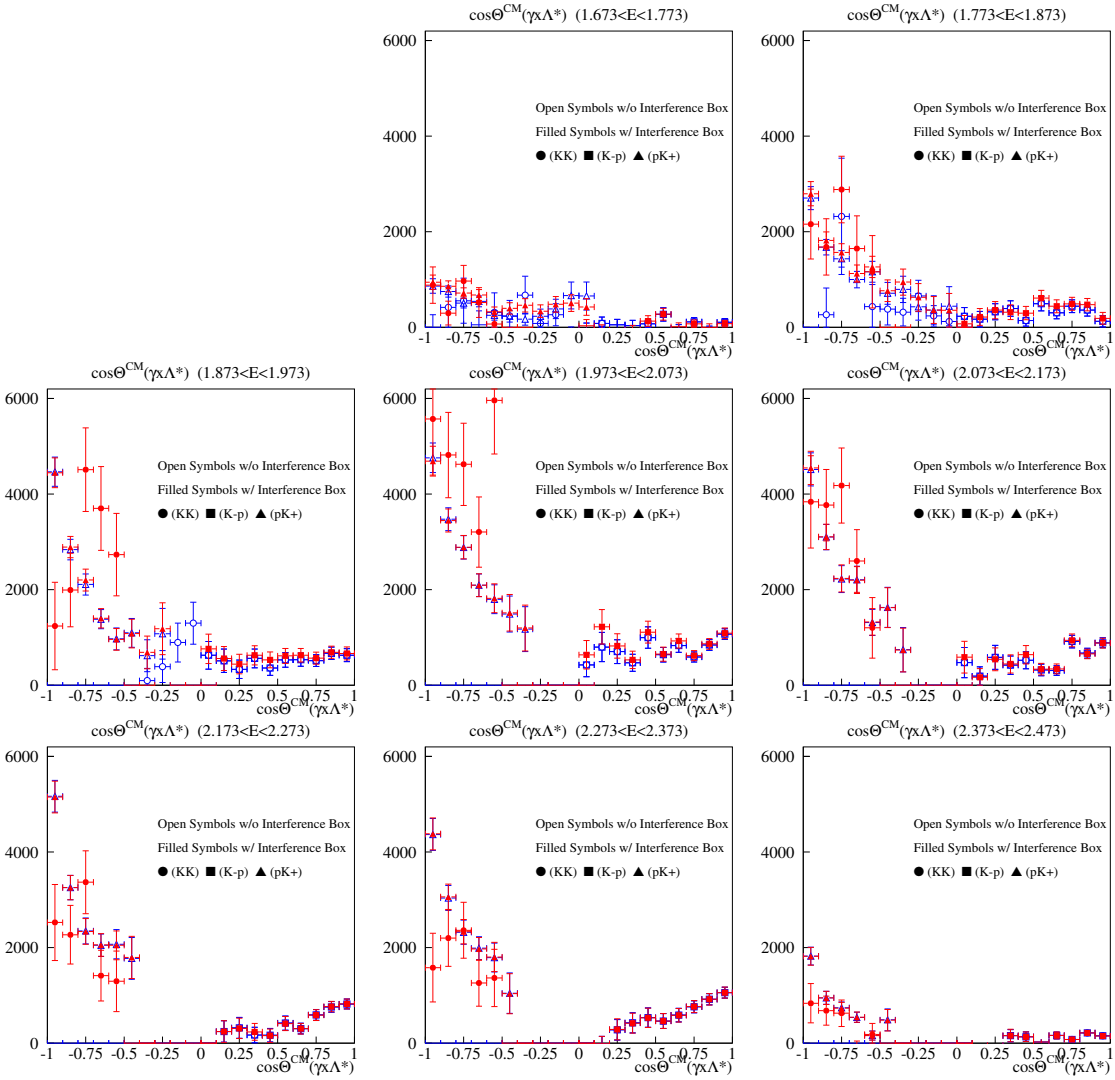

Figure 3.55: Acceptance-corrected angular distributions for $\gamma p \to K^+\Lambda(1520)$. The c.m. angle θ^{CM} is defined as $\cos^{-1} k_\gamma \cdot k_{\Lambda^*}$.

Figure 3.9 shows total cross sections for $\gamma p \to K^+\Lambda(1520)$ in $E_\gamma = 1.673 - 2.473$ GeV. Red circles represents the results with the interference box region, while the blue open circles for the results excluding the box region. The measurement results confirm the previous LEPS results reporting a bump structure at $E_\gamma = 2$ GeV ($\sqrt{s} \approx 2.15$) GeV. The structure proves to be strong at forward and backward K^+ production directions, and still remains at middle angles. The ϕ-$\Lambda(1520)$ interference can appear as the yield difference between the results with and without the interference box region (crossed by the $\Lambda(1520)$ and the ϕ-mass bands). The interference is not as strong as it is statistically significant. There are only a few angle bins in the K^+ forward directions to show a little constructive interference.

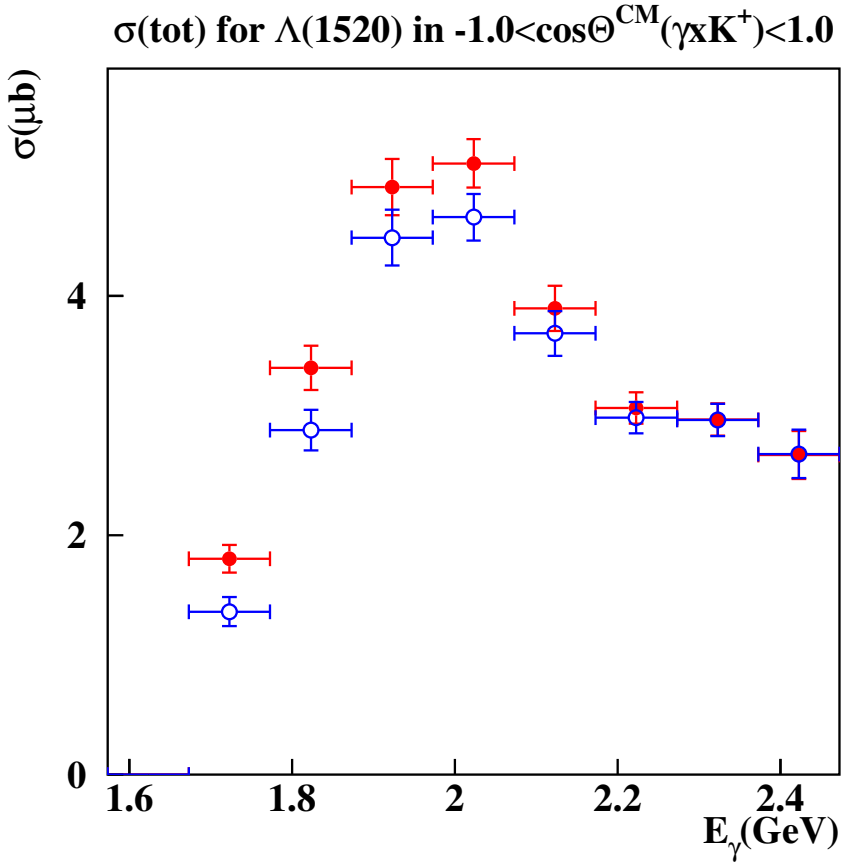

Figure 3.56: Total cross sections for $\gamma p \to K^+\Lambda(1520)$ in $E_\gamma = 1.673 - 2.473$ GeV. Red circles represents the results with the interference box region, while the blue open circles for the results excluding the box region.

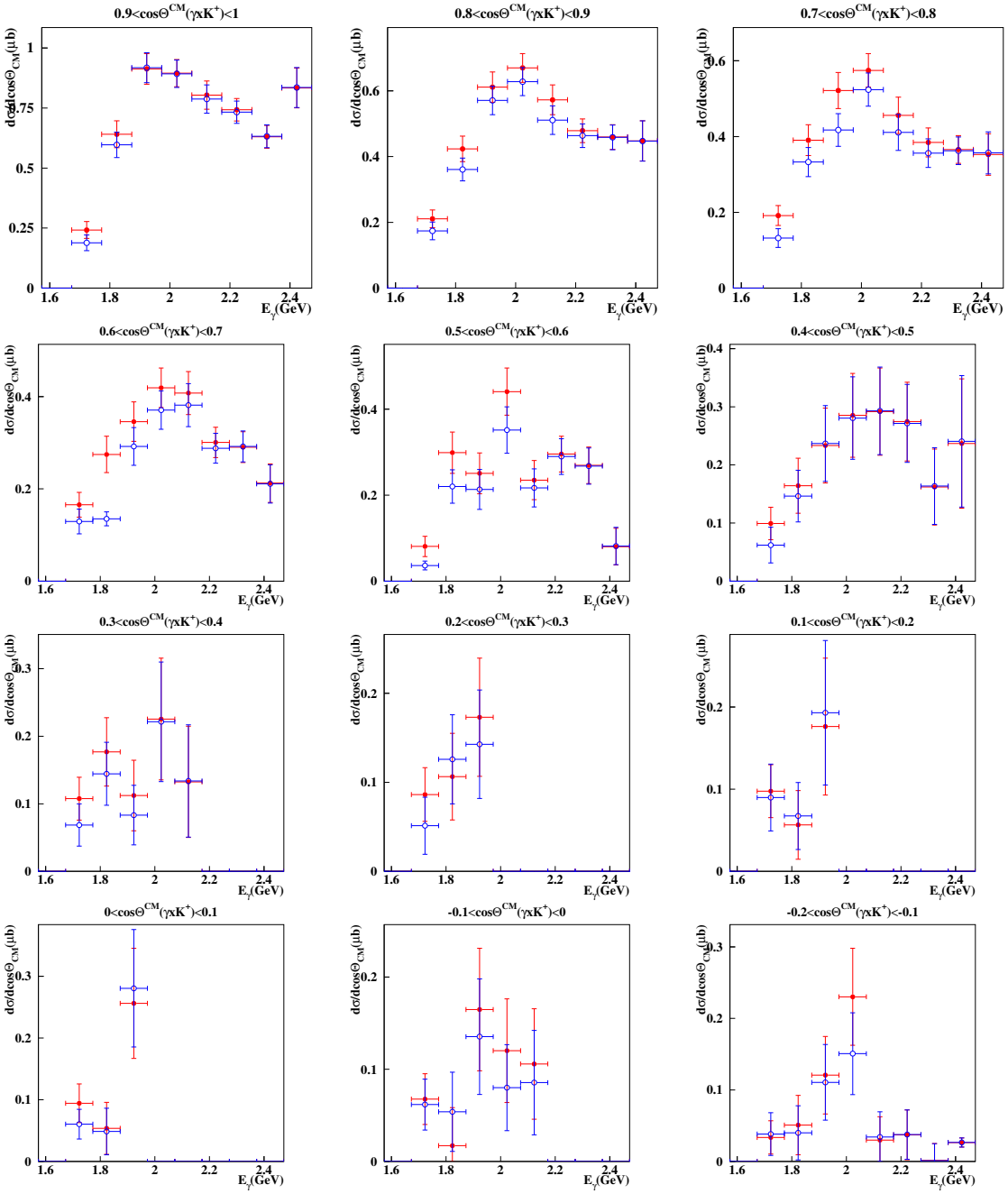

Figure 3.57: Differential cross sections for $\gamma p \to K^+\Lambda(1520)$ in $-0.2 < \cos\theta^{CM} < 1.0$. Red circles represents the results with the interference box region, while the blue open circles for the results excluding the box region.

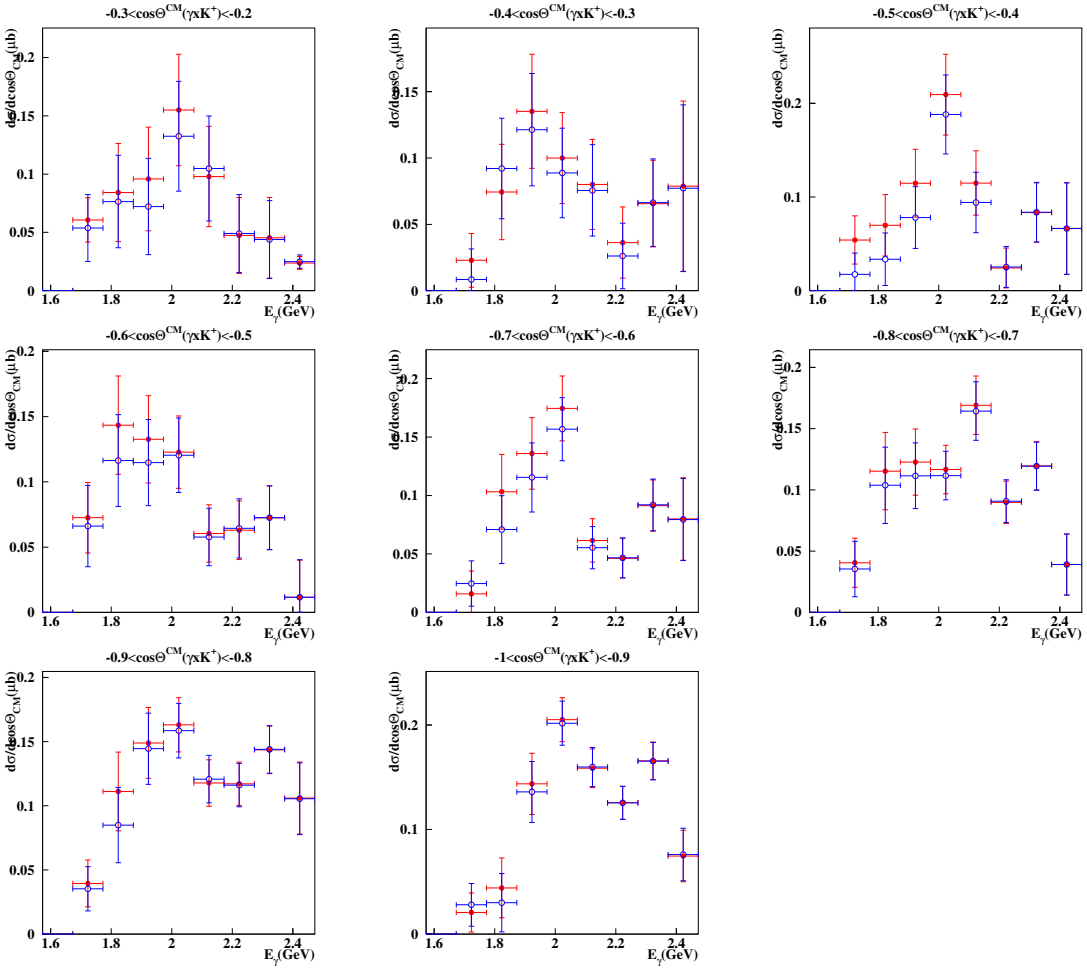

Figure 3.58: Differential cross sections for $\gamma p \to K^+\Lambda(1520)$ in $-1.0 < \cos\theta^{CM} < -0.2$. Red circles represents the results with the interference box region, while the blue open circles for the results excluding the box region.

Chapter 4

Results and Discussion

4.1 Cross Sections for ϕ and $\Lambda(1520)$ Photoproduction

The forward differential cross sections ($\mathrm{d}\sigma/\mathrm{d}t$ at $t = t_{\mathrm{min}}$) for ϕ photoproduction are compared with the previous results from LEPS [1] and SAPHIR [30] near threshold, and from other experiments at higher energies, as shown in Figure 4.1. We reconfirm the existence of the bump structure at $E_\gamma = 2.1$ GeV. The structure appears persistently even with different ϕ-mass windows, different slope parameters, and exclusion of the interference region overlapped with the ϕ and $\Lambda(1520)$ mass bands. The slope parameters of the $|t - t_{\mathrm{min}}|$ distributions turned out to decrease as the photon energy increases. The forward cross sections in Fig 4.1 were obtained from the fit with linearly energy-dependent slope parameters. This indicates that there should be additional highly diffractive process(s) near the threshold, in addition to the known Pomeron-exchange process.

Figure 4.2 shows differential cross sections for $\Lambda(1520)$ photoproduction in the angular bins of $0.7 < \cos\theta^{CM}_{K^+} < 1.0$, which are compared with the previous LEPS results by Kohri *et al.* [31]. While the previous analysis was based on the events with a single K^+ track, this measurement required at least two tracks out of K^-, K^+, and p. As a result, the event statistics in this measurement at forward K^+ angles is much smaller than that from the previous measurement. Albeit low statistics, both results are in a good agreement with each other, which indicate the bump structure near $E_\gamma = 2$ GeV.

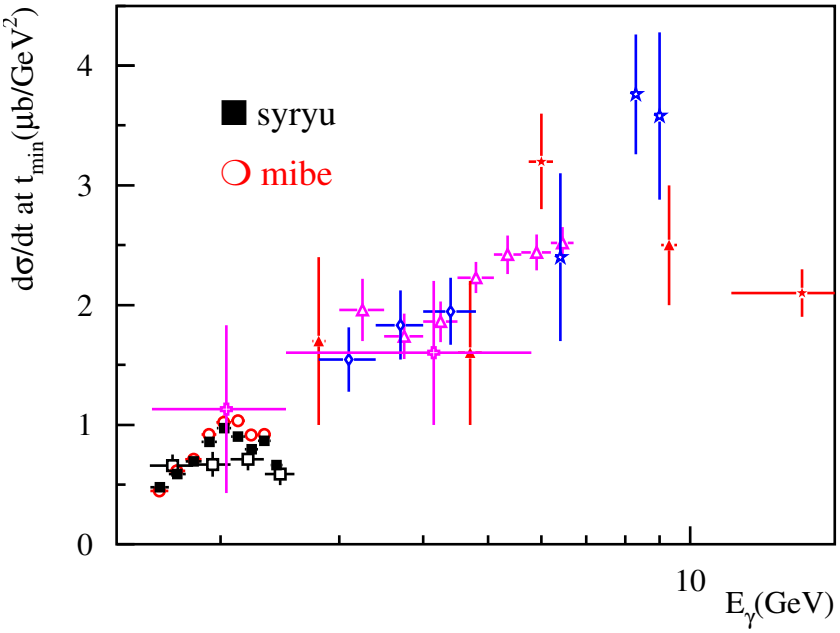

Figure 4.1: The measured forward cross sections for ϕ photoproduction near thereshold are compared with the previous LEPS results [1] and others as well.

The measured cross sections for ϕ (left) and $\Lambda(1520)$ (right) photoproduction in the energy from threshold to 2.473 GeV are shown in Figure 4.3. Red closed circles indicate the results with the interference box region crossed by the ϕ and $\Lambda(1520)$ mass bands, while blue open circles without the box region. For the $\Lambda(1520)$ photoproduction, the total cross sections are plotted in terms of E_γ. Interestingly, both show the bump structure at the same E_γ, which could indicate a strong correlation between ϕ and $\Lambda(1520)$. However, the difference between the cross sections obtained with and without the interference box is not large enough to account for the bump structure.

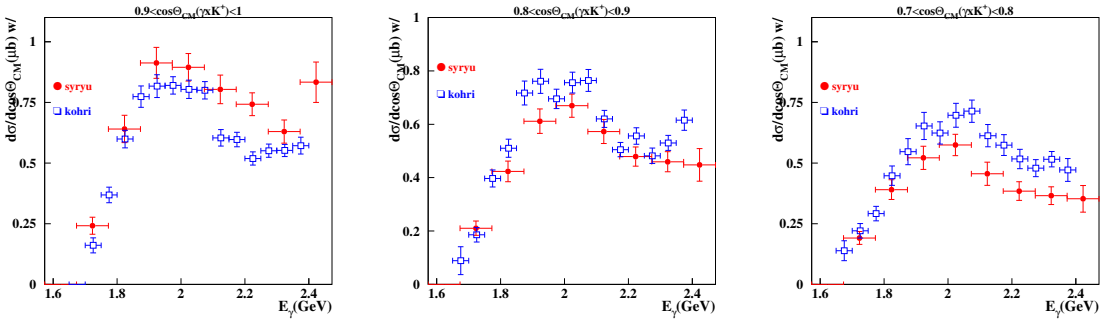

Figure 4.2: The measured differential cross sections for $\Lambda(1520)$ photoproduction are compared with the previous LEPS results [31].

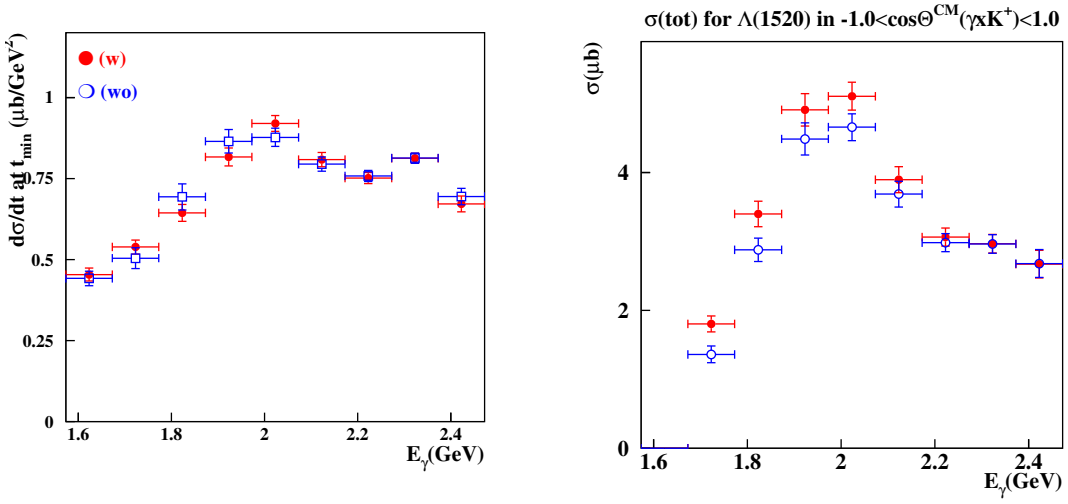

Figure 4.3: The measured cross sections for ϕ and $\Lambda(1520)$ photoproduction processes, respectively.

4.2 Interference Amplitudes between ϕ and $\Lambda(1520)$

The differential cross sections for the ϕ-$\Lambda(1520)$ interference region can be decomposed into

$$\frac{d^2\sigma}{dm_{K^+K^-}dm_{K^-p}} \propto |\mathcal{M}_{\phi} + \mathcal{M}_{\Lambda(1520)} + \mathcal{M}_{\text{others}}|^2 \approx |\mathcal{M}_{\phi} + \mathcal{M}_{\Lambda(1520)}|^2 + |\mathcal{M}_{\text{others}}|^2$$

where $\mathcal{M}_{\phi}$ and $\mathcal{M}_{\Lambda(1520)}$ are the complex amplitudes for ϕ and $\Lambda(1520)$ production processes, respectively. $\mathcal{M}_{\text{others}}$ represents a sum of background processes such as non-resonant K^-K^+p production. We neglected the interference between $\mathcal{M}_{\text{others}}$ and $\phi/\Lambda(1520)$ resonances. This could be a good approximation since Monte Carlo templates without the interference term fit very well with the events in the ϕ and $\Lambda(1520)$ mass bands :

$$\begin{aligned} |\mathcal{M}_{\phi} + \mathcal{M}_{\text{others}}|^2 &\approx |\mathcal{M}_{\phi}|^2 + |\mathcal{M}_{\text{others}}|^2 \\ |\mathcal{M}_{\Lambda(1520)} + \mathcal{M}_{\text{others}}|^2 &\approx |\mathcal{M}_{\Lambda(1520)}|^2 + |\mathcal{M}_{\text{others}}|^2 \end{aligned}$$

The term $\mathcal{M}_{\text{others}}$ contribution was estimated from the fit with Monte Carlo templates.

Events were first excluded in the box region of $|m_{K^+K^-} - m_{\phi}| \leq 4\Gamma_{\phi}$ (ϕ-band) and $|m_{K^-p} - m_{\Lambda(1520)}| \leq 2\Gamma_{\Lambda(1520)}$ ($\Lambda(1520)$-band), where the ϕ-$\Lambda(1520)$ interference may occur. We then extract ϕ and $\Lambda(1520)$ contributions, $|A+B|^2$, by fitting the data in the ϕ and $\Lambda(1520)$ bands without the box region with simulated distributions. The Monte Carlo templates for lineshapes of $m_{K^+K^-}$ and

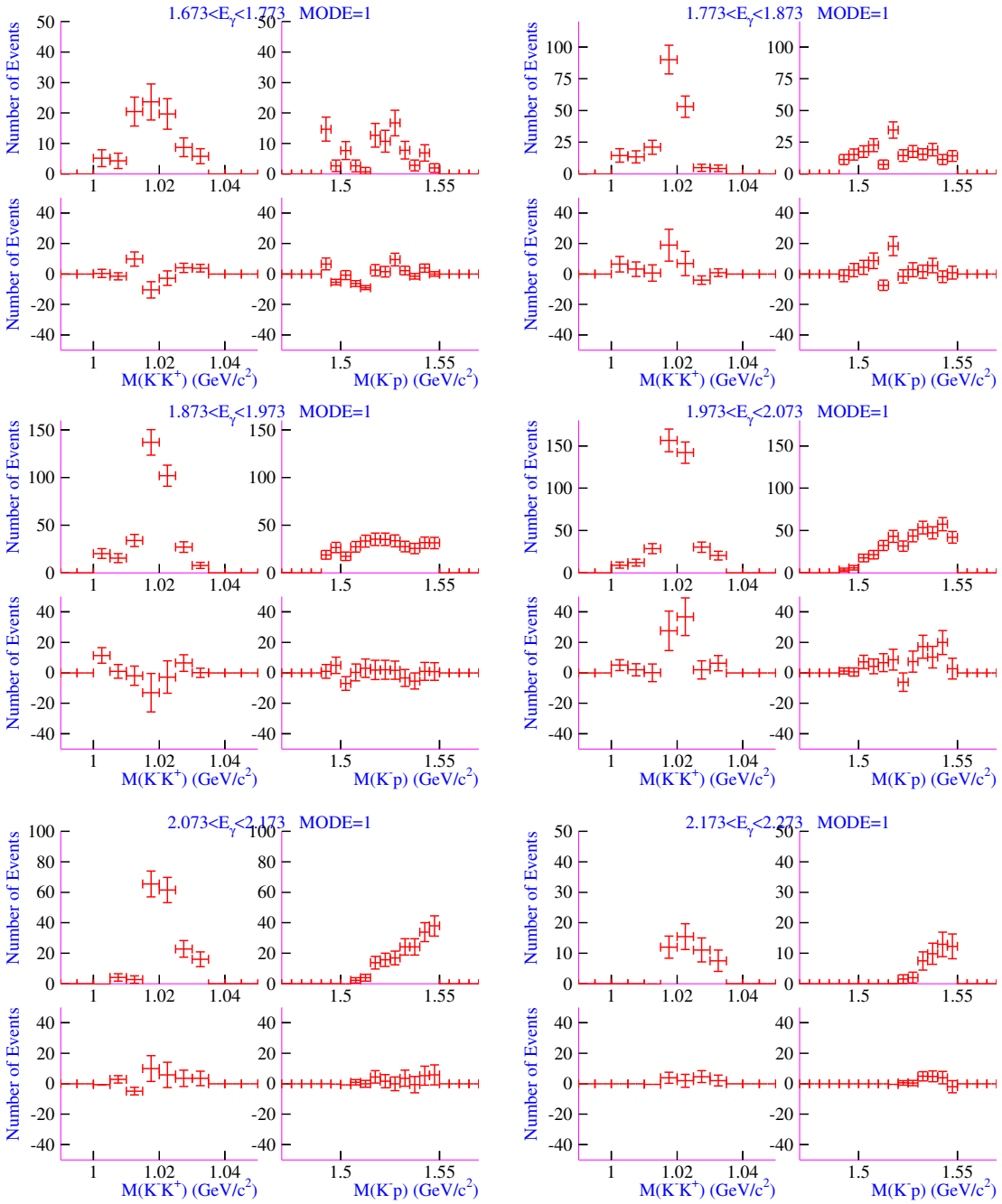

Figure 4.4: The K^-K^+ and K^-p mass distributions for the K^+K^- events (MODE$=1$) in the box region (top two figures in each energy bin) are displayed in the top two figures, while the relative yields compared to the expected yield for no interference are also displayed in the bottom figures.

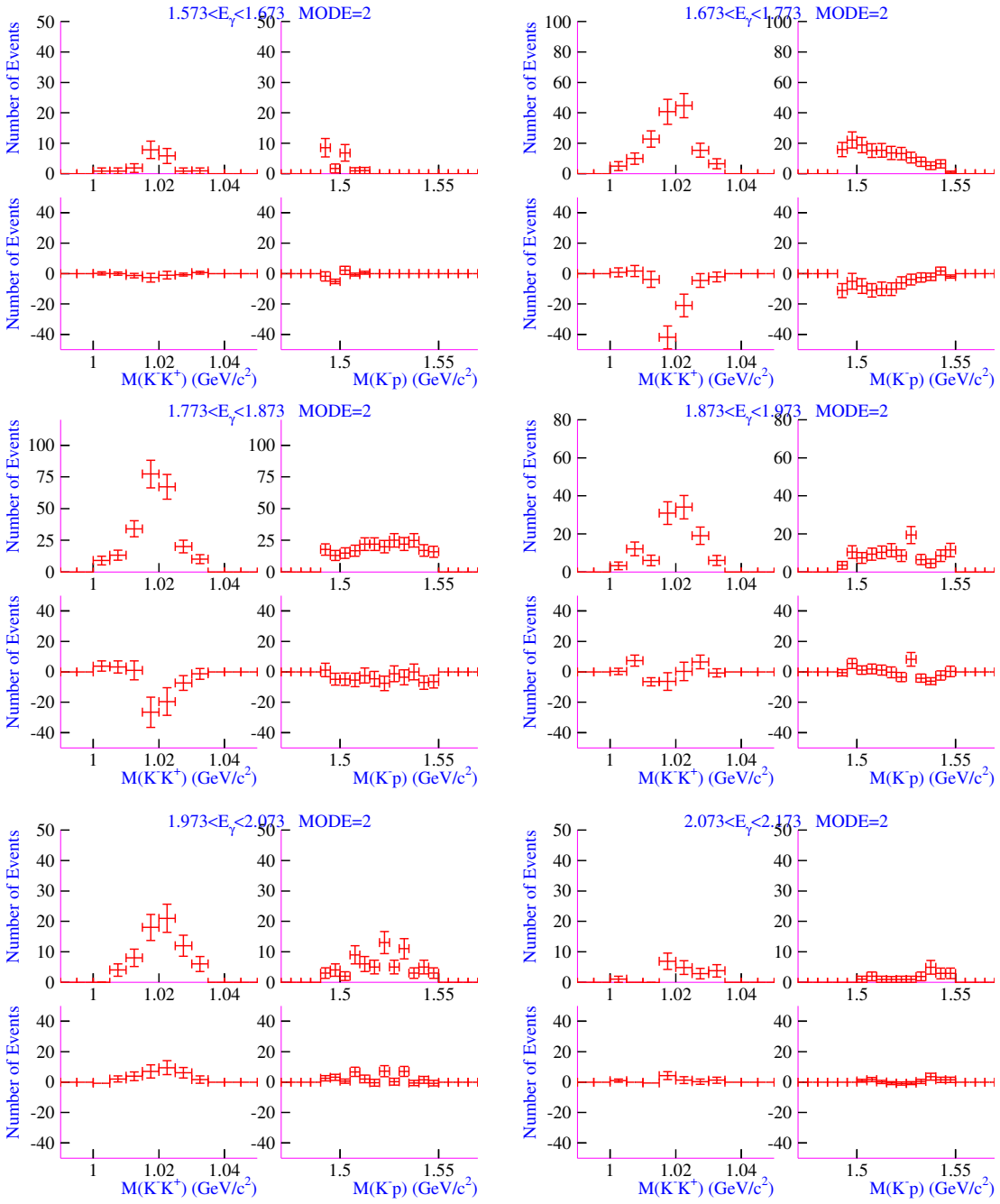

Figure 4.5: The K^-K^+ and K^-p mass distributions for the K^-p events (MODE= 2) in the box region (top two figures in each energy bin) are displayed in the top two figures, while the relative yields compared to the expected yield for no interference are also displayed in the bottom figures.

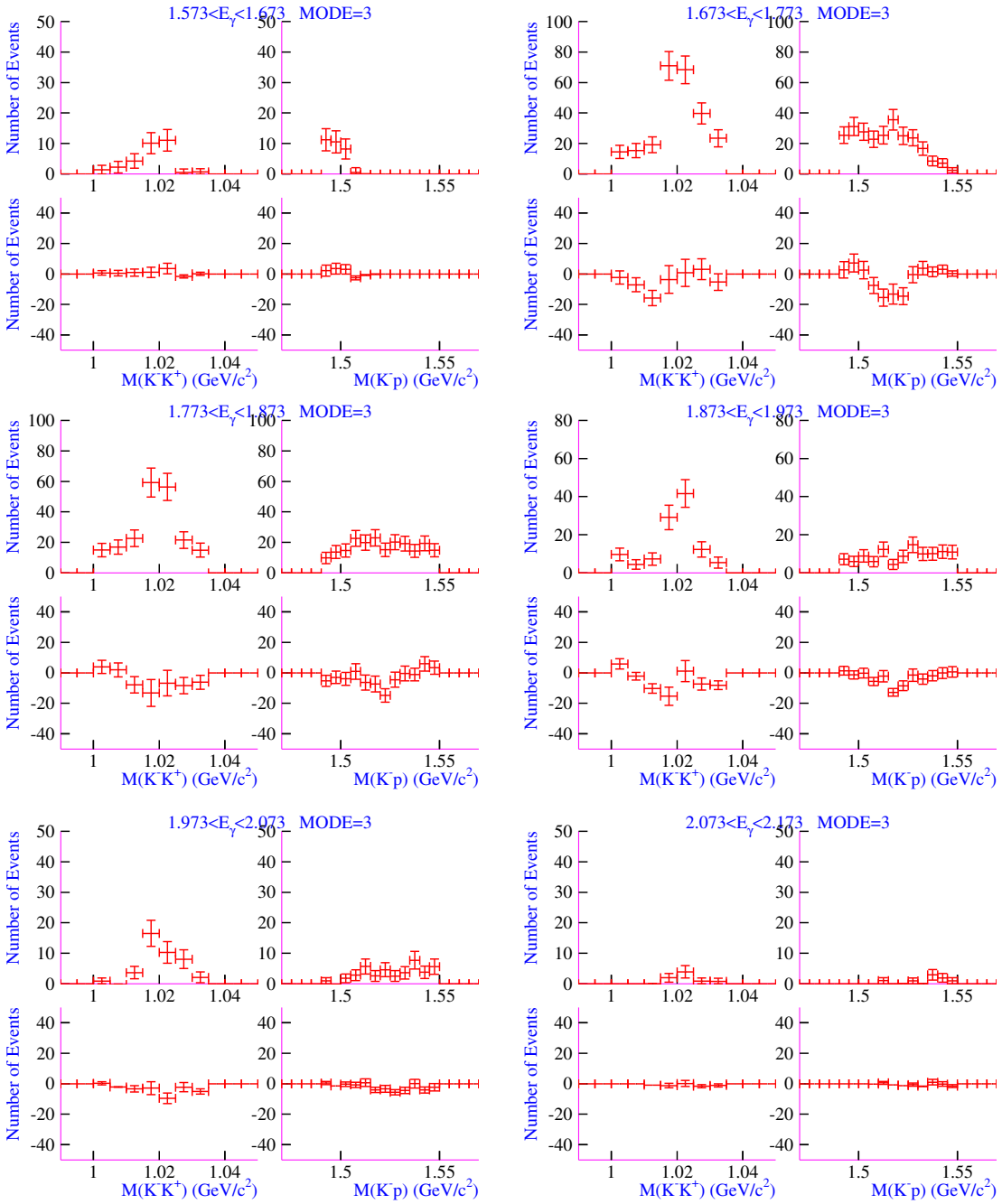

Figure 4.6: The K^-K^+ and K^-p mass distributions for the K^+p events (MODE= 3) in the box region (top two figures in each energy bin) are displayed in the top two figures, while the relative yields compared to the expected yield for no interference are also displayed in the bottom figures.

m_{K^-p} distributions are obtained with the same constraints on the interference box.

The K^-K^+ and K^-p mass distributions for events with K^+K^- (in Fig. 4.4), K^+K^- (in Fig. 4.5) and K^+p (in Fig. 4.6) detected at forward angles in the box region (top two figures in each energy bin) are displayed with only ϕ-$\Lambda(1520)$, where other background contributions were removed. The bottom two figures show the interference yields compared with the maximum interference bounds, respectively.

For the relative phase between the two ϕ and $\Lambda(1520)$ amplitudes, we fit the data with the interference term discussed in Chapter I. The double differential cross section in the interference box is represented as:

$$\begin{aligned}\frac{\mathrm{d}^2\sigma}{\mathrm{d}m_{K^+K^-}\mathrm{d}m_{K^-p}} &\propto |\mathcal{M}_\phi + \mathcal{M}_{\Lambda(1520)}|^2 = \left|\frac{a}{m_\phi^2 - m^2 - im_\phi\Gamma_\phi} + B(m)e^{i\psi}\right|^2, \\ &= \frac{|a|^2}{(m_\phi^2 - m^2)^2 + m_\phi^2\Gamma_\phi^2} + |B(m)|^2 \\ &+ \frac{2(m_\phi^2 - m^2)|aB|\cos\psi + 2\Gamma_\phi m_\phi |aB|\sin\psi}{(m_\phi^2 - m^2)^2 + m_\phi^2\Gamma_\phi^2},\end{aligned}$$

where ψ is the relative phase between a and $B(m)$. The decay width is given by

$$\Gamma_\phi(m) = \Gamma_0 \frac{m_\phi}{m}\left[\frac{q(m)}{q(m_\phi)}\right]^3,$$

where $q(m) = \sqrt{m^2/4 - m_K^2}$ [37]. The last term represents the intereference effect. Here the relative amplitudes a and $B(m)$ are fixed from the simultaneous fit with Monte Carlo templates. $|B(m)|^2$ corresponds to the lineshape of the $\Lambda(1520)$ projected onto the K^+K^- mass axis in the interference box region. As a result, there is only a single parameter, the phase ψ, in the fit.

We first calculated χ^2 values of the fit in terms of the phase ψ from $-\pi/2$ to $\pi/2$, as shown in Figs. 4.7, 4.9, and 4.11 for K^+K^-, K^-p, and K^+p events, respectively. The χ^2 minimization finds the first minimum ψ_1 and also the second minimum ψ_2 (a local minimum) if any. The fit mass range was from 1.005 to 1.035 GeV/c^2 for the wide region (6 data points), and from 1.01 to 1.03 GeV/c^2 for the narrow region (4 data points). The fit was performed in four energy ranges (E3-E6 for K^+K^-, E2-E5 for both K^-p and K^+p events) with the following function:

$$f(m;\psi) = 2|aB(m)|\frac{(m_\phi^2 - m^2)\cos\psi + \Gamma_\phi m_\phi \sin\psi}{(m_\phi^2 - m^2)^2 + m_\phi^2\Gamma_\phi^2},$$

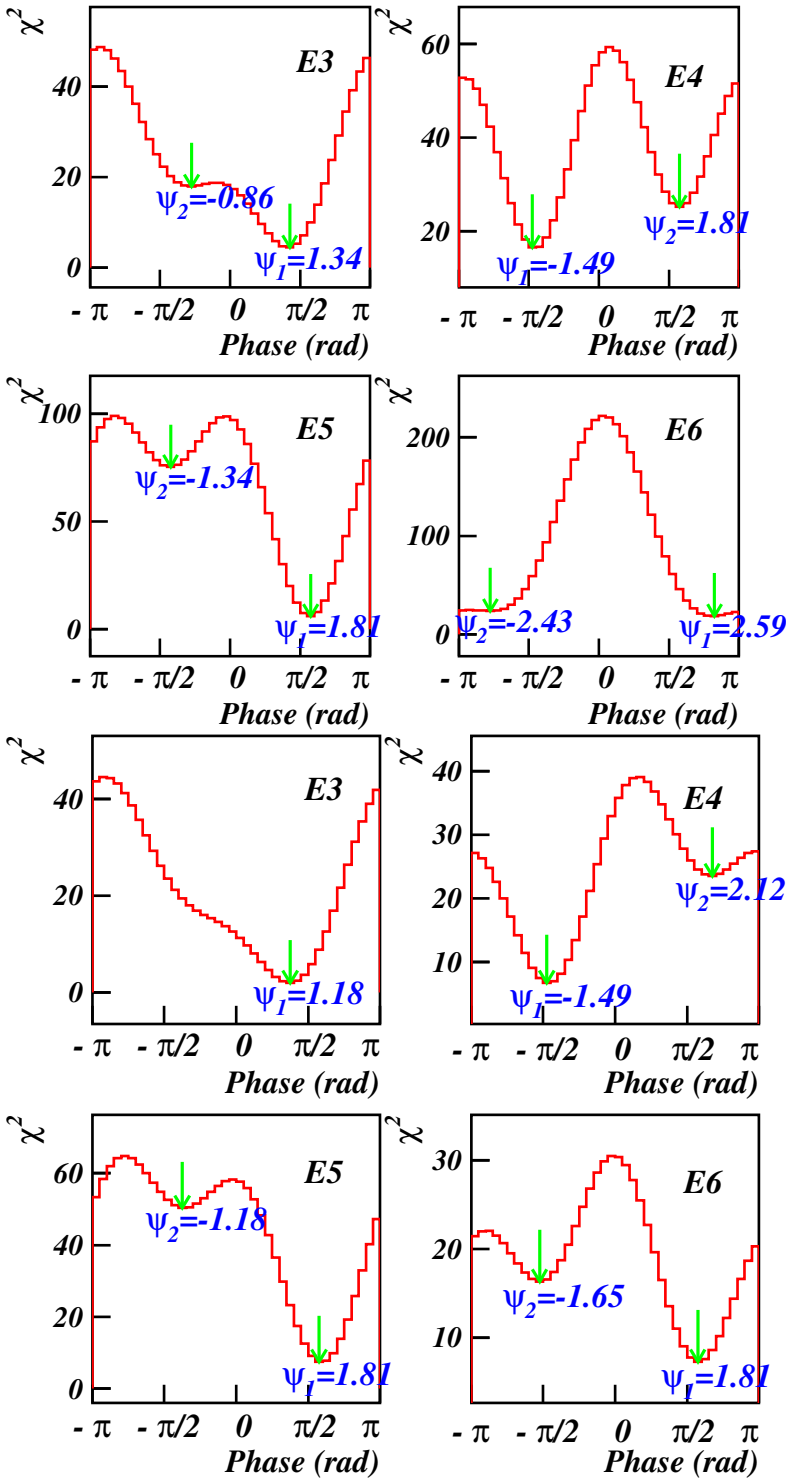

Figure 4.7: χ^2 of the fit for K^+K^- events in terms of the phase ψ from $-\pi/2$ to $\pi/2$ in the wide region (top) and the narrow region (bottom) ψ_1 is the phase at the first minimum and ψ_2 at the second minimum if any.

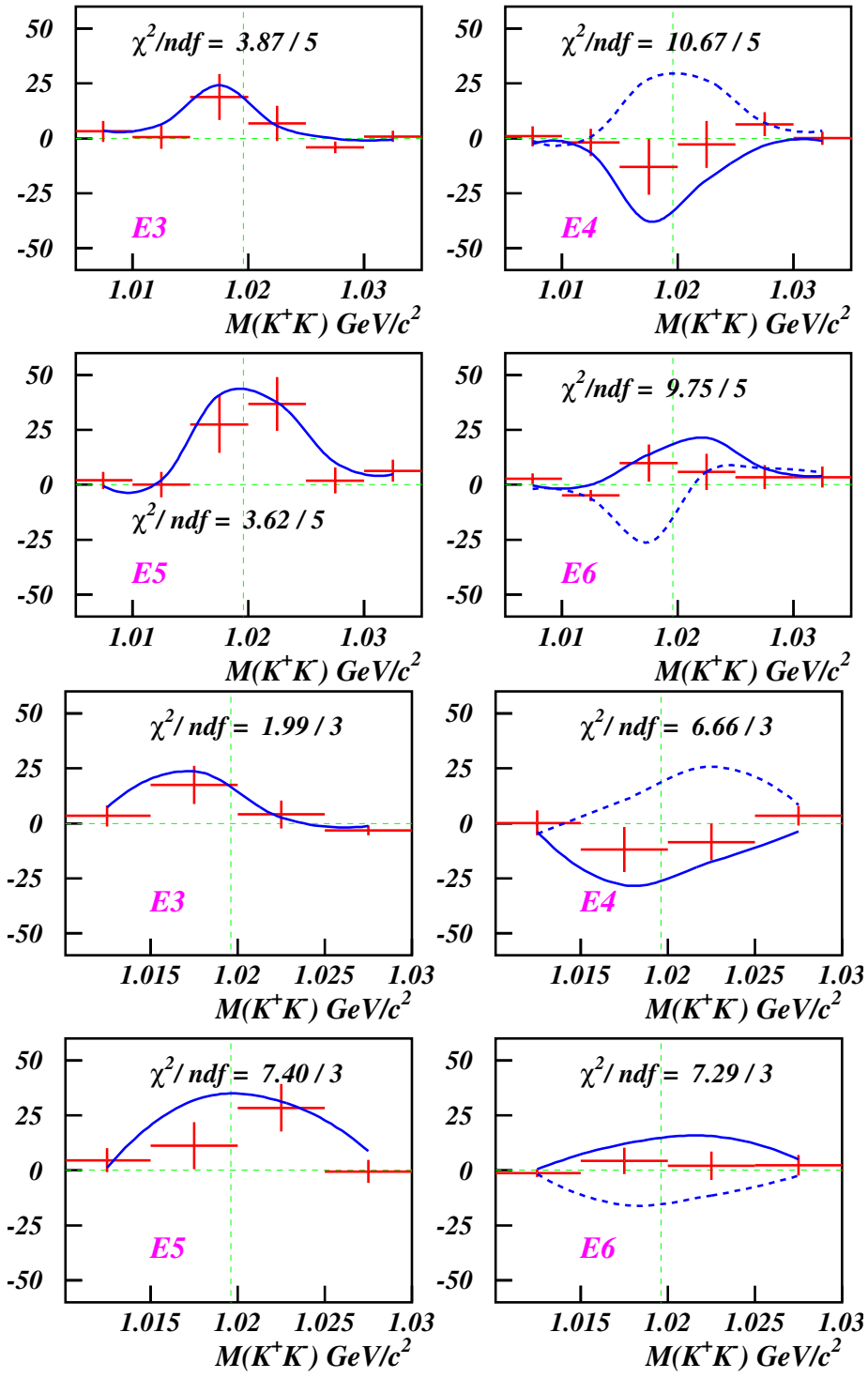

Figure 4.8: Interference yields are overlaid with the interference fit results. Sold lines represent the fit results with the phase ψ_1, while a dashed line depicts the result with the second best-fit phase ψ_2. The wide region results for K^+K^- events are in the top and the narrow region one in the bottom.

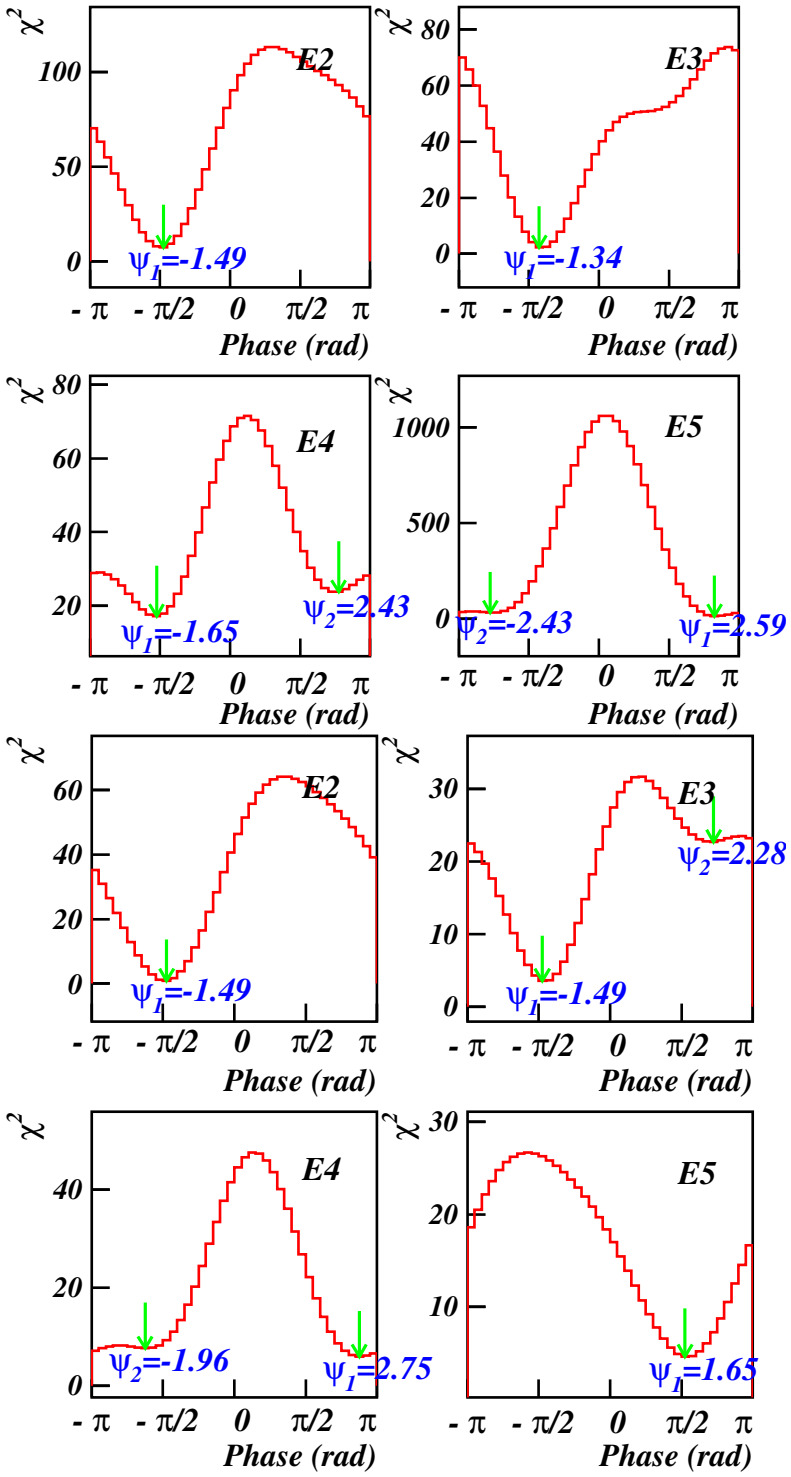

Figure 4.9: χ^2 of the fit for K^-p events in terms of the phase ψ from $-\pi/2$ to $\pi/2$ in the wide region (top) and the narrow region (bottom) ψ_1 is the phase at the first minimum and ψ_2 at the second minimum if any.

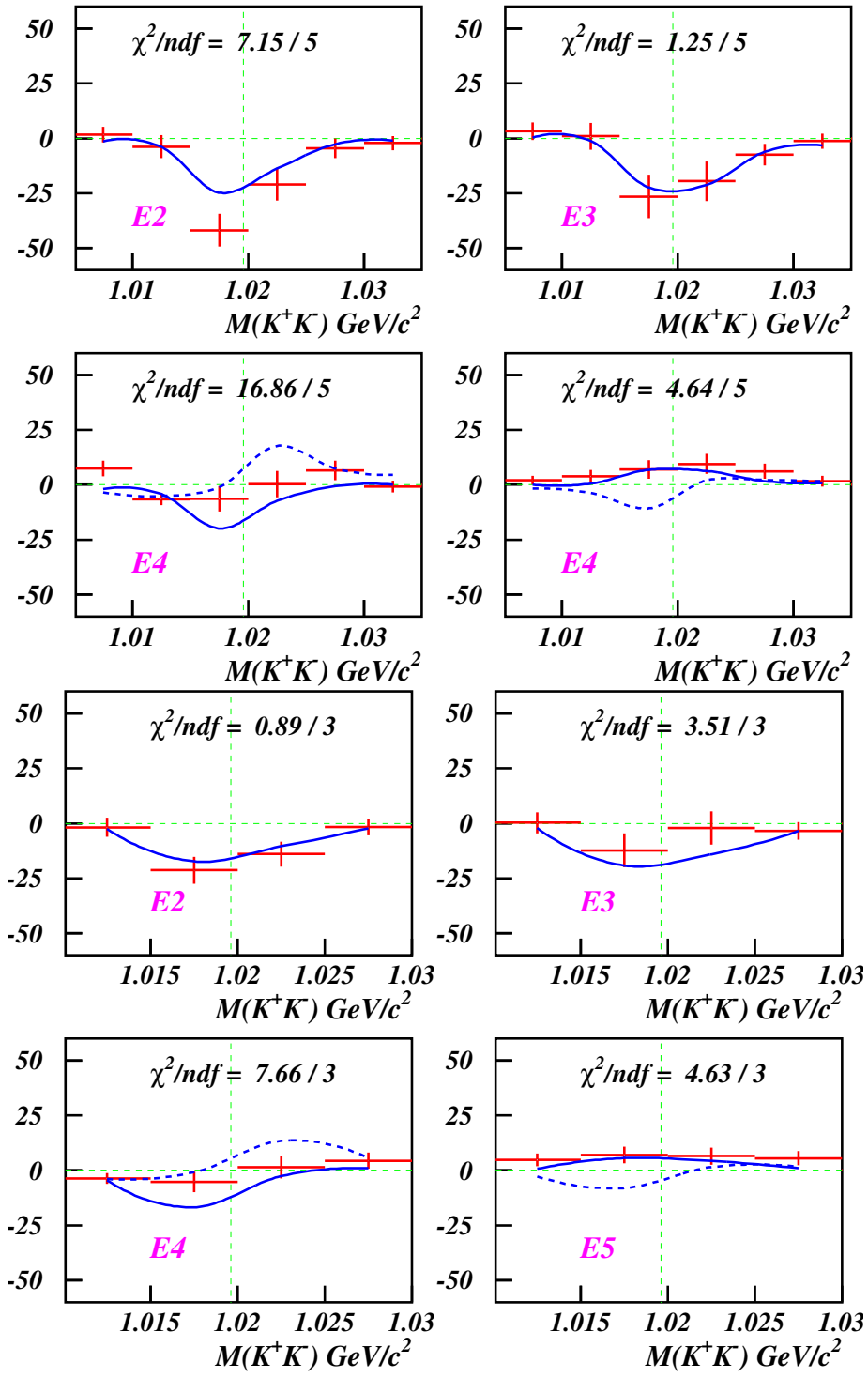

Figure 4.10: Interference yields are overlaid with the interference fit results. Sold lines represent the fit results with the phase ψ_1, while a dashed line depicts the result with the second best-fit phase ψ_2. The wide region results for K^-p events are in the top and the narrow region one in the bottom.

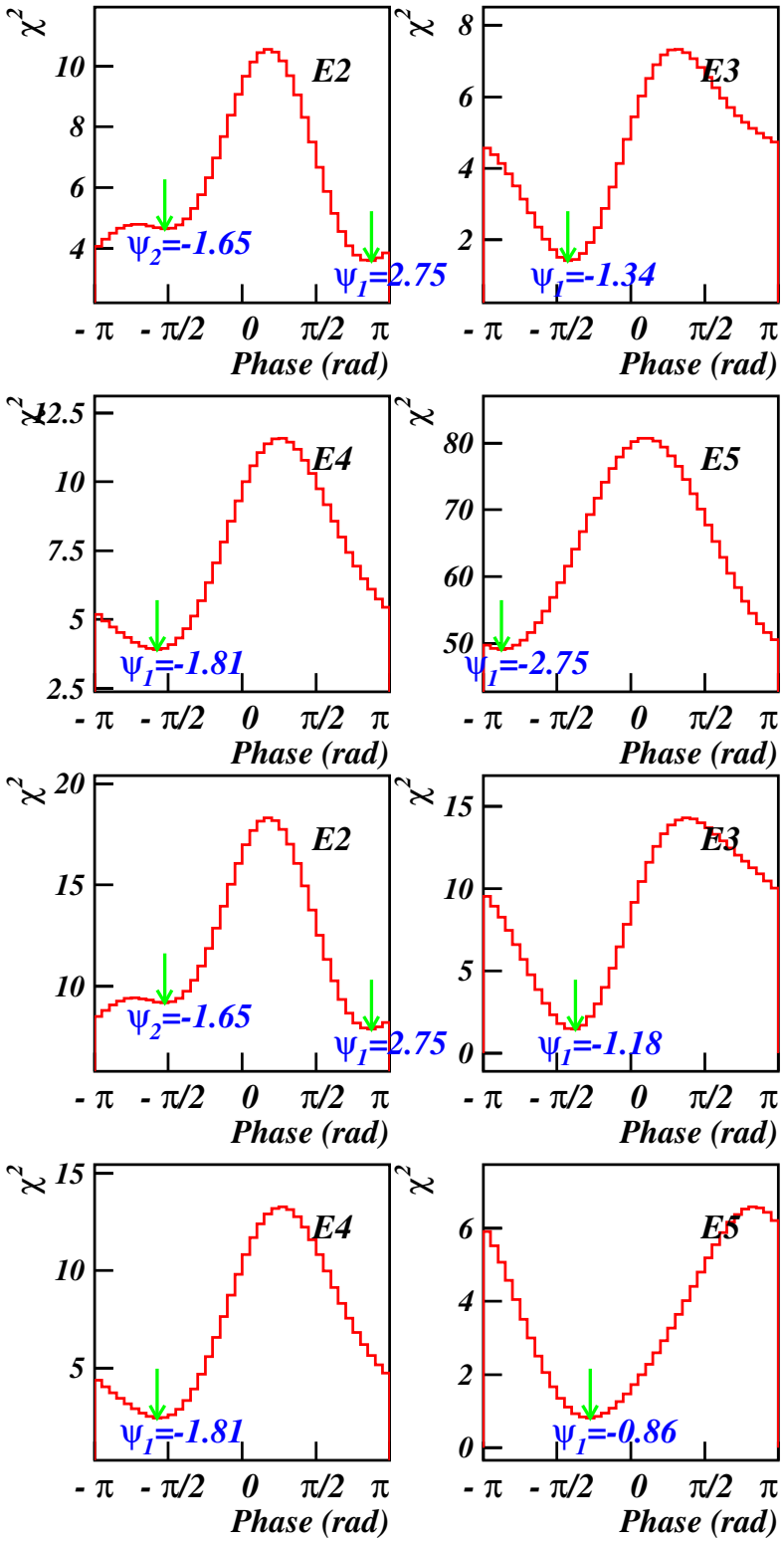

Figure 4.11: Fit χ^2 of K^+p events with the interference term between the ϕ and $\Lambda(1520)$ amplitudes for the wide cross region (top) and the narrow region (bottom).

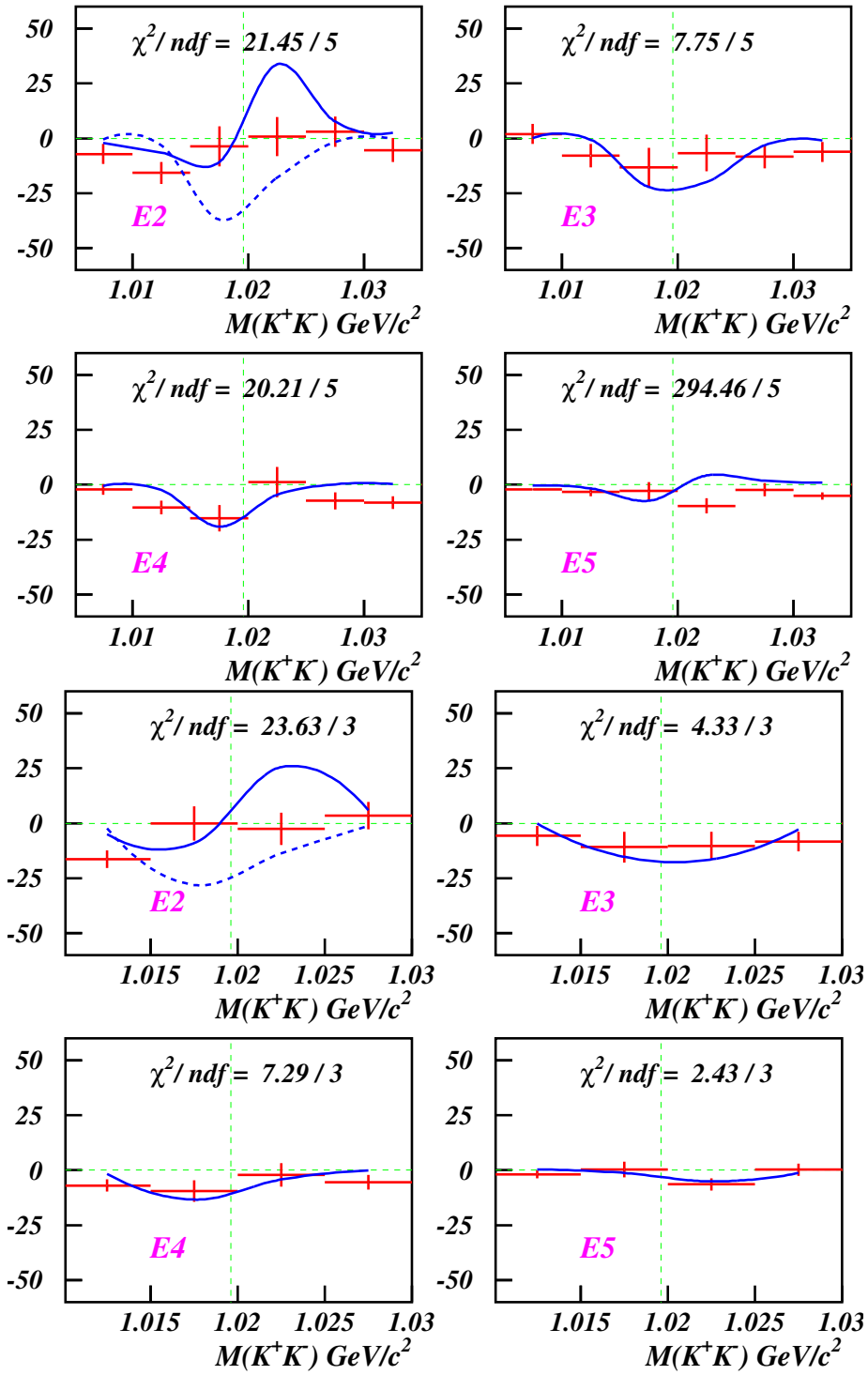

Figure 4.12: Fit results of K^+p events with the interference term between the ϕ and $\Lambda(1520)$ amplitudes for the wide cross region (top) and the narrow region (bottom).

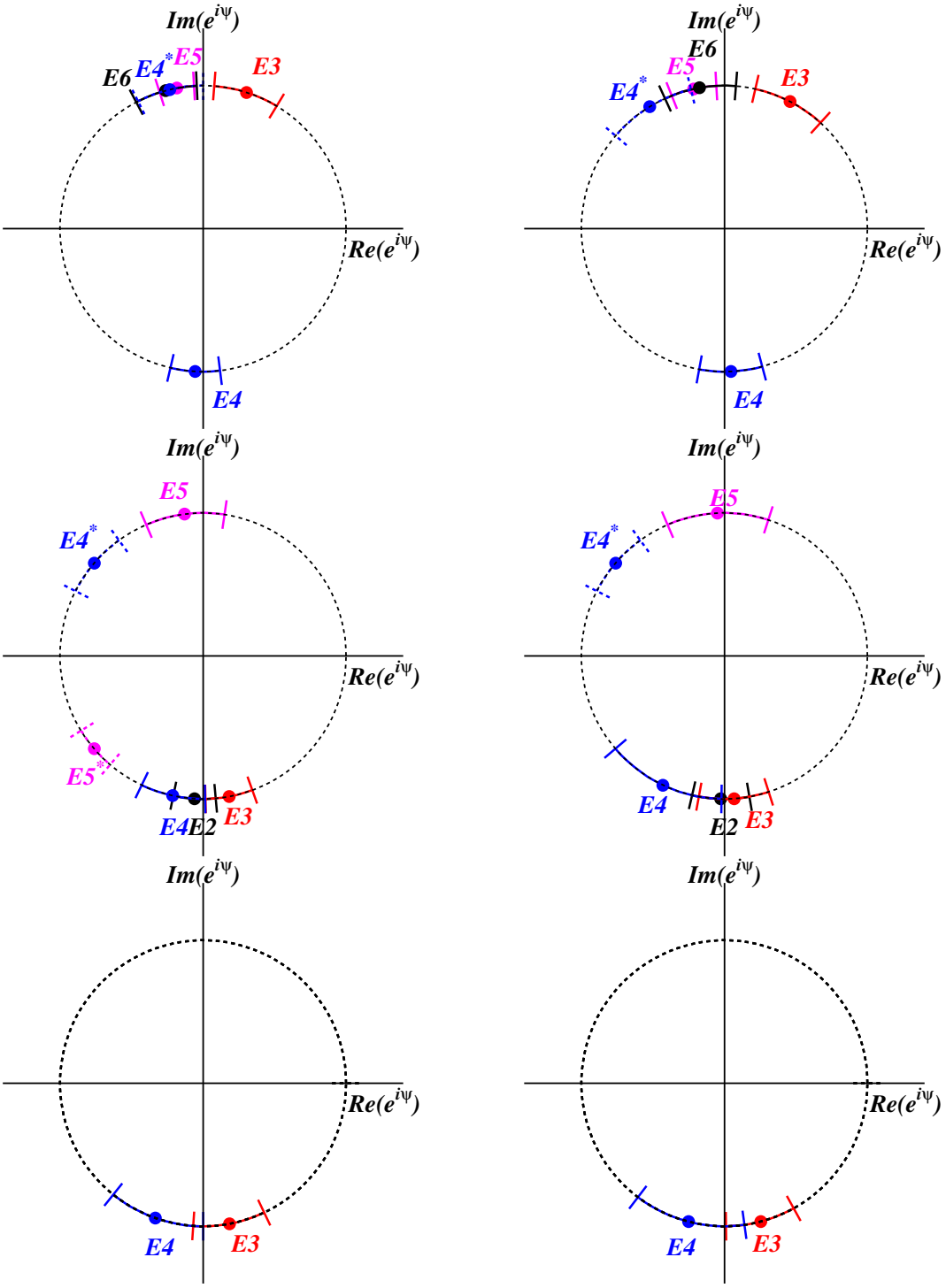

Figure 4.13: Phase angles for K^+K^- (top), K^-p (middle), and K^+p events (bottom) in the wide mass region (left) and the narrow region (right).

Mode	Energy range	ψ_1	ψ_2	$P(\chi^2, 5; \psi_1)$
K^+K^-	E3	$69^o \pm 13^o$		56.8%
	E4	$-86^o \pm 9^o$	$103^o \pm 14^o$	5.8%
	E5	$98^o \pm 7^o$		60.5%
	E6	$141^o \pm 10^o$		8.3%
K^-p	E2	$-92^o \pm 8^o$		21.0%
	E3	$-77^o \pm 9^o$		94.0%
	E4	$-100^o \pm 12^o$	$140^o \pm 14^o$	0.48%
	E5	$145^o \pm 5^o$	$-140^o \pm 9^o$	46.1%
K^+p	E2	$150^o \pm 15^o$	$-94^o \pm 81^o$	0.07%
	E3	$-79^o \pm 15^o$		17.0%
	E4	$-109^o \pm 19^o$		0.11%
	E5	$-162^o \pm 9^o$		0.00%

where m denotes the K^+K^- mass and other are the known constants. The four energy ranges are the intervals where the ϕ-$\Lambda(1520)$ interference may occur: $1.673 < E_\gamma < 1.773$ (E2), $1.773 < E_\gamma < 1.873$ (E3), $1.873 < E_\gamma < 1.973$ (E4), $1.973 < E_\gamma < 2.073$ (E5), and $2.073 < E_\gamma < 2.173$ (E6).

Figure 4.7 shows χ^2 values of the fit for the K^+K^- events. In E4 and E6 two minima with small χ^2 values are found. However, the second minimum gets a higher χ^2 value in the narrow region. For the energy ranges E4 and E6, the fit results with ψ_2 are also dipicted in Figs 4.8 as dashed lines, which largely deviate from the data points. It is clearly seen that there are constructive interferences in E3 and E5, while a destructive interference in E4. For the K^-p events, there are also two energy ranges E4 and E5 where two minima in χ^2 values exist. In the narrow region the second minimum has gone in E5, while it becomes the first minimum in E4. There are clear destructive interferences in the energy ranges E2 and E3. For E4, the two solutions look fit well. The E5 range shows a constructive behavior with a small amplitude. For the K^+p events, there exists the second minimum only in the energy range E2, which stays at unstable points. The amplitudes are relatively small in all the energy ranges.

The fit results for the relative phase are also represented in the complex plane (Re($e^{i\phi}$) and Im($e^{i\phi}$)) in Fig. 4.13. The χ^2 probability ($P(\chi^2)$) was required to exceed 0.1%. The fit results for the wide box (left) and the narrow box (right) are compared, which are in a good agreement with each other. The maximum constructive interference has $\psi = \pi/2$, while the maximum destructive interference does $\psi = -\pi/2$. No interference corresponds to $\psi = 0$ and $\psi = \pi$. From the phase angle plots, it is clearly seen that there is a constructive interference when

K^+K^- go to forward directions, and a desctructive interference for the forward K^-p and K^+p events. Moreover, for the K^+K^- and K^-p events there exist sign changes in the interference term. The asterisk ($*$) energy symbol represents the phase ψ_2 with the second χ^2 minimum. For the K^+K^- events, the phase ψ_2 for the energy range E4 goes to the upper half, which in turn supports a constructive interference. However, for the K^-p events, the E5 phase stays firmly at the upper half, while other energy bins supports destructive interference. It could indicate a change in signs of the interference when K^-p go to forward angles. For the K^+p events, only the E2 point appears in the upper half but it still close to $-\pi$, which corresponds to zero interference.

The interference term for K^+K^- events in the energy range $1.973 < E_\gamma < 2.073$ GeV (E5) was further studied in terms of the K^-p mass around the $\Lambda(1520)$ pole. The phase angles stay near $+\pi/2$ regardless of the K^-p mass, as shown in Fig. 4.14. Since the $\Lambda(1520)$ production amplitude also contains a Breit-Wigner propagator in terms of m_{K^-p}, the lineshape in $m_{K^+K^-}$ changes along the perpendicular axis (m_{K^-p}) with a constant phase ψ.

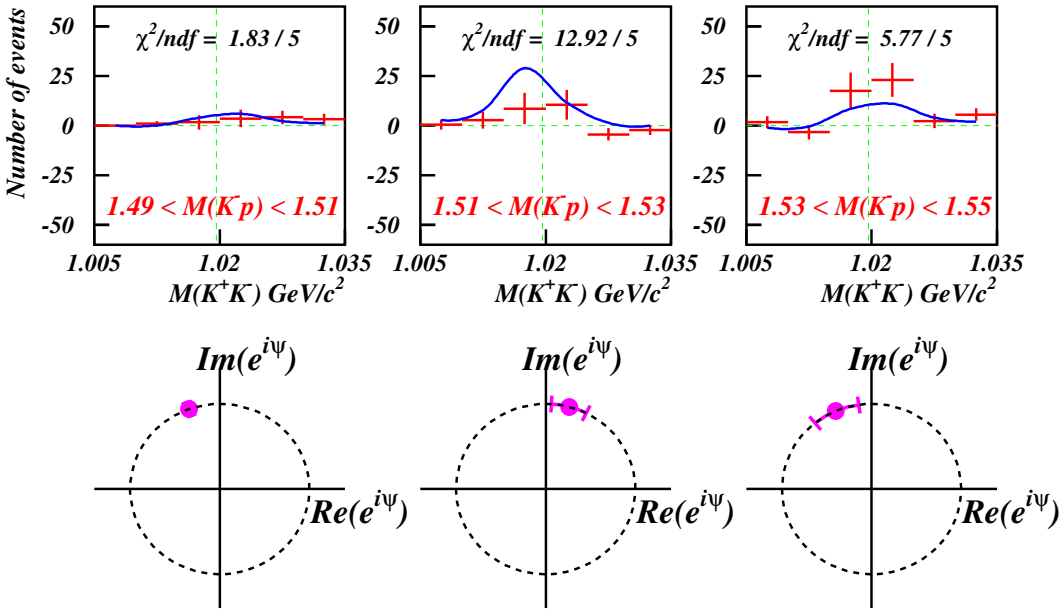

Figure 4.14: Fit results for K^+K^- events in the energy range $1.973 < E_\gamma < 2.073$ GeV (E5) in terms of the K^-p mass regions.

The integrated yields (when K^+K^- pairs are detected at forward angles) in the interference box region (red points) are compared to the predicted levels for the maximum and minimum bounds obtained from the data (blue lines), as showh in Fig. 4.15. The ϕ and $\Lambda(1520)$ yields are calculated by integrating the

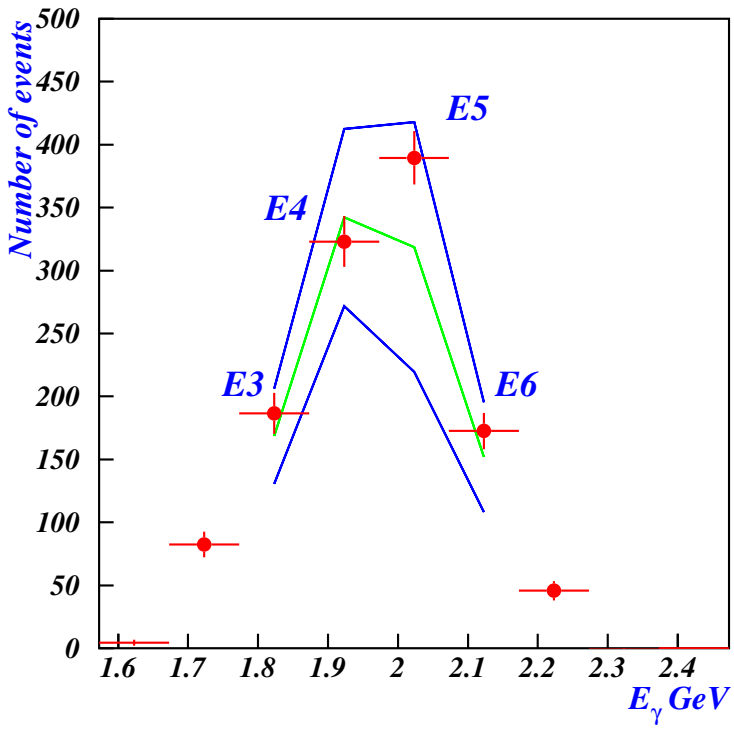

Figure 4.15: The integrated yields (when K^+K^- pairs are detected at forward angles) in the interference box region (red points) are compared to the predicted levels for the maximum and minimum bounds obtained from the ϕ and $\Lambda(1520)$ amplitude measurement (blue lines).

two terms over the mass interval:

$$\int \frac{|a|^2}{(m_\phi^2 - m^2)^2 + m_\phi^2 \Gamma_\phi^2} \mathrm{d}m \quad \text{and} \quad \int |B(m)|^2 \mathrm{d}m.$$

The two extreme bounds were obtained assuming the interference term with the maximum constructive interference phase $\psi = \pi/2$ and the maximum destructive interference phase $\psi = -\pi/2$. It should be emphasized that the integrals of the interference term almost reach the maximum bounds in most energy ranges, which is consistent with the relative phase measurement.

4.3 Conclusion

From this measurement

- We reconfirmed that forward differential cross sections for ϕ photoproduction showed a clear bump structure at around $E_\gamma \sim 2$ GeV.
- We first observed the bump structure in the analysis without the ϕ-$\Lambda(1520)$ interference region. The nature of the bump structure still remains unsolved.
- Yet, we have observed a clear ϕ-$\Lambda(1520)$ interference in the energy ranges from 1.673 to 2.173 GeV. From the fit with the interference amplitude term, the relative phase measurement results suggest a strong constructive interference when K^+K^- pairs are observed at forward angles, while destructive interferences when protons emit at forward angles. There is a change in phase signs for the events with K^-p detected at forward angles.

Based on the measurement results

- Relative phases for forward K^+K^- events are close to $+\pi/2$ except for the energy range of $1.873 < E_\gamma < 1.973$ GeV (E4) with the opposite phase ($\approx -\pi/2$). In the E4 energy range the ϕ-$\Lambda(1520)$ interference box region appears in the central part of the phase space for K^-K^+p final state. For forward K^+K^- events, ϕ is produced at forward, while $\Lambda(1520)$ is produced in the middle angular range.
- Different phases in terms of the event mode (forward K^+K^-, K^-p and K^+p events) might come from different kinematical coverage for photoproduction of ϕ and $\Lambda(1520)$. We could relate the phases near $+\pi/2$ for forward K^+K^- events to the interference between Pomeron exchange amplitude for ϕ and K-exchange amplitude for $\Lambda(1520)$ photoproduction. For forward proton events (K^-p and K^+p), unnatural-parity exchange processes become important in ϕ photoproduction. However, it should be worth noting that the ϕ-$\Lambda(1520)$ interference cannot account for the 2.0-GeV bump structure in forward differential cross sections for ϕ photoproduction.

Chapter 5

Summary

The ϕ-meson production has the unique feature that the gluon dynamics dominates in the reaction process because the process is OZI suppressed due to the dominant $s\bar{s}$ structure of the ϕ-meson, assuming the strangeness component of the proton is small. Because there are no strange s- and u-channel resonances which could couple to the ϕ, only the t-channel exchanges with $J^{PC} = 0^{++}$ and $I = 0$ can contribute. Therefore, ϕ photoproduction is predicted to proceed by the exchange of color singlet gluonic objects such as the Pomeron trajectory which has the same quantum numbers as the vacuum.

The Pomeron is introduced in Regge theory for high-energy hadron scattering and is considered to be dominated by gluon dynamics. Extrapolation from the high-energy region predicts a smooth energy dependence of the cross section down to the threshold energy for the reaction. The LEPS recent observation has shown a strong indication of a bump structure at around $E_\gamma = 2$ GeV. A theoretical explanation is proposed that it could be due to an excitation of missing nucleon resonances with a large $\overline{s}s$ content. However, the bump structure appears only at forward angles. CLAS data (for both K^+K^- and $K^0_L K^0_S$ channels) show that resonance interpretation looks unlikely.

Recent theoretical works relate this to a coupling between the ϕp and $K^+\Lambda(1520)$ channels, since the bump structure appears very close to the threshold of $\Lambda(1520)$ production. Therefore, the structure around $\sqrt{s} \sim 2.1$ GeV has attracted much attention for the nature of ϕ photoproduction mechanism near threshold.

We have measured ϕ photoproduction from protons at SPring-8. Comp-

ton backscattered photons were incident on a 150-mm thick liquid hydrogen target with linear polarization. A large-aperture dipole spectrometer (LEPS) reconstructed charged particles at forward angles. With the 2002/2003 and the 2006/2007 LH_2 data sets from the LEPS, a new analysis on ϕ-$\Lambda(1520)$ photoproduction has been performed using kinematic fits and simultaneous fits on the K^+K^- and K^-p mass spectra with Monte-Carlo templates. This self-consistent analysis made it possible to investigate a possible interference between the ϕ and $\Lambda(1520)$.

It should be emphasized that we have first measured ϕ-$\Lambda(1520)$ interference in $\gamma p \rightarrow K^+K^-p$ reaction near ϕ photoproduction threshold. We reconfirmed that forward differential cross sections for ϕ photoproduction showed a clear bump structure at around $E_\gamma \sim 2$ GeV. We have measured the relative phase angles by building an ampltiude interference function from the Breit-Wigner lineshape for the ϕ and the Monte-Carlo template distributions for the $\Lambda(1520)$ in the kinematic region which the two resonances appear.

We have observed a clear ϕ-$\Lambda(1520)$ interference in the energy ranges from 1.673 to 2.173 GeV. From the fit with the interference amplitude term, the relative phase measurement results suggest a strong constructive interference when K^+K^- pairs are observed at forward angles, while destructive interferences when protons emit at forward angles. There is a change in phase signs for the events with K^-p detected at forward angles.

Bibliography

[1] T. Mibe *et al.* (LEPS Collaboration), Phys. Rev. Lett. **95**, 182001 (2005).

[2] S. Ozaki, A. Hosaka, H. Nagahiro, and O. Scholten, Phys. Rev. **C80**, 035201 (2009).

[3] A. Kishwandhi *et al.*, Phys. Lett. **B691**, 214 (2010).

[4] H-Y. Ryu, A.I. Titov, A. Hosaka, H-Ch. Kim, Prog. Theor. Exp. Phys. 023D03 (2014).

[5] B. Dey *et al.*, Phys. Rev. **C89** 055208 (2014).

[6] K.A. Olive *et al.* (Particle Data Group), Chin. Phys. C, **38**, 090001 (2014).

[7] D. Schildknecht, Acta Physica Polonica B37, 595 (2006).

[8] A. Sibirtsev, H.W. Hammer, U.G. Meissner, and A.W. Thomas, Eur. Phys. J. **A29**, 209 (2006).

[9] A.I. Titov, T.-S. H. Lee, H. Toki, and O. Streltsova, Phys. Rev. **C60**, 035205 (1999).

[10] A.I. Titov, T. Nakano, S. Daté and Y. Ohashi, Mod. Phys. Lett. **A23**, 2301 (2008).

[11] J.-M. Laget, Phys. Lett. **B489**, 313 (2000).

[12] A. Donnachie, H. G. Dosch, P. V. Landshoff and O. Natchmann, Pomeron Physics and QCD, Cambridge University Press (2002).

[13] A. Donnachie and P.V. Landshoff, Nucl. Phys. **B244** 322 (1984).

[14] D.W.G.S. Leith, `SLAC-PUB-1878` (1977).

[15] K. Schilling, P. Seyboth, and G. Wolf, Nucl. Phys. **B15** 397 (1970).

[16] P.J. Gilman *et al.*, Phys. Lett. **31B**, 387 (1970).

[17] H. J. Halpern *et al.*, Phys. Rev. Lett. **29**, 1425 (1972).

[18] H.-J. Behrend *et al.*, Nucl. Phys. **B144**, 22 (1978).

[19] G. McClellan *et al*, Phys. Rev. Lett. **26**, 1593 (1971).

[20] C. Berger *et al.*, Phys. Lett. **39B**, 659 (1972).

[21] J. Ballam *et al.*, Phys. Rev. **D7**, 3150 (1973).

[22] R. M. Egloff *et al.*, Phys. Rev. Lett. **43**, 657 (1979).

[23] J. Busenitz *et al.*, Phys. Rev. **D40**, 1 (1989).

[24] D. P. Barber *et al.*, Phys. Lett. **79B**, 150 (1978).

[25] D. P. Barber *et al.*, Z. Phys. **C12**, 1 (1982).

[26] M. Derrick *et al.* (ZEUS Collaboration), Phys. Lett. **B377** 259 (1996).

[27] J. Breitweg *et al.* (ZEUS Collaboration), Eur. Phys. J. **C14**, 213 (2000).

[28] R. Erbe *et al*. (ABBHHM Collaboration), Phys. Rev. **175**, 1669 (1968).

[29] H. J. Besch *et al.*, Nucl. Phys. **B70**, 257 (1974).

[30] J. Barth *et al*. (SAPHIR Collaboration), Eur. Phys. J. **A17**, 269 (2003).

[31] H. Kohri *et al.* (LEPS Collaboration), Phys. Rev. Lett. **104** 172001 (2010).

[32] A.I. Titov, B. Kampfer, S. Date, and Y.Ohashi, Phys. Rev. **C104** 035206 (2005).

[33] W.C. Chang *et al.*, Phys. Rev. **C82** 015205 (2010).

[34] K. McCormick *et al.* (CLAS Collaboration), Phys. Rev. **C69**, 032203(R) (2004).

[35] H.-Ch. Kim, H.-Y. Ryu, A. Titov, and A. Hosaka, Few-Body Syst. **55**, 787 (2014).

[36] Ya. Azimov, J. Phys. **G37** 023001 (2010).

[37] J.D. Jackson, Nuovo Cim. **34**, 1644 (1964).

[38] S.i. Nam, Private Communications (2015).

[39] A. D'Angelo, O.Bartalini, B. Bellini, P.Levi Sandri D.Moricciani, L.Nicoletti and A. Zucchiatti, Nucl. Instr. Meth. **A455** (2000) 1.

[40] M. Sumihama, *Ph.D dissertation*, Osaka University University, (2003).

[41] J-Y. Chen, *Ph.D dissertation*, National Sun Yat-sen University, (2009).

[42] S.H. Hwang *et al.* (LEPS Collaboration), Phys. Rev. Lett. **108** 092001 (2012).

[43] T. Nakano and H. Toki, in Proceedings of the Interna- tional Workshop on Exciting Physics with New Acceler- ator Facilities, SPring-8, Hyogo, 1997 (World Scientific, Singapore, 1998), p. 48.

[44] A.I. Titov, T. Nakano, S. Date and Y. Ohashi, Mod. Phys. Lett. **A23**, 2301 (2008).

[45] H. Alvensleben *et al.*, Phys. Rev. Lett. **28**, 66 S69 (1972).

[46] R. Anderson *et al.*, Phys. Rev. **D1**, 27 (1970).

[47] R. L. Anderson *et al.*, Phys. Rev. Lett. **30**, 149 (1973).

[48] A. Kiswandhi and S.N. Yang, Phys. Rev. **C86**, 015203 (2012).

[49] R. Muto *et al.*, Phys. Rev. Lett. **98** 042501 (2007).

[50] T. Tabaru *et al.*, Phys. Rev. **C74** 025201 (2006).

[51] R. Erbe *et al.*, Phys. Rev. **175** 1669 (1968).

[52] R.L. Anderson *et al.*, Phys. Rev. **D1** 27 (1970).

[53] M. Effenberger and A. Sibirtsev, Nucl. Phys. **A632** 99 (1998).

[54] T. Ishikawa *et al.*, Phys. Lett. **B608** 215 (2005).

[55] M. Sumihama *et al.*, Phys. Rev. **C73** 035214 (2006).

Appendix A

Properties of the ϕ and the $\Lambda(1520)$

The underlying theory of the strong interactions is Quantum Chromodynamics (QCD). The quark degrees of freedom in QCD are light, strongly interacting fields, called "current quarks", while in the quark model the degrees of freedom, called "constituent quarks" are massive, weakly interacting things. However, both are point-like, spin-1/2 objects with a "color" quantum number.

Mesons are constructed in the quark model out of color singlet pairs of quarks and antiquarks. The intrinsic parity of the $q\overline{q}$ pair is $P = (-1)^{L+1}$, where L is the orbital angular momentum. Therefore, ground state ($L = 0$) mesons have negative parity. If the $q\overline{q}$ are made up with the same flavor, the meson is an eigenstate of the charge conjugation operator. In this case the eigenvalue of the operator can be found to be $C = (-1)^{L+S}$. The mesons are classified in J^{PC} multiplets. The $L = 0$ states are the pseudoscalars (0^{-+}) and the vectors (1^{--}). The orbital excitations $L = 1$ are the scalars (0^{++}), the axial vectors (1^{++} and 1^{+-}), and the tensors (2^{++}). There are nine possible $q\overline{q}$ combinations (for u, d, and s quark flavors) which are grouped into an octet and a singlet. The mass formula for an octet is given by the Gell-Mann-Okubo formula:

$$m^2_{I=0} = \frac{1}{3}(4m^2_{I=1/2} - m^2_{I=1})$$

The states with the same quantum numbers can mix up due to SU(3) breaking, so it is common to group the mesons into nonets rather than octets and singlets.

The two $I = 0$ physical states of the vector nonet can have such an mixing

angle that one of the physical states can be pure or mostly $|s\bar{s}\rangle$:

$$\begin{aligned} |\phi\rangle &= |\omega_1\rangle \sin\theta - |\omega_8\rangle \cos\theta \\ |\omega\rangle &= |\omega_1\rangle \cos\theta + |\omega_8\rangle \sin\theta, \end{aligned}$$

where $|\omega\rangle$ and $|\phi\rangle$ are the physical states, and $|\omega_1\rangle$, $|\omega_8\rangle$ represent the singlet and the octet states, respectively. For ideal mixing, the mixing angle is given by $\tan\theta = 1/\sqrt{2}$ or $\theta = 35.3^o$ ($\sin\theta = 1/\sqrt{3}$, $\cos\theta = \sqrt{2}/\sqrt{3}$), resulting in

$$|\phi\rangle = \frac{1}{\sqrt{3}}(|\omega_1\rangle - \sqrt{2}|\omega_8\rangle), \qquad |\omega\rangle = \frac{1}{\sqrt{3}}(\sqrt{2}|\omega_1\rangle + |\omega_8\rangle).$$

From $|\omega_1\rangle = (\bar{u}u + \bar{d}d + \bar{s}s)/\sqrt{3}$ and $|\omega_8\rangle = (\bar{u}u + \bar{d}d - 2\bar{s}s)/\sqrt{6}$, the physical states can be represented as

$$|\rho^0\rangle = (\bar{u}u - \bar{d}d)/\sqrt{2}, \qquad |\omega\rangle = (\bar{u}u + \bar{d}d)/\sqrt{2}, \qquad |\phi\rangle = \bar{s}s.$$

The lowest vector nonet, $\rho(770)$, $K^*(892)$, $\omega(782)$ and $\phi(1020)$ is indeed ideally mixed; ϕ is practically a pure state of $|s\bar{s}\rangle$ and ω a pure state containing no strange quarks $|(u\bar{u} - d\bar{d})/\sqrt{2}\rangle$, as just shown above.

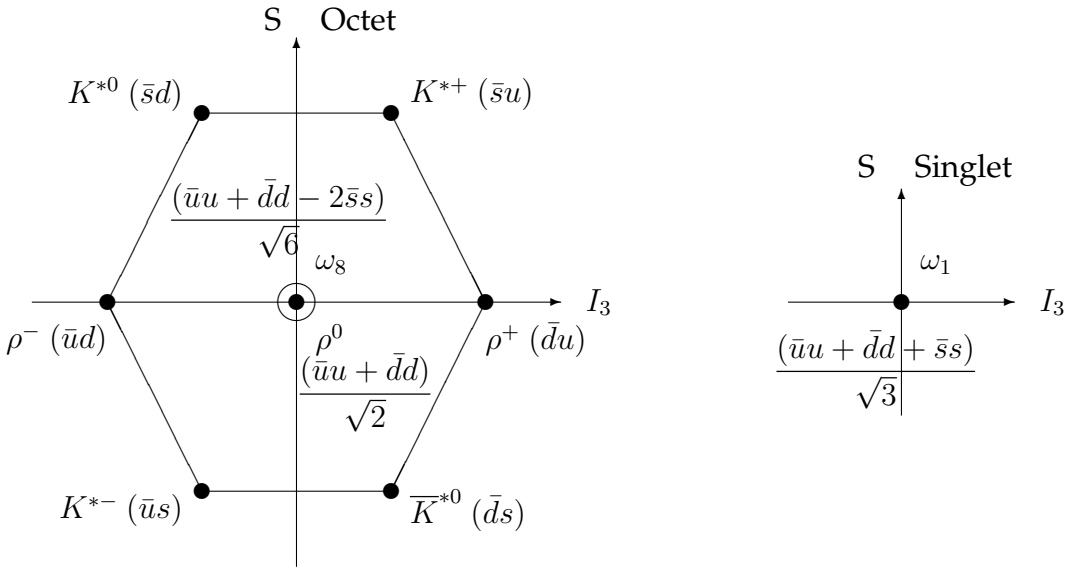

Figure A.1: The nonet of vector mesons.

ϕ **($J^{PC} = 1^{--}$, $s\bar{s}$)**

Mass (MeV)	Γ(MeV)	Br(K^+K^-)	Br($K^0_L K^0_S$)	Br($\rho\pi + \pi^+\pi^-\pi^0$)
1019.461 ± 0.019	4.266 ± 0.031	48.9%	34.2%	15.32%

The ϕ is a neutral isoscalar meson at a mass of 1019.461 MeV with spin, parity and charge conjugation identical to the photon, namely, $J^{PC} = 1^{--}$. The mass difference between two kaons and the ϕ meson yields only

$$m_\phi - 2m_{K^\pm} \approx 32\ \mathrm{MeV},$$

which implies that the decay kaons carry small average momenta of ≈ 127 MeV in the rest frame of the ϕ meson. Little phase space is available for two kaons from the ϕ decay, so the natural width of the ϕ is very small, namely 4.3 MeV.

Baryons are strongly interacting particles with $1/2$ spins. The ground state of this system has all three quarks in a relative $L = 0$ state and positive parity. An approximate flavor $SU(3)$ symmetry requires that baryons made of u, d, and s quarks belong to the multiplets on the right side of

$$\mathbf{3} \otimes \mathbf{3} \otimes \mathbf{3} = \mathbf{10}_S \oplus \mathbf{8}_M \oplus \mathbf{8}_M \oplus \mathbf{1}_A.$$

For the baryons, flavor and spin may be combined in an approximate flavor-spin $SU(6)$. Then the baryons belong to the multiplets on the right side of

$$\mathbf{6} \otimes \mathbf{6} \otimes \mathbf{6} = \mathbf{56}_S \oplus \mathbf{70}_M \oplus \mathbf{70}_M \oplus \mathbf{20}_A,$$

which can be decomposed into flavor $SU(3)$ multiplets as follows:

$$\mathbf{56} = {}^4\mathbf{10} \oplus {}^2\mathbf{8}, \quad \mathbf{70} = {}^2\mathbf{10} \oplus {}^4\mathbf{8} \oplus {}^2\mathbf{8} \oplus {}^2\mathbf{1}, \quad \mathbf{20} = {}^2\mathbf{8} \oplus {}^4\mathbf{1},$$

where the superscript $(2S + 1)$ gives the net spin S of the quarks for each particle in the $SU(3)$ multiplet. The baryons are also classified into bands with the same quantum number N of excitation. Each band consists of a number of super-multiplets specified by $(D, {}^P L_N)$, where D is the dimensionality of the $SU(6)$ representation. The $N = 0$ band contains the nucleon and $\Delta(1232)$ of the $(56, 0_0^+)$ super-multiplet. The $N = 1$ band consists only of the $(70, 1_1^-)$ multiplet and contains the negative-parity baryons with masses below about 1.9 GeV. The $\Lambda(1520)$ belongs to the $N = 1$ band.

The $\Lambda(1520)$ $J^p = 3/2^-$ hyperon is well established in quark model, while from its 10% branching fraction for $\Lambda\pi\pi$ channel, it may have a $\Sigma(1385)\pi$ substructure, as proposed in recent unitarized coupled-channel calculations.

$\Lambda(1520)$ **($J^P = \frac{3}{2}^-$, ($70, 1_1^-$)**

Mass (MeV)	Γ(MeV)	Br($N\overline{K}$)	Br($\Sigma\pi$)	Br($\Lambda\pi\pi$)
1519.5 ± 1.0	15.6 ± 1.0	45%	42%	10%

Appendix B

Fit Results with Monte Carlo Templates

Fit results with Monte-Carlo templates for $\gamma p \to K^+K^-p$ reactions in the narrow mass bands of of $1.01 < m_{K^+K^-} < 1.03$ GeV and $1.50 < m_{K^-p} < 1.54$ GeV for ϕ and $\Lambda(1520)$ are displayed in Fig. B.1, B.2, and B.3. The best-fit lineshapes for the ϕ are overlaid with light blue lines in the K^+K^- and K^-p mass spectra, while those for the $\Lambda(1520)$ are represented as pink lines. Non-resonant K^+K^-p production contributions are shown with blue lines. The green lines describe the contribution from $K^0(896)\Sigma^+$ production.

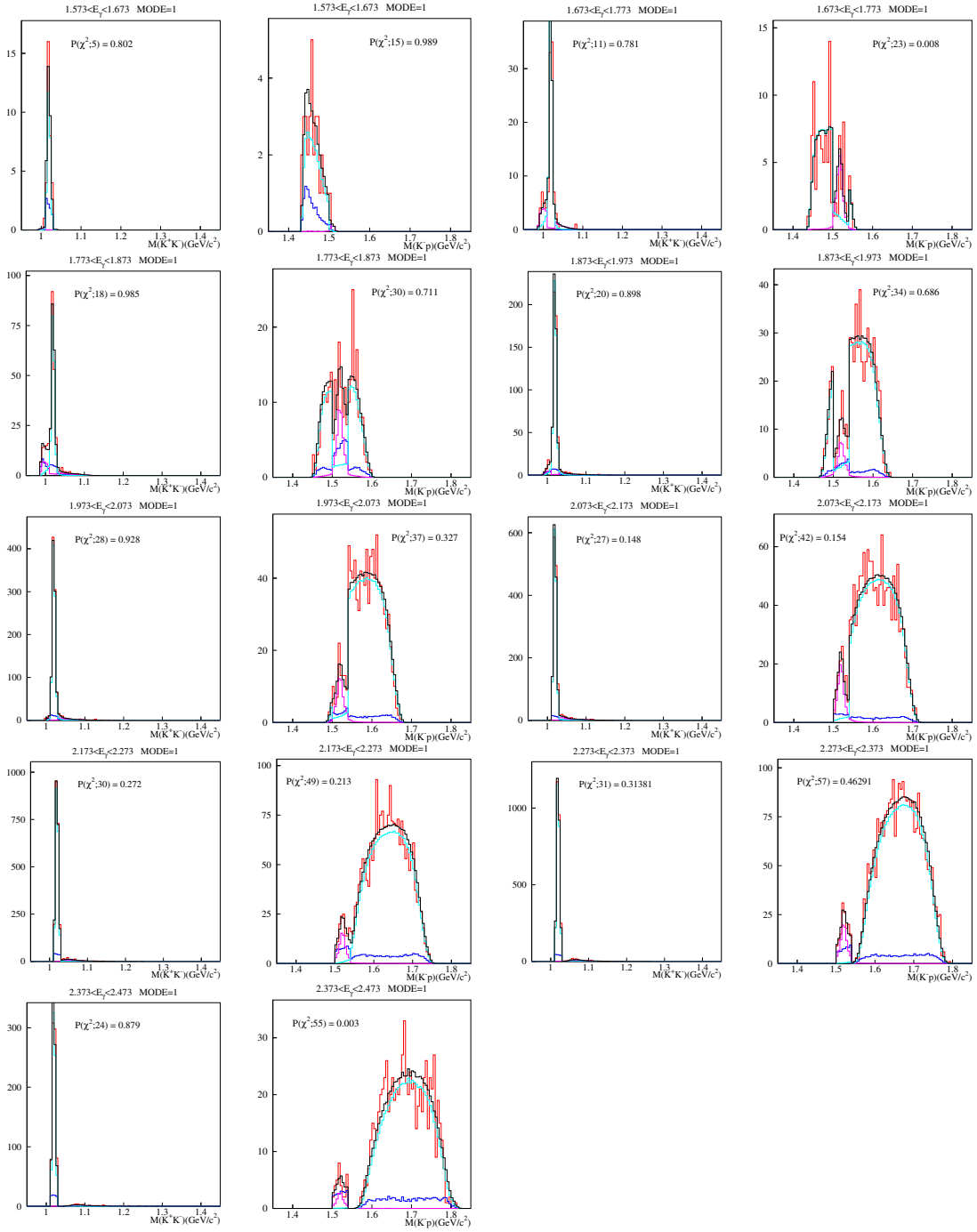

Figure B.1: Fit results with MC templates for $\gamma p \rightarrow K^- K^+(p)$ in the narrow ϕ-$\Lambda(1520)$ bands.

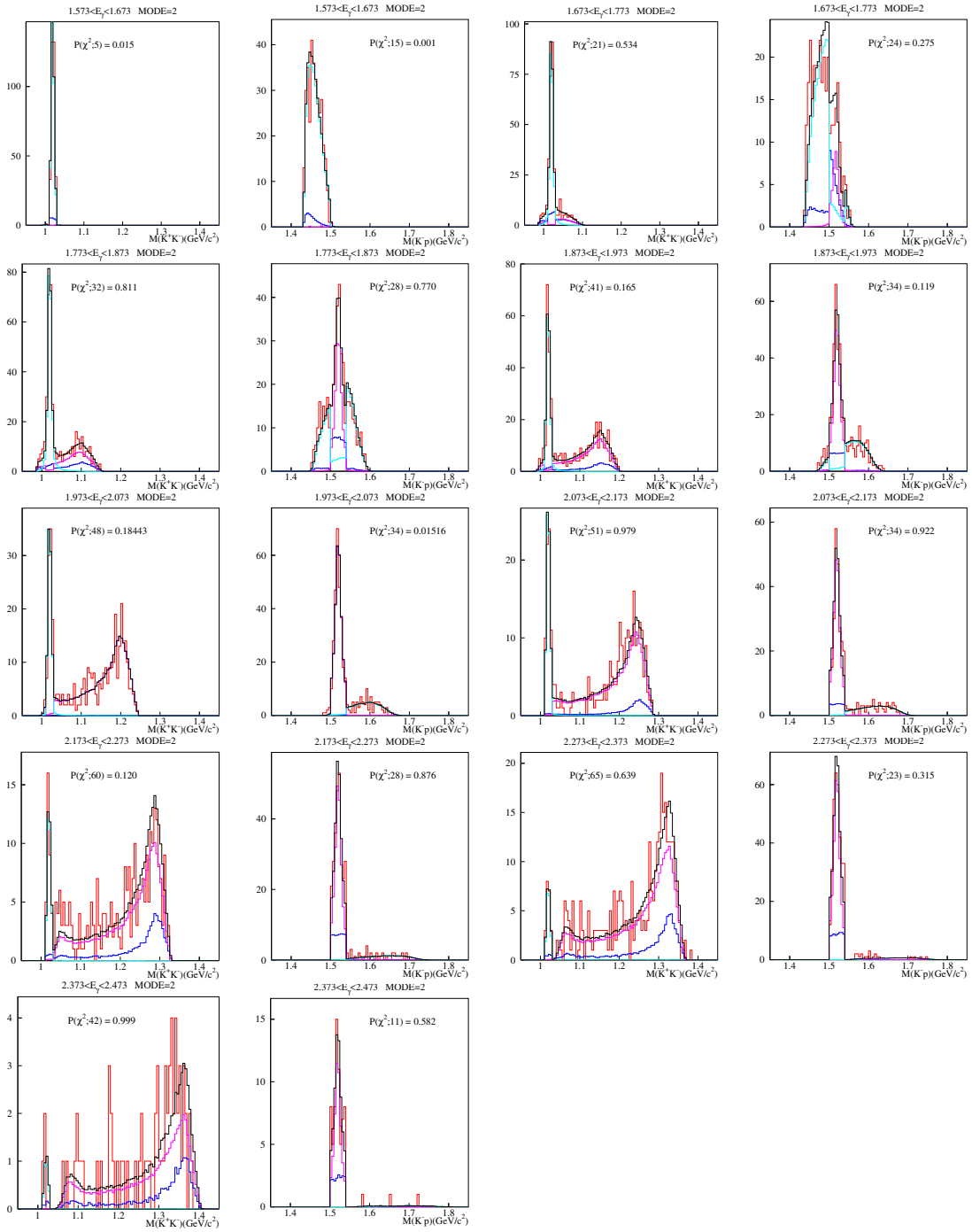

Figure B.2: Fit results with MC templates for $\gamma p \rightarrow K^-(K^+)p$ in the narrow ϕ-$\Lambda(1520)$ bands.

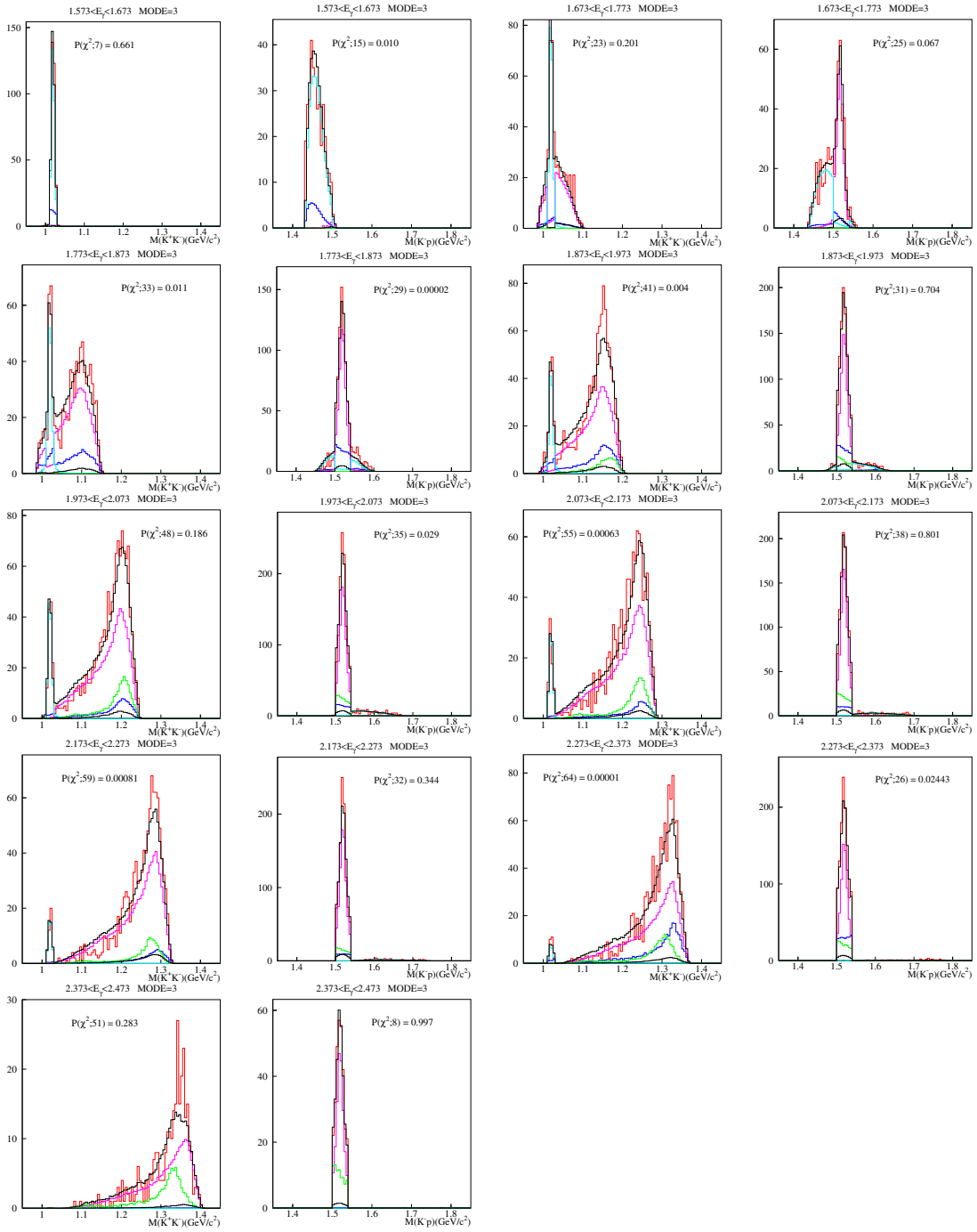

Figure B.3: Fit results with MC templates for $\gamma p \rightarrow (K^-)K^+p$ in the narrow ϕ-$\Lambda(1520)$ bands.

Appendix C

Acceptances and $|t - t_{\min}|$ Distributions

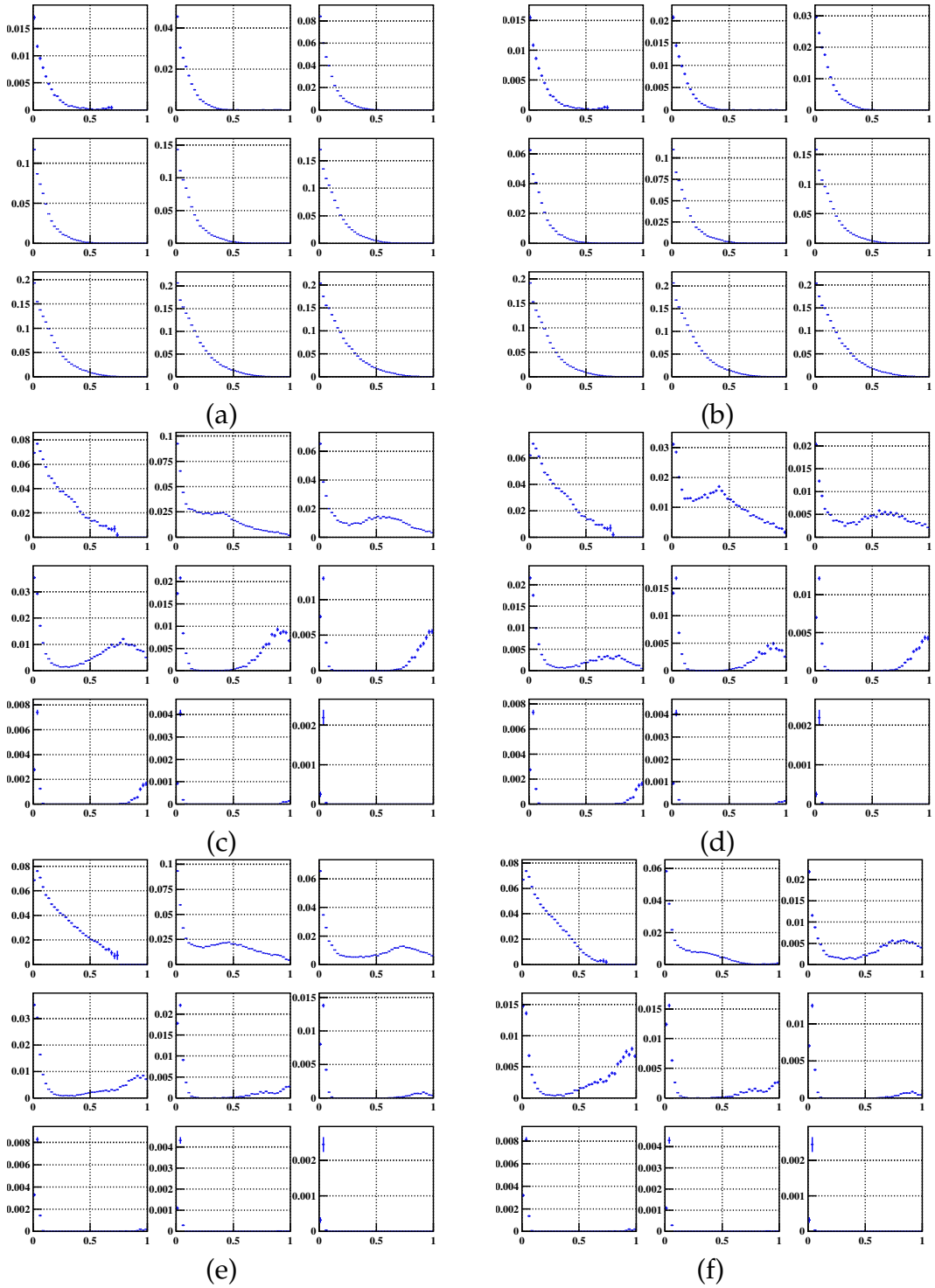

Figure C.1: Acceptance distributions for (a)(b)K^+K^-, (c)(d) K^-p and (e)(f)K^+p modes in terms of the 4-momentum transfer squared t for ϕ photoproduction in the wide mass band with (left) and without (right) the $\phi - \Lambda(1520)$ interference box region.

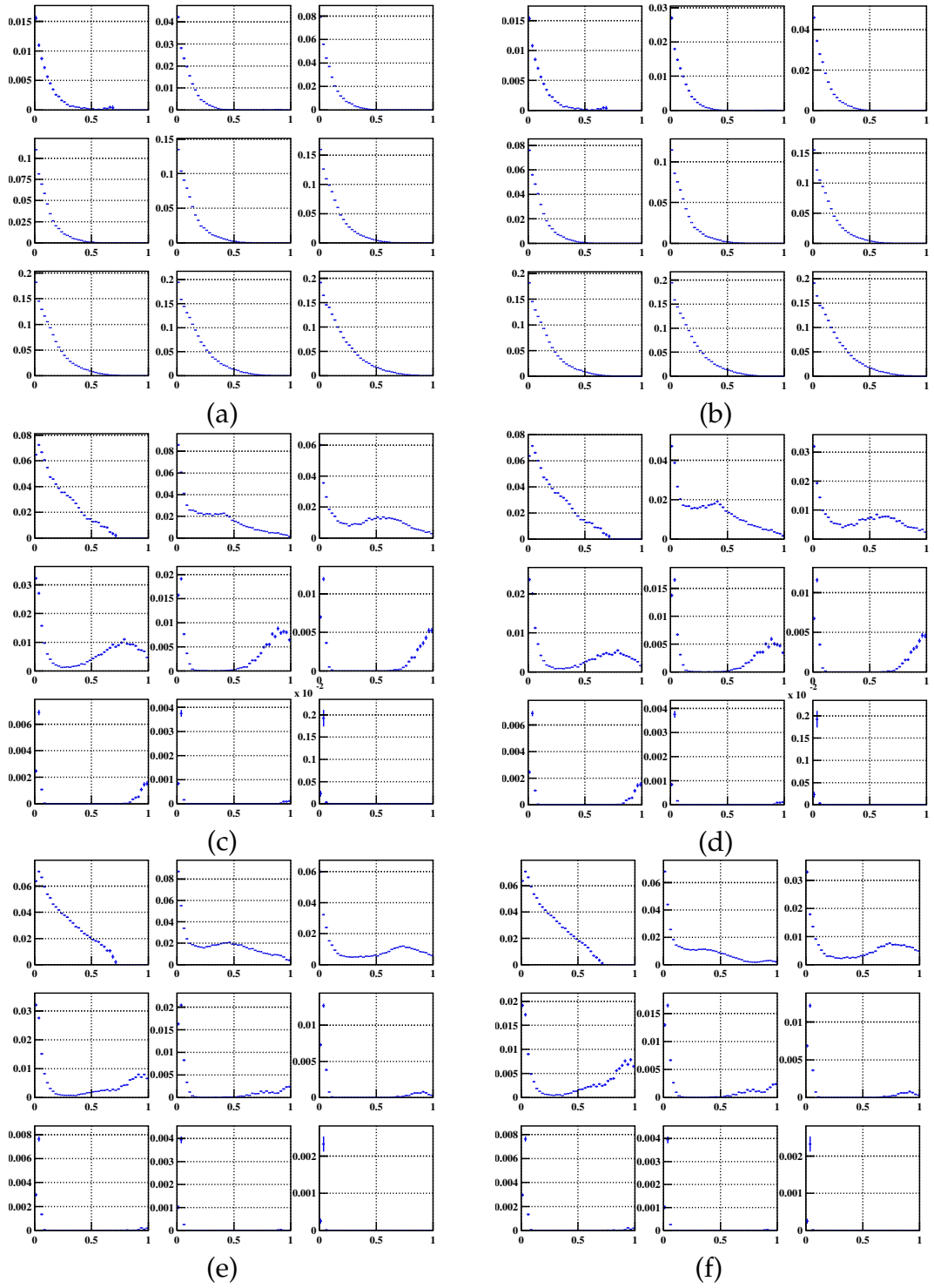

Figure C.2: Acceptance distributions for (a)(b)K^+K^-, (c)(d) K^-p and (e)(f)K^+p modes in terms of the 4-momentum transfer squared t for ϕ photoproduction in the narrow mass band with (left) and without (right) the $\phi-\Lambda(1520)$ interference box region.

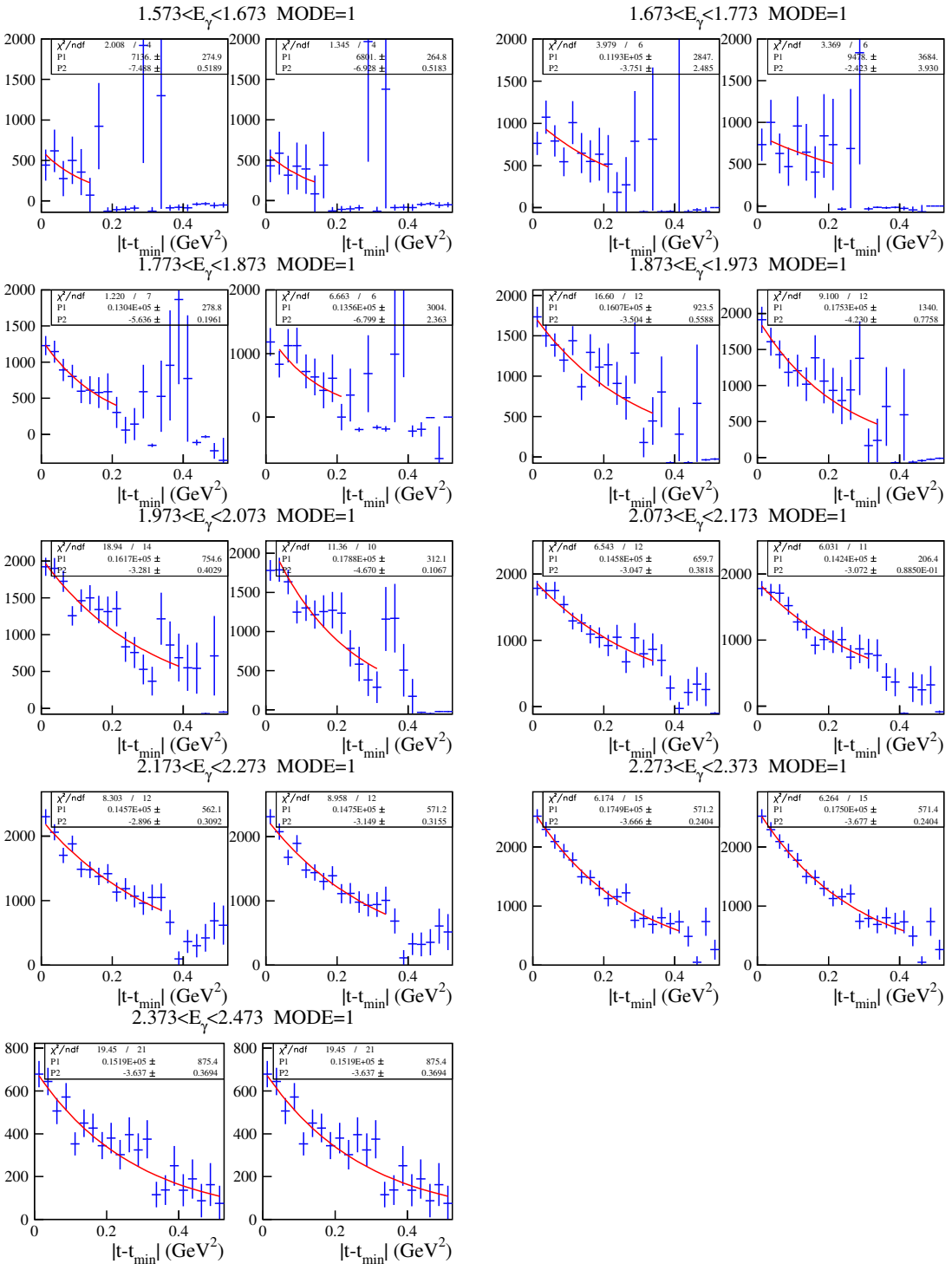

Figure C.3: Acceptance-corrected $|t - t_{\min}|$ distributions for the events with K^-K^+ detected in the wide mass region of $|m_{K^+K^-} - m_\phi| \leq 4\Gamma_\phi$ and $|m_{K^-p} - m_{\Lambda(1520)}| \leq 2\Gamma_{\Lambda(1520)}$ with (left) and without (right) interference box region.

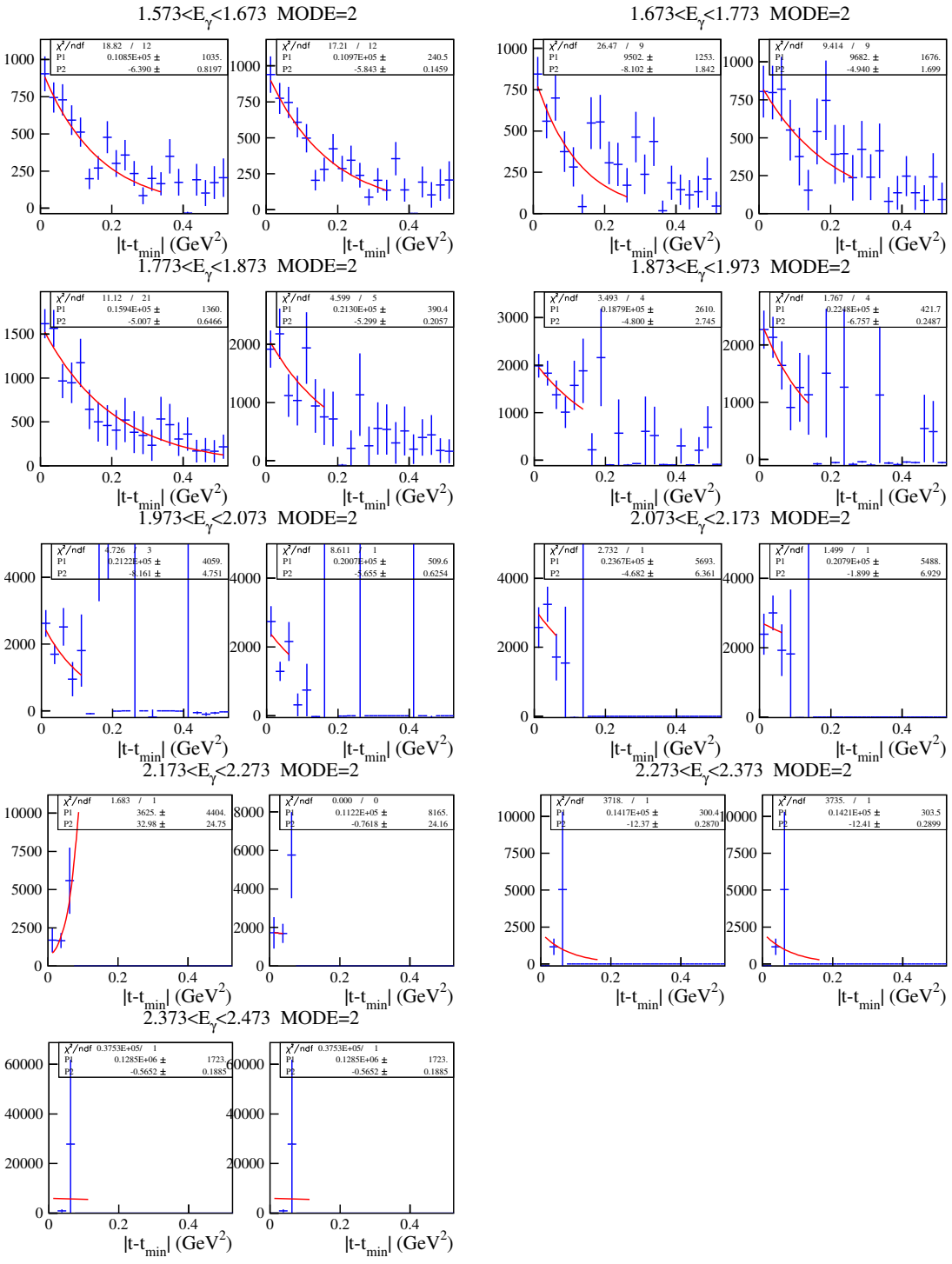

Figure C.4: Acceptance-corrected $|t - t_{\min}|$ distributions for the events with $K^- p$ detected in the wide mass region of $|m_{K^+K^-} - m_\phi| \leq 4\Gamma_\phi$ and $|m_{K^-p} - m_{\Lambda(1520)}| \leq 2\Gamma_{\Lambda(1520)}$ with (left) and without (right) interference box region.

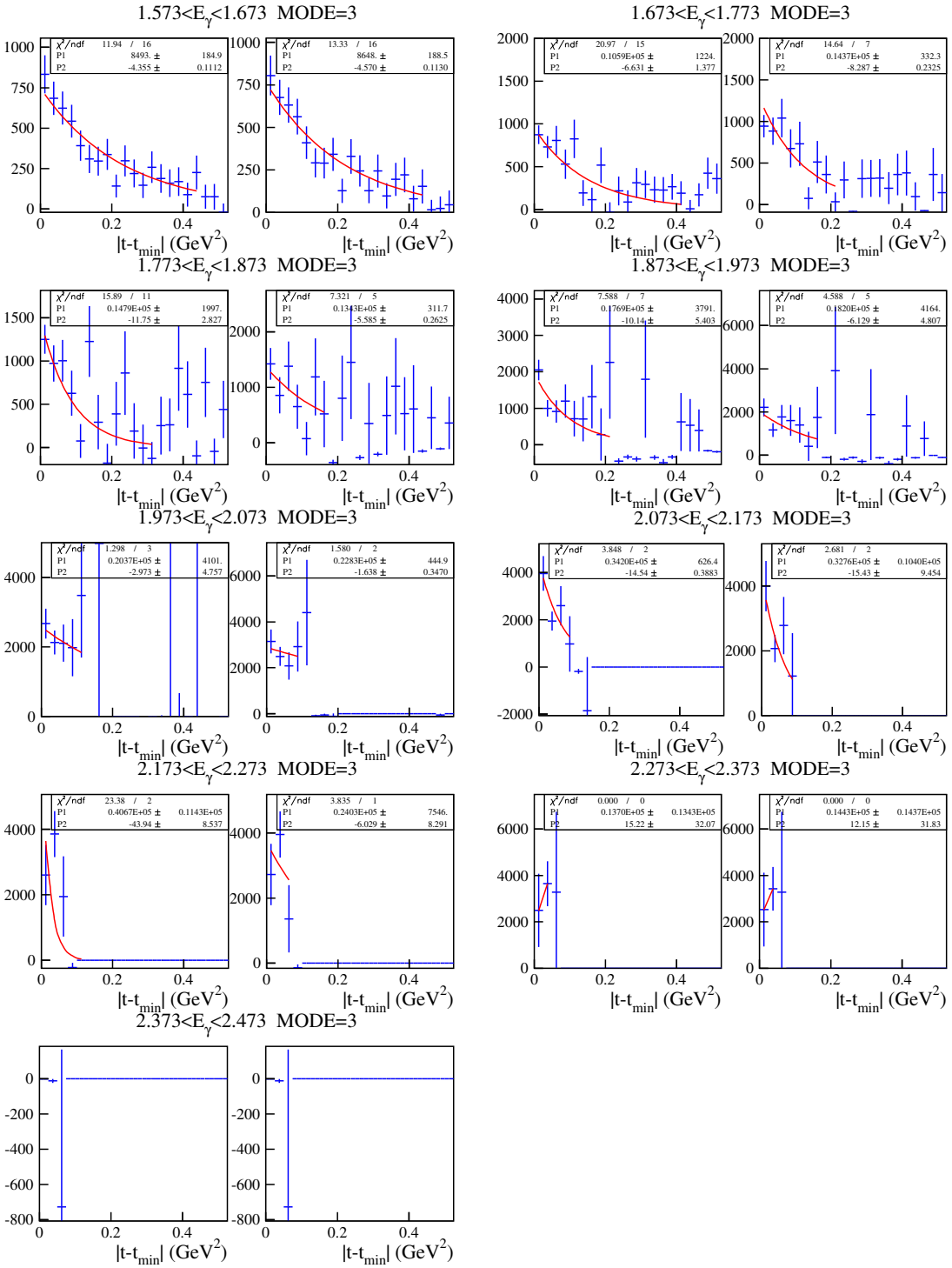

Figure C.5: Acceptance-corrected $|t - t_{\min}|$ distributions for the events with pK^+ detected in the wide mass region of $|m_{K^+K^-} - m_\phi| \leq 4\Gamma_\phi$ and $|m_{K^-p} - m_{\Lambda(1520)}| \leq 2\Gamma_{\Lambda(1520)}$ with (left) and without (right) interference box region.

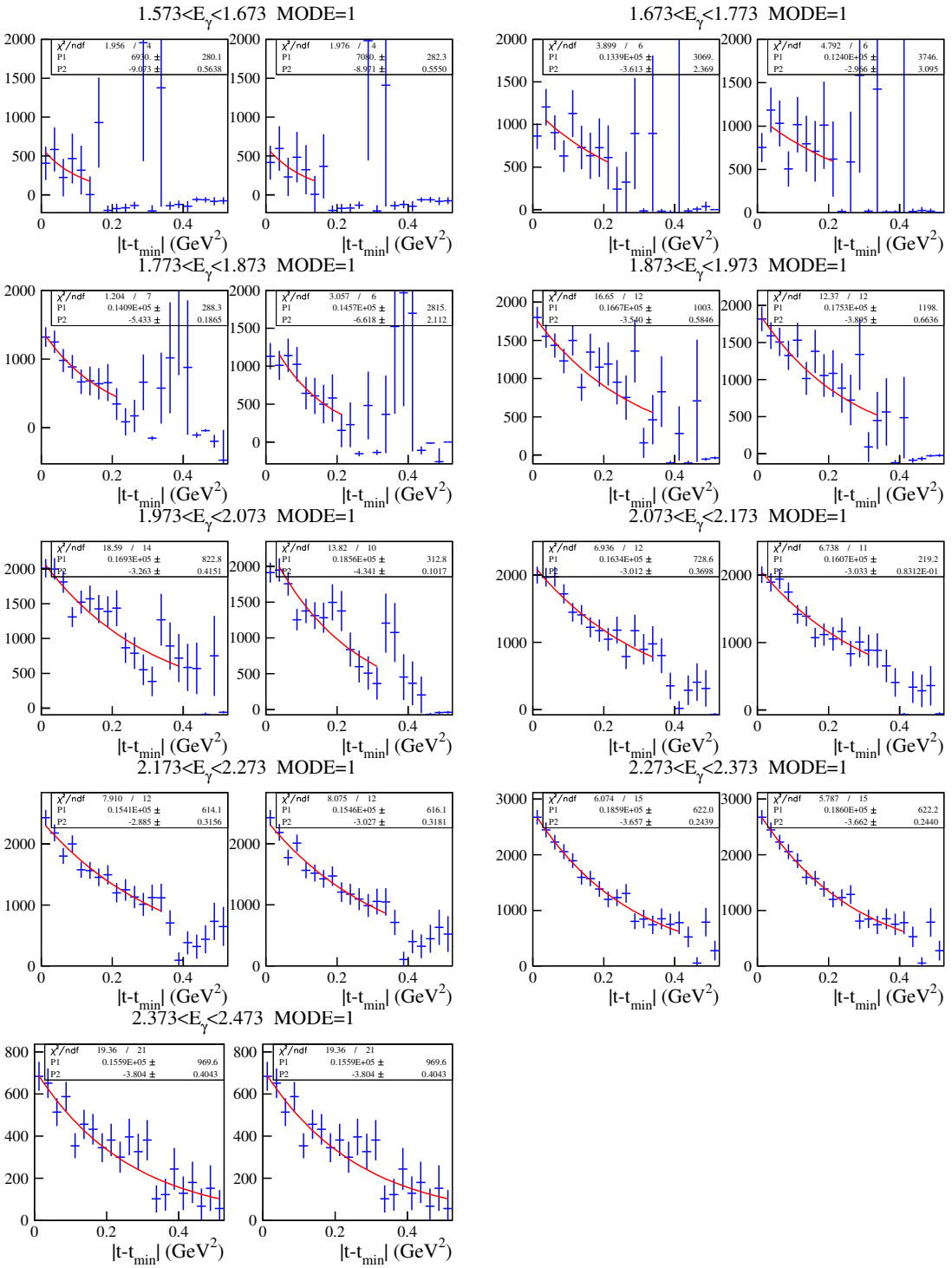

Figure C.6: Acceptance-corrected $|t - t_{\min}|$ distributions for the events with K^-K^+ detected in the narrow mass region of $1.01 < m_{K^+K^-} < 1.03$ GeV and $1.50 < m_{K^-p} < 1.54$ GeV with (left) and without (right) interference box region.

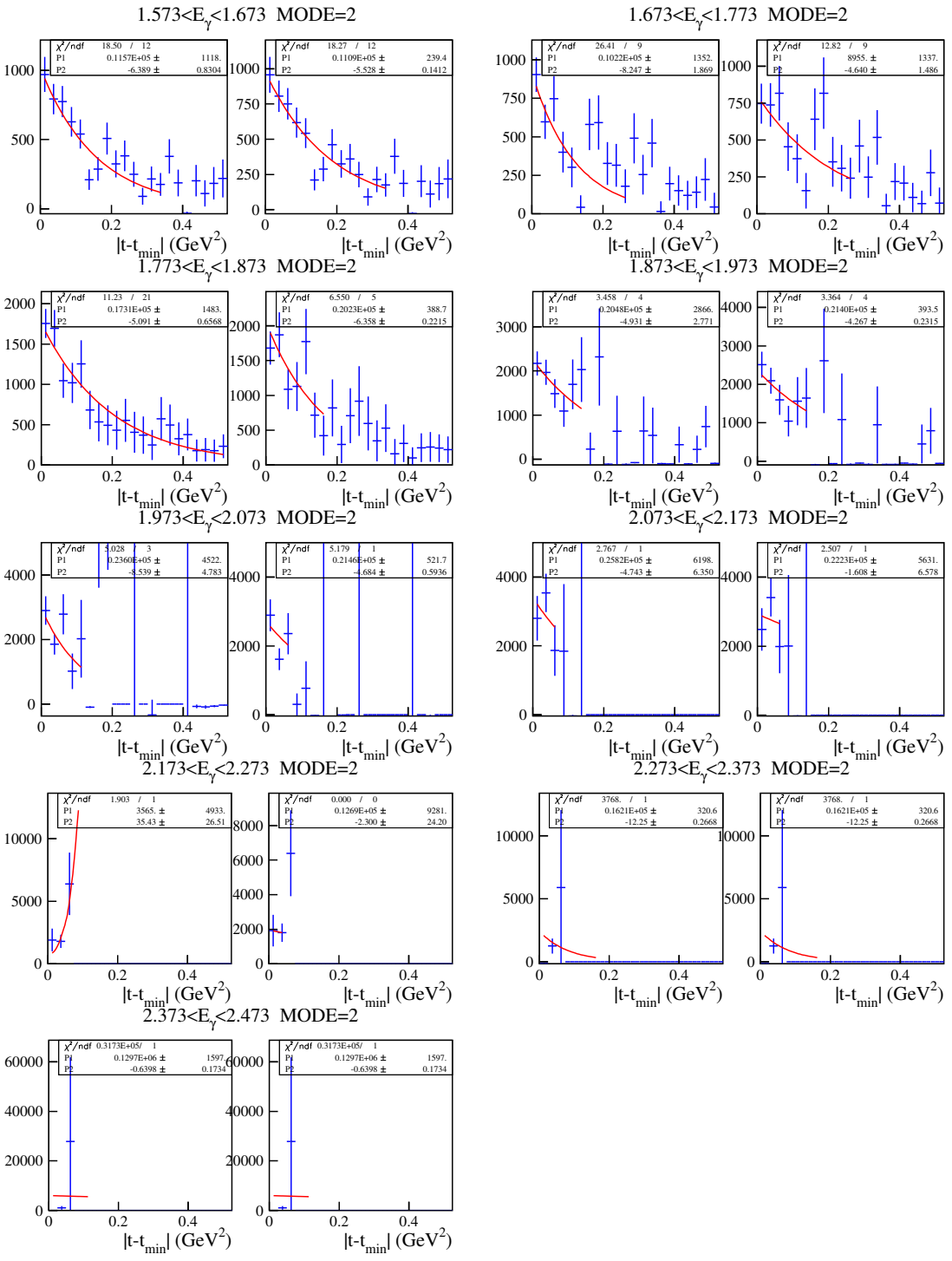

Figure C.7: Acceptance-corrected $|t - t_{\min}|$ distributions for the events with K^-p detected in the narrow mass region of $1.01 < m_{K^+K^-} < 1.03$ GeV and $1.50 < m_{K^-p} < 1.54$ GeV with (left) and without (right) interference box region.

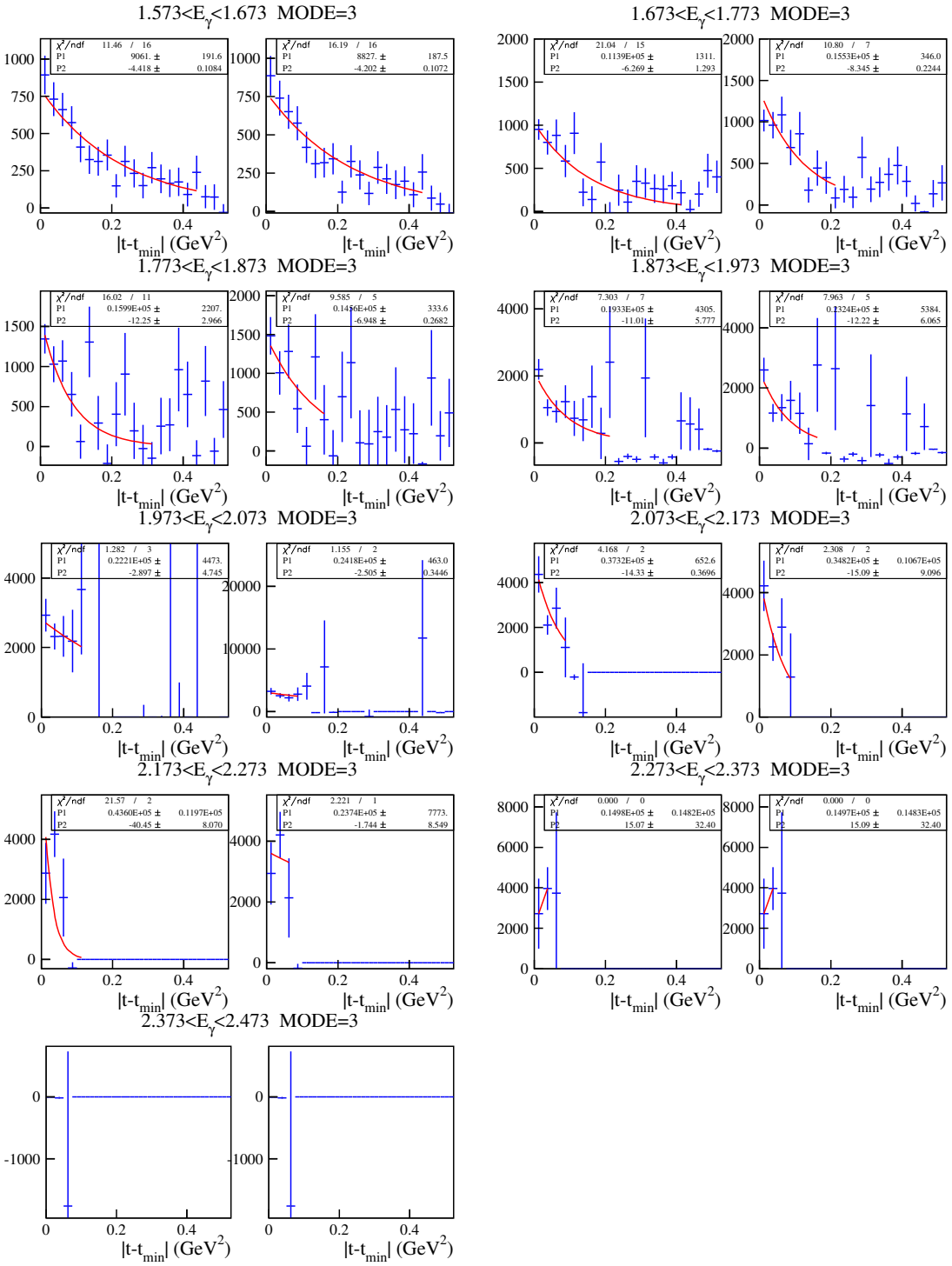

Figure C.8: Acceptance-corrected $|t - t_{\min}|$ distributions for the events with pK^+ detected in the narrow mass region of $1.01 < m_{K^+K^-} < 1.03$ GeV and $1.50 < m_{K^-p} < 1.54$ GeV with (left) and without (right) interference box region.

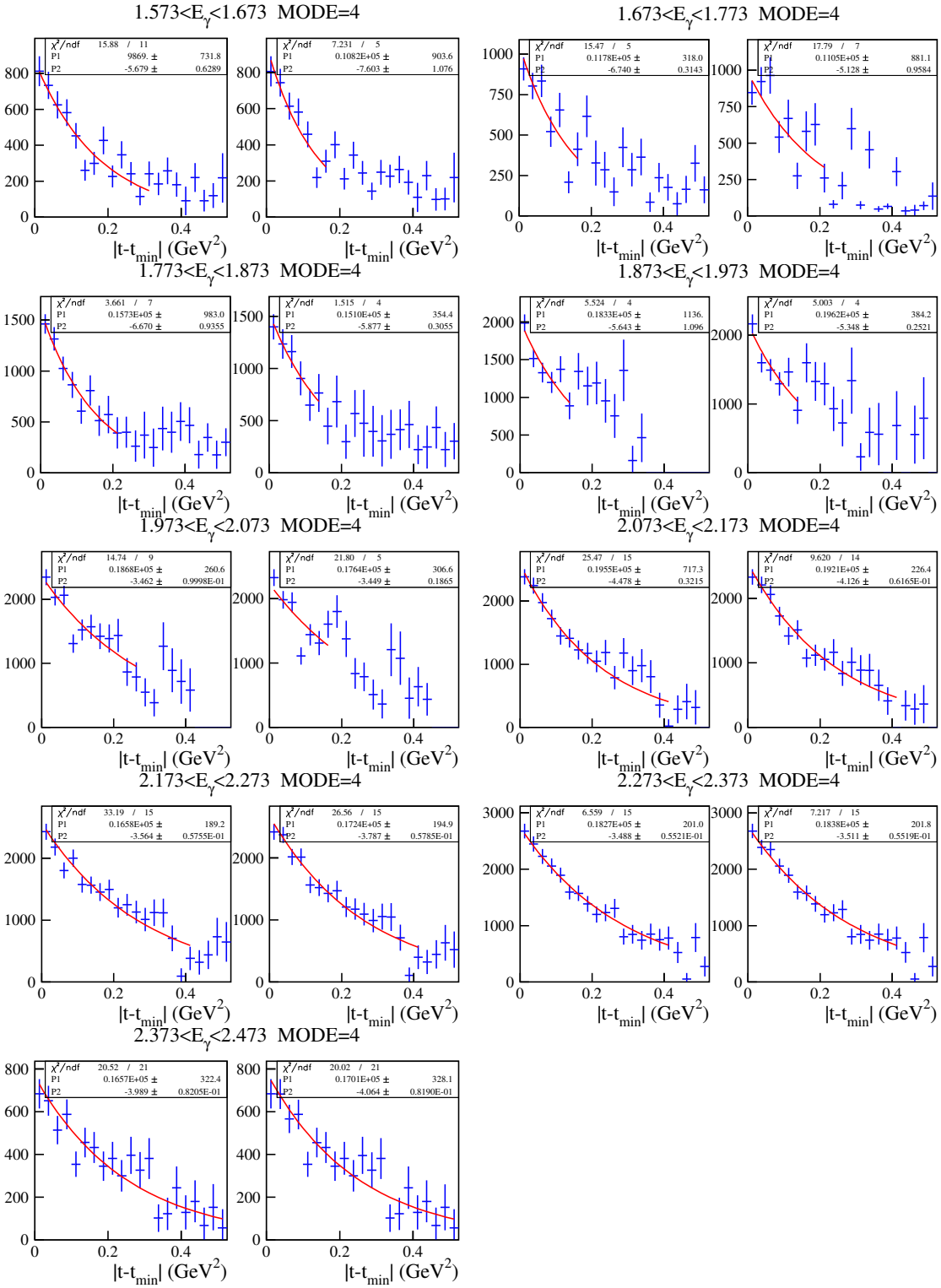

Figure C.9: Acceptance-corrected $|t - t_{\min}|$ distributions for the whole event sets are shown with exponential fit results with varying slope parameter in the narrow mass band. In each energy range, the left plot shows the t-distribution with the interference box region, while the right one without the box region.

Appendix D

Differential Cross Sections (Wide Mass Bands)

Table D.1: Energy dependence of $d\sigma/dt|_{t=t_{\min}}$ with/without the interference region in the mass band of $|m_{K^+K^-} - m_\phi| \leq 4\Gamma_\phi$ (ϕ-band) and $|m_{K^-p} - m_{\Lambda(1520)}| \leq 2\Gamma_{\Lambda(1520)}$ ($\Lambda(1520)$-band).

Slope	E_γ (GeV)	$d\sigma/dt\|^{\rm with}_{t=t_{\min}}$ (μ b/GeV^2)	$d\sigma/dt\|^{\rm without}_{t=t_{\min}}$ (μ b/GeV^2)
varying slope	1 (1.573-1.673)	0.447 ± 0.032	0.488 ± 0.040
	2 (1.673-1.773)	0.511 ± 0.041	0.522 ± 0.048
	3 (1.773-1.873)	0.691 ± 0.043	0.702 ± 0.076
	4 (1.873-1.973)	0.816 ± 0.049	0.926 ± 0.071
	5 (1.973-2.073)	0.827 ± 0.040	0.786 ± 0.047
	6 (2.073-2.173)	0.804 ± 0.032	0.827 ± 0.037
	7 (2.173-2.273)	0.741 ± 0.027	0.767 ± 0.028
	8 (2.273-2.373)	0.814 ± 0.027	0.815 ± 0.027
	9 (2.373-2.473)	0.755 ± 0.045	0.772 ± 0.046
fixed slope $b = -3.67$	1 (1.573-1.673)	0.359 ± 0.016	0.371 ± 0.019
	2 (1.673-1.773)	0.412 ± 0.016	0.442 ± 0.028
	3 (1.773-1.873)	0.573 ± 0.023	0.620 ± 0.036
	4 (1.873-1.973)	0.764 ± 0.026	0.802 ± 0.034
	5 (1.973-2.073)	0.832 ± 0.022	0.793 ± 0.025
	6 (2.073-2.173)	0.783 ± 0.021	0.761 ± 0.021
	7 (2.173-2.273)	0.744 ± 0.017	0.751 ± 0.017
	8 (2.273-2.373)	0.845 ± 0.016	0.846 ± 0.016
	9 (2.373-2.473)	0.755 ± 0.027	0.776 ± 0.028
linear slope $b(E_\gamma)$	1 (1.573-1.673)	0.454 ± 0.020	0.442 ± 0.022
	2 (1.673-1.773)	0.539 ± 0.021	0.504 ± 0.032
	3 (1.773-1.873)	0.644 ± 0.026	0.693 ± 0.040
	4 (1.873-1.973)	0.816 ± 0.028	0.865 ± 0.036
	5 (1.973-2.073)	0.920 ± 0.025	0.877 ± 0.028
	6 (2.073-2.173)	0.808 ± 0.022	0.794 ± 0.022
	7 (2.173-2.273)	0.751 ± 0.017	0.758 ± 0.017
	8 (2.273-2.373)	0.812 ± 0.016	0.813 ± 0.016
	9 (2.373-2.473)	0.672 ± 0.024	0.694 ± 0.025

Table D.2: Differential cross sections for $\gamma p \rightarrow K^{+}\Lambda(1520)$ with/without the interference region in the mass band of $|m_{K^{+}K^{-}} - m_{\phi}| \leq 4\Gamma_{\phi}$ and $|m_{K^{-}p} - m_{\Lambda(1520)}| \leq 2\Gamma_{\Lambda(1520)}$ in $0.6 < \cos\theta^{CM} < 1.0$.

Angle	E_{γ} (GeV)	$d\sigma/dcos\theta^{*with}_{K^{+}}$ (μ b)	$d\sigma/dcos\theta^{*without}_{K^{+}}$ (μ b)
$0.9 < cos\theta^{*} < 1$	1 (1.673-1.773)	0.242 ± 0.035	0.189 ± 0.032
	2 (1.773-1.873)	0.641 ± 0.056	0.596 ± 0.053
	3 (1.873-1.973)	0.913 ± 0.064	0.918 ± 0.062
	4 (1.973-2.073)	0.895 ± 0.057	0.892 ± 0.057
	5 (2.073-2.173)	0.804 ± 0.059	0.787 ± 0.059
	6 (2.173-2.273)	0.743 ± 0.047	0.732 ± 0.046
	7 (2.273-2.373)	0.630 ± 0.047	0.632 ± 0.048
	8 (2.373-2.473)	0.833 ± 0.083	0.835 ± 0.083
$0.8 < cos\theta^{*} < 0.9$	1 (1.673-1.773)	0.211 ± 0.027	0.174 ± 0.027
	2 (1.773-1.873)	0.423 ± 0.039	0.361 ± 0.035
	3 (1.873-1.973)	0.611 ± 0.046	0.571 ± 0.043
	4 (1.973-2.073)	0.670 ± 0.044	0.628 ± 0.043
	5 (2.073-2.173)	0.573 ± 0.045	0.511 ± 0.044
	6 (2.173-2.273)	0.479 ± 0.036	0.464 ± 0.036
	7 (2.273-2.373)	0.460 ± 0.038	0.459 ± 0.038
	8 (2.373-2.473)	0.448 ± 0.061	0.448 ± 0.061
$0.7 < cos\theta^{*} < 0.8$	1 (1.673-1.773)	0.191 ± 0.026	0.132 ± 0.025
	2 (1.773-1.873)	0.391 ± 0.041	0.333 ± 0.038
	3 (1.873-1.973)	0.521 ± 0.048	0.417 ± 0.043
	4 (1.973-2.073)	0.575 ± 0.044	0.524 ± 0.044
	5 (2.073-2.173)	0.456 ± 0.048	0.411 ± 0.048
	6 (2.173-2.273)	0.385 ± 0.038	0.356 ± 0.038
	7 (2.273-2.373)	0.366 ± 0.037	0.363 ± 0.036
	8 (2.373-2.473)	0.353 ± 0.055	0.357 ± 0.056
$0.6 < cos\theta^{*} < 0.7$	1 (1.673-1.773)	0.166 ± 0.027	0.129 ± 0.027
	2 (1.773-1.873)	0.275 ± 0.039	0.135 ± 0.015
	3 (1.873-1.973)	0.346 ± 0.043	0.292 ± 0.041
	4 (1.973-2.073)	0.419 ± 0.043	0.371 ± 0.041
	5 (2.073-2.173)	0.408 ± 0.047	0.381 ± 0.047
	6 (2.173-2.273)	0.301 ± 0.033	0.288 ± 0.032
	7 (2.273-2.373)	0.290 ± 0.033	0.292 ± 0.034
	8 (2.373-2.473)	0.212 ± 0.042	0.211 ± 0.041

Appendix E

Differential Cross Sections (Narrow Mass Bands)

Table E.1: Energy dependence of $d\sigma/dt|_{t=t_{\min}}$ with/without the interference region in the mass band of $1.01 < m_{K^+K^-} < 1.03$ GeV and $1.50 < m_{K^-p} < 1.54$ GeV.

Slope	E_γ (GeV)	$d\sigma/dt\|^{\text{with}}_{t=t_{\min}}$ (μ b/GeV^2)	$d\sigma/dt\|^{\text{without}}_{t=t_{\min}}$ (μ b/GeV^2)
varying slope	1 (1.573-1.673)	0.468 ± 0.035	0.513 ± 0.043
	2 (1.673-1.773)	0.558 ± 0.044	0.524 ± 0.042
	3 (1.773-1.873)	0.745 ± 0.047	0.715 ± 0.063
	4 (1.873-1.973)	0.869 ± 0.054	0.930 ± 0.065
	5 (1.973-2.073)	0.885 ± 0.043	0.836 ± 0.048
	6 (2.073-2.173)	0.926 ± 0.034	0.910 ± 0.039
	7 (2.173-2.273)	0.785 ± 0.029	0.817 ± 0.030
	8 (2.273-2.373)	0.865 ± 0.029	0.871 ± 0.029
	9 (2.373-2.473)	0.785 ± 0.047	0.806 ± 0.049
fixed slope $b = -3.67$	1 (1.573-1.673)	0.377 ± 0.017	0.383 ± 0.020
	2 (1.673-1.773)	0.451 ± 0.018	0.476 ± 0.026
	3 (1.773-1.873)	0.618 ± 0.025	0.595 ± 0.029
	4 (1.873-1.973)	0.803 ± 0.028	0.835 ± 0.032
	5 (1.973-2.073)	0.880 ± 0.024	0.866 ± 0.026
	6 (2.073-2.173)	0.875 ± 0.024	0.854 ± 0.022
	7 (2.173-2.273)	0.788 ± 0.018	0.803 ± 0.018
	8 (2.273-2.373)	0.900 ± 0.018	0.902 ± 0.018
	9 (2.373-2.473)	0.748 ± 0.028	0.780 ± 0.029
linear slope $b(E_\gamma)$	1 (1.573-1.673)	0.477 ± 0.022	0.457 ± 0.023
	2 (1.673-1.773)	0.589 ± 0.023	0.537 ± 0.029
	3 (1.773-1.873)	0.695 ± 0.028	0.666 ± 0.032
	4 (1.873-1.973)	0.858 ± 0.030	0.900 ± 0.034
	5 (1.973-2.073)	0.973 ± 0.026	0.957 ± 0.029
	6 (2.073-2.173)	0.903 ± 0.024	0.891 ± 0.023
	7 (2.173-2.273)	0.795 ± 0.018	0.811 ± 0.018
	8 (2.273-2.373)	0.865 ± 0.017	0.867 ± 0.017
	9 (2.373-2.473)	0.665 ± 0.025	0.692 ± 0.026

Table E.2: Differential cross sections for $\gamma p \rightarrow K^{+}\Lambda(1520)$ with/without the interference region in the mass band of $1.01 < m_{K^{+}K^{-}} < 1.03$ GeV and $1.50 < m_{K^{-}p} < 1.54$ GeV in $0.6 < \cos\theta^{CM} < 1.0$.

Angle	E_{γ} (GeV)	$d\sigma/dcos\theta^{*with}_{K^{+}}$ (μ b)	$d\sigma/dcos\theta^{*without}_{K^{+}}$ (μ b)
$0.9 < cos\theta^{*} < 1$	1 (1.673-1.773)	0.282 ± 0.041	0.236 ± 0.037
	2 (1.773-1.873)	0.699 ± 0.062	0.669 ± 0.058
	3 (1.873-1.973)	0.914 ± 0.073	0.908 ± 0.071
	4 (1.973-2.073)	0.961 ± 0.077	0.921 ± 0.076
	5 (2.073-2.173)	0.897 ± 0.066	0.855 ± 0.064
	6 (2.173-2.273)	0.835 ± 0.055	0.816 ± 0.054
	7 (2.273-2.373)	0.666 ± 0.057	0.666 ± 0.057
	8 (2.373-2.473)	0.907 ± 0.094	0.911 ± 0.095
$0.8 < cos\theta^{*} < 0.9$	1 (1.673-1.773)	0.242 ± 0.031	0.217 ± 0.029
	2 (1.773-1.873)	0.465 ± 0.043	0.425 ± 0.039
	3 (1.873-1.973)	0.610 ± 0.053	0.574 ± 0.050
	4 (1.973-2.073)	0.724 ± 0.058	0.662 ± 0.057
	5 (2.073-2.173)	0.632 ± 0.049	0.572 ± 0.047
	6 (2.173-2.273)	0.537 ± 0.041	0.519 ± 0.040
	7 (2.273-2.373)	0.450 ± 0.053	0.451 ± 0.053
	8 (2.373-2.473)	0.442 ± 0.069	0.441 ± 0.069
$0.7 < cos\theta^{*} < 0.8$	1 (1.673-1.773)	0.217 ± 0.030	0.141 ± 0.025
	2 (1.773-1.873)	0.431 ± 0.045	0.375 ± 0.042
	3 (1.873-1.973)	0.521 ± 0.054	0.450 ± 0.051
	4 (1.973-2.073)	0.621 ± 0.056	0.544 ± 0.055
	5 (2.073-2.173)	0.480 ± 0.047	0.443 ± 0.047
	6 (2.173-2.273)	0.430 ± 0.040	0.407 ± 0.040
	7 (2.273-2.373)	0.372 ± 0.046	0.366 ± 0.045
	8 (2.373-2.473)	0.365 ± 0.062	0.370 ± 0.063
$0.6 < cos\theta^{*} < 0.7$	1 (1.673-1.773)	0.182 ± 0.029	0.133 ± 0.025
	2 (1.773-1.873)	0.291 ± 0.043	0.189 ± 0.013
	3 (1.873-1.973)	0.330 ± 0.048	0.254 ± 0.045
	4 (1.973-2.073)	0.434 ± 0.053	0.404 ± 0.053
	5 (2.073-2.173)	0.434 ± 0.047	0.411 ± 0.047
	6 (2.173-2.273)	0.336 ± 0.037	0.325 ± 0.036
	7 (2.273-2.373)	0.301 ± 0.039	0.303 ± 0.039
	8 (2.373-2.473)	0.248 ± 0.049	0.245 ± 0.048

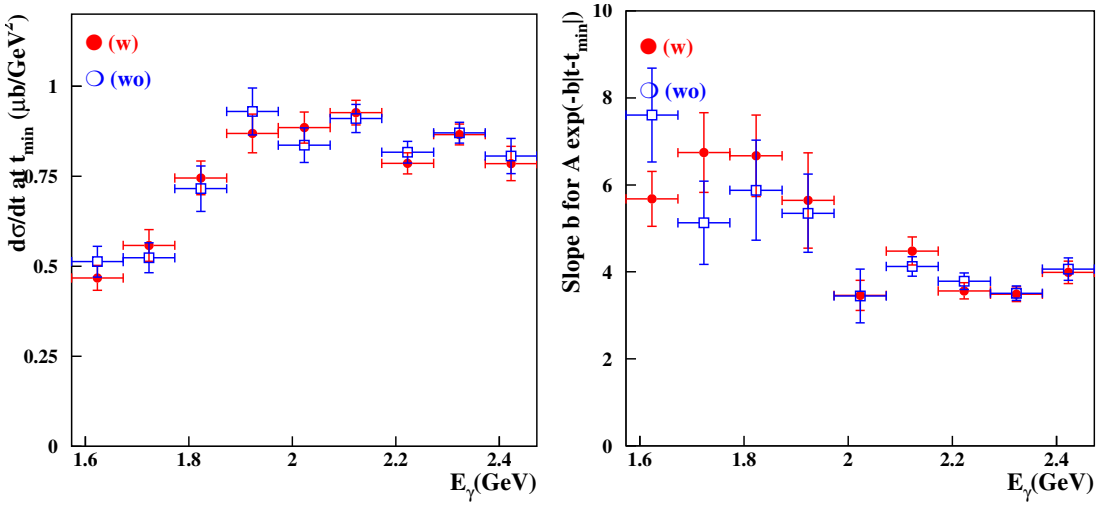

Figure E.1: Energy dependence of $d\sigma/dt|_{t=t_{\min}}$ with varying slopes parameter with/without the interference box in the mass band of $1.01 < m_{K^+K^-} < 1.03$ GeV and $1.50 < m_{K^-p} < 1.54$ GeV.

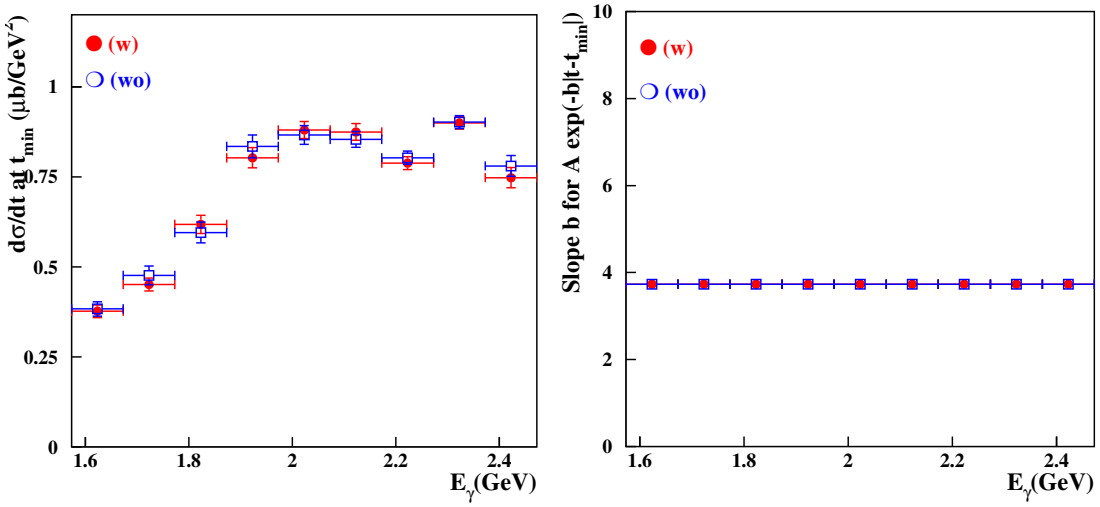

Figure E.2: Energy dependence of $d\sigma/dt|_{t=t_{\min}}$ with a fixed slope $b = -3.67$ with/without the interference box in the mass band of $1.01 < m_{K^+K^-} < 1.03$ GeV and $1.50 < m_{K^-p} < 1.54$ GeV.

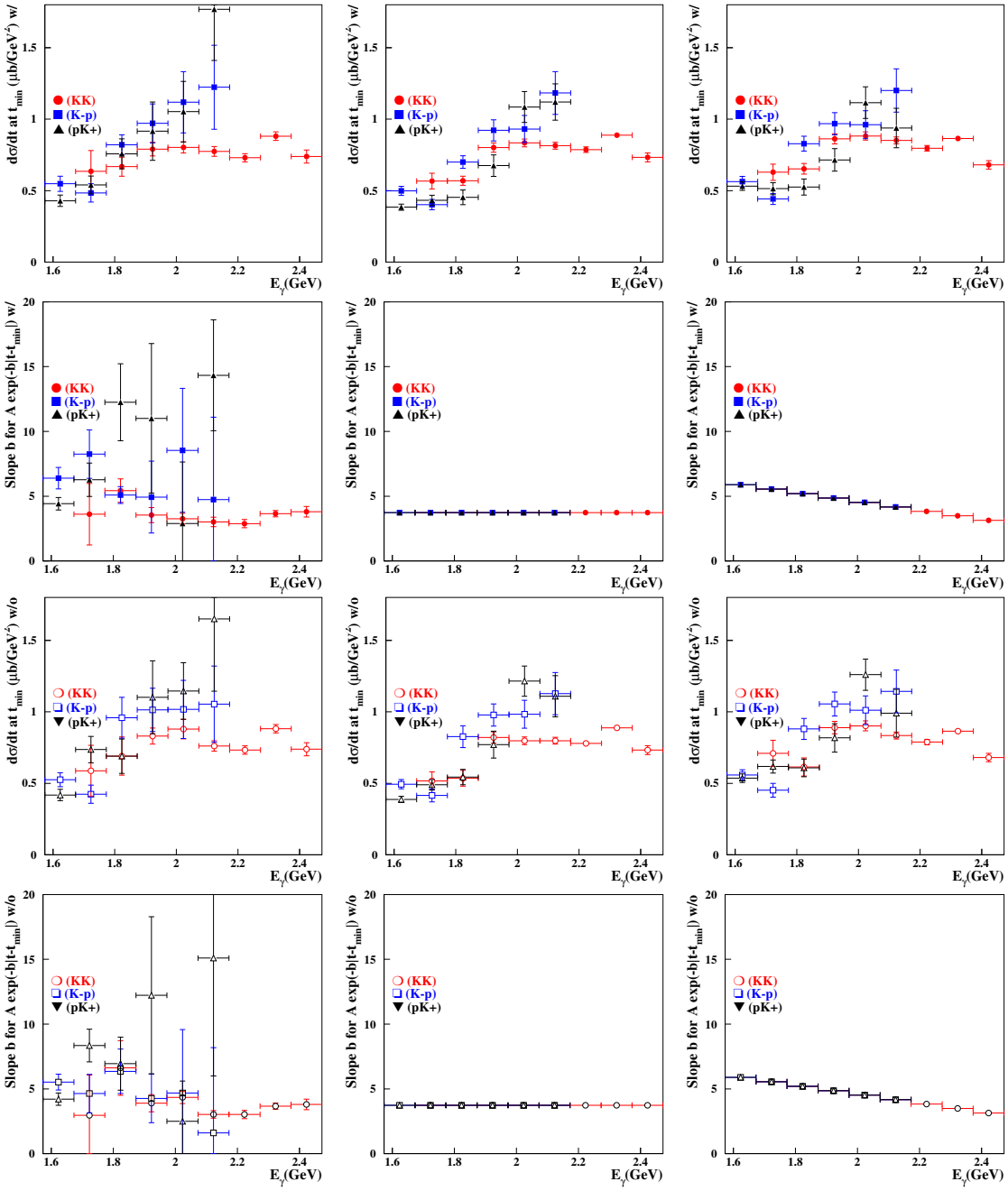

Figure E.3: Intercepts with linear slope parameters for K^+K^-, K^-p, and K^+p modes with (closed symbols) and without (open symbols) interference in the mass band of $1.01 < m_{K^+K^-} < 1.03$ GeV and $1.50 < m_{K^-p} < 1.54$ GeV.

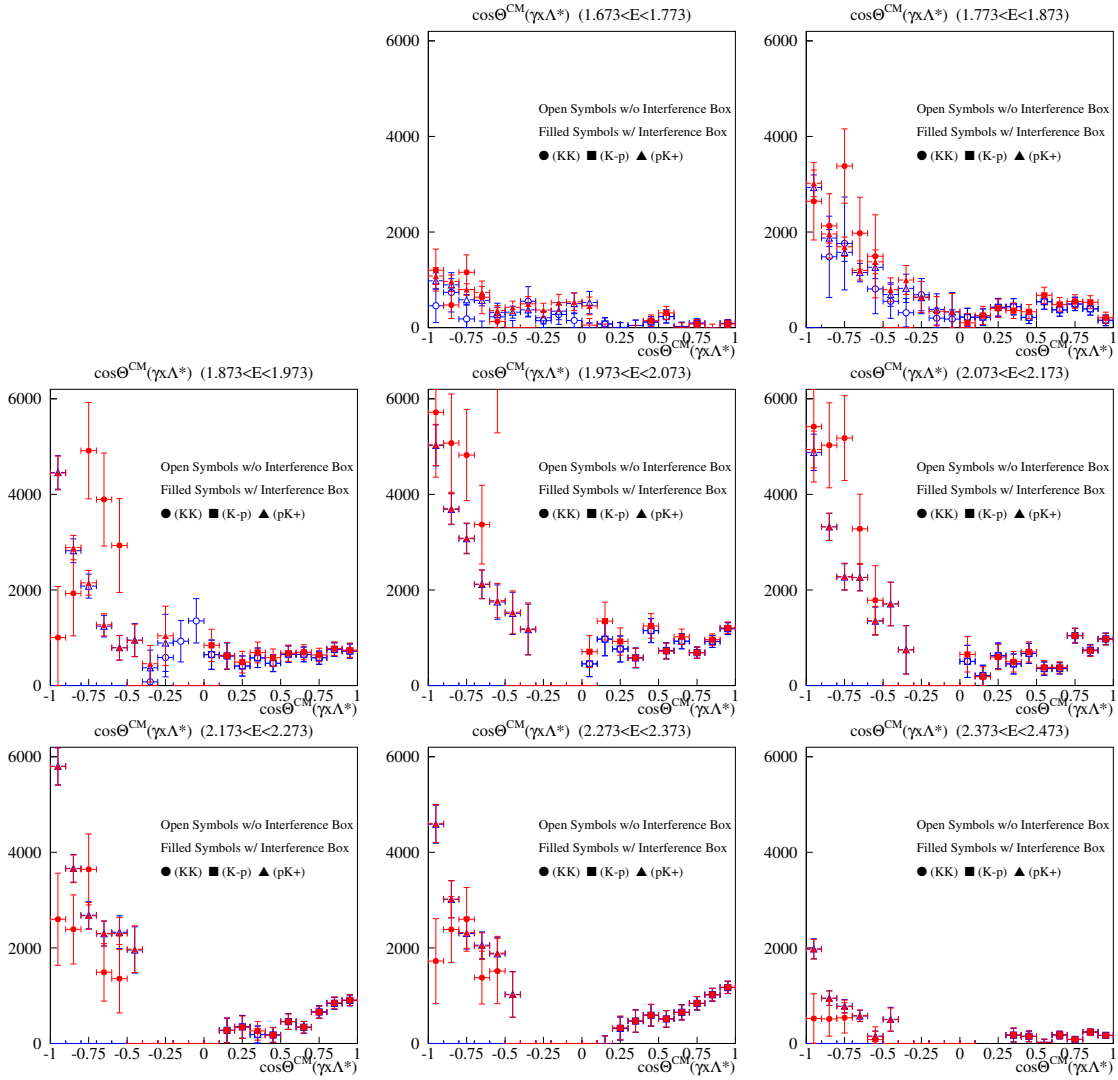

Figure E.4: Angular Distributions for $\gamma p \to K^+\Lambda(1520)$. Angular distributions of $\Lambda(1520)$ in the total cm system ($\cos\theta^*_{\Lambda(1520)} = -\cos\theta^*_{K^+}$) in the mass band of $1.01 < m_{K^+K^-} < 1.03$ GeV and $1.50 < m_{K^-p} < 1.54$ GeV.

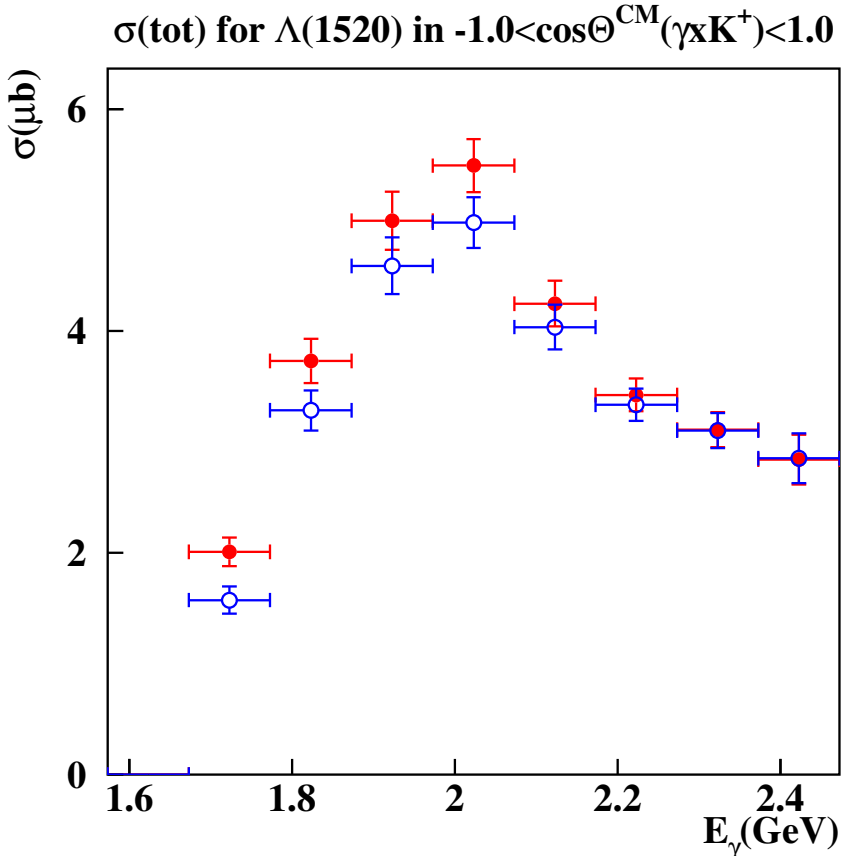

Figure E.5: Total cross sections for $\gamma p \to K^+\Lambda(1520)$ in $E_\gamma = 1.673 - 2.473$ GeV. Red circles represents the results with the interference box region, while the blue open circles for the results excluding the box region.

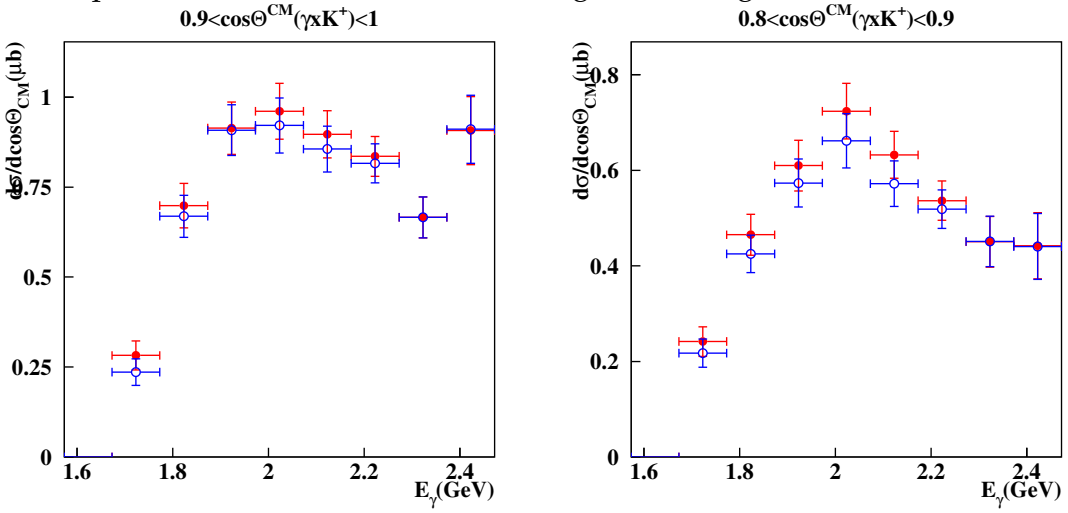

Figure E.6: Differential cross sections for $\gamma p \to K^+\Lambda(1520)$ in $0.8 < \cos\theta^{CM} < 1.0$

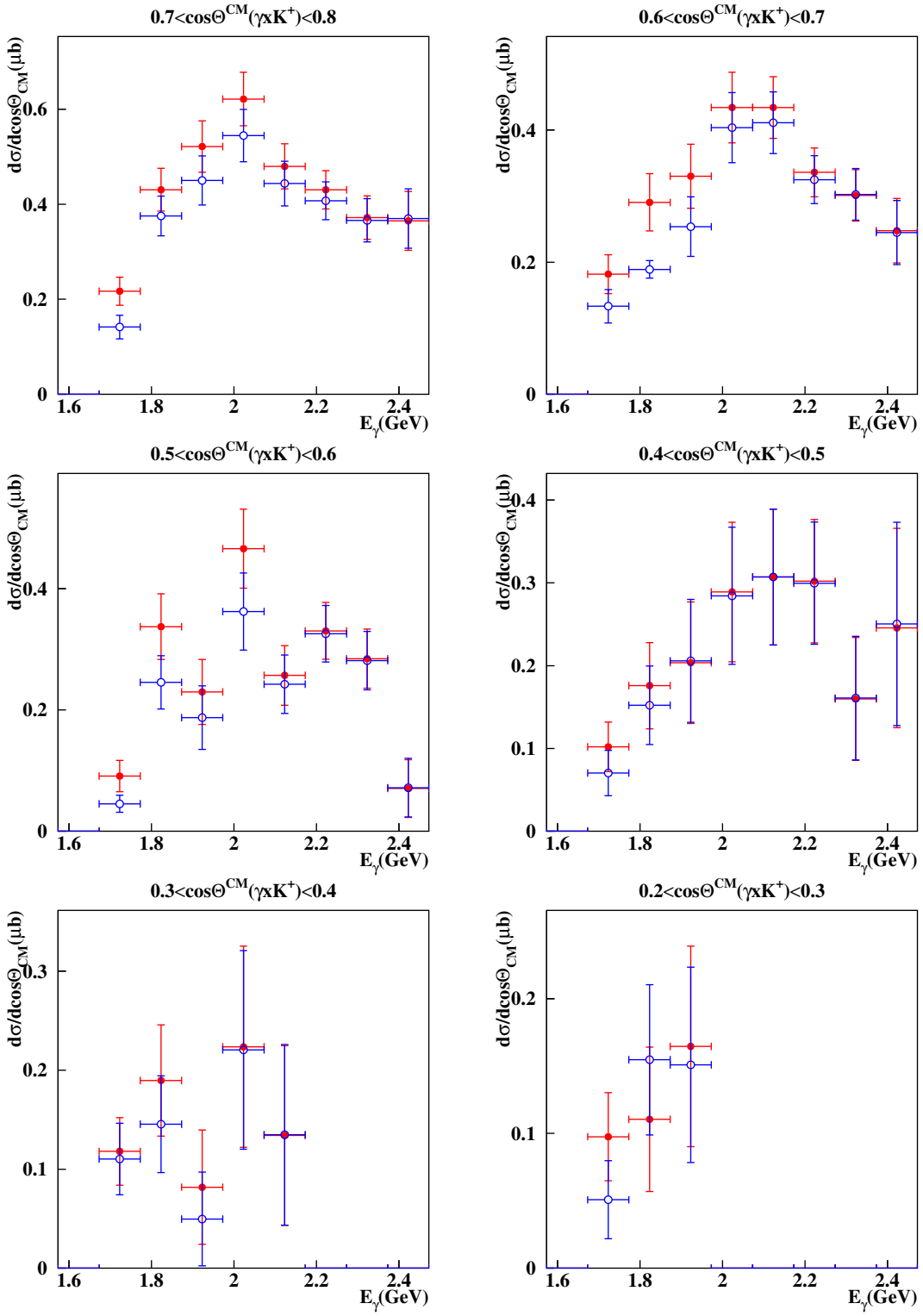

Figure E.7: Differential cross sections for $\gamma p \to K^+\Lambda(1520)$ in $0.2 < \cos\theta^{CM} < 0.8$. Red circles represents the results with the interference box region, while the blue open circles for the results excluding the box region.

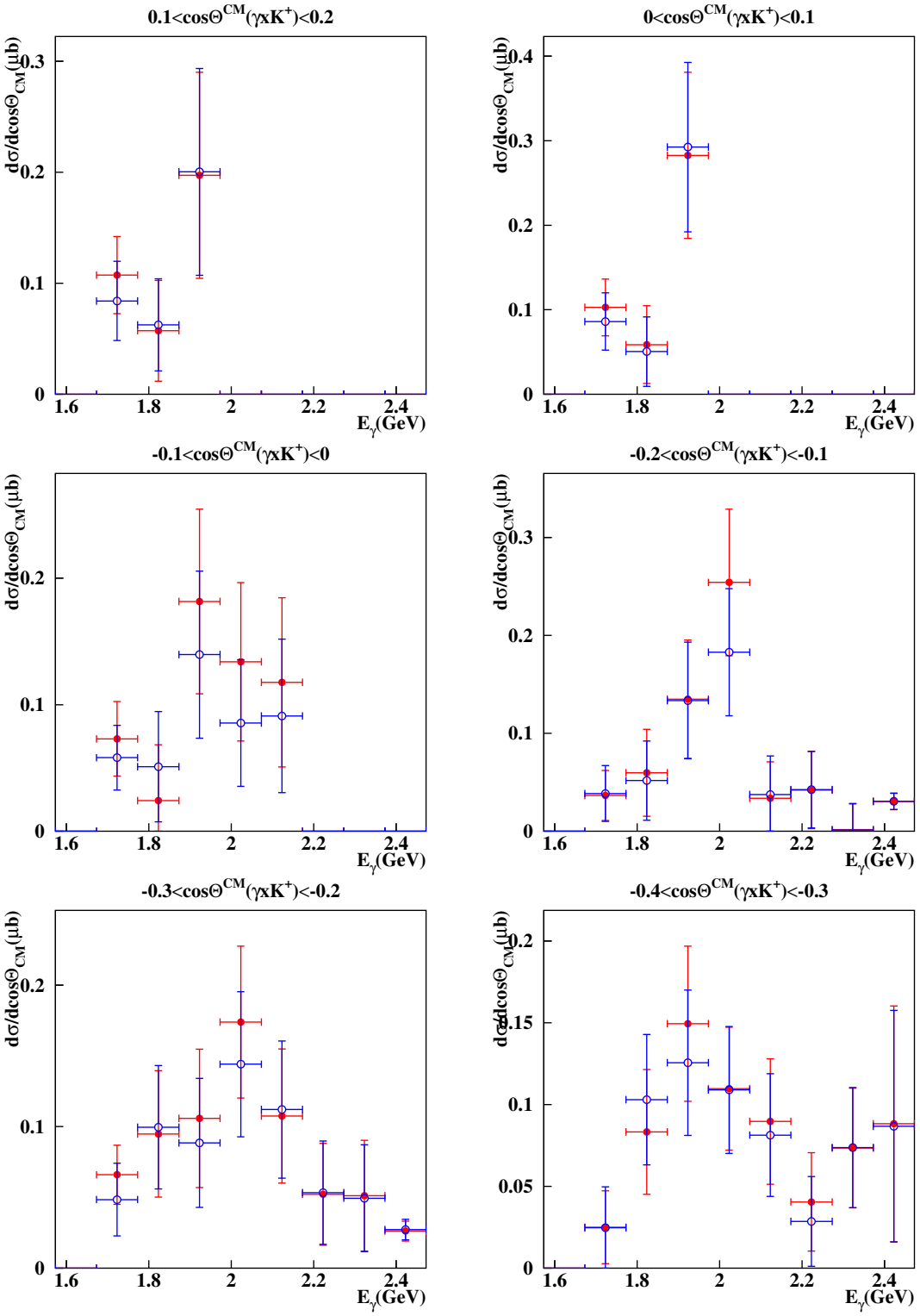

Figure E.8: Differential cross sections for $\gamma p \to K^+\Lambda(1520)$ in $-0.4 < \cos\theta^{CM} < 0.2$. Red circles represents the results with the interference box region, while the blue open circles for the results excluding the box region.

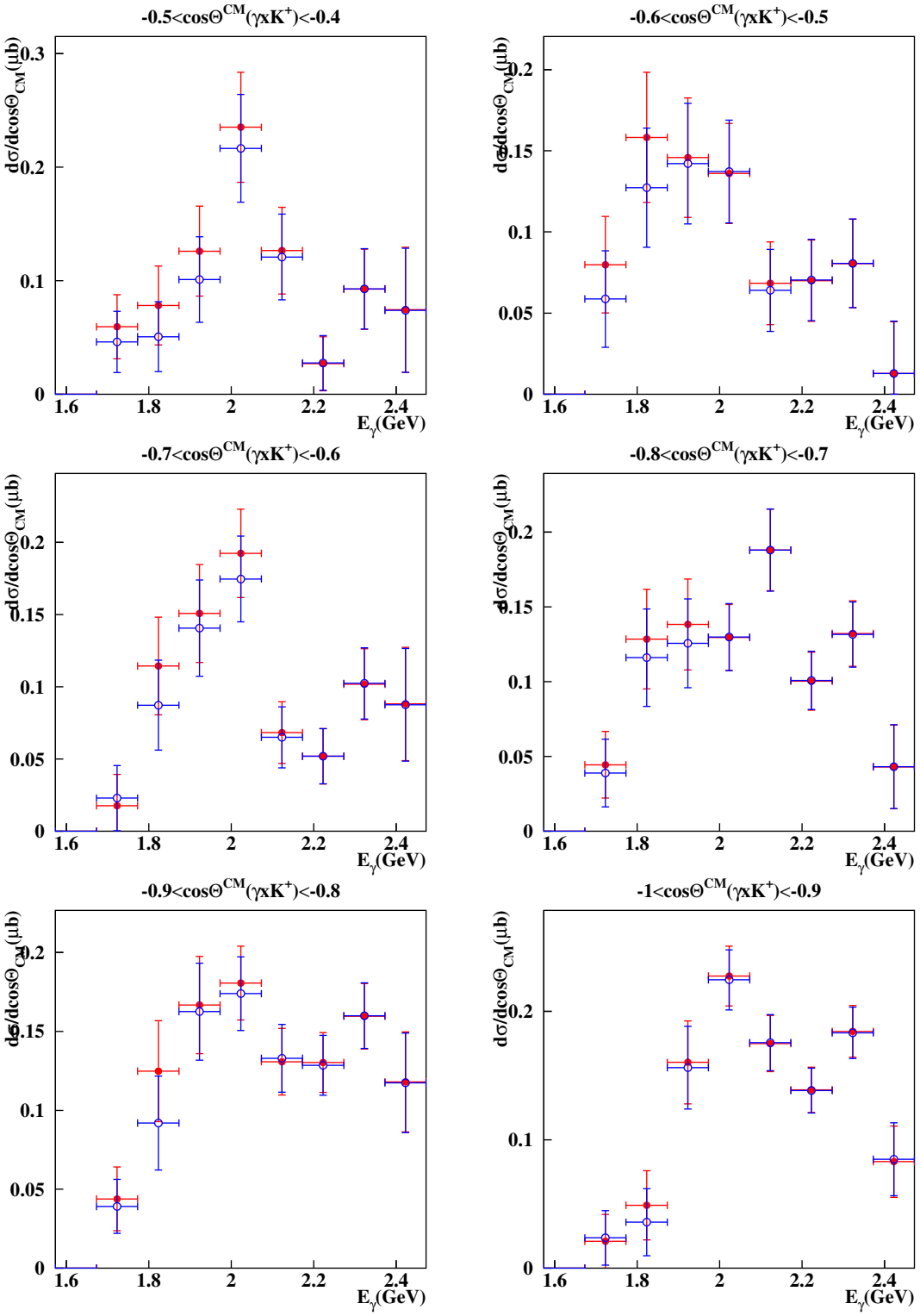

Figure E.9: Differential cross sections for $\gamma p \to K^+\Lambda(1520)$ in $1.0 < \cos\theta^{CM} < -0.4$. Red circles represents the results with the interference box region, while the blue open circles for the results excluding the box region.

Appendix F

Events in the Narrow Interference Region

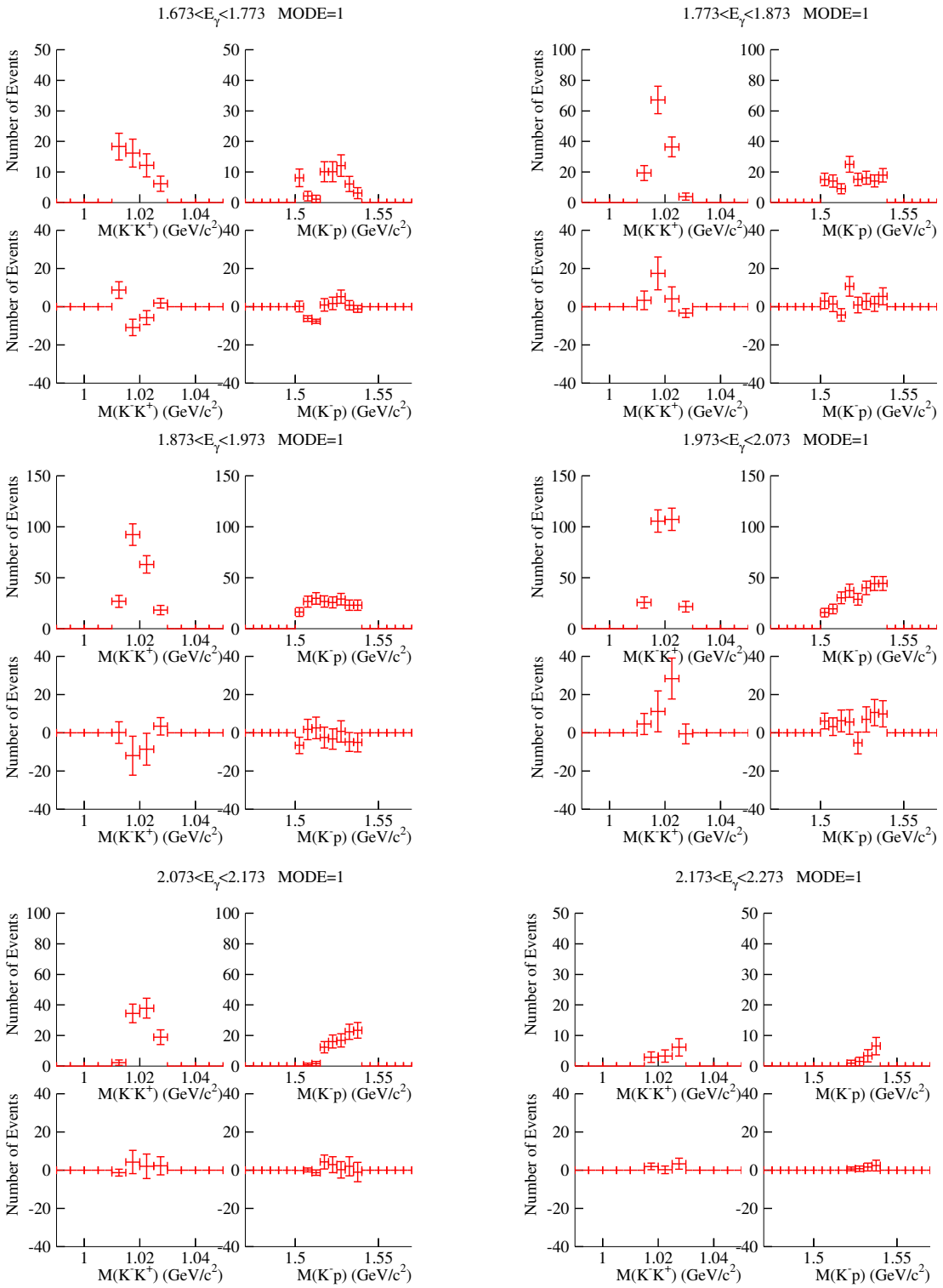

Figure F.1: The K^-K^+ and K^-p mass distributions for the K^+K^- events (MODE$=1$) in the box region (top two figures in each energy bin) are displayed in the top two figures, while the relative yields compared to the expected yield for no interference are also displayed in the bottom figures.

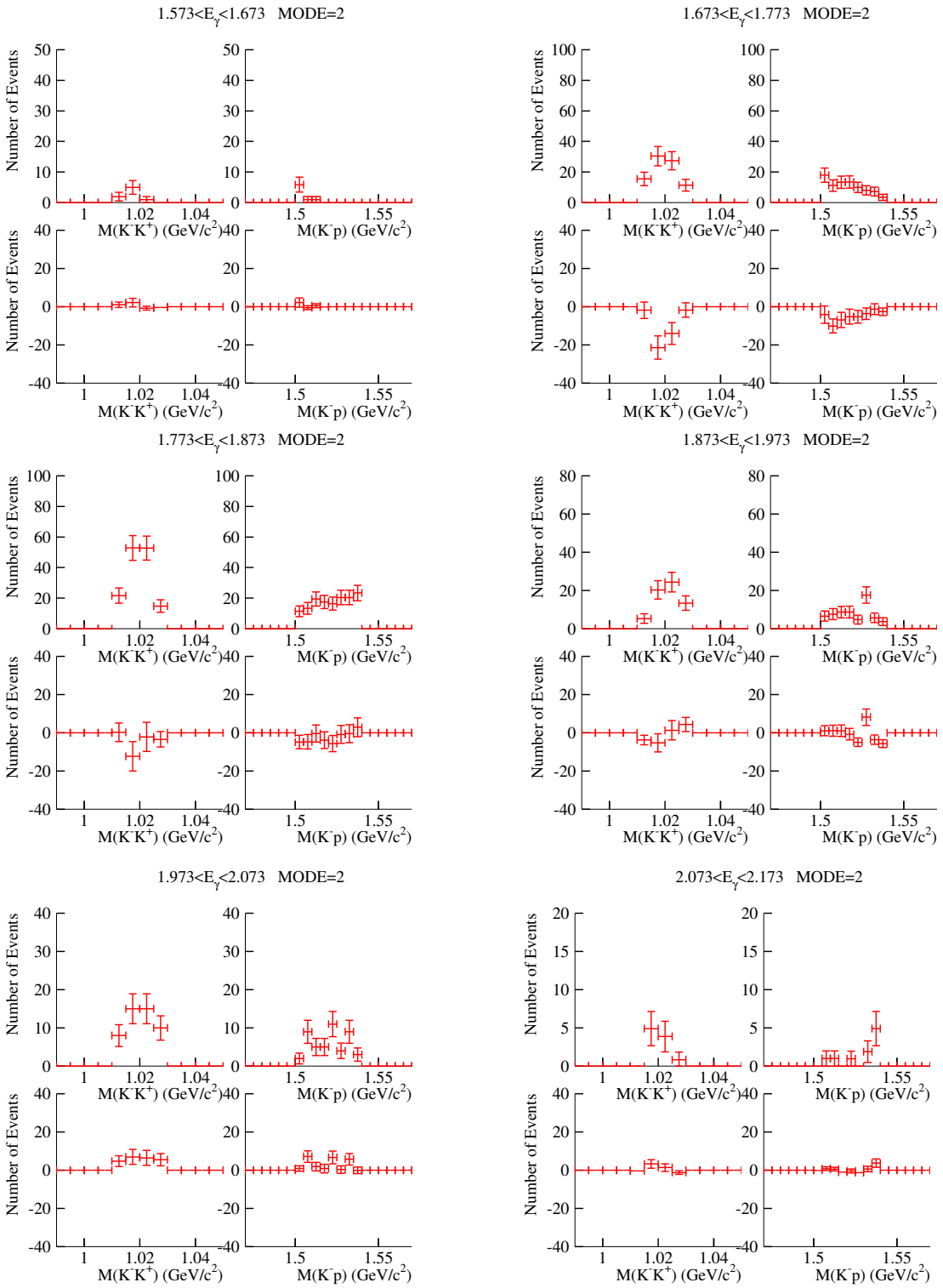

Figure F.2: The K^-K^+ and K^-p mass distributions for the K^-p events (MODE= 2) in the box region (top two figures in each energy bin) are displayed in the top two figures, while the relative yields compared to the expected yield for no interference are also displayed in the bottom figures.

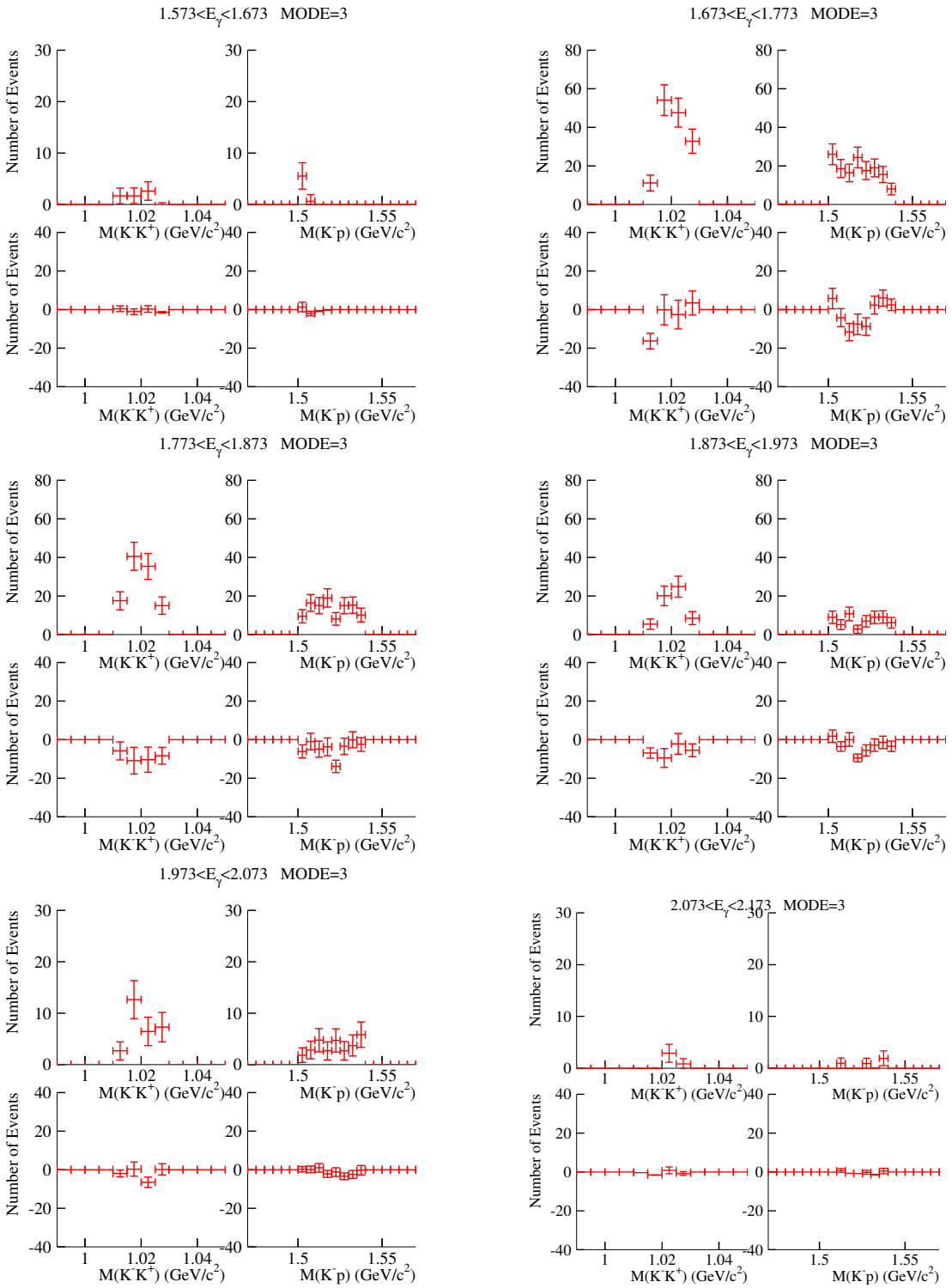

Figure F.3: The K^-K^+ and K^-p mass distributions for the K^+p events (MODE= 3) in the box region (top two figures in each energy bin) are displayed in the top two figures, while the relative yields compared to the expected yield for no interference are also displayed in the bottom figures.

List of Figures

List of Tables